

# Morphological Challenges at the Interface of Lithium Metal and Electrolytes in Garnet-type Solid-State Batteries

Dem Fachbereich Biologie und Chemie  
der Justus-Liebig-Universität Gießen  
vorgelegte Dissertation zur Erlangung  
des akademischen Grades  
Doktor der Naturwissenschaften  
– Dr. rer. nat. –

**Till Fuchs**

————— Dezember 2022 —————



Dekan / Dean	Prof. Dr. Thomas Wilke
1. Gutachter / 1 <sup>st</sup> Reviewer	Prof. Dr. Jürgen Janek (Justus-Liebig-Universität Gießen)
2. Gutachter / 2 <sup>nd</sup> Reviewer	Prof. Dr. Bernd Smarsly (Justus-Liebig-Universität Gießen)
Eingereicht / submitted	19.12.2022
Disputation	22.03.2023



## **Eidesstattliche Erklärung**

Die vorliegende Arbeit wurde im Zeitraum vom 01.11.2019 bis 19.12.2022 am Physikalisch-Chemischen Institut der Justus-Liebig-Universität Gießen unter Betreuung von Prof. Dr. Jürgen Janek angefertigt.

Ich erkläre: Ich habe die vorgelegte Dissertation selbstständig und ohne unerlaubte fremde Hilfe und nur mit den Hilfen angefertigt, die ich in der Dissertation angegeben habe. Alle Textstellen, die wörtlich oder sinngemäß aus veröffentlichten Schriften entnommen sind, und alle Angaben, die auf mündlichen Auskünften beruhen, sind als solche kenntlich gemacht. Ich stimme einer evtl. Überprüfung meiner Dissertation durch eine Antiplagiat-Software zu. Bei den von mir durchgeführten und in der Dissertation erwähnten Untersuchungen habe ich die Grundsätze guter wissenschaftlicher Praxis, wie sie in der „Satzung der Justus-Liebig-Universität Gießen zur Sicherung guter wissenschaftlicher Praxis“ niedergelegt sind, eingehalten.

Gießen, 19.12.2022

---

Till Fuchs



 *Was sagt 'ne Möwe zum Bestatter?*



## Abstract

To achieve a fast transition to renewable energies and electrification of vehicles, developing safe, high energy and power density storage is detrimental. The use of lithium metal anodes in combination with a solid electrolyte in solid-state batteries could offer exactly this combination. Traditional liquid electrolyte-based batteries soon reach their physicochemical limit in terms of energy and power density, as side reactions and dendrites limit these cells to graphite as the anode instead of lithium. Unlike solid-state batteries, lithium-ion batteries furthermore pose greater safety concerns due to the risk of leaking and high flammability. However, while promising, ensuring a safe implantation of electrode|solid electrolyte interfaces is still regarded as the key challenge to overcome. Whereas highly resistive interfaces are the major concern for the cathode|solid electrolyte interface, morphological issues such as dendrites and contact loss limit the anode|solid electrolyte interface.

It was shown that a slow vacancy diffusion within lithium metal inherently limits the applicable current density for discharging a lithium metal anode. For every lithium atom stripped, an electron and a vacancy are left behind within the lithium metal anode. If the vacancy injection rate due to the discharge current is higher than the rate of lithium replenishment by diffusion or plastic deformation, the vacancies will accumulate at the interface and form resistive pores. Another challenge is the control of lithium morphology upon deposition, be it either on a lithium reservoir or on a metal current collector. Frequent issues include the penetration of lithium into the solid electrolyte by the formation of dendritic structures or a very heterogeneous island-like growth, drastically limiting cell cyclability.

Therefore, this dissertation focuses on understanding and mitigating the morphological issues linked to the use of metal anodes and their impact on battery operation. First, however, the interfacial degradation of the used model system of  $\text{Li}|\text{Li}_{6.25}\text{Al}_{0.25}\text{La}_3\text{Zr}_2\text{O}_{12}|\text{Li}$  was investigated using X-ray photoelectron spectroscopy and impedance spectroscopy. After finding a negligibly thin interphase, several strategies were employed and investigated regarding their success in compensating or even suppressing pore formation during anodic lithium dissolution. This includes altering the lithium metal grain structure, dispersing carbon nanotubes into lithium and using ionic liquids as pore filling agents. Especially the latter two methods yield a strong improvement in dissolution capacity to  $> 20 \text{ mAh cm}^{-2}$ . Moreover, the lithium morphology was investigated during deposition on a metal current collector in dependence of the applied current density and metal thickness by developing a novel technique. A direct operando visualization of lithium growth below a thin metal current collector using an electron microscope allowed the observation of the lithium nucleation density as a function of current density.

Overall this dissertation expands the knowledge on morphological challenges occurring at the  $\text{Li}|\text{solid electrolyte}$  interface during discharge and lithium deposition at metals during charge without the presence of a lithium reservoir. Based on this knowledge, several mitigation strategies were developed and investigated, paving the way for future optimization to mitigate and compensate morphological instabilities during operation inherent for lithium metal anodes. For example, it could be shown that it might be necessary to shift away from pure lithium metal to anode composites, as a means to tailor both the anode's electrochemical and mechanical properties to the desired application.



## Zusammenfassung

Um einen zügigen Wandel zu erneuerbaren Energien und eine einhergehende Elektrifizierung von Kraftfahrzeugen zu schaffen, sind sichere Energiespeicher mit hoher Energie- und Leistungsdichte von enormer Relevanz. Durch die Verwendung von Lithium als Metallanode könnten Feststoffbatterien mit einem festen Separator genau diese Bedingungen erfüllen. Batterien mit flüssigem Elektrolyten werden nämlich bald ihr physikochemisches Limit erreichen, da diese aufgrund von chemischer Degradation und Dendritenbildung auf die Verwendung von Graphit als Anodenmaterial beschränkt sind. Feststoffbatterien hingegen bieten bessere Sicherheit, da keine der Komponenten entflammbar sind oder gar auslaufen können. Trotz vielversprechender Eigenschaften gibt es allerdings einige Hürden zu überwinden, bevor eine sichere Implementierung von Metallanoden in Feststoffbatterien möglich ist. Durch die feste Natur der Separatoren limitieren morphologische Probleme wie Kontaktverlust und Dendriten die Stromstärke an der Li|Festelektrolyt-Grenzfläche.

So konnte gezeigt werden, dass die langsame Leerstellendiffusion in Lithium inhärent die Entladestromdichte limitiert, da für jedes oxidierte Lithiumatom eine Leerstelle in das Metall induziert wird. Ist jedoch die Rate des Lithiumnachschiebs zur Grenzfläche geringer als die Leerstelleninduktion, akkumulieren diese sich zu resistiven Poren an der Grenzfläche. Eine andere Hürde ist die ungleichmäßige Lithiumdeposition sowohl auf einem Stromsammelr als auch auf einem Lithiumreservoir während des Ladens. Typischerweise bilden sich heterogene Morphologien aus, welche durch Dendriten- oder Inselwachstum die Zyklisierbarkeit der Zelle limitieren.

Der Fokus dieser Doktorarbeit liegt daher darauf, den Einfluss von morphologischen Problemen und etwaigen Vermeidungsstrategien auf die Batterieoperation zu verstehen. Zunächst wurde dafür ein geeignetes Modellsystem der Art  $\text{Li}|\text{Li}_{6,25}\text{Al}_{0,25}\text{La}_3\text{Zr}_2\text{O}_{12}|\text{Li}$  präpariert und mittels Röntgenphotoelektronenspektroskopie und Impedanzspektroskopie untersucht. Nach Sicherstellung vernachlässigbar dünner Grenzphasen wurden verschiedene Strategien zur Unterdrückung und Kompensation der Porenformation untersucht. Dabei wurde die Mikrostruktur des verwendeten Lithiums gezielt kontrolliert, Kohlenstoffnanoröhren in Lithium dispergiert oder ionische Flüssigkeiten als Mittel zur Porenkompensation eingesetzt. Insbesondere die letzten zwei Möglichkeiten führten zu einer erfolgreichen Verbesserung der Entladekapazität auf  $> 20 \text{ mAh cm}^{-2}$ . Darüber hinaus wurde auch die Lithiummorphologie bei Deposition auf einem Metalleiter in Abhängigkeit der Stromdichte und Ableiterdicke untersucht. Eine neu entwickelte Operando-Methode erlaubte dabei die Visualisierung der Lithiumkeimdichte als Funktion der Stromdichte mittels eines Elektronenmikroskops.

In dieser Dissertation konnten die bestehenden morphologischen Hürden bei der Metallabscheidung und -auflösung in Feststoffbatterien definiert und analysiert werden. Basierend auf den gewonnenen Erkenntnissen wurden neue Konzepte zur Unterbindung der Porenformation untersucht, um die Realisation und Optimierung von Metallanoden voranzubringen. Beispielsweise könnte es nötig sein, statt sich auf reines Lithium auf Anodenkomposite oder Hybridkonzepte zu fokussieren, da es dadurch möglich ist, sowohl die elektrochemischen als auch die mechanischen Eigenschaften der Anode gezielt auf eine mögliche Anwendung zuzuschneiden.



## List of Abbreviations

BEV	battery electric vehicle
CAM	cathode active material
CC	current collector
CCD	critical current density
CCP	critical current density for plating
CCS	critical current density for stripping
CNT	carbon nanotube
FIB	focused ion beam
GB	grain boundary
GEIS	galvanostatic electrochemical impedance spectroscopy
GHG	greenhouse gas
IL	ionic liquid
IPCC	international panel on climate change
LAGP	$\text{Li}_{1.5}\text{Al}_{0.5}\text{Ge}_{1.5}(\text{PO}_4)_3$
LATP	$\text{Li}_{1.5}\text{Al}_{0.5}\text{Ti}_{1.5}(\text{PO}_4)_3$
LE	liquid electrolyte
LIB	lithium ion battery
LiPON	lithium phosphorus oxynitride
LLZO	$\text{Li}_{6.25}\text{Al}_{0.25}\text{La}_3\text{Zr}_2\text{O}_{12}$
LMA	lithium metal anode
MCI	mixed ionic-electronic conducting interphase
NCM	nickel-manganese-cobalt-oxide
ODI	oxygen-deficient interlayer
RFC	reservoir-free-cell
SE	solid electrolyte
SEI	solid electrolyte interphase
SEM	scanning electron microscopy
SSB	solid-state battery
TEM	transmission electron microscopy
ToF-SIMS	time-of-flight secondary-ion mass spectrometry
UHV	ultra-high vacuum
XPS	X-ray photoelectron spectroscopy



## Table of Contents

<b>1</b>	<b>Introduction .....</b>	<b>1</b>
<b>2</b>	<b>Fundamentals.....</b>	<b>5</b>
2.1	Reactivity of Li Solid Electrolyte Interfaces .....	5
2.1.1	General Classifications of the Interface Stability .....	5
2.1.2	Reactivity of Li LLZO:M-Interfaces .....	6
2.2	Reservoir-Free Lithium-Metal-Batteries.....	8
2.2.1	Working Principle of RFCs .....	8
2.2.2	Advantages of RFCs.....	9
2.2.3	Challenges of RFCs.....	9
2.2.4	Influences on the Growth Modes in RFCs .....	11
2.3	Metal SE Interface under Anodic Load.....	14
2.3.1	Vacancy Diffusion Limiting the Applicable Current Density .....	14
2.3.2	Nucleation of a Pore and Surface Diffusion .....	15
2.3.3	Contact Loss at Li LLZO and Arising Constriction .....	15
2.3.4	Solution 1: Facilitating the Diffusion of Vacancies Inside the LMA.....	17
2.3.5	Solution 2: Pressure-Induced Creep Transport.....	18
2.3.6	Solution 3: Alternative Systems with IL or CNTs.....	19
2.4	Metal SE Interfaces during Cycling .....	21
2.4.1	The Concept of CCD Tests and Influential Parameters.....	21
2.4.2	Guideline on How to Test Either the LMA or the SE .....	23
2.4.3	Unidirectional Tests as a Means to Counter the Sensitive Nature of Cycling.....	24
<b>3</b>	<b>Results.....</b>	<b>27</b>
3.1	Publication 1: “Kinetic versus Thermodynamic Stability of LLZO in Contact with Lithium Metal” .....	27
3.2	Publication 2: “Current-Dependent Lithium Metal Growth Modes in ‘Anode-Free’ Solid-State Batteries at the Cu LLZO Interface” .....	37
3.3	Publication 3: “Overcoming Anode Instability in Solid-State Batteries through Control of the Lithium Metal Microstructure”.....	49
3.4	Publication 4: “Increasing the Pressure-Free Stripping Capacity of the Lithium Metal Anode in Solid-State-Batteries by Carbon Nanotubes”.....	60
3.5	Publication 5: “Working Principle of an Ionic Liquid Interlayer During Pressureless Lithium Stripping on $\text{Li}_{6.25}\text{Al}_{0.25}\text{La}_3\text{Zr}_2\text{O}_{12}$ (LLZO) Garnet-Type Solid Electrolyte”.....	72
<b>4</b>	<b>Conclusions.....</b>	<b>85</b>

<b>5</b>	<b>Outlook .....</b>	<b>87</b>
<b>6</b>	<b>References.....</b>	<b>89</b>
<b>7</b>	<b>Appendix.....</b>	<b>101</b>
7.1	Supporting Information .....	101
7.1.1	Publication 1: “Kinetic versus Thermodynamic Stability of LLZO in Contact with Lithium Metal” .....	101
7.1.2	Publication 2: “Current-Dependent Lithium Metal Growth Modes in ‘Anode-Free’ Solid-State-Batteries at the Cu LLZO Interface” .....	106
7.1.3	Publication 3: “Overcoming Anode Instability in Solid-State Batteries through Control of the Lithium Metal Microstructure” .....	113
7.1.4	Publication 4: “Increasing the Pressure-Free Stripping Capacity of the Lithium Metal Anode in Solid-State-Batteries by Carbon Nanotubes” .....	123
7.1.5	Publication 5: “Working Principle of an Ionic Liquid Interlayer During Pressureless Lithium Stripping on $\text{Li}_{6.25}\text{Al}_{0.25}\text{La}_3\text{Zr}_2\text{O}_{12}$ (LLZO) Garnet-Type Solid Electrolyte” .....	136
7.2	Scientific Contributions .....	144
7.2.1	List of publications published online as checked on the 19 <sup>th</sup> of December 2022 ....	144
7.2.2	List of Conference Contributions .....	146
<b>8</b>	<b>Acknowledgements .....</b>	<b>147</b>

## 1 Introduction

According to the International Panel on Climate Change (IPCC), every tenth of a degree Celsius more of an increase in average global temperature has enormous consequences and results in a variety of huge, progressively worse environmental catastrophes.<sup>1</sup> It is therefore worthwhile to reduce greenhouse gas (GHG) emissions and limit climate change as best as possible, even if insufficient with the necessary proposals to limit global warming to 1.5 °C as decided per the Paris Agreement.<sup>2</sup>

One puzzle piece in limiting the GHG emission is the use of rechargeable batteries for energy storage in vehicles or small-scale grid systems. By switching from a vehicle with a traditional combustion engine to a battery electric vehicle (BEV), the overall energy efficiency can be drastically improved by roughly 80 %. Additionally, depending on the vehicle's class, lifetime and mileage a decrease from 28 – 42 % of GHG emission is predicted for electrifying vehicles, due to the more efficient use of renewable energy sources.<sup>3</sup>

Although a wide variety of different battery types is used in technologies today, lithium-ion batteries (LIBs) with liquid electrolytes (LEs) dominate the overall market share of high energy - high power batteries.<sup>4-6</sup> However, LIBs are expected to reach their physicochemical limit in terms of energy density soon. Unlike LEs though, solid electrolytes (SEs) may enable the use of lithium metal as the anode material,<sup>7,8</sup> offering a higher safety by decreasing the flammability, risk for leakages and mechanical penetration by dendrites.<sup>8,9</sup> Solid-state batteries (SSBs) would therefore not only increase the safety of the cell, but also the energy density owing to lithium's lowest redox potential and highest specific capacity.<sup>10,11</sup> Another benefit when using an SE is the possible increase of the cells power density or rather rate capability. The reason is that SEs have a transfer number of lithium ions  $t_{\text{Li}^+}$  of virtually unity and exceed the ionic conductivity of LEs. This limits the polarization that can occur during (dis)charging since no anions migrate as in the case of LEs. Therefore, striving for SSBs is the next logical step for battery technology in terms of safety, as well as energy and power density.

Despite the advantages accompanied by the use of SEs, they chemically react with lithium metal. This can either be in the form of a self-limiting solid electrolyte interphase (SEI) or a continuously propagating mixed conducting interphase (MCI).<sup>12,13</sup> No practically relevant SE with high ionic conductivity is thermodynamically stable in combination with lithium metal.<sup>14</sup> For example, the argyrodite  $\text{Li}_6\text{PS}_5\text{Cl}$  forms an SEI with a thickness of  $> 100$  nm.<sup>12</sup> Other promising SEs such as  $\text{Li}_{1.5}\text{Al}_{0.5}\text{Ge}_{1.5}(\text{PO}_4)_3$  (LAGP) will even degrade completely, forming a mm-thick MCI.<sup>12</sup> Only variants of cubic- $\text{Li}_7\text{La}_3\text{Z}_2\text{O}_{12}$  show a virtually stable interface towards lithium metal, as the SEI is limited to a nm-thin layer of only a few unit cells.<sup>12,15,16</sup> Additionally, lithium will form an inhomogeneous and uncontrollable surface passivation layer even in gloveboxes,<sup>17,18</sup> what further complicates the cell preparation. This motivates so-called "anode-free" cells, in which lithium is plated during the first charging step.<sup>19</sup>

Differently spoken, in "anode-free" cells the lithium reservoir at the anode side is omitted during cell assembly,<sup>19-21</sup> which is why this concept is referred to as a reservoir-free cell (RFC) within this work. This concept works, as cathode active materials (CAMs) are usually synthesized in a lithiated (or discharged) state.<sup>22,23</sup> Excluding lithium loss mechanisms, a lithium reservoir hence only adds unnecessary weight to a cell. In an RFC, the lithium anode is therefore generated by depositing the metal directly on the current collector (CC) during the first charging step. With this cell design, the challenging and expensive handling of lithium foil and its surface degradation is avoided.

Moreover, the time for a reaction to occur between lithium and the SE is limited and begins upon cell cycling instead of directly after assembly. Although some groups seem to have solved this issue,<sup>24</sup> it is yet additionally difficult to properly control the lithium growth to a desired film in RFCs.<sup>19,21</sup>

Another challenge that is present in both traditional SSBs and RFCs occurs due to the stiff and brittle nature of inorganic SEs, since they cannot compensate volume changes of electrode materials during cycling.<sup>8,25,26</sup> Contact issues between electrode material and SE are the most important challenge in order to realize a competitive SSB, independent from the presence of a lithium reservoir. For example, even ductile SEs such as  $\beta$ -Li<sub>3</sub>PS<sub>4</sub> or Li<sub>6</sub>PS<sub>5</sub>Cl cannot compensate the contraction of nickel-manganese-cobalt-oxide (NCM) particles during discharge, which leads to partial loss of contact within the cathode and therefore to a capacity fading.<sup>26</sup> Secondary NCM particles are also prone for cycling-induced cracking, which is not compensated by a non-flowing SE.<sup>27</sup> Several concepts to mitigate contact issues in composite cathodes exist, such as immense stack pressures,<sup>28–30</sup> careful structural engineering of “zero-strain” electrode materials<sup>22</sup> or material combinations.<sup>31</sup>

Contact issues are unfortunately not limited to the cathode side and cathode composites but also occur at metal anodes. For example, the formation of pores during discharge (stripping) is frequently identified as the current-limiting step, as it will ultimately lead to a contact loss between the lithium metal anode (LMA) and SE. Krauskopf et al. identified an insufficient vacancy diffusion within lithium metal as the reason for pore formation.<sup>7,32,33</sup> For every oxidized Li-atom, a Li-ion transfers into the SE, which forms a vacancy at the interface. If the rate of replenishing lithium at the interface is lower than the rate of vacancy injection via stripping, they will accumulate at the interface and form micron-sized pores. The effective electrode area is subsequently decreased and the local current density is increased, which facilitates even faster growth of already existing pores until most of the electrode has lost contact to the SE.

The formation of pores at the interface additionally acts as the main precursor for dendrite initiation.<sup>34</sup> After pores have formed on one electrode and the current direction is switched during cycling, lithium deposition needs to take place at the already porous interface. This leads to a strong increase in local current density and possibly to the growth of lithium filaments into the SE. As shown for both sodium and lithium metal electrodes, pores are only refilled to a low extent by deposited lithium and will continue to grow upon further stripping steps.<sup>35,36</sup> Dendrites will then either dynamically grow and are dissolved again or directly short-circuit the cell during subsequent cycling. This shows that the issue of short-circuiting due to the formation of dendrites is only of secondary nature, since it is heavily facilitated by the prior growth of pores at the interface. It therefore needs to be investigated how to influence the pore formation or possibly even avoid it.

Key parameters influencing the pore formation are the applied current density during stripping and stack pressure. The former is pretty simple, the higher the applied current density, the higher is also the rate of vacancy injection into the metal. However, as the rate of replenishing is rather unaffected by the applied current, pores will grow earlier during the stripping process for higher current densities, which has already been experimentally confirmed.<sup>33,37</sup> On the other hand, pressure will introduce a third factor and influence the balance between vacancy injection and lithium replenishment. When stack pressure is applied, creep within the metal is enhanced. And, if the pressure exceeds the LMAs yield strength, lithium can plastically deform to suppress the formation of pores. However, the pressure required to suppress pore formation of practically relevant current densities  $> 1 \text{ mA cm}^{-2}$  is with several MPa too large to apply in practical cells, requiring more

suitable solutions. Lowering the pressure while simultaneously increasing the discharge capacities for LMAs is possible, e.g. by 3D-interfaces,<sup>38</sup> employing an ionic liquid (IL) as a pore filling agent<sup>39</sup> or altering the LMA by alloying or mixing with other components.<sup>33,40</sup>

In this dissertation, morphological and chemical changes at the Li|SE interface and their respective impact on the LMA performance in SSBs are investigated. Novel concepts, such as using ILs in otherwise all-solid batteries or carbon nanotubes (CNTs) within the LMA as means to mitigate pore formation during discharge are investigated via operando electrochemical measurements and electron microscopy. Paired with a detailed analysis of lithium growth morphology, this work presents an important part in guiding future anode development for SSBs.

In publication 1 of this dissertation, titled “Kinetic versus Thermodynamic Stability of LLZO in Contact with Lithium Metal”, the extent of degradation at the Li|Li<sub>6.25</sub>Al<sub>0.25</sub>La<sub>3</sub>Zr<sub>2</sub>O<sub>12</sub> (LLZO) interface was investigated in dependence on the energy input during lithium deposition. Therefore, thin lithium films were deposited using (i) sputter deposition (high energy), (ii) electron-beam physical vapor deposition (low energy) and (iii) *operando* electron-beam electrochemical deposition. It was shown that a thin interphase only forms when a kinetic barrier is overcome, e.g. by lithium sputtering with high kinetic energy (0.1 – 1.0 eV). This work therefore gives closure to the reoccurring question, whether lithium and LLZO are stable when in contact or not. Gained insights help to optimize the future fabrication of stable interfaces or design of interlayers to enable LMAs with SEs.

In publication 2 of this dissertation, titled “Current-Dependent Lithium Metal Growth Modes in ‘Anode-Free’ Solid-State Batteries at the Cu|LLZO Interface”, the morphology of lithium deposition at the Cu|LLZO interface in RFC designs is investigated in dependence on the applied current density and CC thickness. To investigate the lithium growth morphology in operando during plating, a novel technique was developed, where small and thin copper patches were contacted inside an electron microscope and growing lithium visualized during deposition. It was shown that the nucleation density strongly increases with higher current densities and that thick (> 5 μm) CCs are necessary to suppress a penetration thereof. Ultimately, this work paves the way for future optimization of the CC|LLZO interface and deposition parameters to successfully enable the growth of homogeneous lithium films within RFCs.

Publication 3 – 5 of this dissertation investigate different methods to overcome the pore formation during stripping at metal electrodes, which to date limits the applicable discharge current density.

In publication 3, titled “Overcoming Anode Instability in Solid-State Batteries through Control of the Lithium Metal Microstructure”, an influence of the microstructure of lithium on the stripping properties was observed. It was shown that lithium with large grains is beneficial for the stripping properties when no pressure is applied to the cell. However, if it is possible to apply stack pressures in a cell system (e.g. 2 MPa), small-grained lithium is superior in resupplying lithium to the interface during stripping, since dislocations and grain boundaries enhance the lithium transport through Nabarro-Herring creep and plastic deformation.

In publication 4, titled “Increasing the Pressure-Free Stripping Capacity of the Lithium Metal Anode in Solid-State-Batteries by Carbon Nanotubes” CNTs were added to lithium to form a composite anode. This material proved to be superior to pure lithium without the application of stack pressure, as it increased the discharge capacity to > 20 mAh cm<sup>-2</sup> through expanding the dissolution process from only at the interface to also in the bulk of the LMA. A change of mechanical properties of the anode material was also investigated in detail and correlated with its

electrochemical performance when stack pressure is applied, paving future optimization of anode materials to perfectly fit the respective battery systems and mechanical boundary conditions.

In publication 5, titled “Working Principle of an Ionic Liquid Interlayer During Pressureless Lithium Stripping on  $\text{Li}_{6.25}\text{Al}_{0.25}\text{La}_3\text{Zr}_2\text{O}_{12}$  (LLZO) Garnet-Type Solid Electrolyte”, the concept of using small amounts of an LE at the interface was investigated with regard to its ability of mitigating pore formation during discharge. It could be shown that pores at the interface can be compensated reliably by a flowing liquid to enhance the discharge capacity. This fundamentally challenges the academic view of cells necessarily having to be strictly all-solid, as hybrid approaches may prove to be superior in the end.

Overall, the presented results within this dissertation stress how ensuring good contact between the solid electrodes and the separator is both of utmost importance to guarantee a well cycling battery and simultaneously very difficult due to physicochemical limitations. Furthermore, the lithium growth morphology in RFCs was investigated in dependence of CC thickness and applied current density, for which a novel operando SEM method was developed, allowing the direct visualization of lithium growth at the metal|SE interface. Additionally, different mitigation strategies to avoid contact loss due to pore formation while stripping are conceived and presented, showing great potential to increase the anode discharge capacity to over  $> 20 \text{ mAh cm}^{-2}$ . Fundamentally, this dissertation shows that it may be impossible to achieve good dissolution performance ( $> 5 \text{ mA cm}^{-2}$ ,  $> 5 \text{ mAh cm}^{-2}$ ) with a simple planar Li|SE interface and no applied pressure, which warrants an extensive assessment of mitigation strategies.

## 2 Fundamentals

This chapter serves as a brief summary of the scientific knowledge already present in literature regarding the reactivity between lithium and SEs. However, the main focus is put on morphological issues arising when stripping or plating lithium at metal electrodes. Special attention is given to the pore formation during discharge of a cell, which is identified as the key bottleneck for the implementation of practical SSBs with LMAs.

### 2.1 Reactivity of Li|Solid Electrolyte Interfaces

#### 2.1.1 General Classifications of the Interface Stability

The practical stability between lithium and an SE depends not only on their thermodynamic compatibility but also on the kinetics of possible degradation reactions. Thermodynamically, most promising SEs are not stable in contact with lithium.<sup>14,41</sup> However, despite nearly all SEs being thermodynamically unstable, they differ greatly in their interface properties in combination with lithium electrodes. Whereas thiophosphate SEs react with lithium by forming thick interphases or even continuous bulk reactions, LLZO and its variants are virtually stable bar nanometer-thick interphases.<sup>15,16,42</sup> To answer this striking difference, the nature of the forming interphase needs to be analyzed, which can be one of the following three cases as depicted in Figure 1.<sup>13,43</sup> These cases are generally possible, independent of whether the driving force for the reaction is of chemical or electrochemical nature.<sup>44</sup>

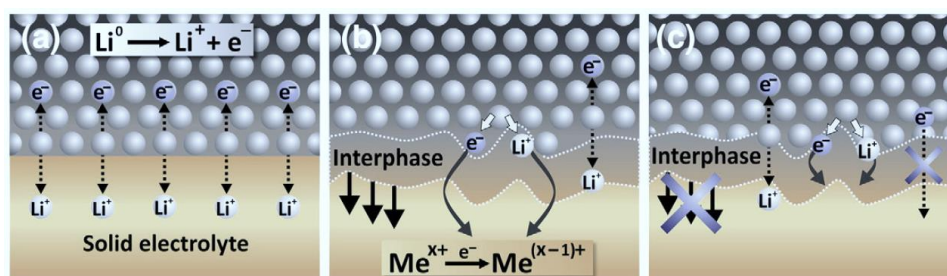


Figure 1. Three types of possibilities at the Li|SE interface: a) thermodynamically stable without any interphase formation, b) an MCI and c) a solely ionically conductive SEI. Reproduced with permission from reference 13. Copyright 2015 Elsevier.

If the Li|SE interface is thermodynamically stable as schematically depicted in Figure 1a, no SE reduction occurs when in contact with lithium. As lithium has the lowest electrode potential of -3.04 V versus the standard hydrogen electrode, Zhu et al. predict that solely some binary lithium compounds like LiF, LiCl or Li<sub>3</sub>N fulfill this condition.<sup>14</sup> No practically relevant SE with conductivities > 1 mS cm<sup>-1</sup> is thermodynamically stable in contact with lithium.

An MCI as shown in Figure 1b forms when the reduction products of the degradation are electronically and ionically conductive. The consequence of such an interphase composition is that it will continuously grow with time and possibly consume the whole electrolyte. If an MCI formation between an SE and lithium is not severely kinetically hindered, the use of that SE in combination with lithium can be ruled out completely due to the high resistance of a thick MCI. One prominent example is the reaction of a Li<sub>1+x</sub>Al<sub>x</sub>Ti<sub>2-x</sub>(PO<sub>4</sub>)<sub>3</sub> (LATP) SE in combination with lithium, which prompts the reduction of Ti<sup>4+</sup> to Ti<sup>0</sup> and therefore induces a large electronic conductivity to the continuously forming interphase.<sup>12,45</sup>

The third possibility is an interphase composed of solely ionically conducting products as seen in Figure 1c. This means that an initial reaction occurs but is self-limited to a very thin layer. The thickness of such an SEI is still topic of recent investigations, but can vary by a large margin in dependence of the material system. For example, the SEI between the argyrodite  $\text{Li}_6\text{PS}_5\text{Cl}$  is measured to be around 150 nm via time-of-flight secondary-ion mass spectrometry (ToF-SIMS).<sup>12</sup> However, many LLZO based SEs show such a thin SEI of only a few unit cells that they were long thought to be thermodynamically stable in contact with lithium metal.<sup>15,16</sup> Note that the concept of a fully electronically insulating interphase is usually not correct when talking about SEIs. However, in cases where the electronic conductivity and the interphase growth is negligible for the application, the term SEI is used.

### 2.1.2 Reactivity of Li|LLZO:M-Interfaces

This chapter focuses on the much discussed and analyzed stability of lithium versus LLZO and its variants. Note that while LLZO generally refers to pentanary cubic compounds such as  $\text{Li}_{6.25}\text{Al}_{0.25}\text{La}_3\text{Zr}_2\text{O}_{12}$  within this thesis, Chapter 2.1.2 uses the notation of LLZO:M to specifically describe what element is substituted into quaternary  $\text{Li}_7\text{La}_3\text{Zr}_2\text{O}_{12}$  due to its relevancy on this specific topic.

$\text{Li}_7\text{La}_3\text{Zr}_2\text{O}_{12}$  is expected to have a reduction potential of 50 mV versus  $\text{Li}^+/\text{Li}$  with the formation of Zr or  $\text{Zr}_3\text{O}$ ,  $\text{La}_2\text{O}_3$  and  $\text{Li}_2\text{O}$  at lower potentials.<sup>14</sup> However, practical examples show that some pentanary materials, such as LLZO:Al and LLZO:Ta are virtually stable in contact with lithium metal and do not exhibit any interfacial impedance associated with charge transfer or an interphase.<sup>7,19,32,46</sup> X-ray photoelectron spectroscopy (XPS) results and impedance analysis further indicate that the stability of LLZO is strongly dependent on the substituents used for stabilizing the desired cubic crystal structure.<sup>47</sup> For example, Li|LLZO:Nb shows an increase in interfacial impedance with time underlined by a strong reduction of  $\text{Zr}^{4+}$  and  $\text{Nb}^{5+}$  shown by XPS. Another work shows the continuous and pronounced reaction of LLZO:Ga with lithium metal,<sup>48</sup> which is therein explained by the tendency of lithium to alloy with gallium.

However, the stability of the most commonly used variant, which is LLZO:Al, with lithium is still debated. On the one hand, several works employing electrochemical impedance spectroscopy show that there is no time-dependent growth in impedance and consequently no indication for interfacial degradation.<sup>32,37,49,50</sup> Additionally, carefully conducted ToF-SIMS depth profiling also cannot find evidence of the formation of any interphase between lithium and LLZO:Al.<sup>12</sup> On the other hand, transmission electron microscopy (TEM) and XPS investigations prove the existence of a very thin interphase with an oxygen deficiency, which results in a tetragonal LLZO layer.<sup>15,47</sup>

Closure to this discrepancy could be brought by comparing the Li|LLZO:Al interface when lithium is deposited with different techniques. It could be shown that when the energy input during deposition is high, for example during sputter deposition, a more pronounced interphase resulting in  $\text{Zr}^{4+}$  reduction is observed.<sup>16</sup> If instead a method like electron-beam vapor deposition is chosen where the energy input is lower by more than an order of magnitude, no  $\text{Zr}^{4+}$  reduction was observed using XPS. A question that subsequently arises is in what capacity this affects the electrochemical performance, e.g. resistance of the interface. Impedance spectroscopy carried out on Li|LLZO:Al interfaces could show that there is no difference between cells in which the electrode was electrochemically plated beforehand, sputtered or deposited by electron-beam vapor deposition. This means that either the resulting interphase has no effect on charge transfer or that the overvoltage during impedance acquisition is already sufficient to form the interphase in cells

previously clear thereof. This therefore presents a confirmation that the Li|LLZO:Al interface is virtually stable and well suited for practical applications and model studies alike.

Another interesting concept is the deliberate use of miniscule changes of the LLZO surface chemistry. For example, it could be possible to introduce dopants at the interface to control which degradation products form and which properties the SEI will have. One recent work explores this concept by a protonation of an LLZO:Ta surface ( $\text{Li}^+/\text{H}^+$  exchange), which in contact with lithium leads to the formation of the insulating  $\text{Li}_3\text{TaO}_4$  phase instead of conductive Ta metal as one of the degradation products.<sup>51</sup> Steering the degradation from electronically conducting Ta metal to insulating  $\text{Li}_3\text{TaO}_4$  therefore changes the interphase from a slow but continuously propagating MCI to a self-limited SEI. Unfortunately, the influence on the electrochemical properties is difficult to assess, since the LLZO surface morphology is changed by protonation as well. However, this concept is still promising to tune the degradation of SEs in contact with lithium without changing the bulk electrolyte, especially as large-scale ion implementation techniques are already available to control the surface concentration of dopants.<sup>52-54</sup>

## 2.2 Reservoir-Free Lithium-Metal-Batteries

Previous works were able to show, that a clean and pristine interface between lithium and an SE is possible in model systems by carefully preparing lithium foils and attaching these to the SE at extreme pressures of  $> 300$  MPa.<sup>32,55</sup> While this is a suitable system for the scientific study of the interface kinetics, large-scale systems with regards to a possible application require a scalable solution. A possible way to circumvent the need for handling lithium metal and simultaneously limiting the reaction with the SE is the use of a so-called “anode-free” cell configuration. Therein, the lithium reservoir is not present during fabrication but rather deposited in the first charging step of the cell. The following chapter therefore deals with the CC|LLZO interface with regards to the very first formation step in RFCs.

### 2.2.1 Working Principle of RFCs

Usually, SSBs are assembled using an SE separator, a cathode composite and lithium metal as the anode material. However, as CAMs are manufactured in a lithiated (discharged) state, the lithium foil on the anode adds unnecessary weight and volume since the cell cannot be further discharged. Therefore, RFCs are simply assembled with a metal CC on the anode side. The lithium anode is then formed in the first charging step by delithiating the CAM as depicted in Figure 2.

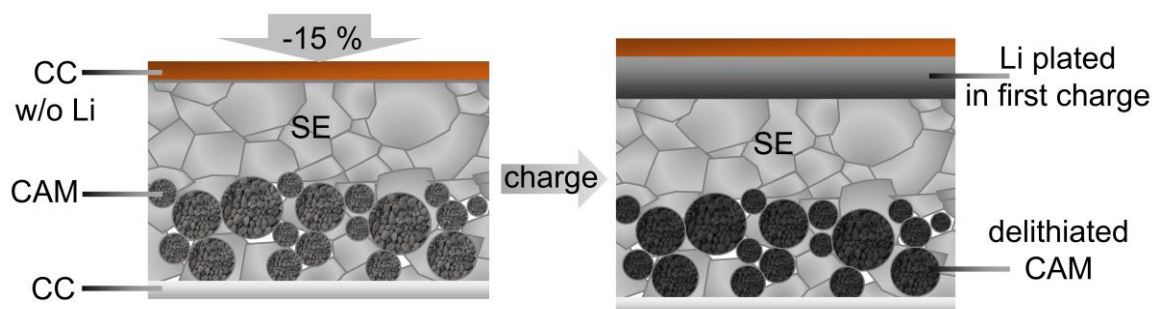


Figure 2. Schematic depiction of the charging process in an SSB without lithium reservoir or RFC. By omitting the lithium reservoir, an increase of around 15 % in energy density can be achieved.

Promising results on RFCs were published by the company QuantumScape,<sup>24</sup> who showed the possibility to charge  $13.3 \text{ mAh cm}^{-2}$  with  $3.3 \text{ mA cm}^{-2}$  at  $25^\circ\text{C}$  and 3.4 bar at a planar Cu|SE interface. It is, however, not clear based on their data if a thin lithium reservoir was plated under milder conditions beforehand or if lithium was plated directly onto the CC during charging.

Another promising concept are carefully engineered silver-carbon composite CCs.<sup>9,56</sup> By incorporating silver nanoparticles into a carbon matrix, it is possible to deposit  $> 20 \mu\text{m}$  of lithium reversibly, which is close to the practical target set by Albertus et al. of  $30 \mu\text{m}$ .<sup>10</sup> However, the working principle and reason for the beneficial properties of the silver-carbon anodes has yet to be fully understood. To elucidate the working principle of such three-dimensional concepts, first the deposition at planar metal|SE interfaces has to be thoroughly understood on a physicochemical level.

### 2.2.2 Advantages of RFCs

#### i. Higher Energy Density

By removing the unnecessary weight of the lithium reservoir upon cell assembly, the volumetric energy density of the cell can be increased up to 15 % when considering a 30  $\mu\text{m}$  lithium reservoir present otherwise.<sup>19,57</sup> It is hereby assumed that no excess lithium is needed to compensate for lithium losses, e.g. by interphase or “dead” lithium formation.<sup>58,59</sup>

#### ii. Simpler Fabrication

The biggest motivation to consider the use of RFCs are practical advantages. The anode in RFCs can be assembled by depositing a suitable metal layer onto the SE, which can be done by a variety of different methods, for example thermal vapor deposition,<sup>21</sup> sputtering,<sup>60–62</sup> high temperature diffusion bonding<sup>19,63</sup> or just simple mechanical lamination.

Thereby, the need to handle lithium metal is omitted, which introduces a lot of practical benefits. As previously discussed, lithium will always react with the surrounding atmosphere due to trace amounts of  $\text{O}_2$ ,  $\text{H}_2\text{O}$ ,  $\text{N}_2$  and other gases,<sup>17</sup> forming unpredictable and resistive passivation layers. Not only is it more practical and cost-effective to circumvent the handling of lithium foils, it is additionally safer due to its highly reactive nature.

#### iii. Predictable Storage and Interface Degradation

Benefits of RFCs additionally arise when considering the timeline from fabrication until use of the battery cell. After assembly, no lithium metal is present yet in RFCs. What follows is that the requirements and precautions needed for the storage of RFCs are also easier. Besides the improved safety when storing cells without lithium metal, practical benefits regarding the interface to the SE arise as well.

When considering the interface between an SE and lithium metal, the thickness of possible interphases will depend on the duration the materials are in contact, especially in the case of MCIs.<sup>13</sup> This means that cells being assembled will then form different interphases in dependence on their storage duration before use, which requires a logistically sophisticated system of cell distribution and storage time. In contrast, SEs are usually stable in contact to the metal layers used as CCs in RFCs, which means that no interphase is formed and the cells remain unchanged during storage. If lithium metal is then deposited at the anode during the first charging step of an RFC, a definitive time can be calculated since when a degradation may occur in the cell.

### 2.2.3 Challenges of RFCs

Besides a plethora of advantages, different challenges need to be overcome before a practical realization of RFCs. However, due to promising first results from companies like Samsung and QuantumScape,<sup>9,24</sup> RFCs seem to be viable even in larger cell systems and not only at laboratory-scale. Both the influential parameters and challenges of RFCs are summarized in Figure 3 and explained in the following.

#### i. Necessity for Higher CAM Loadings due to the Formation of “Dead” Lithium

Now that no lithium excess is present in RFCs, lithium loss in the cell cannot be compensated by a lithium reservoir. Since small lithium losses to SEI formation or contact loss directly lead to a reduction in capacity, the requirements for the RFCs Coulomb efficiency are even higher for the desired long cycle-life of the cells. Lithium loss additionally occurs by lithium alloying with the

CC metal, as even copper incorporates up to 14 at% (1.5 wt%) of lithium into its crystal structure.<sup>64–67</sup> Other metals like gold or silver even form different alloy phases with lithium, changing the electrode potential irreversibly, thereby also decreasing the Coulomb efficiency.<sup>68,69</sup>

Alternatively, instead of increasing the Coulomb efficiency, the cathode design has to be tuned to compensate for an initial lithium loss. This then has strong implications on the cathode loading, microstructure, tortuosity and general electrochemical performance,<sup>70–72</sup> which needs to be considered for RFCs.

#### ii. Challenge to Deposit Homogeneous Lithium Films

For an RFC to have a long cycle life and high Coulomb efficiency, the control of the morphology of plated lithium is of utmost importance. The growth of a homogeneous film without dendrites and whiskers with a thickness of around 30 – 40  $\mu\text{m}$  is desired for a competitive cell.<sup>19,57</sup> Currently, however, it proves to be very challenging to grow thick, homogeneous films with the best success only coming close to the target when applying about 1 – 5 MPa of pressure during film formation.<sup>19</sup>

A frequent issue during film formation is the growth of whiskers, which penetrate the CC layer above the SE<sup>21</sup> and are not to be confused for dendrites. This leads to an inhomogeneous contact area between lithium and the SE and ultimately to current focusing at these whiskers. Said current focusing can facilitate the formation of dendrites into the SE, ultimately short-circuiting the cell. Additionally, the local current density will be much higher upon stripping from this morphology, as the electrode area is overestimated under the assumption of a homogenous film. This then can lead to contact loss of the whole electrode.

Another difficulty is the delamination of the CC from the SE caused by the pressure built up from the growing lithium underneath.<sup>63</sup> This effectively reduces the active contact area and also leads to whisker formation. When delamination occurs, it is impossible to nucleate new lithium particles by reducing  $\text{Li}^+$ , since the electronic connection between the surface of the SE and the CC is disrupted.

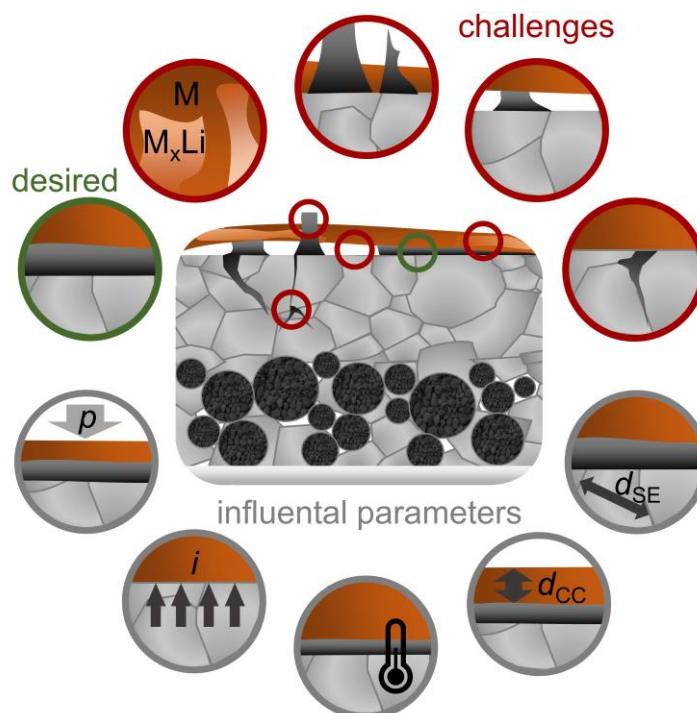


Figure 3. Schematic depiction of suboptimal plated lithium in an RFC with a composite cathode, solid separator and planar CC on the anode side. The top circles show different morphologies during growth, of which the film-growth is desired (green circle). Alloying with the CC, penetration thereof and whisker growth as well as dendritic growth are fundamentally damaging to the cell properties (red circles). Influential parameters are depicted in the bottom half of the figure, mainly being the applied stack pressure, current density, ambient temperature, CC thickness and SE properties, such as grain size (grey circles).

#### 2.2.4 Influences on the Growth Modes in RFCs

In the previous chapter, the different possibilities of detrimental lithium growth in RFCs were discussed. What remains subject of current research is how to control the nucleation and growth of lithium to be a homogeneous film and suppress the formation of whiskers and dendrites. Therefore, this chapter defines several key parameters to influence the lithium growth morphology. However, while frequently used interchangeably in literature, the nucleation and growth of lithium needs to be distinguished. Common experimental methods, such as SEM, are not able to resolve the formation of actual lithium nuclei the size of  $< 1$  nm and rather investigate the growth occurring after nucleation. Therefore, knowledge of the nucleation itself and its influences is very sparse, which is why the next paragraphs focus on the subsequent growth of lithium, if not explicitly stated otherwise.

A key variable to control the morphology of growing lithium is the applied current density and connected nucleation overpotential. Several works of Motoyama et al. show a proportionality between the current density and the area density of growing lithium particles at the CC|lithium phosphorus oxynitride (LiPON) interface.<sup>60–62,73</sup> It is theorized that a higher overpotential, e.g. by high plating currents, will lead to a higher density of supersaturated regions of  $\text{Li}^+$  within the amorphous SE at the interface to the metal, which then results in a higher density of nucleating lithium particles. This is corroborated with a particle density increase from around  $2 \cdot 10^6 \text{ cm}^{-2}$  ( $50 \mu\text{A cm}^{-2}$ ) to around  $20 \cdot 10^6 \text{ cm}^{-2}$  ( $1000 \mu\text{A cm}^{-2}$ ) at  $60 \text{ }^\circ\text{C}$ . This suggests that a more homogeneous or film-like growth surprisingly is easier, if higher current densities are used.

Whether these findings can be transferred to polycrystalline SEs, such as LLZO or  $\text{Li}_6\text{PS}_5\text{Cl}$ , is unclear as no work has yet been published investigating the current dependent deposition of lithium at these interfaces. A valid concern is that higher current densities also facilitate lithium growth into the SE, as observed for plating on a lithium reservoir.<sup>21,74–78</sup>

Much like the applied current density, the temperature also affects the overpotential for plating lithium at the CC|SE interface. In line with the above-mentioned theory, higher temperatures during plating should lead to lower overpotentials and therefore, also to a less homogeneous lithium growth. Observations made at the Cu|LiPON interface fit exactly this prediction, as the nucleation density decreases from around  $10^7 \text{ cm}^{-2}$  (60 °C) to  $10^6 \text{ cm}^{-2}$  (100 °C) at  $500 \mu\text{A cm}^{-2}$  as observed by operando SEM measurements.<sup>60</sup> Like the influence of current density, this has yet to be investigated for common polycrystalline SEs.

The application of stack pressure is expected to play a crucial role in the coalescence of separated lithium particles grown into lithium films. However, due to the buried nature of the CC|SE interface, extended studies on the pressure influence on the growth morphology are sparse. Another challenge is tuning the thickness of the applied CC layer. For very thin ( $< 1 \mu\text{m}$ ) layers, lithium can penetrate the CC during growth, which has a variety of negative consequences. For one, a penetration of the CC layer can lead to the growth of whiskers and overall low contact area between lithium and the SE.<sup>21</sup> Secondly, the loss of structural integrity means that the interface will deteriorate over time, possibly leading to suboptimal lithium growth during subsequent cycling of the cell. Additionally, the possible application of stack pressure is pointless in this case, because lithium will just get deformed after penetrating the CC, which consequently does not generate a higher contact area between lithium and the SE. Therefore, thick ( $>5 \mu\text{m}$ ) CC layers are needed to properly suppress the formation of lithium whiskers.

Despite the poor accessibility of the CC|SE interface, one study published by Kazyak et al. investigated the growth in operando by observing the top of the CC through a conducting but transparent glass using confocal microscopy.<sup>63</sup> With this setup, they could observe and quantify the influence of pressure on the coalescence of grown lithium islands through morphology changes of the attached copper foil. It was shown that already 1 – 5 MPa are sufficient to deform lithium islands into film-like structures by plastic deformation, which decreases the average height of islands by a factor of 2.<sup>63</sup>

The SE properties will naturally also influence the plating morphology. For example, surface defects like grain boundaries, holes or scratches from polishing can induce preferential sites for lithium plating.<sup>21,79</sup> Therefore, polycrystalline SEs will induce differences in lithium plating from amorphous or single crystalline materials. Depending on grain size, surface preparation and exact chemical composition, there can also be differences when using the same type of SE.

In publication 5 of this work, the influence of applied current density during plating was investigated at the Cu|LLZO system. It was found that for polycrystalline SEs, the nucleation density is also increasing as a function of current density like for amorphous LiPON.<sup>60</sup> Three different growth modes could be identified, which are (i) the isolated growth of small particles, (ii) a desired coalescence into a lithium film and (iii) a penetration of lithium into the SE by growing dendrites. The growth modes can occur simultaneously and strongly depend on the applied current density and thickness of the CC, which is summarized in Figure 4. For thin CCs, a penetration thereof is frequently observed, which impedes the coalescence of isolated lithium particles to homogeneous film.

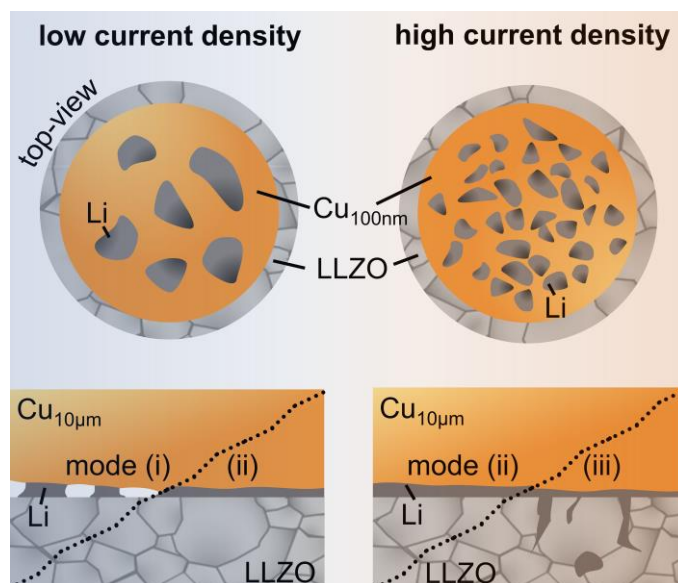


Figure 4. Schematic showing the dependency of different growth modes occurring at the Cu/LLZO interface for thin CC films (top) and thick CC foils (bottom) for low and high current densities. This figure was reproduced from reference 80.

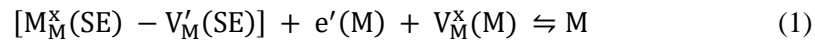
Interestingly, measurements on single-crystalline surfaces additionally highlight defects being present as important for low overpotential nucleation, as the nucleation density is at a minimum when no defect is present and does not show any dependency on the applied current density. This is very interesting, because measurements on defect-free LiPON show the contrary,<sup>60,73</sup> which indicates general differences between the SEs regarding nucleation and cannot be explained as of now. Possibly, density fluctuations within the LiPON SE act as preferential sites for lithium nucleation. All in all, the powerful operando techniques developed within this dissertation will be used in future studies to investigate metal deposition at SE|CC interfaces.

### 2.3 Metal|SE Interface under Anodic Load

Unlike LEs, an SE can only compensate morphological changes of the electrodes to a certain extent.<sup>8,26,31</sup> Knowledge of the interface properties to an electrode is therefore of utmost importance to ensure a stable and predictable cell operation. While this statement is true for every electrode in SSBs, this chapter will focus mostly on the implications at planar metal|SE interfaces and is applied to both classical SSBs with a lithium reservoir and RFCs.

#### 2.3.1 Vacancy Diffusion Limiting the Applicable Current Density

The oxidation of a metal species at the interface to an SE is a well-established concept in solid-state ionics. Schmalzried and Janek proposed a mechanism for the anodic dissolution of silver in contact with SEs which was translated to the Li|SE interface by Krauskopf et al.<sup>32,81</sup> Within this model, a vacancy  $V_M^x$  and an electron  $e'(M)$  are left behind within the metal once an atom is oxidized and moves into the SE as described in equation (1). This ion then occupies vacancy  $V_M'(SE)$  or interstitial  $V_I^x(SE)$  sites within the SE.



After the vacancy is injected into the parent metal, it can diffuse into the bulk of the material with a certain diffusion flux governed by the vacancy diffusion coefficient. Competing with this vacancy diffusion flux  $j_{V_{Li}}$  is the flux  $j_{Applied}$  of  $M^+$  within the SE, governed by the applied current density  $i$ . Within this simplified picture, vacancies will accumulate at the interface if

$$j_{Applied} > j_{V_{Li}} \quad (2)$$

as vacancies cannot be transported away from the interface at a sufficient rate. Thus, this will subsequently lead to a formation of pores and a morphologically unstable cell at a macroscopic level.<sup>32,37,81–83</sup> If, however, the applied current density  $i$  is low, i.e.

$$j_{Applied} < j_{V_{Li}} \quad (3)$$

a stationary concentration of vacancies is induced at the interface. Hence, it is morphologically stable over the duration of the applied current density. Therefore, the case where the vacancy concentration reaches a maximum but is still stable can be considered as the critical case which should not be exceeded during cell operation. The critical current density  $i_{crit}$  is then defined as

$$i_{crit} = z \cdot F \cdot j_{V_{Li}} \quad (4)$$

$$i_{crit} = z \cdot F \cdot \left(1 - \frac{c_{V,Max}}{c_V^0}\right) \cdot c_V^0 \sqrt{\frac{D_V}{\tau_V}} \quad (5)$$

where  $D_V$  and  $\tau_V$  denote the diffusion coefficient of vacancies inside the parent metal and the relaxation time until an equilibrium concentration of vacancies is established. The maximum vacancy concentration at the interface is given by  $c_{V,Max}$  and the equilibrium vacancy concentration within the parent metal by  $c_V^0$ . Strategies on how to overcome this fundamental limitation are discussed in the following Chapters 2.3.4 – 2.3.6.

### 2.3.2 Nucleation of a Pore and Surface Diffusion

It was already established above (Chapter 2.3.1) that pore formation will occur above a certain current density threshold  $i_{\text{crit}}$ . However, works by Krauskopf et al. and Wang et al. also show that the contact loss accompanied by strong voltage increase still takes up to 10 hours at moderate current densities (or  $1 \text{ mAh cm}^{-2}$ ) to occur, despite  $i_{\text{crit}}$  being exceeded.<sup>32,33,37</sup> To have proper control and knowledge over the morphology of the Li|SE interface, it is therefore crucial to know exactly at what point pore formation is starting or rather nucleating,<sup>84,85</sup> instead of the time where full contact loss occurs. Especially in an actual cell undergoing cycling, small morphological changes at the interface can get amplified and eventually lead to cell failure by contact loss coupled with the propagation of dendrites.

In an approach combining both carefully designed stripping experiments with theoretical kinetic Monte Carlo simulations in a joint work with Prof. Albe exactly this  $i_{\text{crit}}$  was estimated. Therefore, the stripping current density was incrementally increased in a symmetrical Li|LLZO|Li cell without changing its direction until very small changes in interface-related impedance are observed, indicating the onset of morphological deterioration. With  $30 \mu\text{A cm}^{-2}$ ,  $i_{\text{crit}}$  is found to be quite low, which is expected however, since Krauskopf et al. already saw progressing pore formation at  $50 \mu\text{A cm}^{-2}$  for both lithium and Li-Mg alloys.<sup>33</sup> This value is then verified by a statistical approach employing kinetic Monte Carlo simulations.<sup>86</sup> Interestingly, independent calculations based on bond counting additionally show that the rate-limiting step may not necessarily be the diffusion of vacancies into the bulk of lithium metal. While this process is energetically favored, the detachment from the interface itself has the highest activation barrier.<sup>87</sup> In reality, however, both processes determine  $i_{\text{crit}}$ , otherwise concepts increasing the effective diffusion coefficient within the anode<sup>33</sup> could not lead to a beneficial stripping performance. Other calculations furthermore show via nucleation and growth theory that the critical pore radius for nucleation is inversely proportional to the applied current density.<sup>88</sup>

Once pores have formed at the interface, another important mechanism influences the rate of lithium replenishment. The existence of pores also opens up the possibility of lithium diffusion along pore surfaces with a diffusion coefficient  $D_s$ , which is expected to be faster than the complementary process within the bulk ( $D_v$ ).<sup>32</sup> Therefore, the contact loss by pore formation gets delayed by adatom diffusion along the pore walls. The effect of this phenomenon on the available discharge capacity was investigated in a joint work with Dr. Srinivasan.<sup>89</sup> One main result is that the pore shape is directly connected to the ratio  $D_v/D_s$ , where the shape of the growing pore is more spherical with higher ratios while the overall available discharge capacity decreases. This can be explained by the improved ability of the LMA to resupply lithium to the interface via surface diffusion.

### 2.3.3 Contact Loss at Li|LLZO and Arising Constriction

In Chapter 2.3.1, the vacancy accumulation and subsequent pore formation was discussed on a physicochemical level. Within this chapter, the implications of pores at the metal|SE interface on the cell impedance and general battery operation shall be discussed. The most prominent example of pore formation during anodic dissolution occurs at the LMA, effectively limiting the current density feasible during discharge and acting as a precursor for dendrite nucleation upon charging.

At first thought, it could be expected that when  $i_{\text{crit}}$  is exceeded during discharge a slow and hyperbolic increase in cell voltage occurs due to pore formation, because the cell impedance is inversely proportional to interface area. However, unidirectional experiments show that during stripping, a long and stable voltage plateau followed by a very steep and sharp increase in cell

voltage occurs instead.<sup>32,33,37,82</sup> The reason for this behavior, as schematically depicted in Figure 5, is a complicated convolution of different effects all influencing the total cell impedance. These different contributions to the cell's impedance are expanded on in the next paragraphs.

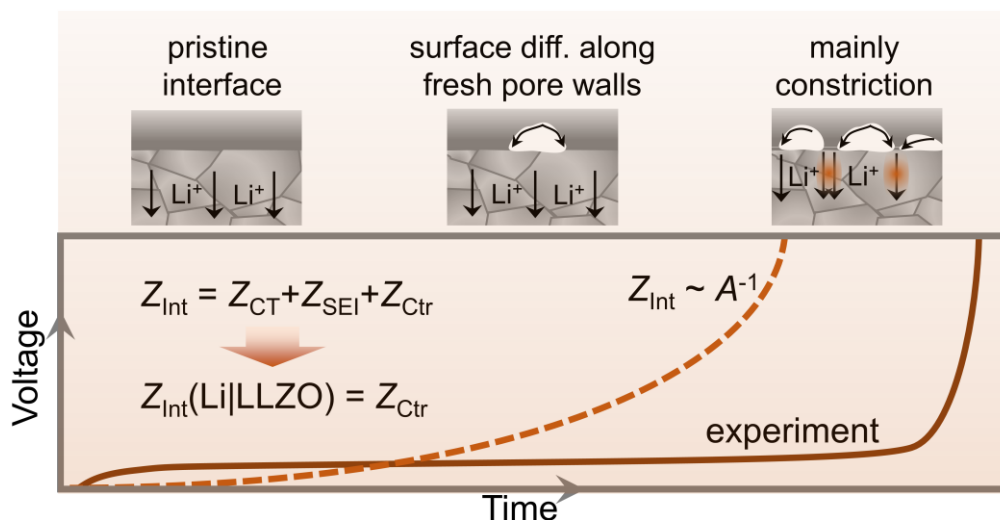


Figure 5. Schematic voltage profile that occurs during progressing pore formation at the Li|LLZO interface while stripping. Instead of having a hyperbolic profile because of the shrinking electrode area, this interface shows a long plateau with a very fast subsequent increase, as surface diffusion along emerging pore walls delays contact loss by supplying lithium to the interface.

The voltage evolution is bound to the impedance evolution via Ohm's law. To interpret the voltage profile, the evolution of the different impedance contributions present in a Li|LLZO|Li cell needs to be understood first. Typically, the total impedance  $Z_{\text{total}}$  is composed of the sum of the bulk transport impedance  $Z_{\text{Bulk}}$ , grain boundary impedance  $Z_{\text{GB}}$  and interface-related impedances  $Z_{\text{Int}}$ . Several works show that  $Z_{\text{Bulk}}$  and  $Z_{\text{GB}}$  are constant during the anodic dissolution of this system,<sup>32,33,39,40</sup> which actually is surprising, since a hyperbolic increase as a function of decreasing area would be expected. To understand this, the nature and evolution of  $Z_{\text{Int}}$  needs to be considered in detail.

Generally,  $Z_{\text{Int}}$  consists of three different contributions, which are often incorrectly used interchangeably in literature, being the impedance of a degradation layer  $Z_{\text{SEI}}$ , the resistance of the physicochemical charge-transfer at the interface  $Z_{\text{CT}}$  and the geometric constriction impedance  $Z_{\text{Ctr}}$ . Both  $Z_{\text{CT}}$  and  $Z_{\text{SEI}}$  are negligible when considering Li|LLZO interfaces, meaning that solely the constriction impedance  $Z_{\text{Ctr}}$  needs to be responsible for the steep increase in cell impedance.

Constriction impedances are generally not linked to one specific transport process, as it is the case for example with the charge transfer. Instead, they arise from a constriction within the SE that lead to ionic current focusing through a volume much smaller than in principle available.<sup>90-93</sup> This can be due to insulating passivation layers on the metal electrode,<sup>17</sup> but most frequently occurs because the metal|SE interface is deteriorating due to pore formation. To fully understand the constriction effect, a differentiation between contact area and electrode area is necessary. The electrode area is then defined as the macroscopic area of the lithium sheet that is applied to the SE and therefore constant throughout a stripping experiment. The contact area, however, is defined as the actual physical area where the lithium is in contact with the SE and therefore decreases during stripping and pore formation.

Why  $Z_{\text{Bulk}}$  and  $Z_{\text{GB}}$  are constant during the pore formation can then be explained when considering the characteristic frequencies of the transport processes. The evolving pores at the interface can be interpreted as the introduction of several capacitors at the interface. At very high frequencies, where typically the bulk ( $\sim 3$  MHz) and GB ( $\sim 50$  kHz) transport occur,<sup>94</sup> these capacitors are dielectrically conductive.<sup>95</sup> Therefore, the impedance data acquisition at very high frequencies is blind to micron-sized pores, which means that the bulk and GB transport contributions solely depend on the constant electrode area, therefore also being constant. However, when measuring the impedance at low frequencies, the pores (capacitors) become insulating and a current constriction occurs within the SE volume in the vicinity of remaining contact spots to the LMA. This signal is then interpreted as  $Z_{\text{Cr}}$  at low frequencies of  $\sim 1$  kHz and strongly depends on contact area instead of electrode area. Quantitative calculations estimating the magnitude and frequency dependency of the constriction signal in relation to interface morphology were carried out in another joint work with Eckhardt et al.<sup>95,96</sup>

Additionally, lowering the contact area between the LMA and SE by stripping will lead to an increase in the local current density at the remaining contact spots. This not only is followed by a self-accelerating and even faster pore formation at the contact points, but also higher constriction impedances. With progressing pore formation, the aforementioned effect of surface diffusion along pore surfaces is amplified, resupplying lithium to the SE at a higher rate as possible by bulk diffusion, which is why the final steep increase in cell impedance and voltage is delayed. This leads to a long plateau during stripping, despite exceeding the critical current density for pore formation.

It can therefore be concluded that the voltage profile during stripping of metal electrodes at chemically stable interfaces arises from a complex interplay of different morphological and geometric effects. This discussion is independent from the type of SE used in combination with lithium metal. However, if a material other than LLZO is used, the charge transfer between SE and anode as well as the transport through a resistive SEI could further complicate the impedance measured of the metal|SE interface. Therefore, a recipe was developed in a joint work with Eckhardt et al. which allows the unequivocal determination of contributions to the interface impedance present in a given cell system.<sup>97</sup>

### 2.3.4 Solution 1: Facilitating the Diffusion of Vacancies Inside the LMA

It was described above (Chapter 2.3.1) how the current induced injection of vacancies into lithium is competing with the diffusion thereof inside the anode to replenish the depleted interface. Therefore, one possibility to mitigate the pore formation is by an increase of the effective diffusion coefficient of the vacancies inside the lithium. A higher vacancy diffusion coefficient would allow higher stripping rates before reaching the tipping point where pores nucleate.

A simple, yet effective way of improving the effective diffusion coefficient is by raising the temperature. For example, it is possible to easily strip over  $2.5 \text{ mAh cm}^{-2}$  without pore formation at the Li|LLZO interface at  $50 \text{ }^\circ\text{C}$ ,<sup>33</sup> whereas pores will form after only around  $1.2 \text{ mAh cm}^{-2}$  at  $25 \text{ }^\circ\text{C}$ .<sup>32,37</sup> It was also shown in several works employing cycling tests, that symmetrical cells are able to withstand much higher current densities at higher temperatures, likely because pore formation is avoided due to increased diffusivities and also decreased interface impedances.<sup>76,98,99</sup> Increasing the temperature even above the melting point of lithium to  $195 \text{ }^\circ\text{C}$  further corroborates this, as no pore formation can be observed when stripping from a liquid lithium reservoir.<sup>100</sup> However, elevated temperatures introduce other difficulties, such as the facilitation of side reactions,<sup>101</sup> or the need for appropriate thermal cell management.

Therefore, it is desired to elevate the  $\text{Li}^0$  diffusion coefficient of the anode material itself, e.g. by alloying with different metals. Krauskopf et al. explored the possibility of using  $\text{Li}_{0.9}\text{Mg}_{0.1}$  alloys to enhance the effective diffusion coefficient, thereby improving the discharge capacity by nearly a factor of 2 compared to pure lithium.<sup>33</sup> A schematic of the pore formation in lithium as well as the case of elevated diffusion coefficients by alloying is depicted in Figure 6a and Figure 6b.

However, using alloys as anode materials introduces new challenges. Not only is the specific energy density of the material reduced by decreasing its lithium content, the anode potential is also increased and can even change during cycling. Furthermore, the mechanical properties, such as yield strength or elastic modulus, will change. Overall, the changing lithium concentration in the alloy during cell operation will induce complex dynamics of electro-chemo-mechanical effects, which are difficult to predict and impossible to properly account for. Another solution is desired to enable the use of pure lithium metal as the LMA, which could be the application of stack pressure.

### 2.3.5 Solution 2: Pressure-Induced Creep Transport

In Chapter 2.3.1 the balance between the current induced strain-rate of the LMA and the vacancy diffusion-based resupply of lithium to the interface is discussed if no external pressure is applied. However, if the  $\text{Li}|\text{SE}$  system is subject to externally applied stack pressure as depicted in Figure 6c, this balance needs to be completed with a lithium flux governed by the creep of lithium  $j_{\text{Creep}}$  to the interface as described in

$$j_{\text{Applied}} \leq j_{\text{V}_{\text{Li}}} + j_{\text{Creep}} \quad (6)$$

It is reasonable to assume that above a certain threshold, the current induced stripping rate will always be larger than the rate of resupply by vacancy diffusion. In this case, there must exist a critical stack pressure as a function of the applied current density, which is just sufficient to balance the mass flux of lithium at the interface during stripping and suppress the pore formation by creep and plastic deformation. This current dependent critical stack pressure was recently quantified by Wang et al. by decreasing the applied stack pressure during unidirectional stripping in a stepwise manner until the voltage increases.<sup>37</sup> This then indicates pore formation and being below the critical pressure needed. Using this method, it was possible to determine a critical pressure of 0.4 MPa at  $100 \mu\text{A cm}^{-2}$  and 2.0 MPa at  $400 \mu\text{A cm}^{-2}$ . However, due to morphological instabilities at the counter electrode, it was not possible to investigate practical current densities  $> 1 \text{ mA cm}^{-2}$ .

Additionally, Wang et al. formulate a mathematical description to calculate the pressure induced strain rate  $\dot{\epsilon}_{\text{Creep}}$  for metal electrodes as

$$\dot{\epsilon}_{\text{Creep}} = K \cdot \sigma^m \cdot \exp\left(-\frac{E_A}{RT}\right) \quad (3)$$

where  $K$  denotes a material parameter,  $\sigma$  the applied stress with power-law creep exponent  $m$ ,  $E_A$  an activation energy and  $R$  and  $T$  the universal gas constant and temperature, respectively. For lithium, the power-law creep is reported to be dominated by dislocation climb with  $m = 6.6$  at room temperature.<sup>102,103</sup> However, this value is not constant due to frictional and adhesive forces between lithium and the SE,<sup>104</sup> further complicating the matter.

Another method to assess the critical pressure for higher current densities is a theoretical model developed in a joint work together with Dr. Srinivasan from Argonne National Laboratory.<sup>89</sup> Within this model, the  $\text{Li}^+$  flux does not only compete with the effective vacancy diffusion within bulk lithium metal, but also with faster surface diffusion along the pore walls. Based on this model,

critical stack pressures in the range of 50 – 60 MPa are needed for planar interfaces at  $1 \text{ mA cm}^{-2}$ , which is well above what is deemed to be practically feasible.<sup>57</sup> Another estimation from Kasemchainan et al. predicts that 10 MPa of pressure is required for a stable cycling at  $1 \text{ mA cm}^{-2}$ .<sup>36</sup> This large spread suggests that further investigation is needed on this matter.

An explanation for the large spread of required pressures is that when pore formation occurs, the mechanical constraints at the Li|SE interface change, which results in a very dynamic and interdependent system. For example, the applied stack pressure may not be above the critical pressure when pores have not yet formed but high enough to deform the metal at the interface once pores of certain size are present. These pores then get annihilated by creep and the initial morphological state of the interface is regained. This phenomenon of an oscillating interface morphology was studied in depth by Majoni and Janek et al. for Ag|AgX systems but is also believed to occur for the lithium electrode.<sup>83,105</sup> Additionally, the mechanical properties of lithium are highly dependent on the concentration of other non-equilibrium defects, like grain boundaries and dislocations, which heavily depends on the thermomechanical history of the used lithium.<sup>106,107</sup>

To summarize this chapter, applying stack pressure is an excellent tool to stabilize the LMA during anodic dissolution and prevent the formation of pores. However, with several tens of MPa, the pressures required to suppress the contact loss are unfeasibly high to compensate high stripping rates of  $> 1 \text{ mA cm}^{-2}$ , which is even more difficult for large, stacked cell systems. Therefore, alternative anode concepts may need to be considered to circumvent the issue of pore formation altogether.

### 2.3.6 Solution 3: Alternative Systems with IL or CNTs

Instead of altering the properties of the materials itself, it is also possible to employ macroscopic solutions to compensate or mitigate the formation of pores. Note that 3D-interfaces of Li|LLZO as fabricated by Wachsman and co-workers are not topic of this discussion.<sup>38,108–111</sup> While they are very promising and also challenging regarding the preparation thereof, they do not fundamentally change the physicochemical properties at the Li|SE interface but rather reduce the local current density by having an increased contact area.

Different concepts to suppress and mitigate pore formation are schematically depicted in Figure 6d. Publication 4 within this dissertation showed that CNTs dispersed in lithium metal change both electrochemical and chemo-mechanical properties of the anode material.<sup>40</sup> Despite the Li-CNT electrode being employed in a planar arrangement to the SE, very high stripping capacities  $> 20 \text{ mAh cm}^{-2}$  showed that the stripping has fundamentally changed. Cryogenic focused-ion-beam (FIB)-SEM revealed that the lithium was also stripped from the bulk of the electrode and most likely transported to the interface through the present CNTs, which suppressed and delayed the contact loss by pore formation. Interestingly, bulk mechanical investigation also showed a significant increase in yield strength, Vickers hardness and elastic modulus of the anode material. Subsequent electrochemical investigations under pressure were able to correlate a less pressure-sensitive stripping performance of the Li-CNT anode on its ability to resist deformation. However, this also means that if pressure can be applied during discharge of this cell, pure lithium metal and its ability to creep and deform at lower pressures is advantageous when compared to Li-CNT.

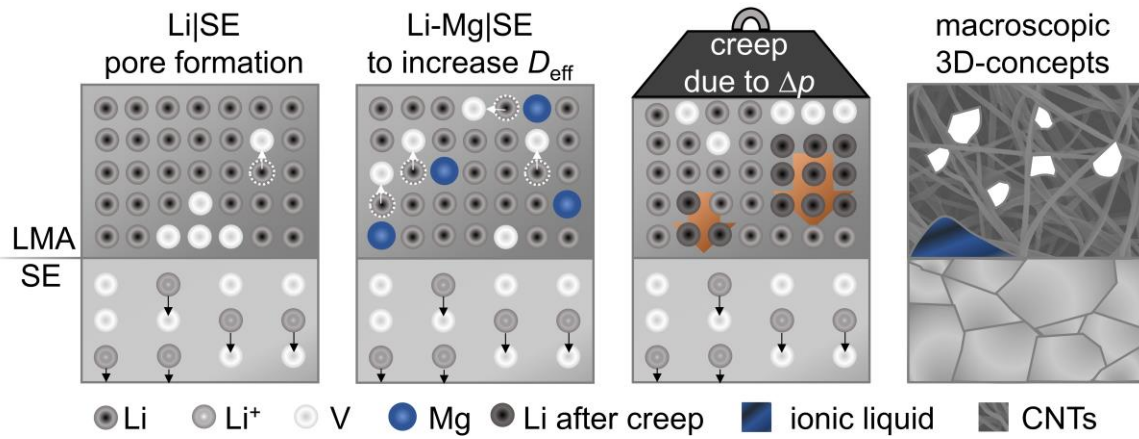


Figure 6. The issue of pore formation explained at the atomistic scale in a). An increase in effective vacancy diffusion by alloying is shown in b) at hand of Li-Mg alloys. Utilizing pressure to supply lithium by creep and plastic deformation is visible in c). Macroscopic concepts to avoid or mitigate pore formation are shown in d) at hand of CNTs incorporated into lithium and an IL electrolyte present at the interface between LMA and SE.

Another concept is using LEs in an otherwise solid-state cell to have a free-flowing agent at the interface capable of compensating growing pores during stripping. In publication 3 within this dissertation, it was proven that even viscous LEs, such as ILs, are capable of increasing the stripping capacity by a factor of ten to  $> 15 \text{ mAh cm}^{-2}$ . Cryogenic FIB-SEM revealed that the IL will keep the ionic contact between the LMA and solid separator by flowing into the pores until its volume is not sufficient anymore to compensate the pore volume. This working mechanism is underlined by the viscosity of the employed LE having a pronounced impact on the available stripping capacity. As less viscous LEs flow more easily into tight pores, they result in higher capacity values and a delayed contact loss.

## 2.4 Metal|SE Interfaces during Cycling

### 2.4.1 The Concept of CCD Tests and Influential Parameters

To determine the resilience of (a)symmetrical cells to short-circuiting by the formation of dendrites, testing of the critical current density (CCD) is a standard tool frequently used in literature.<sup>38,50,74,75,77,112,113</sup> While CCD tests are easy to interpret superficially, their result heavily depends on the testing protocol and conditions used. Additionally, the CCD basically can be induced by either a failure of the Li|SE interface or due to failure of the SE itself, e.g. by lithium penetration and cracking. In the first case, pores form during anodic dissolution and then facilitate the growth of dendrites due to current focusing at the remaining contact spots.<sup>34</sup> This is not an inherent limitation imposed by the SE but rather the Li|SE interface. In the second case, the Li|SE interface is still in a low-impedance, conformal state but dendrites still penetrate the SE, which rather is a limitation imposed by the SE and not the interface. Therefore, it needs to be decided prior to investigation if the Li|SE interface or rather the SE itself is of interest and suitable test parameters need to be chosen, before CCD measurements are conducted.

Since not the whole community is aware of the delicate dependency of the CCD and connected failure mechanisms on the testing parameters, a reasonable testing protocol is needed to be able to compare results from different laboratories or even different researches within the same group. Due to the amplification of small defects or issues during testing, the CCD is immensely sensitive to external factors and variables. This is evident when the CCD values obtained for Li|LLZO|Li cells measured by different groups with different protocols are compared. These values are depicted in Figure 7 and show a huge spread from 30  $\mu\text{A cm}^{-2}$  to 1  $\text{mA cm}^{-2}$ .

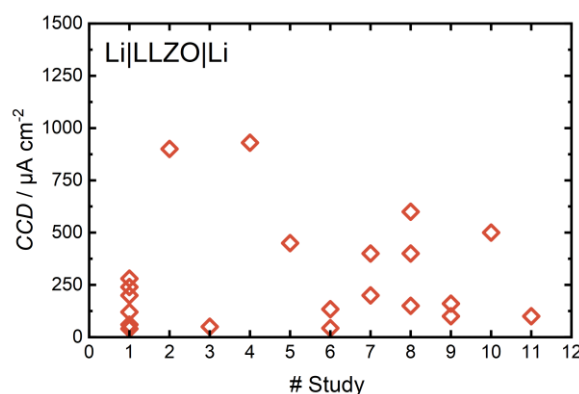


Figure 7. CCD results obtained from different studies on Li|LLZO|Li symmetrical cells. Note that while different substitutions were used for stabilizing cubic-LLZO, the CCD results vary over a huge range of values. This plot is based on a summary published by Flatscher et al. and excludes microelectrode measurements.<sup>114</sup>

To give guidelines on how to properly determine the CCD on a given system, first, however, the relevant variables are discussed in the following paragraphs.

#### i. Applied Current Profile

Usually during CCD tests, current steps are applied and incrementally increased while the cell voltage is recorded. One very important factor that influences the outcome of the test is the duration of one step, i.e. the charge being shuttled. If extremely low charges per step are considered, a very high CCD is expected, simply because the charge plated per step is insufficient to grow a lithium filament from one electrode to another in thick laboratory samples. This phenomenon is sometimes

referred to as “dynamic short circuiting”,<sup>21</sup> implying that a CCD threshold is exceeded without the typical hard drop to zero in cell voltage. Shuttling a large amount of charge therefore results in a more reliable CCD value. In extreme cases it is also possible that a very high current ( $> 10 \text{ mA cm}^{-2}$ ) is shuttled unknowingly through a lithium filament, yielding extremely high but incorrect values of the CCD.<sup>115,116</sup>

On the other hand, if large charges are shuttled during every step, pore formation may occur at the anode of the cell, which would lead to quick short circuiting upon current reversal. However, if only the dendrite susceptibility of the SE is the property of interest, the actual CCD will therefore be underestimated. The current density increase per step itself is also of relevance. Large incremental steps in applied current density will lead to an overestimation of the CCD, because the true value may have been surpassed within the steps.

#### ii. Applied Pressure and Waiting Time

One very underestimated and also underreported factor influencing the CCD is a pause before current reversal. This pause can be introduced either deliberately as a waiting step, but also unintentionally by acquiring an impedance spectrum over several minutes. If no pressure is applied during the measurement, this waiting step is expected to be less influential. However, if pressure is applied during the test, this waiting step will change the interface morphology due to creep or plastic deformation within the LMA.<sup>102,117</sup> For example, if pores have formed during the prior step and would facilitate the growth of dendrites, they could get closed and the interface morphology would return to its pristine state. If probing the SE is of interest, this can be desired. However, if the Li|SE interface is probed with the addition of long waiting times, the CCD is severely overestimated, especially if considerable stack pressures are applied.

#### iii. Interface Conditions

The initial morphology and interfacial impedances are of utmost importance and will influence the CCD test drastically.<sup>50</sup> As the impedance  $Z_{\text{int}}$  of pristine Li|LLZO interfaces is mainly governed by constriction, high initial interfacial impedances result from a bad contact area. This can either be the case with passivation layers like  $\text{Li}_2\text{CO}_3$  on LLZO or just because of inappropriate lithium preparation.<sup>17</sup> An optimization of the interface is also the reason why the measured CCD in LLZO progressively improved over the years, not because of inherent changes of the SE. For example, in 2011 a CCD of  $< 25 \text{ } \mu\text{A cm}^{-2}$  was obtained with an initial  $Z_{\text{int}}$  of  $> 5000 \text{ } \Omega \text{ cm}^2$ .<sup>118</sup> Despite no changes of the SE, this value quickly improved to  $150 \text{ } \mu\text{A cm}^{-2}$  at an  $Z_{\text{int}}$  of  $< 50 \text{ } \Omega \text{ cm}^2$  in 2015,<sup>119</sup> followed by  $> 300 \text{ } \mu\text{A cm}^{-2}$  at an  $Z_{\text{int}}$  of  $< 5 \text{ } \Omega \text{ cm}^2$  in 2017.<sup>50</sup> For optimized interfaces with negligible interfacial impedance, a CCD of  $1000 \text{ } \mu\text{A cm}^{-2}$  was achieved.<sup>78</sup> However, measurements at single-crystalline LLZO without stack pressure imply that the CCD of Li|LLZO would only be around  $280 \text{ } \mu\text{A cm}^{-2}$ ,<sup>114</sup> which is well below practical targets.<sup>10,120</sup> Nevertheless, the discussed measurements undeniably show that the CCD is not an inherent material property and thus is strongly influenced by testing conditions and interface engineering.

#### iv. Electrode and Pellet Geometry

Another underreported variable is the cell geometry used for testing the CCD. Because if different geometries are used, tests cannot be reasonably compared. For example, the thicker a pellet or SE sheet is for testing the CCD, the higher is its resistance to filament penetration. In the case of dynamic short circuiting, a thicker pellet is able to withstand higher current densities simply due to the fact that a dendrite has a further distance to grow. Furthermore, in mm-thick pellet type SEs the electric field across the cell can be homogenized, if constriction occurs at one of the respective

electrodes.<sup>96</sup> A thin separator sheet with a thickness of only several tens of  $\mu\text{m}$  might not be able to prevent current constriction occurring at a porous interface to also influence the plating performance at the opposite electrode, even if this one still shows conformal contact.

But not only the SE thickness has a profound influence on the CCD outcome, also the absolute electrode area and shape will influence the result. For example, the chance for an electrode to contact macroscopic pits and damaged spots on an SE pellet is higher for larger electrodes. Since such defects also facilitate the growth of dendrites, using larger electrodes may lead to short circuiting at lower current densities despite no fundamental change in the systems properties.

#### v. Influence of Temperature

The temperature will naturally influence the CCD by enhancing both the SE ionic conductivity as well as the vacancy diffusion within the lithium metal, which will induce very complex changes to the outcome of the CCD test. However, most importantly, lithium metal is even more ductile at higher temperatures. When stack pressure is applied, this will enable the healing of pores induced by stripping and therefore increase the obtained CCD. Furthermore, temperatures above the melting point of lithium can help to negate the issue of pore formation completely, since the vacancy diffusion coefficient in liquid lithium is orders of magnitude higher than in the solid state.<sup>100</sup> For CCD values to be comparable, it is crucial for tests to be carried out at the same temperature. A general trend for higher CCD values is expected with increasing temperature.

#### 2.4.2 Guideline on How to Test Either the LMA or the SE

Within this chapter, guidelines will be given on how to test symmetrical cells regarding their CCD. Before choosing the test parameters, however, it needs to be decided if the SE itself shall be tested or rather the interface to the LMA. For example, if parameters only concerning the SE are changed within a study, such as grain size or chemical composition, it is reasonable to design a test to probe for SE failure. However, if the interface conditions are varied instead, as in the case of surface treatments or interlayers, the Li|SE interface should rather be probed with a CCD test that will not induce a direct SE failure. While designing a test that completely differentiates between the two different extremes is difficult, it still is useful to rationally design the test to probe the desired property of the cell. The different failure cases are schematically depicted in Figure 8.

For probing the SE, it is suggested to impede the formation of pores as a precursor for dendrite formation. Avoiding the pore formation is possible by applying stack pressures of a few MPa during the test and by introducing a waiting period between the steps. In general, the pressure helps to supply lithium via plastic deformation to the interface to avoid pore formation during stripping and additionally closes any pores that formed nonetheless during the waiting period.<sup>121,122</sup> Similarly, it is useful to increase the temperature as a tool to facilitate lithium deformation and vacancy diffusion. However, depending on the material system and geometry of the investigated cell, very high pressures can also lead to a fracturing of the SE and facilitate dendrite growth.

On the other hand, probing the Li|SE interface is possible when no stack pressure is applied and larger amounts of lithium are shuttled per cycling step. In this case, pores form above a certain current density, which then act as a precursor for dendrite growth because of current focusing at the remaining contact spots.

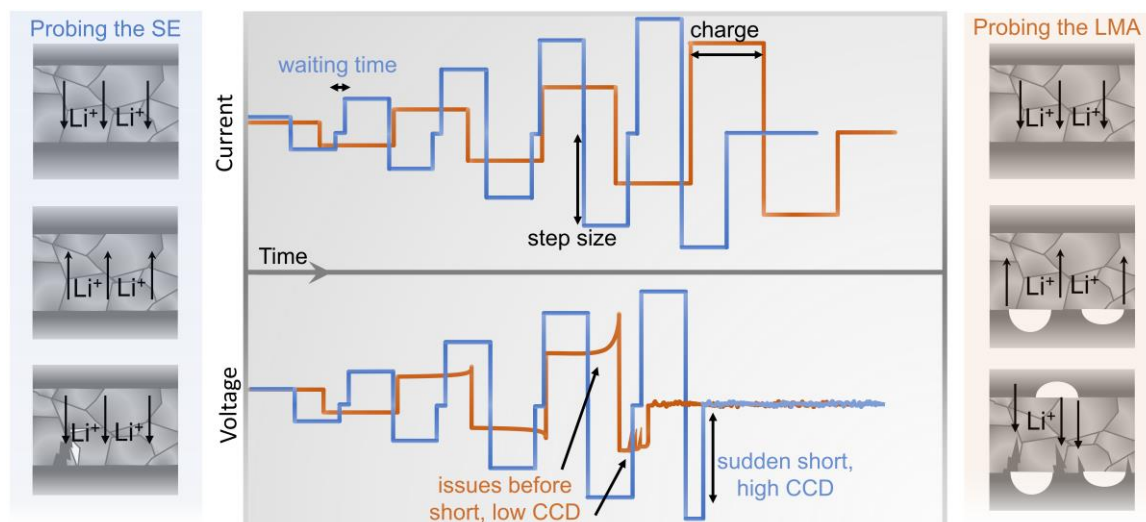


Figure 8. Idealized schematic current (top) and voltage (bottom) profile to probe either the dendrite susceptibility of the SE itself (blue) or rather the Li|SE interface (orange) at the example of a symmetrical Li|SE|Li cell.

Figure 8 shows two current profiles that could be used for testing the SE (blue) or rather the Li|SE interface (orange) with corresponding voltage profiles. Additionally, the interface morphology evolution is schematically depicted at the sides of the figure for each test protocol used. It can be observed that the CCD for the blue test protocol is higher as pressure is applied, which avoids pore formation. Moreover, a sudden short-circuit is observed for the testing of the SE, as the impedance remains constant until a filament is rapidly growing and shorting the cell. On the other hand, the orange protocol testing the LMA has a larger charge per step and no pressure applied. Here, an onset of issues occurring even before the short circuiting is visible, such as increased voltages due to pore formation as also observed by Zhao et al.<sup>123</sup> or noise due to spallations and dendrite growth.<sup>121</sup> Subsequently, the CCD obtained with the orange test is substantially lower as a different failure mechanism occurs.

#### 2.4.3 Unidirectional Tests as a Means to Counter the Sensitive Nature of Cycling

Unfortunately, the differentiation made in Chapter 2.4.2 between probing the SE or the LMA is not as clear-cut as it seems. Especially at higher current densities, it will be difficult to suppress the pore formation even when stack pressure is applied. Furthermore, cycling symmetrical cells over a high number of steps will amplify small interfacial issues that may arise during preparation. For example, small pores upon cell assembly or surface defects within the SE are quite negligible at the beginning. However, they will act as nucleation points for morphological instabilities, be it either pores or dendrites, and get amplified and influence the CCD at later steps.

Two strategies exist to circumvent the very sensitive nature of classical CCD tests. The first is to conduct a high number of tests and perform a statistical analysis of CCD results, which is immensely time-consuming and not very feasible in everyday laboratory conditions. The second strategy is the execution of unidirectional tests, which offers a variety of benefits when compared to cycling.<sup>21,33,39,40,124</sup>

In unidirectional tests, the current direction is not alternating between the steps as shown in Figure 9. This limits the overlap of different phenomena occurring at a single electrode, since lithium is consistently deposited at one electrode and stripped at the other electrode, drastically

limiting the interdependency of these different microscopic effects. Hence, contact loss or dendrite formation as indicated by voltage features within the test can be unequivocally linked to one of the respective electrodes.

Therefore, it is reasonable to define two different critical current densities based on the respective failure mechanism.<sup>35,36</sup> If the LMA fails during stripping because of pore formation and contact loss, the critical current density for stripping (CCS) is exceeded. If, however, a short-circuit occurs at the plating electrode, the critical current density for plating (CCP) is exceeded. While both effects overlap in cycling tests, unidirectional tests allow a differentiation.

Obviously, impedances arising from plating and stripping cannot be completely decoupled in a symmetrical cell without a reference electrode. Consequently, testing parameters need to be chosen with care to either induce a failure of the electrode of interest with the other electrode practically being unchanged. Several parameters can be adjusted to account for this. Like for classical CCD tests discussed in Chapter 2.4.2, applied pressure, temperature, step size and height as well as waiting time between steps will influence unidirectional tests in a similar way.

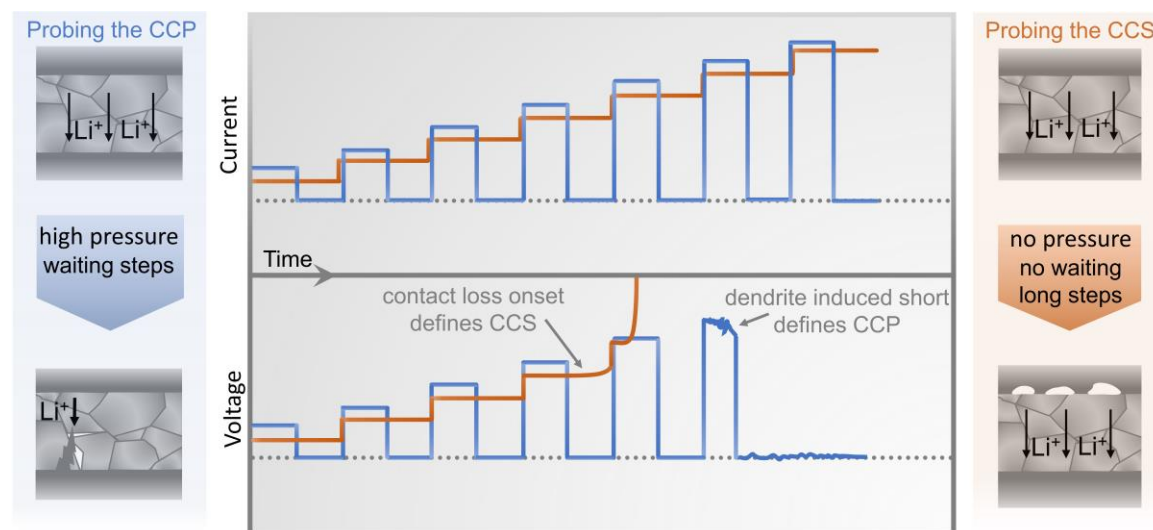


Figure 9: Idealized schematic showing a proposal for unidirectional testing of the CCP (blue) or CCS (orange). The bottom part shows expected voltage responses to the current densities applied as seen in the top part. Furthermore, the graphics on the sides show the respective failure mechanisms for the CCP (dendrites) and CCS (pore formation) and parameters on how to influence what mechanisms likely occurs.

To influence the test to rather probe the CCP, it is of utmost importance to suppress pore formation at the stripping electrode. Like in CCD tests, this can be done by resupplying lithium to the interface via plastic deformation and creep, both being enhanced by increasing the temperature and applied stack pressure. Waiting steps while holding the pressure will also shift the test to rather probe the SE in unidirectional tests. However, the stripped electrode, which is not of interest in a CCP test, still needs to be able to provide enough lithium. Depending on the test parameters, thick foils  $> 100 \mu\text{m}$  may need to be employed as the counter electrode.

Choosing the right capacity per step is even more detrimental than in CCD tests when testing unidirectionally. Choosing a capacity that is too low results in an overestimation of the CCS/CCP, because the failure onset may already occur in one step but is progressing to noticeable cell failure only in the subsequent step. For example, the CCS may be exceeded during a stripping step but not enough charge is passed for pore formation to be observed. The pore formation would then only be

noticed in the subsequent step, leading to an overestimation of the CCS. For ideally reversible Li|LLZO interfaces, the amount of charge that results in pore formation is around  $1 \text{ mAh cm}^{-2}$ .<sup>32,46,125</sup> To avoid such an underestimation, it is possible to test multiple cells. Each cell is then stripped with a higher current density until failure. While time-consuming, this procedure prevents erroneous interpretation of CCS or CCP results, especially as the CCS seems to be substantially lower than the CCP.<sup>32,36</sup>

### 3 Results

#### 3.1 Publication 1: “Kinetic versus Thermodynamic Stability of LLZO in Contact with Lithium Metal”

In publication 1 of this dissertation, the reaction at the interface between lithium and  $\text{Li}_{6.25}\text{Al}_{0.25}\text{La}_3\text{Zr}_{12}\text{O}_{12}$  was investigated using XPS and electrochemical impedance spectroscopy in dependence on the lithium deposition method. This work serves as an important puzzle piece in understanding the reaction of two of the most promising battery materials, lithium and LLZO.

To assess the influence of the energy input during the deposition of lithium onto the SE on the reactivity, three different ultra-high vacuum (UHV) techniques were used. Thin films were deposited using (i) sputter deposition, (ii) electron-beam physical vapor deposition and (iii) *operando* electron-beam electrochemical deposition. It could be shown in line with previous works, that a very thin oxygen deficient interlayer (ODI) forms by the reduction of  $\text{Zr}^{4+}$  to  $\text{Zr}^{2+}$  or even  $\text{Zr}^0$ . Interestingly, this ODI only forms, when a kinetic barrier is overcome, e.g. by lithium sputtering with high kinetic energy (0.1 – 1.0 eV). Lithium that was deposited via electron-beam deposition though does not show any reaction at all as observed by XPS due to the lower energy input (0.01 – 0.1 eV). However, no implication of this difference was observed for the electrochemical performance and interfacial impedance for the different samples, which may have two different reasons. Either, the ODI forms anyway upon measuring the impedance due to the applied overvoltage or the thin ODI does not influence the interfacial impedance.

Either way, publication 1 brings closure to a much-discussed question in literature if the Li|LLZO interface is stable or not. The generated knowledge that the energy input during deposition of lithium or even of possible interlayers also helps to optimize the future fabrication of stable interfaces or interlayers to enable LMAs with SEs.

The experiments for this work were designed and planned in collaboration with the groups of Dr. S. Tepavcevic (Argonne National Laboratory) and Prof. J. Sakamoto (University of Michigan) which resulted in a shared first authorship between Dr. J. Connell and T. Fuchs. XPS experiments conducted in Giessen were performed by Dr. T. Krauskopf and H. Hartmann and were supervised by Dr. J. Sann and Prof. J. Janek. The manuscript was written by the first authors and edited by all co-authors.

## Kinetic versus Thermodynamic Stability of LLZO in Contact with Lithium Metal

Justin G. Connell,<sup>▽</sup> Till Fuchs,<sup>▽</sup> Hannah Hartmann, Thorben Krauskopf, Yisi Zhu, Joachim Sann, Regina Garcia-Mendez, Jeff Sakamoto, Sanja Tepavcevic,\* and Jürgen Janek\*



Cite This: *Chem. Mater.* 2020, 32, 10207–10215



Read Online

ACCESS |



Metrics & More



Article Recommendations



Supporting Information

**ABSTRACT:**  $\text{Li}_7\text{La}_3\text{Zr}_2\text{O}_{12}$  (LLZO) garnet-based oxides are a promising class of solid electrolytes used as the separator in all-solid-state batteries (ASSBs). While LLZO is considered to have a wide electrochemical stability window, its intrinsic stability in contact with lithium metal is not sufficiently well understood, and there is still a debate on the key question of whether LLZO does or does not form passivation layers before and during cycling. Utilizing both *in situ* and *operando* X-ray photoelectron spectroscopy techniques, we reveal the presence of a kinetic barrier to the reduction of LLZO by Li metal, with the extent of oxygen-deficient interphase (ODI) formation depending sensitively on the energetics of Li metal arriving at the Li|LLZO interface. Despite the clear presence of a kinetic barrier to reduction, the electrochemical response of the Li|LLZO interface is unchanged by the presence of the ODI, indicating that ODI formation during electrochemical cycling does not hinder charge transfer across the Li|LLZO interface. Overall, these results reveal that the reactivity of LLZO with Li metal depends not only on the material properties of the adjoining phases (i.e., surface purity and active contact) and their resulting thermodynamic stability but also on the energy input at the interface and the resulting reaction kinetics. Furthermore, the presence of a kinetic barrier to reduction highlights the additional complexities governing the reactivity of solid-state interfaces in ASSBs and underscores the importance of *operando* characterization of interfacial stability to design more robust, high-performance protection strategies for solid electrolytes in contact with reactive electrodes.



### INTRODUCTION

The successful implementation of the reversible lithium metal anode (LMA) is one of the most promising strategies in the quest for future battery technologies with significantly increased energy density.<sup>1–4</sup> In principle, LMAs are conceivable for batteries with liquid, polymer, or inorganic solid electrolytes. However, the LMA in batteries with liquid or polymer electrolytes is afflicted with notorious problems like low Coulombic efficiency (liquids), poor rate capability (polymers), and significant dendrite growth (liquids and polymers).<sup>5–8</sup> In contrast, all-solid-state batteries (ASSBs) based on inorganic solid electrolytes (ISEs) have been shown to be able to mitigate or eliminate many of these issues<sup>9–11</sup> and are therefore promising for a wide range of applications such as transportation, which require both high power and energy density to compete with existing Li-ion technologies.

Among the many types of ISEs that have been discovered, the garnet-type superionic conductor  $\text{Li}_7\text{La}_3\text{Zr}_2\text{O}_{12}$  (LLZO) has attracted significant interest in the last decade due to its high ionic conductivity at room temperature ( $\sim 1 \text{ mS cm}^{-1}$ )<sup>12,13</sup> and because it is one of the few candidate materials with apparent stability in contact with lithium metal.<sup>14,15</sup> However, despite intensive research, the intrinsic stability of LLZO in contact with lithium is still not sufficiently well understood, and there is still a debate on the central question of whether LLZO does or does not form a passivation layer in contact with lithium metal.<sup>15</sup> Experimental techniques like X-

ray diffraction (XRD) can resolve the presence or absence of progressive interphase formation that continues into the bulk,<sup>16–19</sup> but are insensitive to the formation of a very thin, self-limited interphase. Transmission electron microscopy (TEM)-based investigations have enabled direct imaging of the Li|LLZO interface; however, *in situ* measurements indicate the formation of a lithium-rich tetragonal interlayer,<sup>20</sup> while *ex situ* studies indicate no significant structural changes.<sup>21</sup> Studies utilizing X-ray photoelectron spectroscopy (XPS) have similarly found different results, with some studies showing no evidence for reduction, while recent work by some of the authors has shown the reduction of  $\text{Zr}^{4+}$  at the interface of doped LLZO with lithium metal.<sup>22</sup> Theoretical investigations of the stability of LLZO to Li metal have focused primarily on undoped LLZO,<sup>13</sup> which is tetragonal at room temperature with a low ionic conductivity of  $\sim 10^{-3} \text{ mS cm}^{-1}$ . Even for the undoped material, different theoretical prediction methods also yield different results, with the “band gap” approach (also referred to as the “electrochemical stability” approach) predicting sufficient stability in contact with lithium metal.<sup>23</sup>

Received: September 30, 2020

Revised: November 11, 2020

Published: November 30, 2020



and the chemical stability approach predicting a decomposition reaction at 0.05 V vs  $\text{Li}^+/\text{Li}$ .<sup>24–26</sup> However, it should be noted that kinetic considerations are not included in either approach.

Indeed, the question of reaction kinetics remains largely unaddressed, as many measurements and theoretical insights rely on analysis of the thermodynamic ground state of the system to determine stability. As our previous work indicates, some of the discrepancies that exist in the literature likely derive from differences in surface cleanliness (i.e., the presence or absence of surface  $\text{Li}_2\text{CO}_3$  and  $\text{LiOH}$  layers), with even relatively thin reaction layers modifying the interfacial reactivity of LLZO with Li metal.<sup>22,27,28</sup> Furthermore, the specific dopant used to stabilize the cubic phase clearly impacts the nature and extent of reactivity between LLZO and Li, with Ta-doped LLZO exhibiting very little reactivity as compared to Nb-doped LLZO, whose reactivity with Li propagates into the bulk via the likely formation of a mixed conducting interphase (MCI).<sup>22,29</sup> However, these results still do not directly address the kinetics of the reactivity of Li metal with LLZO, as no time-dependent evolution of the oxygen-deficient interphase (ODI) layer discovered in this work was resolved for either Ta- or Al-doped LLZO. In this context, it has to be noted that even a thin, nanometer-sized MCI layer can have a strong impact on the rate performance of the Li|ISE interface, as they have been shown to cause diffusion-related transport limitations in other systems.<sup>30,31</sup> Characteristic low-frequency contributions hinting toward transport limitations have also been reported for the Li|LLZO interface.<sup>22,32</sup> Furthermore, the formation of an ODI layer with higher electronic conductivity compared to the pristine LLZO layer induces a transfer number gradient in the solid electrolyte across the interface region and could facilitate internal lithium nucleation inside the LLZO ceramic.<sup>4,33</sup> This indicates that more precise knowledge of interfacial stability is needed to advance the understanding of lithium metal electrode kinetics and dendrite growth in LLZO-based solid-state batteries. Indeed, determining the critical link between chemical reactivity and electrochemical performance is essential to enable ISEs for next-generation ASSBs.

To develop such insights, we have utilized a variety of different *in situ* and *operando* XPS techniques, coupled with electrochemical measurements, to investigate in detail the factors impacting the interfacial stability of Al-doped LLZO in contact with lithium metal. It is shown that Li metal deposited onto the LLZO surface via different techniques (i.e., magnetron sputtering, electron beam evaporation, and electrochemical deposition) results in different reactivities that depend sensitively on the energetics of arriving Li species. The results demonstrate that the reactivity of LLZO with Li metal does not only depend on the material properties of the adjoining phases (i.e., their surface purity and active contact) and their resulting thermodynamic stability but also on the energy present at the interface and the resulting reaction kinetics. Despite the clear presence of a kinetic barrier to chemical reactivity during formation of the interface, the resulting electrochemical response of the Li|LLZO interface is unchanged by the presence or absence of the ODI layer. Overall, the presence of a kinetic barrier to reduction highlights the additional complexities governing the reactivity of solid-state interfaces in ASSBs and underscores the importance of *operando* characterization of interfacial stability to design more robust, high-performance protection strategies for solid electrolytes in contact with reactive electrodes.

## RESULTS

Vacuum deposition of Li<sup>1,9,16,17</sup> provides an alternative to the use of bulk Li foils and serves as a critical component of interface design, as it avoids the introduction of extrinsic reaction products at the Li|LLZO interface (e.g.,  $\text{LiOH}$ ,  $\text{Li}_2\text{CO}_3$ ). For all experiments, we selected Al-doped LLZO with the composition  $\text{Li}_{6.25}\text{Al}_{0.25}\text{La}_3\text{Zr}_2\text{O}_{12}$ , as this material was shown previously to exhibit significant, measurable reduction in contact with Li metal while still forming a self-limiting ODI layer.<sup>22</sup> Two different vacuum deposition techniques were employed—specifically, magnetron sputtering (Figure 1a) and

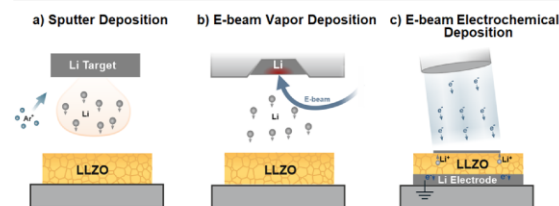


**Figure 1.** Schematics of the different lithium deposition processes that were utilized in this work. (a) Sputter deposition of lithium and transfer under UHV conditions for XPS measurements, (b) e-beam vapor deposition with UHV transfer for the XPS measurements, and (c) *operando* electrochemical deposition inside the XPS chamber via the electron beam electrode method.

electron beam (e-beam) evaporation (Figure 1b)—to compare the impact of vacuum deposition techniques with differing Li deposition energetics on the observed ODI layer formation. These results were compared to *operando* electrochemical deposition of Li via the electron beam electrode method<sup>34,35</sup> (Figure 1c) to interrogate the reactivity of the Li|LLZO interface under operating conditions.

**Impact of Vacuum Deposition Technique on Li|LLZO Reactivity.** Prior to vacuum deposition of Li metal, Al-LLZO surfaces were vacuum annealed to remove any residual carbonate and hydroxide layers (Figure 2a,b). The Li metal was deposited by both magnetron sputtering and e-beam evaporation, after which samples were transferred under ultrahigh vacuum (UHV) conditions to analyze their reactivity by XPS (see the [Experimental Section](#) for details). In both cases, Li was found to readily coat the LLZO surface, resulting in a decrease in the overall XPS signal (Figures 2b and S1). Importantly, the majority of the Li deposits as Li metal, even in relatively thin films (~10 nm), as demonstrated by the sharp peak in the Li 1s core-level spectrum at 54.2 eV (Figure 2b, inset). Our previous work demonstrated that Li metal reacts with the top atomic layers of LLZO to form oxidized Li (Li–O) and reduced Zr species, resulting in the creation of the ODI layer between LLZO and Li.<sup>16</sup> The Li–O content at 55.2 eV (Figure 2b, inset) is related to the intrinsic Li–O content in LLZO itself, as well to the changed local atomic and electronic structure of oxygen in the ODI. However, parts of Li–O species may also form by the reaction of Li with residual oxygen still present in the UHV atmosphere.

To better understand the morphology of Li thin films, atomic force microscopy (AFM) measurements were performed on Li films deposited on atomically smooth, single-crystal  $\text{SrTiO}_3$  (STO) (001) substrates. These substrates were chosen specifically to remove the contribution of extrinsic roughness introduced by topographic nonuniformities on

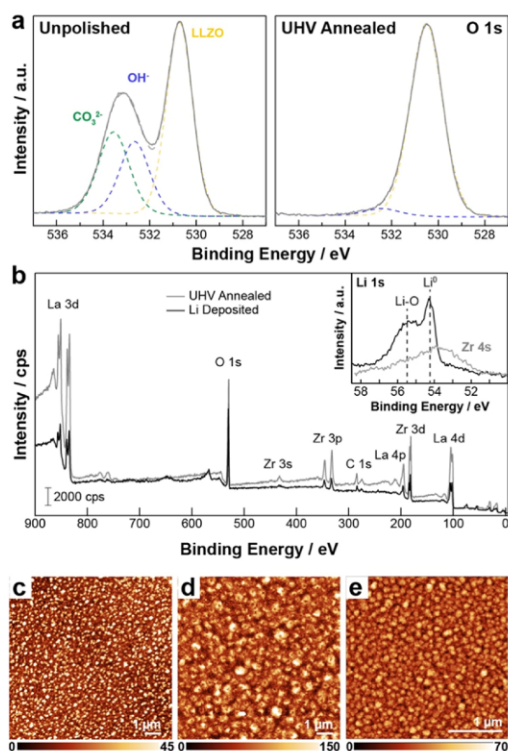


**Figure 2.** (a) Representative O 1s core-level XPS spectra from unpolished (left) and polished, UHV-annealed (right) LLZO pellets. (b) Survey spectra of Al-doped LLZO surfaces before and after Li sputter deposition. The inset shows the Li 1s core level before and after Li deposition. (c–e) Atomic force microscopy (AFM) images of the Li film morphology on STO(001) after (c) 8 min sputter deposition, (d) 30 min sputter deposition, and (e) 10 s e-beam evaporation. Color scales represent height in nanometers.

polished, polycrystalline LLZO. Furthermore, films deposited on STO substrates exhibit a similar degree of XPS signal attenuation (as well as a similar color) to the films deposited on LLZO pellets, indicating a similar degree of coverage for a given deposition time.<sup>36</sup> AFM images of a series of thin Li films deposited by sputter (Figure 2c,d) and e-beam (Figure 2e) deposition reveal that deposition takes place by three-dimensional (3D) island growth and that the islands coalesce with increasing deposition time. In addition, the overall morphology of the films is very similar regardless of the deposition technique, with e-beam evaporation yielding slightly smaller islands at similar nominal coverage (i.e., similar attenuation of the XPS signal, Figure S1). In all cases, the surfaces are relatively smooth (rms roughness  $\sim 8$  nm), suggesting continuous coverage that yields a highly conformal Li/LLZO interface.

It was assumed in our prior work that the reactivity observed was “intrinsic” to the Li/LLZO interface and, therefore, another Li vacuum deposition technique applied after the same LLZO cleaning procedure would result in the same ODI formation. Surprisingly, no ODI layer formation is observed when Li deposition is performed via e-beam evaporation despite similar coverage by the deposited Li layer. Specifically, the partial reduction of  $\text{Zr}^{4+}$  to  $\text{Zr}^{2+}$  and  $\text{Zr}^0$  is observed after sputter

deposition of Li metal (Figure 3a), whereas there is no indication of any species other than  $\text{Zr}^{4+}$  after Li deposition onto LLZO by e-beam evaporation (Figure 3b). The extent of reactivity is not impacted by the thickness of the Li layer (Figure S2), suggesting that increased deposition time and Li layer thickness cannot drive additional reactivity, nor is it affected by the specific LLZO processing method. As the morphology of the deposited lithium was not found to differ significantly between both techniques, it is also unlikely that the morphology of the deposited lithium metal or the size of the Li crystallites can account for differences in apparent reactivity. The observed differences also cannot be explained by external parameters of the deposition techniques (i.e., presence of residual  $\text{O}_2$  in the UHV chamber). While sputter deposition of the film roughly takes 30 min instead of seconds for e-beam deposition, the absolute time is not sufficient to account for the observed reactions under UHV conditions. Furthermore, more  $\text{O}_2$  is intrinsically present during sputter deposition due to the orders of magnitude higher background pressure relative to e-beam deposition ( $1 \times 10^{-3}$  vs  $\sim 1 \times 10^{-7}$  mbar, respectively), confirming that the oxidation of Li by residual  $\text{O}_2$  cannot drive the lower reactivity of Li observed on e-beam-deposited samples.

Despite the observed differences in chemical reactivity, electrochemical impedance spectroscopy (EIS) measurements of Li|SEI|Li symmetric cells made from sputter- and e-beam deposited Li yield similar interfacial resistances (Figure 4). Slight variations originate from the use of different cell setups and potentiostats for measuring the spectra. For comparison, the EIS spectrum of a symmetrical Au/LLZO/Au blocking cell is shown and demonstrates the bulk and grain boundary contributions in the high-frequency range (4 MHz and 500 kHz, respectively). As expected, bulk and grain boundary contributions are similar for the Li/LLZO/Li symmetric cells, and although these contributions were not resolved for the sputtered Li electrodes due to a lower frequency range, calculated bulk plus grain boundary resistances for cells with e-beam-deposited Li match well with those resolved directly in blocking electrode measurements (181 and 197  $\Omega \text{ cm}^2$ , respectively). Distinct from the blocking electrode measurements, symmetric Li–Li cells possess additional contributions in the low-frequency range that are attributable to the Li/LLZO interface. Deviation from R–C behavior was observed at low frequencies ( $\leq 10$  Hz). Such counterintuitive deviation from R–C behavior when using a nonionically blocking electrode is rationalized by the presence of pits on the surface of the solid electrolytes that were sanded with SiC sandpaper of 400 and 600 grit (22 and 16  $\mu\text{m}$  abrasive particle size, respectively). The increase in roughness of the solid electrolyte surface likely arises from pull out of crystallites modifying the capacitive component of the low frequency impedance behavior as reported previously in sintered  $B'$  alumina by Armstrong and Burnham.<sup>37</sup> Note that all bulk, grain boundary, and interface contributions were fit with parallel R–P elements, with P being a nonideal capacity. Full equivalent circuits used to fit are displayed in Figure S3. Table 1 displays the obtained values for the resistances and capacitances of each element, if it was possible to resolve them separately. We estimated the error on the obtained resistance values to be around 15% based on experimental uncertainties, like different cell geometries, electrode areas, and used potentiostats. As bulk and grain boundary contributions overlap in the frequency range for the Au and e-beam Li electrodes, the obtained individual

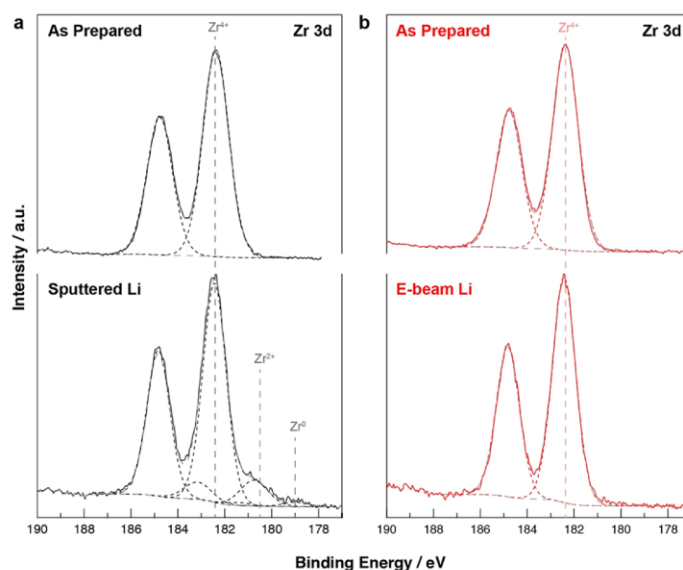


Figure 3. Evolution of the Zr 3d signal for the (a) sputter and (b) e-beam deposition of lithium on LLZO.

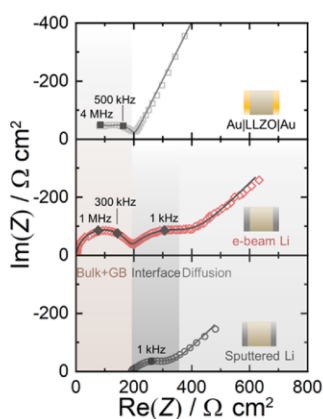


Figure 4. Impedance spectra obtained for blocking electrodes (Au) as well as nonblocking electrodes (e-beam Li and sputtered Li). The corresponding fit to the data (open symbols) is displayed in solid gray lines.

resistances may be flawed to some extent. However, peak frequencies and calculated capacitances are in agreement with literature data and support our interpretation of the different processes.<sup>38</sup> Furthermore, cycling of these cells at a current density of  $10 \mu\text{A cm}^{-2}$  (Figure S4) reveals almost identical polarization behavior, consistent with the similar interfacial resistances calculated by fitting of the impedance spectra.

The similarity in impedance behavior of the LiLLZO/Li cells suggests one of two possibilities—either the ODI layer formation does not measurably alter the charge transfer resistance from that of unreacted LLZO or that the ODI layer formation is somehow induced during the EIS measurement. Induced reactivity may be caused by small currents at the interface during data collection at the low-frequency limit of the EIS spectra (0.01 Hz), which is close to actual DC measurements; however, these conditions are not accessed until after the high-frequency response corresponding to charge transfer resistance has already been measured, making it unlikely that ODI formation is somehow induced by the electrochemical measurement. Therefore, it seems that the formation of the ODI in LLZO does not affect the interfacial kinetics significantly. Differences between sputter and e-beam deposition will be more thoroughly explored below to better understand the underlying driving forces for Li reactivity with LLZO and its impact on electrochemical performance.

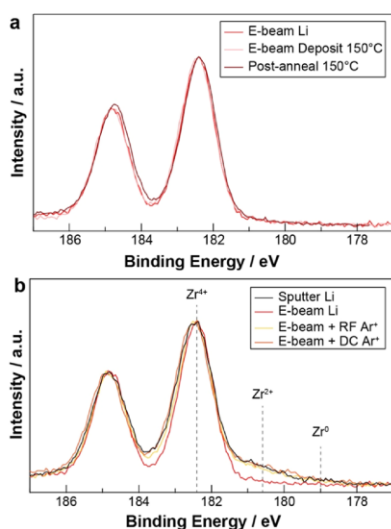
**Influence of Deposition Energetics on the Chemical Reactivity.** Having eliminated extrinsic differences between samples as possible explanations for the observed differences in chemical reactivity and resulting ODI layer formation, we hypothesize that the LiLLZO reactivity must stem from some intrinsic differences between the sputter and e-beam deposition techniques. While both deposition techniques rely on relatively low energy input, magnetron sputtering does result in the generation of more energetic species than those produced by e-beam evaporation. Typical energies of species deposited via e-beam and sputter deposition are 0.01–0.1 and

Table 1. Summary of Obtained Resistances and Capacitances for the Different Contributions Obtained from Fitting the Impedance Spectra in Figure 4

electrodes	$R_{\text{Bulk}}/\Omega \text{ cm}^2$	$C_{\text{Bulk}}/\text{F}$	$R_{\text{GB}}/\Omega \text{ cm}^2$	$C_{\text{GB}}/\text{F}$	$R_{\text{Int}}/\Omega \text{ cm}^2$	$C_{\text{Int}}/\text{F}$
Au	$118 \pm 18$	$1.35 \times 10^{-11}$	$79 \pm 12$	$1.13 \times 10^{-9}$		
e-beam Li	$114 \pm 17$	$9.12 \times 10^{-10}$	$67 \pm 10$	$1.95 \times 10^{-9}$	$176 \pm 26$	$1.15 \times 10^{-6}$
sputtered Li					$137 \pm 20$	$1.36 \times 10^{-7}$

0.1–1.0 eV, respectively.<sup>39</sup> In addition to differences in energy, sputter deposition also results in the formation of ions within the plasma present at the sputter target surface (i.e.,  $\text{Li}^+$  and  $\text{Ar}^+$ ), whereas the only species present during e-beam evaporation are lithium atoms (i.e.,  $\text{Li}^0$ ). It is therefore possible that differences in Li chemistry and/or energetics drive the observed differences in reactivity. Although some fraction of  $\text{Li}^+$  species are certainly formed during sputtering and deposit onto the LLZO surface, it is highly unlikely that  $\text{Li}^+$  species can drive ODI layer formation on LLZO as they have no 2s electrons with which to reduce  $\text{Zr}^{4+}$ . As a result, the majority of Li species deposited via sputter deposition must be neutral  $\text{Li}^0$ , indicating that the chemical composition of Li species deposited by both e-beam and sputter deposition are likely the same.

This strongly suggests that differences in the energetics of the two processes instead drive the apparent differences in reactivity. Heating to 150 °C during or after Li deposition via e-beam evaporation also yields no reduction of Zr species (Figure 5a), suggesting that thermal energies below the Li



**Figure 5.** Zr 3d core-level XPS spectra demonstrating the effect of  $\text{Ar}^+$  ion bombardment on  $\text{Zr}^{4+}$  reduction by e-beam-deposited Li metal on LLZO.

melting point ( $\sim 0.04$  eV at 150 °C) are insufficient to bridge the difference in energetics between the sputtering and e-beam processes. As there is certainly a high density of  $\text{Ar}^+$  species present during sputter deposition that are not present during e-beam evaporation, it is likely that the flux of these ions to the substrate provides the necessary additional energy and facilitates the observed reactivity. Indeed, brief irradiation of e-beam-deposited Li films with  $\text{Ar}^+$  ions, either via direct current ion bombardment or radio-frequency plasma, is able to directly reproduce the observed  $\text{Zr}^{4+}$  reduction and ODI layer formation that takes place intrinsically during sputter deposition (Figure 5b). Similar reduction of  $\text{Zr}^{4+}$  is not observed after  $\text{Ar}^+$  irradiation when Li metal is not present on the LLZO surface (Figure S5), confirming that reduction is not caused by  $\text{Ar}^+$  ion bombardment alone, but rather by the additional energy provided to  $\text{Li}^0$ . Given the overall low

energies involved in either vacuum deposition process, this difference strongly suggests the presence of a kinetic barrier to LLZO reduction, as the thermodynamic reduction potential of LLZO is predicted to be  $\sim 50$  mV above that of Li metal,<sup>24</sup> implying that LLZO should reduce in contact with Li regardless of the deposition technique used. The fact that reduction is not observed for the e-beam samples but is observed for sputter deposition indicates that there must be a kinetic barrier to reduction. The presence of more energetic ionic species during the sputter deposition process likely provides enough energy to overcome this kinetic barrier, driving  $\text{Zr}^{4+}$  reduction and ODI formation.

**Electrochemical Reactivity of Li Metal with LLZO and Kinetic Considerations.** To determine whether such a kinetic barrier does, in fact, exist, it is necessary to observe the reactivity of the Li/LLZO interface during electrochemical deposition of Li metal. To simulate electrochemically formed Li/LLZO interfaces in a clean UHV environment, we performed electrochemical deposition of Li via the electron beam electrode technique<sup>34</sup> (Figure 1c), which utilizes an incident, low-energy electron beam current to drive the deposition of Li metal at the LLZO surface while simultaneously measuring XPS. This method enables visualization of the Li/LLZO interface under *operando* conditions that closely mimic the deposition of lithium metal without the presence of a lithium metal reservoir, which are currently being discussed for the concept of “anode-free” lithium metal batteries.<sup>11,40–42</sup>

*Operando* XPS measurements of electrochemical Li deposition also reveal the reduction of  $\text{Zr}^{4+}$  to  $\text{Zr}^{2+}$  and  $\text{Zr}^0$  (Figure 6a), with the extent of reduction almost identical to that observed in annealed LLZO samples with sputter-deposited Li (Figure 6b). Consistent with previous time-dependent EIS measurements,<sup>22</sup> *operando* XPS measurements reveal that ODI formation is self-limiting, with very little change in the extent of  $\text{Zr}^{4+}$  reduction with increased Li deposition time after  $\sim 1.5$  min. The fact that reduction is observed after electrochemical Li deposition onto these samples is even more significant considering that, due to slightly poorer vacuum quality in the electron beam electrode XPS system, the starting LLZO surfaces contained some residual  $\text{Li}_2\text{CO}_3/\text{LiOH}$  species (Figure S6). As the presence of such species has been shown to impede Li reactivity with LLZO, it is possible that even more reactivity would be observed after electrochemical Li deposition onto  $\text{Li}_2\text{CO}_3/\text{LiOH}$ -free surfaces. Nevertheless, realistic cell assembly conditions will inevitably introduce some of these species to the interface, and therefore, the surface cleanliness of these samples more closely mirrors those present in an actual coin cell.

As a result, these measurements provide clear evidence that the electrochemical deposition of Li metal does indeed result in the reduction of the LLZO surface, resulting in ODI formation that is consistent with previous results by sputter deposition. Furthermore, these results support the hypothesis that there is a kinetic barrier to LLZO reduction by Li, as the application of sufficient overpotential to electrochemically nucleate and grow Li metal provides sufficient energy to drive  $\text{Zr}^{4+}$  reduction at the Li/LLZO interface. Indeed, the only case in which no reduction is observed is in the case of very low incident Li deposition energies during e-beam evaporation. The presence of a kinetic barrier further explains the similar lack of reduction observed after simple physical contact of Li metal with LLZO surfaces, even at temperatures above the

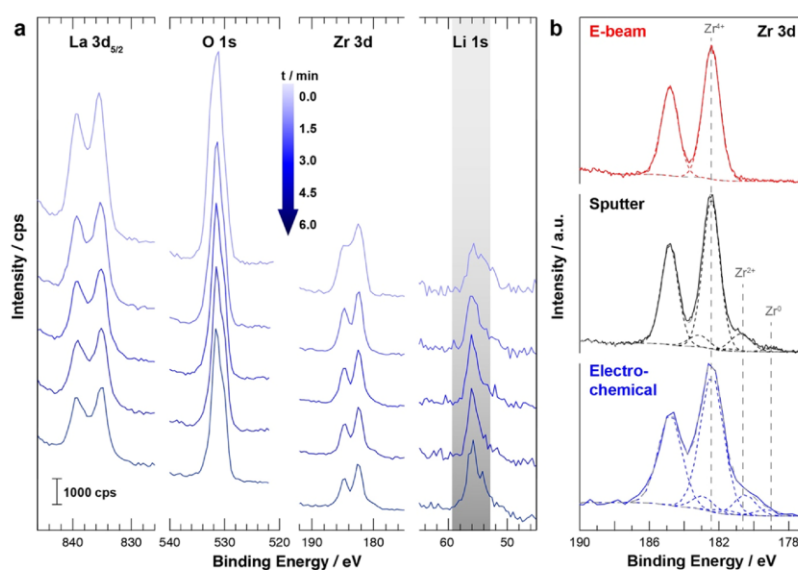


**Figure 6.** (a) *Operando* XPS measurements of individual core-level spectra during electrochemical deposition of Li showing their evolution with increasing Li deposition time. All core-level spectra are plotted on the same absolute scale in counts per second except Li 1s spectra, which are magnified by 10× for clarity. (b) Zr 3d core-level spectra comparing the extent of  $Zr^{4+}$  reduction as a function of the deposition technique.

melting point.<sup>16</sup> Therefore, it can be concluded that the formation of an ODI is dependent on the lithium energy during the deposition process and that under further electrochemical cycling conditions, ODI formation is expected to occur.

## CONCLUSIONS

Through the use of both *in situ* and *operando* XPS methodologies, we demonstrate the presence of a kinetic barrier to the reduction of LLZO by Li metal. The extent of ODI formation is found to depend sensitively on the energetics of Li metal as it arrives at the LLZO surface, with electrochemical and sputter deposition intrinsically leading to the reduction of  $Zr^{4+}$  and resulting in ODI layer formation. Lower energy e-beam evaporation does not result in any reduction of  $Zr^{4+}$ , even when Li is deposited at elevated temperatures; however, subsequent irradiation of e-beam-deposited Li by energetic  $Ar^+$  species is able to reproduce the extent of ODI formation observed from electrochemical and sputter deposition. Despite the presence of a kinetic barrier to reduction, EIS measurements of Li|LLZO|Li coin cells reveal an identical response whether or not the ODI is present, indicating that interphase formation does not impede the charge transfer kinetics of Li ions across the Li|LLZO interface and likely explaining the favorable electrochemical performance of LLZO-based ASSBs. However, a possible link between the formation of the ODI layer in LLZO and dendrite nucleation should be considered in future work. Overall, these results highlight the additional complexities governing the reactivity of solid-state interfaces in ASSBs and underscore the importance of *operando* characterization of interfacial stability to design more robust, high-performance protection strategies for solid electrolytes in contact with reactive electrodes.

## EXPERIMENTAL SECTION

**Preparation of an LLZO Solid Electrolyte Pellet.** Two different approaches for the processing of  $Li_{6.25}Al_{0.25}La_3Zr_2O_{12}$  were employed to exclude a dependence of the reactivity toward lithium as a function of the synthesis route. A high-temperature (1230 °C) sintering route under dry oxygen was used as reported in previous work.<sup>32</sup> Synthesis by rapid induction hot-press (RHIP) was performed as follows:  $Li_{6.25}Al_{0.25}La_3Zr_2O_{12}$  solid electrolyte was synthesized from starting powders of  $Li_2CO_3$ ,  $Al_2O_3$ ,  $La_2O_3$ , and  $ZrO_2$  by a solid-state reaction method and calcined at 1000 °C for 4 h in dry air. Densification of Al-LLZO was achieved by RHIP of green bodies of calcined Al-LLZO at 1225 °C and 47 MPa for 40 min in an argon atmosphere. The slight change in densification temperature is expected to affect the resulting grain size of the samples, having larger grains by the former route. However, the interpretation of the results in this work would not be affected by the grain size of the samples. Most importantly, both sample preparation methods yielded pellets with identical densities ( $95 \pm 3\%$ ), ionic conductivity values ( $0.1 \text{ mS cm}^{-1}$  at 25 °C), and surface chemistry. E-beam deposition of Li metal onto both types of samples also resulted in a similar lack of reactivity (Figure S2). Additionally, a low concentration of impurities was obtained via both processing routes ( $\leq 2 \text{ wt } \%$ , Figure S7).

The hot-pressed pellets were cut into 1.5 mm nominal thicknesses using a diamond saw with mineral oil as the cutting fluid. The LLZO hot-pressed disks were sanded with a lapping fixture and 400 grit SiC sandpaper onto a glass plate to achieve parallel faces. Further grinding was conducted with 600 and 1200 grit SiC sandpaper followed by polishing steps using diamond pastes of nominal abrasive size of 15, 6, 1, 0.5, and 0.1  $\mu\text{m}$  and a glycol-based diamond paste extender as the polishing fluid. Samples were cleaned off with ethanol and acetone between polishing steps. A Au layer was sputtered onto the electrolyte surface for ionic conductivity measurements.

**Surface Preparation and Vacuum Deposition of Li.** LLZO pellets were first sanded using 400 and 600 grit paper and were then immediately transferred into the UHV system to prevent any further oxidation. Sanded LLZO samples were then heated in the XPS analysis chamber up to 500 °C with a heating rate  $\sim 100 \text{ }^\circ\text{C h}^{-1}$  to remove residual hydroxides and carbonates that remained on the LLZO surface.

Vacuum deposition of Li was performed in a separate chamber (base pressure  $5 \times 10^{-10}$  mbar) connected to the XPS analysis system by a UHV transfer line (base pressure  $1 \times 10^{-10}$  mbar).<sup>25</sup> DC magnetron sputter deposition was performed for 30 min using an Ar background pressure of  $1 \times 10^{-3}$  mbar, target power of 40 W, and a target-to-substrate distance of 17 cm, yielding a nominal Li film thickness of 10 nm. E-beam evaporation was performed in the same system using a 5 kV accelerating voltage and 3 mA emission current at a source-to-substrate distance of ca. 50 cm. Deposition times were varied to yield Li films of varying thicknesses, as discussed above. The background pressure was  $\leq 5 \times 10^{-7}$  mbar throughout e-beam deposition. RF Ar<sup>+</sup> bombardment was performed in the deposition chamber immediately after e-beam Li deposition using 25 W plasma power applied directly to the sample holder for 90 s ( $2.5 \times 10^{-2}$  mbar Ar pressure). DC Ar<sup>+</sup> bombardment was performed after UHV transfer of the Li-deposited sample to the *in situ* XPS chamber using a 5 kV ion beam at 10 mA emission current for 30 s ( $2.7 \times 10^{-7}$  mbar chamber pressure).

**In Situ and Operando X-ray Photoelectron Spectroscopy.** *In situ* XPS measurements were performed using a Specs PHOIBOS 150 hemispherical energy analyzer with a monochromated Al K $\alpha$  X-ray source. Charge neutralization was carried out for insulating LLZO samples using a low-energy flood gun (5 eV electron energy), with the neutralization conditions optimized on the basis of the degree of charging present for a given sample. Survey spectra were measured using a pass energy of 40 eV at a resolution of 0.2 eV/step and a total integration time of 0.1 s/point. Core-level spectra were measured using a pass energy of 20 eV at a resolution of 0.05 eV/step and a total integration time of 0.5 s/point. Deconvolution was performed using CasaXPS software with a Shirley-type background and 70–30 Gaussian–Lorentzian peak shapes. Spectra were charge referenced to the position of Zr 3d<sub>5/2</sub> peak for Zr<sup>4+</sup> at 182.4 eV, as discussed previously.<sup>22</sup>

The electrochemical deposition of Li via the electron beam electrode method and the *operando* XPS measurements were performed using an XPS PHI 5000 VersaProbe II (Physical Electronics, Inc.). The plating current density was measured to be 10–12  $\mu\text{A cm}^{-2}$ , and 6 min deposition time corresponded to  $\sim 6$  nm Li deposition. The pressure inside the vacuum chamber was between  $10^{-8}$  mbar and  $10^{-9}$  mbar. The deposition process resulted from electron bombardment via neutralization settings with a grounded sample holder. For neutralization, an electron gun with an emission current of 20  $\mu\text{A}$  and a beam diameter of about 5 mm was employed. A monochromated Al K $\alpha$  X-ray source with a beam diameter of 200  $\mu\text{m}$  at 50 W was used. The analyzer pass energy was set to 23.5 eV for obtaining detailed spectra. Charge referencing and spectral fitting were performed as described above.

**Symmetric Cell Assembly and Electrochemical Impedance Spectroscopy.** Thicker lithium films were deposited on both sides of UHV-annealed LLZO pellets for EIS measurements (200–300 nm total Li thickness). After sputtering Li onto one side of the pellet, the sample was removed from UHV, and a clean Li foil was placed onto the Li film to prevent direct contact between the Li film and the stainless steel sample holder after flipping over to coat the other side. After depositing Li on the backside, samples were transferred back into a glovebox and another clean Li foil was placed on the freshly deposited Li film. The Li/LLZO/Li symmetric cell was then assembled into a coin cell inside the same glovebox. Impedance measurements of assembled symmetric coin cells were performed using a potentiostat with a frequency response analyzer (FRA) module (Metrohm Autolab, Herisau, Switzerland) capable of monitoring frequencies 1 MHz to 10 mHz (sputtered Li) and 10 MHz to 10 mHz (e-beam Li). All measurements were taken at room temperature outside of the glovebox, and no preconditioning was performed prior to measurements of EIS spectra. Fitting of impedance data was carried out using rhd instruments RelaxIS 3 software. Bulk, grain boundary, and interfacial contributions were modeled via a parallel circuit of resistance and constant phase element (RP-circuit). Each capacitance was calculated with the semicircle resistance,  $\alpha$ -, and capacity values.

## ■ ASSOCIATED CONTENT

### Supporting Information

The Supporting Information is available free of charge at <https://pubs.acs.org/doi/10.1021/acs.chemmater.0c03869>.

Additional XPS measurements; equivalent circuit diagrams for EIS fitting; electrochemical cycling data; and XRD of LLZO pellets synthesized via sintering and RHIP (PDF)

## ■ AUTHOR INFORMATION

### Corresponding Authors

Sanja Tepavcevic – Materials Science Division, Argonne National Laboratory, Lemont, Illinois 60439, United States; Email: [sanja@anl.gov](mailto:sanja@anl.gov)

Jürgen Janek – Institute of Physical Chemistry and Center for Materials Research (ZfM), Justus-Liebig-University Giessen, D-35392 Giessen, Germany; [orcid.org/0000-0002-9221-4756](https://orcid.org/0000-0002-9221-4756); Email: [juergen.janek@pc.jlug.de](mailto:juergen.janek@pc.jlug.de)

### Authors

Justin G. Connell – Materials Science Division and Joint Center for Energy Storage Research, Argonne National Laboratory, Lemont, Illinois 60439, United States; [orcid.org/0000-0002-2979-2131](https://orcid.org/0000-0002-2979-2131)

Till Fuchs – Institute of Physical Chemistry and Center for Materials Research (ZfM), Justus-Liebig-University Giessen, D-35392 Giessen, Germany

Hannah Hartmann – Institute of Physical Chemistry and Center for Materials Research (ZfM), Justus-Liebig-University Giessen, D-35392 Giessen, Germany

Thorben Krauskopf – Institute of Physical Chemistry, Justus-Liebig-University Giessen, D-35392 Giessen, Germany

Yisi Zhu – Materials Science Division, Argonne National Laboratory, Lemont, Illinois 60439, United States

Joachim Sann – Institute of Physical Chemistry and Center for Materials Research (ZfM), Justus-Liebig-University Giessen, D-35392 Giessen, Germany

Regina Garcia-Mendez – Department of Materials Science and Engineering, University of Michigan, Ann Arbor, Michigan 48109, United States

Jeff Sakamoto – Department of Materials Science and Engineering and Department of Mechanical Engineering, University of Michigan, Ann Arbor, Michigan 48109, United States

Complete contact information is available at:

<https://pubs.acs.org/doi/10.1021/acs.chemmater.0c03869>

### Author Contributions

<sup>†</sup>J.G.C. and T.F. contributed equally to this work.

### Notes

The authors declare no competing financial interest.

## ■ ACKNOWLEDGMENTS

This work was conducted as part of the US-German joint collaboration on "Interfaces and Interphases in Rechargeable Li-metal based Batteries" supported by the US Department of Energy (DOE) and German Federal Ministry of Education and Research (BMBF). This work has been partly funded by the German Federal Ministry of Education and Research (BMBF) under the project "LiSI", grant identifier 03XP0224E. Research at Argonne National Laboratory was funded by the U.S. Department of Energy, and support from Tien Duong of the

Office of Energy Efficiency and Renewable Energy Vehicle Technologies Program is gratefully acknowledged. We also acknowledge support from the Office of Science, Office of Basic Energy Sciences and Materials Sciences and Engineering Division. Li sputtering/e-beam evaporation, XPS and EIS measurements were performed at the Electrochemical Discovery Laboratory, a Joint Center for Energy Storage Research facility at Argonne National Laboratory. T.K. acknowledges financial support (Kekulé scholarship) by the Funds of the Chemical Industry (FCI).

## REFERENCES

- (1) Randau, S.; Weber, D. A.; Kötz, O.; Koerver, R.; Braun, P.; Weber, A.; Ivers-Tiffée, E.; Adermann, T.; Kulis, J.; Zeier, W. G.; Richter, F. H.; Janek, J. Benchmarking the Performance of All-Solid-State Lithium Batteries. *Nat. Energy* **2020**, *5*, 259–270.
- (2) Wang, H.; Yu, D.; Kuang, C.; Cheng, L.; Li, W.; Feng, X.; Zhang, Z.; Zhang, X.; Zhang, Y. Alkali Metal Anodes for Rechargeable Batteries. *Chem* **2019**, *5*, 313–338.
- (3) Betz, J.; Bieker, G.; Meister, P.; Placke, T.; Winter, M.; Schmuch, R. Theoretical versus Practical Energy: A Plea for More Transparency in the Energy Calculation of Different Rechargeable Battery Systems. *Adv. Energy Mater.* **2019**, *9*, No. 1900761.
- (4) Krauskopf, T.; Richter, F. H.; Zeier, W. G.; Janek, J. Physicochemical Concepts of the Lithium Metal Anode in Solid-State Batteries. *Chem. Rev.* **2020**, 7745–7794.
- (5) Long, L.; Wang, S.; Xiao, M.; Meng, Y. Polymer Electrolytes for Lithium Polymer Batteries. *J. Mater. Chem. A* **2016**, *4*, 10038–10039.
- (6) Lin, D.; Liu, Y.; Cui, Y. Reviving the Lithium Metal Anode for High-Energy Batteries. *Nat. Nanotechnol.* **2017**, *12*, 194–206.
- (7) Cheng, X. B.; Zhang, R.; Zhao, C. Z.; Zhang, Q. Toward Safe Lithium Metal Anode in Rechargeable Batteries: A Review. *Chem. Rev.* **2017**, *117*, 10403–10473.
- (8) Tarascon, J. M.; Armand, M. Issues and Challenges Facing Rechargeable Lithium Batteries. *Nature* **2001**, *414*, 359–367.
- (9) Shen, Y.; Zhang, Y.; Han, S.; Wang, J.; Peng, Z.; Chen, L. Unlocking the Energy Capabilities of Lithium Metal Electrode with Solid-State Electrolytes. *Joule* **2018**, *2*, 1674–1689.
- (10) Janek, J.; Zeier, W. G. A Solid Future for Battery Development. *Nat. Energy* **2016**, *1*, 1–4.
- (11) Lee, Y.; Fujiki, S.; Jung, C.; Suzuki, N.; Yashiro, N.; Omoda, R.; Ko, D.; Shiratsuchi, T.; Sugimoto, T.; Ryu, S.; Ku, J. H.; Watanabe, T.; Park, Y.; Aihara, Y.; Im, D.; Han, I. T. High-Energy Long-Cycling All-Solid-State Lithium Metal Batteries Enabled by Silver–Carbon Composite Anodes. *Nat. Energy* **2020**, *5*, 299–308.
- (12) Flatscher, F.; Philipp, M.; Ganschow, S.; Wilkening, H. M. R.; Rettenwander, D. The Natural Critical Current Density Limit for  $\text{Li}_7\text{La}_3\text{Zr}_2\text{O}_{12}$  Garnets. *J. Mater. Chem. A* **2020**, 15782–15788.
- (13) Thangadurai, V.; Narayanan, S.; Pinzar, D. Garnet-Type Solid-State Fast Li Ion Conductors for Li Batteries: Critical Review. *Chem. Soc. Rev.* **2014**, *43*, 4714–4727.
- (14) Wang, C.; Fu, K.; Kammampata, S. P.; McOwen, D. W.; Samson, A. J.; Zhang, L.; Hitz, G. T.; Nolan, A. M.; Wachsmann, E. D.; Mo, Y.; Thangadurai, V.; Hu, L. Garnet-Type Solid-State Electrolytes: Materials, Interfaces, and Batteries. *Chem. Rev.* **2020**, *120*, 4257–4300.
- (15) Hofstetter, K.; Samson, A. J.; Narayanan, S.; Thangadurai, V. Present Understanding of the Stability of Li-Stuffed Garnets with Moisture, Carbon Dioxide, and Metallic Lithium. *J. Power Sources* **2018**, *390*, 297–312.
- (16) Wolfenstine, J.; Allen, J. L.; Read, J.; Sakamoto, J. Chemical Stability of Cubic  $\text{Li}_7\text{La}_3\text{Zr}_2\text{O}_{12}$  with Molten Lithium at Elevated Temperature. *J. Mater. Sci.* **2013**, *48*, 5846–5851.
- (17) Kotobuki, M.; Munakata, H.; Kanamura, K.; Sato, Y.; Yoshida, T. Compatibility of  $\text{Li}_7\text{La}_3\text{Zr}_2\text{O}_{12}$  Solid Electrolyte to All-Solid-State Battery Using Li Metal Anode. *J. Electrochem. Soc.* **2010**, *157*, A1076.
- (18) Murugan, R.; Thangadurai, V.; Weppner, W. Fast Lithium Ion Conduction in Garnet-Type  $\text{Li}_7\text{La}_3\text{Zr}_2\text{O}_{12}$ . *Angew. Chem., Int. Ed.* **2007**, *46*, 7778–7781.
- (19) Rettenwander, D.; Wagner, R.; Reyer, A.; Bonta, M.; Cheng, L.; Doeff, M. M.; Limbeck, A.; Wilkening, M.; Amthauer, G. Interface Instability of Fe-Stabilized  $\text{Li}_7\text{La}_3\text{Zr}_2\text{O}_{12}$  versus Li Metal. *J. Phys. Chem. C* **2018**, *122*, 3780–3785.
- (20) Ma, C.; Cheng, Y.; Yin, K.; Luo, J.; Sharafi, A.; Sakamoto, J.; Li, J.; More, K. L.; Dudney, N. J.; Chi, M. Interfacial Stability of Li Metal–Solid Electrolyte Elucidated via in Situ Electron Microscopy. *Nano Lett.* **2016**, *16*, 7030–7036.
- (21) Tao, X.; Liu, Y.; Liu, W.; Zhou, G.; Zhao, J.; Lin, D.; Zu, C.; Sheng, O.; Zhang, W.; Lee, H. W.; Cui, Y. Solid-State Lithium–Sulfur Batteries Operated at 37 °C with Composites of Nanostructured  $\text{Li}_7\text{La}_3\text{Zr}_2\text{O}_{12}$ /Carbon Foam and Polymer. *Nano Lett.* **2017**, *17*, 2967–2972.
- (22) Zhu, Y.; Connell, J. G.; Tepavcevic, S.; Zapol, P.; Garcia-Mendez, R.; Taylor, N. J.; Sakamoto, J.; Ingram, B. J.; Curtiss, L. A.; Freeland, J. W.; Fong, D. D.; Markovic, N. M. Dopant-Dependent Stability of Garnet Solid Electrolyte Interfaces with Lithium Metal. *Adv. Energy Mater.* **2019**, *9*, 1–11.
- (23) Thompson, T.; Yu, S.; Williams, L.; Schmidt, R. D.; Garcia-Mendez, R.; Wolfenstine, J.; Allen, J. L.; Kioupakis, E.; Siegel, D. J.; Sakamoto, J. Electrochemical Window of the Li-Ion Solid Electrolyte  $\text{Li}_7\text{La}_3\text{Zr}_2\text{O}_{12}$ . *ACS Energy Lett.* **2017**, *2*, 462–468.
- (24) Zhu, Y.; He, X.; Mo, Y. Origin of Outstanding Stability in the Lithium Solid Electrolyte Materials: Insights from Thermodynamic Analyses Based on First-Principles Calculations. *ACS Appl. Mater. Interfaces* **2015**, *7*, 23685–23693.
- (25) Binner, T.; Marcolongo, A.; Mottet, M.; Weber, V.; Laino, T. Comparison of Computational Methods for the Electrochemical Stability Window of Solid-State Electrolyte Materials. *J. Mater. Chem. A* **2020**, *8*, 1347–1359.
- (26) Richards, W. D.; Miara, L. J.; Wang, Y.; Kim, J. C.; Ceder, G. Interface Stability in Solid-State Batteries. *Chem. Mater.* **2016**, *28*, 266–273.
- (27) Sharafi, A.; Yu, S.; Naguib, M.; Lee, M.; Ma, C.; Meyer, H. M.; Nanda, J.; Chi, M.; Siegel, D. J.; Sakamoto, J. Impact of Air Exposure and Surface Chemistry on Li– $\text{Li}_7\text{La}_3\text{Zr}_2\text{O}_{12}$  Interfacial Resistance. *J. Mater. Chem. A* **2017**, *5*, 13475–13487.
- (28) Sharafi, A.; Kazyak, E.; Davis, A. L.; Yu, S.; Thompson, T.; Siegel, D. J.; Dasgupta, N. P.; Sakamoto, J. Surface Chemistry Mechanism of Ultra-Low Interfacial Resistance in the Solid-State Electrolyte  $\text{Li}_7\text{La}_3\text{Zr}_2\text{O}_{12}$ . *Chem. Mater.* **2017**, *29*, 7961–7968.
- (29) Wenzel, S.; Leichtweiss, T.; Krüger, D.; Sann, J.; Janek, J. Interphase Formation on Lithium Solid Electrolytes — An in Situ Approach to Study Interfacial Reactions by Photoelectron Spectroscopy. *Solid State Ionics* **2015**, *278*, 98–105.
- (30) Wang, Y.; Lu, D.; Xiao, J.; Harvey, G. J.; Wang, C.; Zhang, J. G.; Liu, J. Superionic Conduction and Interfacial Properties of the Low Temperature Phase  $\text{Li}_7\text{P}_2\text{S}_8\text{Br}_{0.5}\text{I}_{0.5}$ . *Energy Storage Mater.* **2019**, *19*, 80–87.
- (31) Bron, P.; Rölling, B.; Dehnen, S. Impedance Characterization Reveals Mixed Conducting Interphases between Sulfidic Superionic Conductors and Lithium Metal Electrodes. *J. Power Sources* **2017**, *352*, 127–134.
- (32) Krauskopf, T.; Hartmann, H.; Zeier, W. G.; Janek, J. Toward a Fundamental Understanding of the Lithium Metal Anode in Solid-State Batteries - An Electrochemo-Mechanical Study on the Garnet-Type Solid Electrolyte  $\text{Li}_{6.25}\text{Al}_{0.25}\text{La}_3\text{Zr}_2\text{O}_{12}$ . *ACS Appl. Mater. Interfaces* **2019**, *11*, 14463–14477.
- (33) De Jonghe, L. C. Transport Number Gradients and Solid Electrolyte Degradation. *J. Electrochem. Soc.* **1982**, *129*, 752.
- (34) Wood, K. N.; Steirer, K. X.; Hafner, S. E.; Ban, C.; Santhanagopalan, S.; Lee, S. H.; Teeter, G. Operando X-ray Photoelectron Spectroscopy of Solid Electrolyte Interphase Formation and Evolution in  $\text{Li}_2\text{S-P}_2\text{S}_5$  Solid-State Electrolytes. *Nat. Commun.* **2018**, *9*, No. 2490.

(35) Janek, J.; Rohnke, M.; Pölleth, M.; Meiss, S. A. *Electrodeposition from Ionic Liquids*; Wiley-VCH, 2008; pp 258–285.

(36) Connell, J. G.; Zhu, Y.; Zapol, P.; Tepavcevic, S.; Sharafi, A.; Sakamoto, J.; Curtiss, L. A.; Fong, D. D.; Freeland, J. W.; Markovic, N. M. Crystal Orientation-Dependent Reactivity of Oxide Surfaces in Contact with Lithium Metal. *ACS Appl. Mater. Interfaces* **2018**, *10*, 17471–17479.

(37) Armstrong, R. D.; Burnham, R. A. The Effect of Roughness on the Impedance of the Interface between a Solid Electrolyte and a Blocking Electrode. *J. Electroanal. Chem. Interfacial Electrochem.* **1976**, *72*, 257–266.

(38) Irvine, J. T. S.; Sinclair, D. C.; West, A. R. Electroceramics: Characterization by Impedance Spectroscopy. *Adv. Mater.* **1990**, *2*, 132–138.

(39) Ohring, M. *Materials Science of Thin Films: Deposition and Structure*; Academic Press: San Diego, CA, 2002.

(40) Krauskopf, T.; Dippel, R.; Hartmann, H.; Pepler, K.; Mogwitz, B.; Richter, F. H.; Zeier, W. G.; Janek, J. Lithium-Metal Growth Kinetics on LLZO Garnet-Type Solid Electrolytes. *Joule* **2019**, *3*, 2030–2049.

(41) Qian, J.; Adams, B. D.; Zheng, J.; Xu, W.; Henderson, W. A.; Wang, J.; Bowden, M. E.; Xu, S.; Hu, J.; Zhang, J. G. Anode-Free Rechargeable Lithium Metal Batteries. *Adv. Funct. Mater.* **2016**, *26*, 7094–7102.

(42) Pande, V.; Viswanathan, V. Computational Screening of Current Collectors for Enabling Anode-Free Lithium Metal Batteries. *ACS Energy Lett.* **2019**, *4*, 2952–2959.

### 3.2 Publication 2: “Current-Dependent Lithium Metal Growth Modes in ‘Anode-Free’ Solid-State Batteries at the Cu|LLZO Interface”

In publication 2 of this dissertation, the morphology and nucleation density of lithium being plated in RFCs is investigated in dependence on the applied current density and CC thickness. Powerful operando techniques were therefore developed, where small and thin electrode patches were structured via an FIB and contacted within an SEM to directly visualize lithium growth beneath the thin film. As a model system to study the general physicochemical dependency of the metal deposition, the interface between thin copper films (100 nm) and LLZO was investigated with this technique.

By using microelectrode patches with 15  $\mu\text{m}$  in diameter and 100 nm in thickness, it is possible to avoid the influence of large, three-dimensional surface defects, such as holes and dust, on lithium deposition. By using such a thin CC, the deposition between copper and LLZO is visible with top-view imaging. This allowed to show that the nucleation density is strongly dependent on the applied current density. Whereas around  $10^7$  particles  $\text{cm}^{-2}$  are plated with  $50 \mu\text{A cm}^{-2}$ , this increases to  $6 \cdot 10^7$  particles  $\text{cm}^{-2}$  at a current density of  $1000 \mu\text{A cm}^{-2}$ . Since the charge deposited was kept constant, higher particle densities are accompanied by a smaller particle size. It is therefore reasonable to assume that a higher density of smaller particles will rather coalesce into a homogeneous film, when thicker CCs or stack pressure is used, which is desirable to achieve in RFCs.

Furthermore, the influence of CC thickness on deposition was investigated. Cu|LLZO interfaces with a thick (10  $\mu\text{m}$ ) foil were prepared by Prof. J. Sakamoto’s working group (University of Michigan) by diffusion bonding the foil onto the ceramic using a hot-press. Cross-sections were then prepared with an FIB allowing the operando observation of lithium deposition at this otherwise buried interface. This direct observation revealed that the higher thickness of the CC offers an improved mechanical integrity, which suppresses the formation of whiskers and guides the deposition of more homogeneous morphology. Still, due to inhomogeneities at the interface, it is yet difficult to obtain thick homogeneous lithium films, if no pressure is applied during the deposition.

T. Fuchs and J. Becker contributed equally to this work by designing and conducting all of the experiments from JLU presented, which were additionally supported by C. Lerch. C. Haslam supported the work by preparing samples in Prof. J. Sakamoto’s group. The original draft was written by T. Fuchs and then edited and supervised by Prof. J. Sakamoto, Dr. F. H. Richter and Prof. J. Janek.

## RESEARCH ARTICLE



www.advenerymat.de

# Current-Dependent Lithium Metal Growth Modes in “Anode-Free” Solid-State Batteries at the Cu|LLZO Interface

Till Fuchs, Juri Becker, Catherine G. Haslam, Christian Lerch, Jeff Sakamoto, Felix H. Richter,\* and Jürgen Janek\*

Controlling the lithium growth morphology in lithium reservoir-free cells (RFCs), so-called “anode-free” solid-state batteries, is of key interest to ensure stable battery operation. Despite several benefits of RFCs like improved energy density and easier fabrication, issues during the charging of the cell hinder the transition from lithium metal batteries with a lithium reservoir layer to RFCs. In RFCs, the lithium metal anode is plated during the first charging step at the interface between a metal current collector and the solid electrolyte, which is prone to highly heterogeneous growth instead of the desired homogeneous film-like growth. Herein, the lithium morphology during the first charging step in RFCs is explored as a function of current density and current collector thickness. Using operando scanning electron microscopy, an increase in the lithium particle density is observed with increasing current density at the Cu|Li<sub>6.25</sub>Al<sub>0.25</sub>La<sub>3</sub>Zr<sub>2</sub>O<sub>12</sub> interface. This observation is then applied to improve the area coverage of lithium by pulsed plating. It is also shown that thin current collectors ( $d = 100$  nm) are unsuited for RFCs, as lithium whiskers penetrate them, resulting in highly heterogeneous interfaces. This suggests the use of thicker metal layers (several  $\mu\text{m}$ ) to mitigate whisker penetration and facilitate homogeneous lithium plating.

T. Fuchs, J. Becker, C. Lerch, F. H. Richter, J. Janek  
Institute of Physical Chemistry  
Justus-Liebig-University Giessen  
35392 Giessen, Germany  
E-mail: juergen.janek@phys.Chemie.uni-giessen.de

T. Fuchs, J. Becker, C. Lerch, F. H. Richter, J. Janek  
Center for Materials Research (ZfM)  
Justus-Liebig-University Giessen  
35392 Giessen, Germany  
E-mail: Felix.H.Richter@pc.jlug.de

C. G. Haslam, J. Sakamoto  
Department of Materials Science and Engineering  
University of Michigan  
Ann Arbor, MI 48109, USA

C. G. Haslam, J. Sakamoto  
Department of Mechanical Engineering  
University of Michigan  
Ann Arbor, MI 48109, USA

The ORCID identification number(s) for the author(s) of this article can be found under <https://doi.org/10.1002/aenm.202203174>.

© 2022 The Authors. Advanced Energy Materials published by Wiley-VCH GmbH. This is an open access article under the terms of the Creative Commons Attribution-NonCommercial-NoDerivs License, which permits use and distribution in any medium, provided the original work is properly cited, the use is non-commercial and no modifications or adaptations are made.

DOI: 10.1002/aenm.202203174

## 1. Introduction

Lately, solid-state batteries (SSBs) generated increasing attention as they hold the potential to outperform lithium-ion batteries (LIBs) as energy storage devices.<sup>[1,2]</sup> Although they are expected to fulfill higher safety standards,<sup>[3]</sup> their main benefit is the use of lithium metal as the anode material, which could be enabled by the use of solid electrolytes (SE).<sup>[4,5]</sup> The lithium metal anode is an appealing target for next-generation lithium batteries due to its low redox potential of  $-3.04$  V and high theoretical specific capacity of  $3861$  mAh g<sup>-1</sup>.<sup>[6,7]</sup>

The high reactivity of lithium metal, however, poses a number of challenges during the handling of lithium foils and fabricating low-resistance interfaces to SEs.<sup>[8–11]</sup> Lithium usually has a thin surface passivation layer consisting of mainly Li<sub>2</sub>CO<sub>3</sub>, LiOH, and Li<sub>2</sub>O even when stored under an argon atmosphere with a low amount of H<sub>2</sub>O and O<sub>2</sub>.<sup>[8]</sup> This passiva-

tion layer depends strongly on the exact storage conditions and is difficult to analyze and predict in detail. Therefore, tedious preparation steps are needed to fabricate low-resistance interfaces to SEs, which include mechanical processing of lithium, polishing of SEs, high pressures (3–300 MPa), and heat treatments.<sup>[9,10,12–14]</sup> While these methods work well on the laboratory scale, they are not suitable for large-scale fabrication of cells.

Lithium-reservoir-free cells (RFCs) provide an elegant way to circumvent the aforementioned challenges.<sup>[3,15,16]</sup> After assembly, the simplest RFC consists of a separator with a cathode on one side and a current collector (CC) attached to the other side. As cathode materials like LiNi<sub>x</sub>Mn<sub>y</sub>Co<sub>z</sub> are typically fabricated in the discharged (lithiated) state,<sup>[17,18]</sup> it is possible to extract lithium from the cathode and deposit it as lithium metal onto the current collector in the first charging step.<sup>[15,19–21]</sup> During subsequent cycling, the lithium metal can either be formed anew in every charging step or a small reservoir of lithium may be left during discharge. The superior method depends on the employed cell design and formation step of the lithium metal.

Several advantages are gained by eliminating the need of handling lithium metal during cell fabrication. First, by avoiding the excess lithium present in an SSB the cell energy density

increases significantly<sup>[21]</sup> as all lithium needed for cycling is introduced with the lithiated CAM during cell assembly.<sup>[15]</sup> Additionally, lithium metal may be the battery component most sensitive to trace amounts of water, oxygen, and nitrogen in the atmosphere it is processed in. Therefore, the fabrication of RFCs may open a variety of processing techniques, like solvent or heat treatments, previously rendered impossible by lithium metal. Also, the handling and storage of RFCs prior to the formation step of lithium metal is safer as an RFC prior to charging cannot short circuit.

The key challenge that currently hinders the development of RFCs is the non-uniform morphology of plated lithium after the formation step. Ideally, a lithium film is uniformly deposited in a layer-by-layer manner. The formation of isolated islands, dendrites, or whiskers must be avoided as they lead to a high interface resistance due to low contact area, current focusing, and nucleation sites for dendrites. It is still elusive, how external parameters like applied stack pressure, current density, and temperature influence the lithium metal morphology at the CC|SE interface.

A clear influence of temperature and current density on the plating morphology of lithium at Cu|LIPON and Cu|liquid electrolyte (LE) interfaces have already been observed.<sup>[19,22,23]</sup> Comparing the Cu|LIPON and Pt|LIPON interfaces, it seems that a high overvoltage during nucleation leads to more, but also smaller, particulates of lithium at the copper CC.<sup>[23,24]</sup> Wang et al. additionally propose that a higher overvoltage results in smaller critical radii of forming lithium nucleates.<sup>[15]</sup> A high overvoltage can thereby be achieved either by applying a high current density or by decreasing the temperature. Vice versa, applying low current densities at high temperatures (100 °C) leads to only a few but larger particulates of lithium,<sup>[23]</sup> which means that the interface is more heterogeneous.

It is, however, not clear how well these results on lithium nucleation translate to cells using the Cu|Li<sub>6.25</sub>Al<sub>0.25</sub>La<sub>3</sub>Zr<sub>2</sub>O<sub>12</sub> (LLZO) interface. While LIPON is an amorphous and defect-free SE, LLZO is polycrystalline and has a variety of surfaces defects, like grain boundaries, pinholes, dislocations, and different crystallographic facets, which can act as preferential nucleation sites.<sup>[16]</sup> Kazyak et al. already observed the positive effect of pressure on controlling the growth of lithium after nucleation using operando optical microscopy.<sup>[25]</sup> We believe that our work employing operando SEM can further elucidate the factors that affect homogeneous anode formation, especially during the nucleation and the very beginning of the deposition of lithium particles. Therefore, this paper focuses on the lithium plating as a function of the current density and current collector thickness at the Cu|LLZO interface and shows a strong dependence of the obtained lithium microstructure on the applied current density.

## 2. Results and Discussion

### 2.1. Using Operando SEM Plating to Study the Growth at Thin Cu-CC Films

To investigate the lithium deposition at metal CCs as a function of the applied current density, galvanostatic experiments were

carried out on Li<sub>id</sub>|LLZO|Cu<sub>film</sub> cells while under observation with an SEM. This cell configuration was deliberately chosen as the employed Li<sub>id</sub> counter electrode does not show any impedance contribution during the experiment,<sup>[9,26,27]</sup> which means that changes in resistance can solely be attributed to current constriction at the Cu<sub>film</sub>|LLZO interface.<sup>[28,29]</sup> LLZO was chosen because of its practical stability to lithium metal, which makes it well suited for this model system.<sup>[5,30,31]</sup> The metal current collector was a 100 nm thin copper film, which was deposited via thermal vapor deposition on the LLZO pellet. This allows the observation of lithium nucleation from above through the current collector as deposited lithium deforms this film. Copper was chosen as the current collector material as it is known to have a low lithium solubility at room temperature to prevent the possibility of alloy formation that could influence the deposition.<sup>[32]</sup>

The working principle of the herein-used setup is schematically depicted in Figure 1a. A Li<sub>id</sub>|LLZO|Cu<sub>film</sub> cell was prepared as described above. Subsequently, a microscopic electrode pattern was cut into the 100 nm thin copper current collector film with a FIB. This enables the measurement of several different spots with very similar interface properties. Additionally, a measurement with an electrode covering the size of the whole pellet would lead to large defects, such as holes or polishing lines being contacted, which would distort the results. Also, the patterned electrode with a size of around 15 μm in diameter still includes several grains with different orientations and grain boundaries as the mean grain size for this material is around 4 μm. Such a pattern is visible in the low magnification image in Figure 1b, where one current collector spot is electrically contacted with the tungsten microelectrode.

The voltage profile shown in Figure 1c is obtained when plating lithium with a current density of 100 μA cm<sup>-2</sup> at a single copper current collector patch. It can be seen that  $E_{WE}$  decreases until around -100 mV, at which point lithium nucleation sets in with an ohmic overvoltage  $\eta_{IR}$  of around -100 mV. Usually, a nucleation overpotential  $\eta_{nuc}$  is expected, which manifests itself in a minimum in the potential profile,<sup>[15,23]</sup> but is not present herein. Possibly  $\eta_{nuc}$  is overshadowed by the oscillation of  $E_{WE}$  induced by the scanning procedure. However, this limits the maximum value of  $\eta_{nuc}$  to around 50 mV in this case.

As depicted in the split image in Figure 1d, the plated lithium morphology can then be monitored in situ and directly correlated with electrochemical findings. The lithium breaks through the copper CC, which allows an assessment of nucleation density at a certain current density. At 100 μA cm<sup>-2</sup>, small and separate lithium columns grow and do not form a conformal film. The necessity to grow a conformal film is clear when the plated electrode is subject to discharge/stripping. Figure S1, Supporting Information shows an in situ plated lithium electrode before and after stripping was performed. Due to the low areal coverage, high local current densities are present at the lithium particles, which lead to a fast progression of pore formation and therefore, low Coulomb efficiency. After a successful proof of principle, this setup is therefore used to investigate the relationship between deposition morphology and current density, as described in the next chapter.

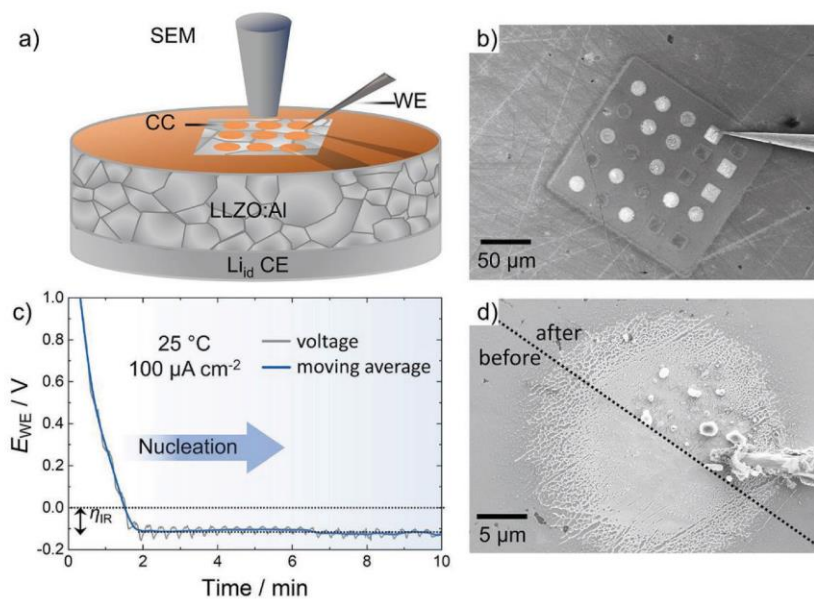


**Figure 1.** a) Schematic of the operando SEM setup used to characterize lithium plating in a  $\text{Li}_d|\text{LLZO}|\text{Cu}_{\text{film}}$  cell stack. b) SEM overview of the investigated microscopic current collector patches as prepared via FIB patterning. c) Voltage profile when plating lithium with this setup. Note that the strong oscillations in this profile occur because of the SEM electron beam scanning, thus interfering with the measurement at very low currents. d) Magnified image of the same contacted copper current collector patch before and after lithium plating. Note that the frayed edge is an effect induced by the FIB cutting. Additionally, the material on the needle sides is thought to be dust particulates that do not influence the measurement.

## 2.2. Influence of Current Density on Lithium Growth Morphology

The in situ SEM plating technique described above is now used to characterize lithium plating with different current densities. While higher current densities lead to more lithium particles per area for  $\text{Cu}|\text{LLPON}$  and  $\text{Cu}|\text{LE}$ ,<sup>[22,23]</sup> it was hitherto unknown what happens at the interface to a polycrystalline ceramic SE. To be able to compare our findings with the literature, the same current densities as in the work of Motoyama et al. were

investigated herein.<sup>[23]</sup> Figure 2a–d, therefore, shows SEM images of  $16 \mu\text{Ah cm}^{-2}$  lithium plated with 50, 100, 500, and  $1000 \mu\text{A cm}^{-2}$ .

The micrographs in Figure 2a–d show a clear change in size, shape, and density of the lithium particles plated at the  $\text{Cu}|\text{LLZO}$  interface. With increasing current density, the shape of the lithium nucleation spots is increasingly heterogeneous. For example, lithium plated with  $50\text{--}100 \mu\text{A cm}^{-2}$  is nearly spherical in shape but for higher current densities, elongated lithium nucleates are plated. Moreover, the overall lithium

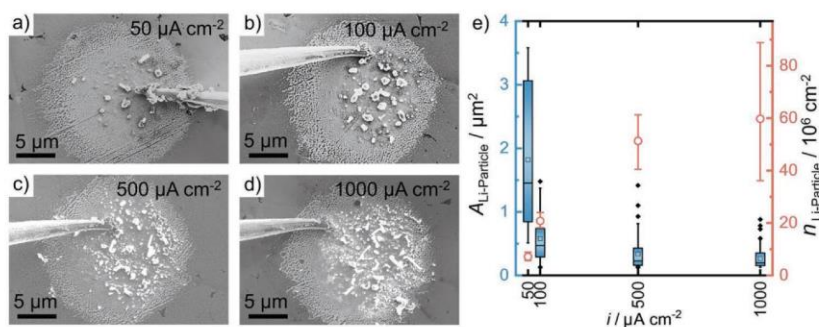


**Figure 2.** SEM micrographs of lithium plated at the  $\text{Cu}|\text{LLZO}$  interface with a) 50, b) 100, c) 500, and d)  $1000 \mu\text{A cm}^{-2}$ . In each case, the amount of lithium or charge plated was  $16 \mu\text{Ah cm}^{-2}$ , corresponding to a thickness of 77 nm, if plated homogeneously. The projected size  $A_{\text{Li-Particle}}$  of each lithium particle and the particle density  $n_{\text{Li-Particle}}$  are depicted in (e). The distribution of lithium particle sizes is presented as a box plot, comprising 11 ( $50 \mu\text{A cm}^{-2}$ ), 32 ( $100 \mu\text{A cm}^{-2}$ ), 79 ( $500 \mu\text{A cm}^{-2}$ ), and 92 ( $1000 \mu\text{A cm}^{-2}$ ) particles, respectively. The average  $A_{\text{Li-Particle}}$  is shown as a square inside each box plot.  $n_{\text{Li-Particle}}$  is represented as the orange data points.

particle density  $n_{\text{Li-Particle}}$  seems to be a lot higher for 500 and 1000  $\mu\text{A cm}^{-2}$ . Unlike observed by Wang et al.,<sup>[15]</sup> no coalescence of lithium nuclei/particles to form a continuous film was observed herein, which most likely would require applied stack pressure or thicker CCs or both.<sup>[25]</sup>

To quantitatively compare the nucleation for Cu|LLZO and Cu|LIPON interfaces, image analysis was carried out of the size and morphology of lithium particles in Figure 2a–d. The projected size of each lithium particle  $A_{\text{Li-Particle}}$  and  $n_{\text{Li-Particle}}$  are depicted in Figure 2e. As the plated charge is the same for all herein depicted experiments, lower  $A_{\text{Li-Particle}}$  values are expected for higher current densities with larger  $n_{\text{Li-Particle}}$ . This is confirmed by digital image analysis, which shows that  $A_{\text{Li-Particle}}$  decreases from around 4  $\mu\text{m}^2$  at 50  $\mu\text{A cm}^{-2}$  to only 0.5  $\mu\text{m}^2$  at 1000  $\mu\text{A cm}^{-2}$ . Interestingly, the spread of  $A_{\text{Li-Particle}}$  also decreases for higher current densities according to the box plots in Figure 2e. A six-fold increase of the lithium particle number is obtained from 11 per current collector area at 50  $\mu\text{A cm}^{-2}$  to around 92 per current collector area at 1000  $\mu\text{A cm}^{-2}$ . As the current collector area is approximately 150  $\mu\text{m}^2$ ,  $n_{\text{Li-Particle}}$  is between  $10 \times 10^6 \text{ cm}^{-2}$  at 50  $\mu\text{A cm}^{-2}$  and  $60 \times 10^6 \text{ cm}^{-2}$  at 1000  $\mu\text{A cm}^{-2}$ , confirming the observation previously made directly from the images. Note that the particle area is only a projection of its shape onto the copper current collector as the topology could not be quantified with SEM.

The nucleation densities observed for Cu|LLZO are quite similar to what Motoyama et al. observed for Cu|LIPON.<sup>[23]</sup> This is interesting, as, unlike LIPON, LLZO shows various surface defects, for example, grain boundaries and dislocations, within the current collector area. These defects may facilitate the nucleation of lithium as observed before.<sup>[16,33]</sup> To better understand the influence of surface defects on the large-scale nucleation at interfaces, similar plating experiments were carried out on single-crystalline Cu|LLZO<sub>sc</sub> interfaces.

Using an LLZO pellet with a grain size larger than the 15  $\mu\text{m}$  wide copper current collector spot generates a Cu|LLZO<sub>sc</sub> interface mostly free of surface defects, that mimics a single crystal experiment. For this experiment, 100 nm of copper were deposited on a freshly broken cross-section of large-grained LLZO, which was thereafter patterned via FIB for microelectrode preparation. The micrographs in Figure S2a–d, Supporting Information show the lithium grown after plating at these Cu|LLZO<sub>sc</sub> interfaces with 50 to 1000  $\mu\text{A cm}^{-2}$ . A clear difference is observed compared to the polycrystalline material regarding  $n_{\text{Li-Particle}}$ . For the defect-free LLZO, lithium plating is solely observed at one spot in the vicinity of the microelectrode contact, independent of the applied current density. Furthermore,  $\eta_{\text{nuc}}$  is larger than at polycrystalline surfaces, for example, 200 mV (Cu|LLZO<sub>sc</sub>) versus < 50 mV (Cu|LLZO). This highlights the necessity for surface defects to facilitate homogeneous and planar lithium growth at the Cu|LLZO interface. However, the grain orientation was not determined, which may have a strong impact on the nucleation of lithium at the interface.

Generally, the herein obtained results for polycrystalline LLZO in contact with copper current collector films confirm the current density-dependent nucleation observed at the Cu|LIPON interface. This is remarkable as LLZO is a polycrystalline material, which exhibits surface defects. While LIPON

is an amorphous and basically defect-free material,<sup>[34]</sup> LLZO shows grain boundaries, grain orientations, pores, dislocations, and other defects such as scratches induced by polishing. Possibly, local variations in density act as nucleation sites in LIPON, which is why it performs similarly to polycrystalline LLZO instead of LLZO<sub>sc</sub>.

### 2.3. Advanced Charging Protocol to Obtain a Favorable Lithium Morphology

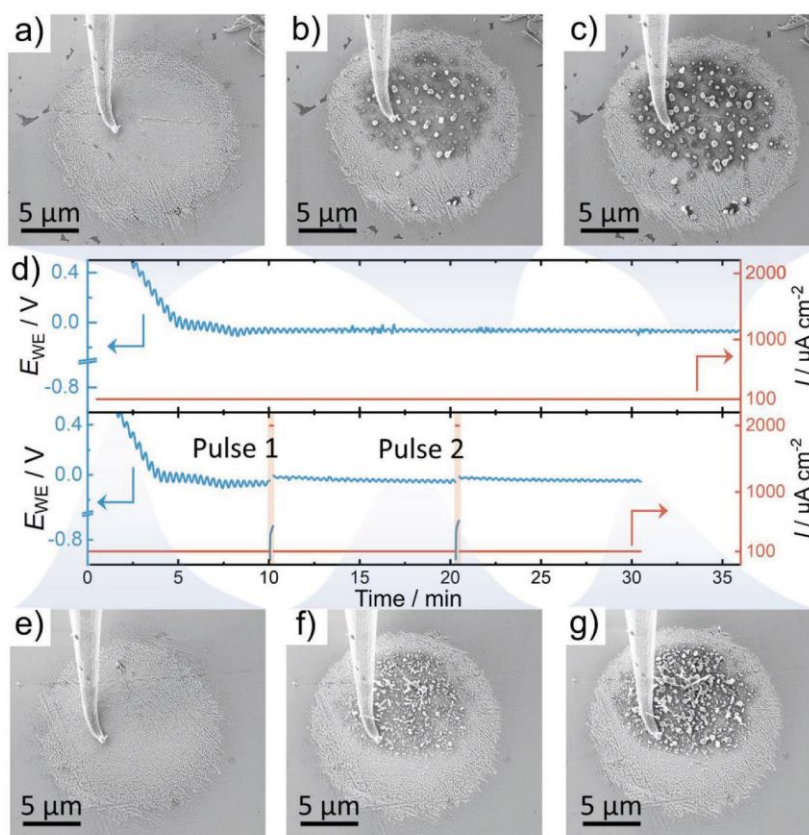
While high current densities lead to a beneficial higher density of lithium particles, continuous charging with high current densities is detrimental to the overall cell properties. Not only do high charge currents lead to (chemo)-mechanical issues like contact loss at the cathode interface,<sup>[17,35,36]</sup> dendrite and filament growth are facilitated as well.<sup>[14,37]</sup> However, a combination of high and low current densities could be an optimal charging protocol for the plating of a homogeneous lithium film. To test this hypothesis, continued plating with low current densities (100  $\mu\text{A cm}^{-2}$ ) was interrupted repeatedly by high current pulses (1000  $\mu\text{A cm}^{-2}$ ). A control experiment was carried out in which the same amount of charge was plated with a continuous and uninterrupted current of 100  $\mu\text{A cm}^{-2}$ . The respective voltage profiles and morphology evolutions are depicted in Figure 3.

SEM micrographs were acquired during the plating with 100  $\mu\text{A cm}^{-2}$  and are depicted in Figure 3a–c. They respectively show the beginning, middle, and end of the lithium growth process. The images are linked to the respective voltage profile depicted in Figure 3d. Similarly, Figure 3e,f show the lithium morphology during growth after the first pulse and after the end of the process.

After the same amount of charge was plated in both experiments, clear differences in lithium morphology and particle density are observed. Figure 3c shows that a rather defined space between different lithium particles is present, with lithium growing similar in size up to around 0.5–1.0  $\mu\text{m}$ , not covering the whole Cu|LLZO interface. However, as depicted in Figure 3g, more and smaller lithium particles nucleate when short pulsing steps are incorporated into the growth process. Additionally, the spacings between the particles appear shorter with less Cu|LLZO interface uncovered.

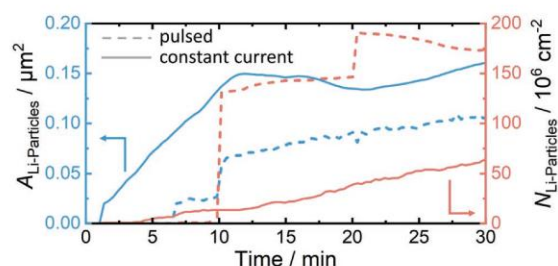
A different lithium coverage of the Cu|LLZO interface also manifests itself in the lower  $\eta_{\text{IR}}$  seen while plating. While a constant  $\eta_{\text{IR}}$  of around –65 mV is observed after nucleation occurred for the control experiment,  $\eta_{\text{IR}}$  decreases from around –65 mV (before the 1<sup>st</sup> pulse) to –42 mV (after 1<sup>st</sup> pulse) and finally to around –35 mV (after 2<sup>nd</sup> pulse) for the advanced plating process. This means that more lithium is in contact with the SE after the pulsing steps. This also explains the voltage profile during the pulses, which are depicted in Figure S3, Supporting Information. Here, a  $\eta_{\text{nuc}}$  of –30 mV is observed, which means that particles nucleate additionally during the pulse besides lithium already being present.

Figure 4 displays the particle density and size thereof during the pulse experiment and the constant current control experiment. In the control experiment with continuous plating, a continuous but slow increase in  $n_{\text{Li-Particle}}$  up to  $60 \times 10^6 \text{ cm}^{-2}$



**Figure 3.** a–c) SEM micrographs at different stages during lithium plating with  $100 \mu\text{A cm}^{-2}$ . The corresponding voltage and current profiles are depicted in the top part of (d). The bottom part of (d) shows the voltage and current profiles during plating with  $100 \mu\text{A cm}^{-2}$  and interrupting current pulses of  $2000 \mu\text{A cm}^{-2}$ . Note that the oscillations of the voltage profiles are induced by the scanning of the electron beam. The respective SEM micrographs during different stages of the plating are visible in (e–g). Videos of both experiments can be found in Video S1, Supporting Information.

is observed. When pulses are utilized within the plating, sharp jumps in  $n_{\text{Li-Particle}}$  are observed during the pulses, corresponding well to the observation of a nucleation overvoltage present during the pulse and the nucleation of additional particles. After the same charge of  $60 \mu\text{Ah cm}^{-2}$  is plated,  $n_{\text{Li-Particle}}$  is



**Figure 4.** Evolution of lithium particle density and projected area as a function of the plating time for the pulsed measurement and the control experiment with a constant current density as depicted in Figure 3.

around  $170 \times 10^6 \text{ cm}^{-2}$ , which is nearly three times higher than in the continuous plating experiment.

Furthermore, the average projected area of the nuclei is analyzed and depicted in Figure 4. For the control experiment without current pulses, a steady and mostly linear increase in particle area up to  $0.15 \mu\text{m}^2$  is observed in the first 10 minutes, followed by stagnation of average particle area, explained by the simultaneous growth of few but very small lithium particles. The pulsed plating shows a more tentative growth at the beginning, followed by a step increase during the first pulse up to around  $0.06 \mu\text{m}^2$ . Afterward, the projected area slowly increases up to  $0.10 \mu\text{m}^2$ . Interestingly, no step change is observed for the second pulse, which may be explained by the high number of particles already present.

The size distribution of particles at different points during plating is additionally shown in Figure S4, which confirms a sharper size distribution of grown lithium particles for the pulsed plating. For better visualization of the process, the reader is referred to Video S1, Supporting Information of the plating process.

Interestingly, during all plating experiments, a change of image contrast happens prior to and during the nucleation of lithium particles. This darkening may be caused by lithium being reduced at the Cu|LLZO interface and diffusion at the surface of the Cu current collector. This lowers the average electron density of the material, thus appearing darker when observed with an SEM. Copper supposedly is able to alloy with up to 14 at.% of lithium,<sup>[38,39]</sup> as measured by reacting fine copper powder with lithium.<sup>[32]</sup> This and time-of-flight secondary ion mass spectrometry (ToF-SIMS) analyses suggest very strong lithium diffusion along copper grain boundaries when present.<sup>[40,41]</sup> However, even if the maximum amount of 14 at% of lithium is alloying with the CC, this still only amounts to 1.5 wt%. Consequently, no amount of lithium significant enough to change our morphological analysis is lost within the copper CC, but still enough to change the contrast as observed via SEM.

All of the above experiments were conducted using thin copper electrodes with a thickness of around 100 nm. Clear trends are observed, showing that the plating morphology can be controlled by current density. However, lithium breaking through the current collector layer is not beneficial for practical application, as it inhibits the growth of a lithium film and renders the application of stack pressure useless. Therefore, thicker metal layers of several micrometers are needed to assess the nucleation and growth of lithium in practically relevant systems. In this case, our top-view in situ method cannot be applied and it is yet unclear, how the morphology and interface between LLZO and thick copper foils evolve during lithium growth.<sup>[15]</sup>

#### 2.4. Operando Study of Lithium Growth at Thick Cu-CC Foils

In the following, lithium nucleation and growth were investigated at Cu<sub>foil</sub>|LLZO interfaces. As it is not possible to see any deformation at this buried interface during plating, operando experiments were carried out at cross-sections, which were prepared prior to the experiment by a focused ion beam. It is expected that lithium is not able to penetrate through a thick copper foil in the same way it does when using thin copper films. When using thick ( $\approx 10 \mu\text{m}$ ) metal foils, three different modes of growth at the CC<sub>foil</sub>|LLZO interface have been proposed.<sup>[15]</sup> These are 1) CC|LLZO separation and gap formation by vertical whisker growth of lithium; 2) horizontal growth or creep induced by stack pressure opening the CC|LLZO interface without gap formation, and 3) plating at the nucleate edges into the solid electrolyte, forming dendrites. The second growth mode is the preferred option to obtain large-area lithium electrodes without severe mechanical degradation or dendrite formation. However, it is still unknown how these processes depend on current density, current collector thickness, and applied pressure.

Therefore, operando experiments at Cu<sub>foil</sub>|LLZO interfaces were carried out by looking at the cross-section during lithium plating with different current densities. Figure 5a depicts a schematic of the herein-used operando setup for cross-sectional analysis. A low-magnification image of the whole prepared crater and micromanipulator used as the working electrode is visible in Figure 5b with the analyzed area marked with a blue dashed line.

Interestingly, when plating with  $100 \mu\text{A cm}^{-2}$  the voltage profile shown in Figure 5c shows two minima, which may arise from a convolution of two separate contributions. One minimum is caused by  $\eta_{\text{nuc}}$ , typically observed for Cu|SE interfaces,<sup>[15,16,23]</sup> the other one could be caused by the subsequent opening of the interface by lithium growth, temporarily reducing the effective electrode area. Afterward, the plating is quite stable and only shows a small decrease in  $\eta_{\text{R}}$ , caused by the increasing electrode area by lateral lithium growth.

The evolution of the interface during plating is shown in Figure 5d–g and Video S2, Supporting Information. The pristine interface shows a heterogeneous distribution of contact spots, with some areas showing direct contact and others showing that thin gaps ( $< 1 \mu\text{m}$ ) are still present. At the beginning, where the potential is still falling and nucleation has not occurred yet (Figure 5e), a darkening of the copper current collector is observed like in previous experiments. As a full lithiation of the copper CC (14 at% or 1.5 wt% of Li) would take around 5 h with  $100 \mu\text{A cm}^{-2}$ , this can be ruled out. The color change, therefore, is most likely explained by the fast surface diffusion of lithium along the copper CC, changing the electronic properties enough to result in a slightly different SEM image contrast.

After nucleation, lithium growth is observed at a previous contact spot between copper and LLZO. These small islands then get thicker and also slowly grow laterally while simultaneously opening the gap between copper and LLZO to around  $2 \mu\text{m}$  at the end of the experiment. What follows is that at  $100 \mu\text{A cm}^{-2}$  and no applied pressure, a combination of growth mechanisms 1) and 2) occurs. The lateral growth of lithium and closing of pores is especially interesting, as previously this was only expected when stack pressure is applied. A reason could be that the force induced only by the deformation of the copper foil is enough for the deformation of small lithium pillars.<sup>[25]</sup> A similar experiment was carried out with  $50 \mu\text{A cm}^{-2}$ , which is shown in Figure S5, Supporting Information and shows the same trends as plating with  $100 \mu\text{A cm}^{-2}$ . Interestingly, contrary to what was stated by Kazyak et al., lithium does not start to nucleate at the pore walls in the free space at the interface, but rather at the direct contact spots between Cu and LLZO – highlighting that a pore-free CC|LLZO interface is favorable for Li plating.

Similarly, plating with  $500 \mu\text{A cm}^{-2}$  was carried out at a Cu<sub>foil</sub>|LLZO cross-section with the respective voltage profile displayed in Figure 6a. Several SEM images linked to different stages in the plating progress are depicted in Figure 6b–e. While the pristine interface of the image area seems to be in better contact than in the previous measurement, the overall contact area seems to be quite similar for all investigated cross-sections as depicted in low-magnification SEM images in Figure S6, Supporting Information.

Due to a large overvoltage induced by the higher current density, the minima in the voltage profile are not as pronounced as they are in the previous measurement with  $100 \mu\text{A cm}^{-2}$ . After a stable initiation of the plating process, large voltage fluctuations occur, which correspond well to the growth of lithium within the solid electrolyte away from the interface as seen in Figure 6c.<sup>[46]</sup> This is direct evidence of lithium penetration into the solid electrolyte and dendrite

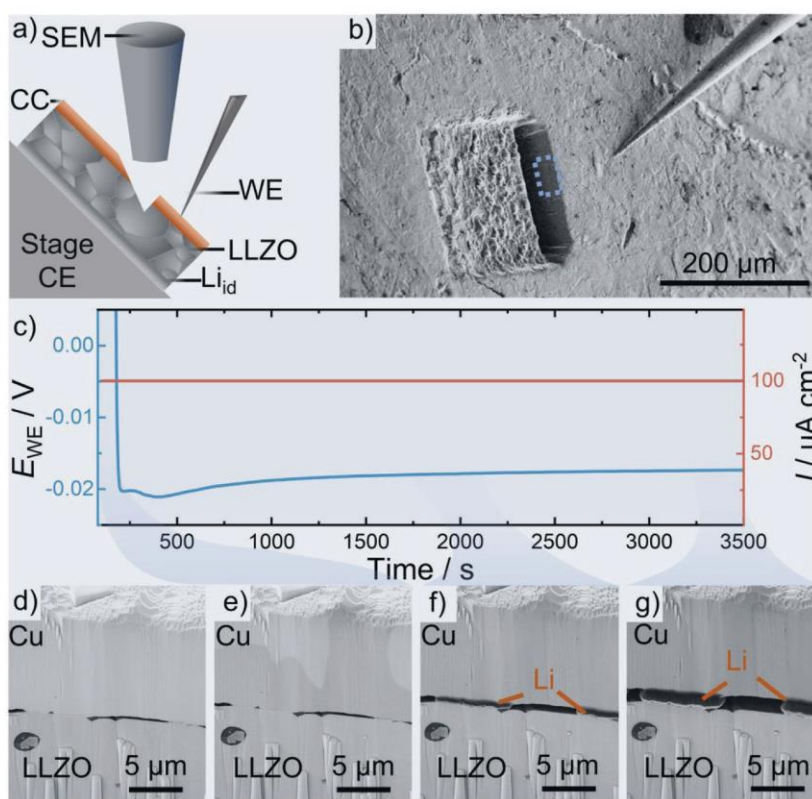


**Figure 5.** a) Schematic setup used to observe lithium plating with  $100 \mu\text{A cm}^{-2}$  at the interface at  $\text{Cu}_{\text{foil}}|\text{LLZO}$ . Due to the high electronic conductivity of both tungsten and copper, the point contact between the micromanipulator and copper foil is not relevant to the experiment. A low-magnification SEM image of the setup is shown in (b). The voltage profile during plating is depicted in (c). Several screenshots of the video during plating were taken at different stages, which are shown in (d–g). Note that some of the remaining lines and pillars are due to “curtaining” and “rippling”, which frequently occurs during the FIB-cutting process.<sup>[42–45]</sup>

growth. Still, upon further plating, a homogenous film grows at the  $\text{Cu}_{\text{foil}}|\text{LLZO}$  interface. At a later stage, also large protrusions of lithium are visible at the interface. These, however, may not be representative of the growth occurring at the buried interface due to more space being available where some of the material was removed to be able to observe the process in cross-section.

The growth occurring with  $500 \mu\text{A cm}^{-2}$  can overall be classified to growth mode 3), showing that even though a very thin layer of metal is plated at the interface, the majority of plated lithium is deposited as filaments and dendrites in the bulk of the solid electrolyte.

A similar cross-sectional experiment was carried out with thin  $\text{Cu}_{400 \text{ nm}}$  current collectors and a current density of  $20 \mu\text{A cm}^{-2}$ . The breakthrough process of a lithium whisker through the copper can easily be observed therein as depicted in Figure S7, Supporting Information. This furthermore highlights the necessity of a thick CC as a means to suppress lithium breaking through the metal layer. The exact thickness needed to suppress whisker penetration depends on various factors, like current density used for plating, if a foil or depos-

ited film is used, conformity of the  $\text{CC}|\text{SE}$  interface and applied pressure. In the case of vapor-deposited films onto LLZO, we found that  $5 \mu\text{m}$  of copper is sufficiently mechanically stable to suppress whisker penetration through itself as depicted in Figure S8, Supporting Information.

### 2.5. Summarizing the Different Growth Modes of Lithium at $\text{Cu}|\text{LLZO}$ Interfaces

The different lithium growth modes discussed by Wang et al. are also observed within this work and were investigated regarding their occurrence under different interface conditions and current densities as summarized in Figure 7. As we observed the simultaneous occurrence of different growth modes, this chapter aims to give guidelines on how to control the lithium growth morphology within RFCs.

By investigating thin copper films ( $d = 100 \text{ nm}$ ), it was possible to quantify the lithium particle density as a function of the applied current density. A strong increase in particle density and area coverage of lithium is observed for higher current

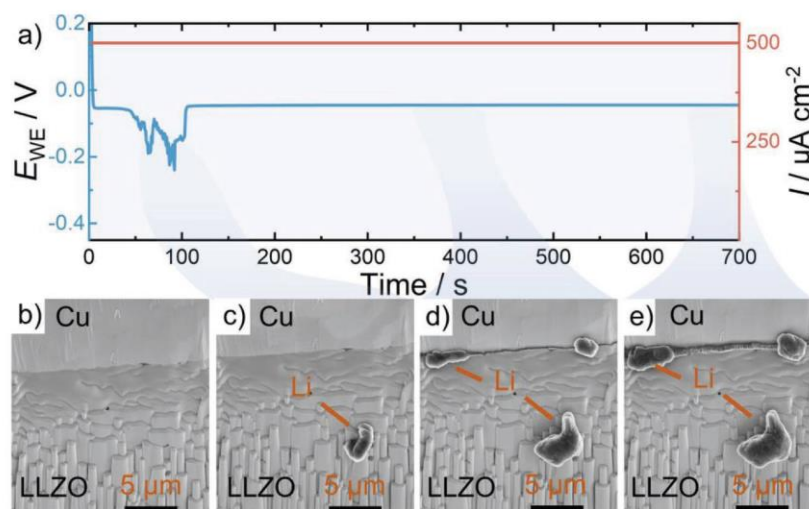


**Figure 6.** a) Voltage profile during plating with  $500 \mu\text{A cm}^{-2}$ . Screenshots of a video recorded during the plating and lithium growth process are depicted in (b–e) with their respective time indicated by a marking in the voltage profile.

densities as shown in Figure 7. However, as high current densities facilitate the growth of dendrites in RFCs, as seen in Figure 6, we propose using only a very short initial pulse of high current density to spawn a large number of lithium particles. This could be expanded to using current pulses as an interruption to low current plating as depicted in Figure 5.

Despite a conformal initial contact of thin vapor deposited metal films ( $d = 0.1\text{--}1 \mu\text{m}$ ) on the SE, which is evident from

the impedance shown for  $\text{Cu}_{\text{film}}|\text{LLZO}|\text{Li}$  in Figure S9a, Supporting Information, thin current collector films are not suitable for long-term plating of  $\mu\text{m}$ -thick lithium films as they offer no mechanical stability. During the initial plating, lithium penetrates such thin current collector films, which facilitates the vertical growth of whiskers instead of films. Even if pressure is applied in our particular case, lithium is just flattened above the current collector films after whisker penetration, which offers no beneficial increase in the contact area between lithium and the SE. This evolution is evident from the resistance evolution shown in Figure S9b, Supporting Information and proven by the SEM images shown in Figure S8c,d, Supporting Information. As no new contact area between lithium and the SE is formed,  $R_{\text{int}}$  is converging to a certain value of several  $100 \Omega \text{ cm}^2$  despite a continuous growth of lithium.

Therefore, we propose the use of thicker metal CCs, such as  $\text{Cu}_{\text{foil}}$  ( $d = 10 \mu\text{m}$ ) or  $\text{Cu}_{\text{film}}$  ( $d = 5 \mu\text{m}$ ) to suppress the penetration of the metal. In this case, three different growth modes can be identified, namely, i) the vertical growth of whiskers where the current collector was in contact with the SE, ii) a desired film-like growth, and iii) the growth of lithium into the SE as dendrites. As summarized in Figure 7, we could observe the simultaneous occurrence of different growth modes, however, their contributions can be tuned by plating with different current densities.

At low current densities ( $< 100 \mu\text{A cm}^{-2}$ ), a mixture between whisker growth and film growth could be observed, depending on the local microstructure and interface properties of the analyzed system. A more conformal contact and stiffer current collector would therefore rather shift the balance to the desired film growth, whereas a current collector foil without conformal contact facilitates the growth of whiskers. At high current densities ( $> 500 \mu\text{A cm}^{-2}$ ), an overlap between film and dendrite growth was observed. This balance is expected to depend

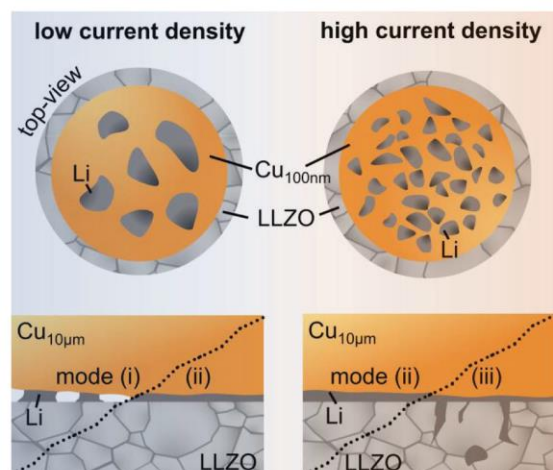


**Figure 7.** Schematic explaining the occurrence of different lithium growth modes when using thin current collector films (top) or thick current collector foils (bottom) when different current densities are applied. Note that in the herein analyzed experiments, usually a combination of growth modes was observed.

strongly on the SE microstructure, with denser SEs being able to suppress dendrites better than porous variants.

The influence of pressure on the lithium growth morphology is also very important and was recently investigated by Kazyak et al. using operando video microscopy.<sup>[25]</sup> Based on their results of lithium blisters getting flattened by pressure in the range of 1–5 MPa, it is expected that the balance of growth modes is shifted to the desired film growth already at moderate pressures and that dendritic growth is favored at very high pressures.

### 3. Conclusion

In this study, we investigated the current density-dependent lithium growth morphology and particle density at Cu|LLZO interfaces by contacting small current collector patches or interface cross-sections (prepared by FIB patterning) in an SEM. With this novel technique, a strong increase in lithium particle density and current collector coverage was observed with increasing current density. Our experiments show that – while thin metal films as CCs are good model systems to observe lithium growth underneath – a thicker and more mechanically stable current collector foil is needed to suppress the detrimental penetration of lithium whiskers through the CC. Three different lithium growth modes were observed without the application of stack pressure in Cu<sub>foil</sub>|LLZO systems: i) vertical whisker growth, ii) film growth, and iii) dendritic growth. Usually, a combination of these growth modes is observed with a strong dependence on local microstructure and conformity of the Cu<sub>foil</sub>|LLZO interface. A general shift from whisker growth to film or dendritic growth occurs with increasing current densities when plating. Therefore, we suggest not only using thick CCs (several  $\mu\text{m}$ ) to suppress its penetration by whiskers, but also carefully choosing the current density and plating protocol to optimize the electrode system for growing homogeneous lithium films with respect to the presented findings.

### 4. Experimental Section

**Preparation of Solid Electrolytes:** The formal composition of the LLZO:Al prepared within this work was  $\text{Li}_{6.25}\text{Al}_{0.25}\text{La}_3\text{Zr}_2\text{O}_{12}$ . At first,  $\text{Li}_2\text{CO}_3$  (> 99.0%, Sigma-Aldrich),  $\text{ZrO}_2$  (99.9%, Sigma-Aldrich),  $\text{La}(\text{OH})_3$  (99.9%, Sigma-Aldrich), and  $\text{Al}_2\text{O}_3$  (99.8%, abcr) were homogenized using a planetary ball-mill two times (10 min with 20 min pause at 350 rpm for 24 cycles). Thereafter, calcination (4 h at 1000 °C) of 25 mm diameter pellets was carried out in MgO-crucibles under 150 sccm  $\text{O}_2$  flow. The samples were subsequently handled exclusively under an argon environment ( $p(\text{H}_2\text{O})/p < 1.0$  ppm,  $p(\text{O}_2)/p < 0.1$  ppm).

To obtain LLZO powder with a smaller particle size, the above mixture was ball-milled with the same parameters for 40 cycles. Sintering was then carried out with pellets isostatically pressed beforehand at 380 MPa under  $\text{O}_2$  flow in MgO crucibles with mother powder (calcined LLZO powder). The heating procedure was as follows. Samples were first heated for 9 h to 900 °C, which was held for 5 h. Afterward, the temperature was increased for 2 h to 1100 °C and again held for 5 h. The temperature was then increased again to 1230 °C in 1 h and held for 4 h, followed by natural cooling.

For cells utilizing a thick (10  $\mu\text{m}$ ) copper foil laminated on the electrolyte surface, LLZO:Ta with a composition of  $\text{Li}_{6.5}\text{Ta}_{0.5}\text{La}_3\text{Zr}_{1.5}\text{O}_{12}$

was synthesized through a solid-state method. The powders were densified into billets (diameter 12.7 mm) using rapid-induction hot-pressing.<sup>[47]</sup> The dense pellets (>96% relative density) were ground with sandpaper up to 1200 grit, followed by polishing using diamond paste up to a final step of 0.1  $\mu\text{m}$ .

**Cell Assembly and Electrochemical Characterization:** Cells were assembled by polishing the garnet pellets with grit P1000 SiC-paper and subsequent electrode attachment. As a counter electrode, a resistance-free ideal electrode  $\text{Li}_{\text{id}}$  was prepared according to previous publications utilizing high isostatic pressure (380 MPa for 30 min).<sup>[9,26]</sup> The foil used for  $\text{Li}_{\text{id}}$  electrodes was prepared by removing surface degradation layers from a lithium chunk with a ceramic knife and subsequently pressing it into a thin foil directly before attaching it to the pellet.

Thin copper electrodes of approximately 100 nm thickness were deposited onto LLZO under vacuum using a homemade thermal evaporation system attached to a glovebox with a rate of 0.2 nm  $\text{s}^{-1}$ , which was controlled by an oscillating quartz sensor. The patterning of small Cu patches ( $A \approx 150 \mu\text{m}^2$ ) was achieved by cutting with a plasma-FIB. Thick (10  $\mu\text{m}$ ) copper foils were laminated onto LLZO:Ta by hot-pressing as described in the works of Wang et al. and Kazyak et al.<sup>[15,25]</sup> which resulted in good conformal contact between the foil and pellet.

Electrochemical characterization was carried out using a VMP300 potentiostat (BioLogic) in combination with the software EC-Lab (ver. 11). Temperature-dependent measurements were carried out in a climate chamber WKL 64 (Weiss Technik GmbH). For electrochemical measurements, cells were contacted with nickel current collector tabs and sealed in pouch cells. The current collector tabs are fixed using tape.

If not stated otherwise, potentiostatic electrochemical impedance spectroscopy (PEIS) measurements were carried out in a frequency range between 7 MHz and 100 mHz. Galvanostatic EIS (GEIS) measurements were carried out in a different frequency range, 7 MHz to 1 Hz, as the acquisition of one spectrum needs to be faster in this measuring mode to not disturb the DC current. Usually, 10% of the DC current is used as amplitude to measure the impedance response of the cell. Impedance data interpretation as well as fitting thereof was carried out by RelaxIS 3 (RhD Instruments).

**FIB-SEM Measurements:** Focused-ion-beam (FIB)-cutting imaging was carried out using a XEIA3 GMU SEM/Plasma-FIB (Tescan) in combination with a Leica VCT500 transfer module at room temperature. SEM imaging was carried out using a Zeiss Merlin HRSEM.

**Operando Scanning Electron Microscopy (SEM):** For the microelectrode measurements (prober module, Kamrath & Weiss GmbH) with tungsten micromanipulators (Simac Masic & TSS by) were attached to the sample stage of the Zeiss Merlin HRSEM. The microelectrodes then acted as a working electrode, whereas the counter electrode was contacted via the sample stage itself. When measuring cross-sections, the sample was tilted by 45° to obtain a view into the crater, which was previously prepared under a 90° angle with a FIB.

**Digital Image Analyses:** The acquired SEM images were graphically analyzed using the open-source software *Fiji* and a trainable *Weka* segmentation. The area of analysis was determined with *Fiji* and the first criteria to distinguish between lithium particles and the current collector surface were manually specified to train the *Weka* segmentation. Using a machine learning approach, *Weka* generates selection criteria, such as contrast or shape. Based on the selection criteria learned, *Weka* can segment further images and differentiate between lithium particles and the surrounding environment. Particle size and particle count were then obtained by processing the segmented image with *Fiji*. In order to avoid too large errors, the smallest analyzed particle size was set to  $A_{\text{Li-Particle, min}} = 0.02 \mu\text{m}^2$ . This lower limit was chosen because particles with a size > 0.02  $\mu\text{m}^2$  were still easily visible in the micrographs. Thus, it is possible to control the analyzed images and doublecheck the selection of the *Weka* segmentation. Due to the variety of shapes of the particles, the circularity was set to be between zero and one. Therefore, all particles in between a perfect circle (circularity = 1) and largely elongated particles (circularity = 0) were considered.

### Supporting Information

Supporting Information is available from the Wiley Online Library or from the author.

### Acknowledgements

T.F. and J.B. contributed equally to this work. The authors want to thank Pascal Schweitzer for fruitful scientific discussions. We further want to thank Elisa Monte for her support with designing our ToC image. This work was conducted as part of the US-German joint collaboration on "Interfaces and Interphases in Rechargeable Li-metal based Batteries" supported by the US Department of Energy (DOE) and German Federal Ministry of Education and Research (BMBF). This work has been partly funded by the German Federal Ministry of Education and Research (BMBF) under the projects "LiSI", grant identifier 03XP0224E and "LiSI2", grant identifier 03XP0509B.

Open access funding enabled and organized by Projekt DEAL.

### Conflict of Interest

The authors declare no conflict of interest.

### Data Availability Statement

The data that support the findings of this study are available from the corresponding author upon reasonable request.

### Keywords

anode-free-cell, kinetics, Li-metal, morphology, operando SEM

Received: September 19, 2022

Revised: October 12, 2022

Published online:

- [1] J. Janek, W. G. Zeier, *Nat. Energy* **2016**, *1*, 16141.
- [2] S. Randau, D. A. Weber, O. Kötz, R. Koerver, P. Braun, A. Weber, E. Ivers-Tiffée, T. Adermann, J. Kulisich, W. G. Zeier, F. H. Richter, J. Janek, *Nat. Energy* **2020**, *5*, 259.
- [3] Y. Lee, S. Fujiki, C. Jung, N. Suzuki, N. Yashiro, R. Omoda, D. Ko, T. Shiratsuchi, T. Sugimoto, S. Ryu, J. H. Ku, T. Watanabe, Y. Park, Y. Aihara, D. Im, I. T. Han, *Nat. Energy* **2020**, *5*, 299.
- [4] T. Krauskopf, F. H. Richter, W. G. Zeier, J. Janek, *Chem. Rev.* **2020**, *120*, 7745.
- [5] Y. Zhu, X. He, Y. Mo, *ACS Appl. Mater. Interfaces* **2015**, *7*, 23685.
- [6] Y. Chen, Z. Wang, X. Li, X. Yao, C. Wang, Y. Li, W. Xue, D. Yu, S. Y. Kim, F. Yang, A. Kushima, G. Zhang, H. Huang, N. Wu, Y. W. Mai, J. B. Goodenough, J. Li, *Nature* **2020**, *578*, 251.
- [7] C. Niu, H. Lee, S. Chen, Q. Li, J. Du, W. Xu, J. G. Zhang, M. S. Whittingham, J. Xiao, J. Liu, *Nat. Energy* **2019**, *4*, 551.
- [8] S. K. Otto, Y. Moryson, T. Krauskopf, K. Peppeler, J. Sann, J. Janek, A. Henss, *Chem. Mater.* **2021**, *33*, 859.
- [9] T. Krauskopf, H. Hartmann, W. G. Zeier, J. Janek, *ACS Appl. Mater. Interfaces* **2019**, *11*, 14463.
- [10] A. Sharafi, E. Kazyak, A. L. Davis, S. Yu, T. Thompson, D. J. Siegel, N. P. Dasgupta, J. Sakamoto, *Chem. Mater.* **2017**, *29*, 7961.
- [11] S. K. Otto, T. Fuchs, Y. Moryson, C. Lerch, B. Mogwitz, J. Sann, J. Janek, A. Henss, *ACS Appl. Energy Mater.* **2021**, *4*, 12798.
- [12] F. Flatscher, M. Philipp, S. Ganschow, H. M. R. Wilkening, D. Rettenwander, *J. Mater. Chem. A* **2020**, *8*, 15782.
- [13] N. J. Taylor, S. Stangeland-Molo, C. G. Haslam, A. Sharafi, T. Thompson, M. Wang, R. Garcia-Mendez, J. Sakamoto, *J. Power Sources* **2018**, *396*, 314.
- [14] E. Kazyak, R. Garcia-mendez, W. S. Lepage, A. Sharafi, A. L. Davis, A. J. Sanchez, K. Chen, C. Haslam, J. Sakamoto, N. P. Dasgupta, *Matter* **2020**, *2*, 1025.
- [15] M. J. Wang, E. Carmona, A. Gupta, P. Albertus, J. Sakamoto, *Nat. Commun.* **2020**, *11*, 1.
- [16] T. Krauskopf, R. Dippel, H. Hartmann, K. Peppeler, B. Mogwitz, F. H. Richter, W. G. Zeier, J. Janek, *Joule* **2019**, *3*, 2030.
- [17] R. Koerver, I. Aygün, T. Leichtweiß, C. Dietrich, W. Zhang, J. O. Binder, P. Hartmann, W. G. Zeier, J. Janek, *Chem. Mater.* **2017**, *29*, 5574.
- [18] F. Strauss, L. de Biasi, A.-Y. Kim, J. Hertle, S. Schweidler, J. Janek, P. Hartmann, T. Brezesinski, *ACS Mater. Lett.* **2020**, *2*, 84.
- [19] B. J. Neudecker, N. J. Dudney, J. B. Bates, *J. Electrochem. Soc.* **2000**, *147*, 517.
- [20] A. J. Louli, M. Genovese, R. Weber, S. G. Hames, E. R. Logan, J. R. Dahn, *J. Electrochem. Soc.* **2019**, *166*, A1291.
- [21] R. Weber, M. Genovese, A. J. Louli, S. Hames, C. Martin, I. G. Hill, J. R. Dahn, *Nat. Energy* **2019**, *4*, 683.
- [22] A. Pei, G. Zheng, F. Shi, Y. Li, Y. Cui, *Nano Lett.* **2017**, *17*, 1132.
- [23] M. Motoyama, M. Hirota, T. Yamamoto, Y. Iriyama, *ACS Appl. Mater. Interfaces* **2020**, *12*, 38045.
- [24] M. Motoyama, M. Ejiri, T. Yamamoto, Y. Iriyama, *J. Electrochem. Soc.* **2018**, *165*, A1338.
- [25] E. Kazyak, M. J. Wang, K. Lee, S. Yadavalli, A. J. Sanchez, M. D. Thouless, J. Sakamoto, N. P. Dasgupta, *Matter* **2022**, *5*, 3912.
- [26] T. Fuchs, B. Mogwitz, S. Otto, S. Passerini, F. H. Richter, J. Janek, *Batteries Supercaps* **2021**, *4*, 1145.
- [27] T. Krauskopf, B. Mogwitz, C. Rosenbach, W. G. Zeier, J. Janek, *Adv. Energy Mater.* **2019**, *9*, 1902568.
- [28] J. K. Eckhardt, P. J. Klar, J. Janek, C. Heiliger, *ACS Appl. Mater. Interfaces* **2022**, *14*, 35545.
- [29] J. K. Eckhardt, T. Fuchs, S. Burkhardt, P. J. Klar, J. Janek, C. Heiliger, *ACS Appl. Mater. Interfaces* **2022**, *14*, 42757.
- [30] Y. Zhu, J. G. Connell, S. Tepavcevic, P. Zapol, R. Garcia-Mendez, N. J. Taylor, J. Sakamoto, B. J. Ingram, L. A. Curtiss, J. W. Freeland, D. D. Fong, N. M. Markovic, *Adv. Energy Mater.* **2019**, *9*, 1.
- [31] J. G. Connell, T. Fuchs, H. Hartmann, T. Krauskopf, Y. Zhu, J. Sann, R. Garcia-mendez, J. Sakamoto, S. Tepavcevic, J. Janek, *Chem. Mater.* **2020**, *32*, 10207.
- [32] W. Klemm, B. Volavsek, *Z. Anorg. Allg. Chem.* **1958**, *296*, 184.
- [33] K. Peppeler, M. Pölleth, S. Meiss, M. Rohnke, J. Janek, *Z. Phys. Chem.* **2006**, *220*, 1507.
- [34] J. D. LaCoste, A. Zakutayev, L. Fei, *J. Phys. Chem. C* **2021**, *125*, 3651.
- [35] S. H. Jung, U. H. Kim, J. H. Kim, S. Jun, C. S. Yoon, Y. S. Jung, Y. K. Sun, *Adv. Energy Mater.* **2020**, *10*, 1903360.
- [36] R. Koerver, W. Zhang, L. De Biasi, S. Schweidler, A. O. Kondrakov, S. Kolling, T. Brezesinski, P. Hartmann, W. G. Zeier, J. Janek, *Energy Environ. Sci.* **2018**, *11*, 2142.
- [37] P. Bai, J. Li, F. R. Brushett, M. Z. Bazant, *Energy Environ. Sci.* **2016**, *9*, 3221.
- [38] S. Lv, T. Verhallen, A. Vasileiadis, F. Ooms, Y. Xu, Z. Li, Z. Li, M. Wagemaker, *Nat. Commun.* **2018**, *9*, 1.
- [39] H. Okamoto, *J. Phase Equilib. Diffus.* **2011**, *32*, 172.
- [40] R. Rupp, B. Caerts, A. Vantomme, J. Fransaer, A. Vlad, *J. Phys. Chem. Lett.* **2019**, *10*, 5206.
- [41] D. Rehnlund, Z. Wang, L. Nyholm, *Adv. Mater.* **2022**, *34*, 2108827.
- [42] T. H. Loeber, B. Laegel, S. Wolff, S. Schuff, F. Balle, T. Beck, D. Eifler, J. H. Fitschen, G. Steidl, *J. Vac. Sci. Technol., B: Nanotechnol. Microelectron.: Mater., Process., Meas., Phenom.* **2017**, *35*, 06GK01.
- [43] S. Liu, L. Sun, J. Gao, K. Li, *J. Microsc.* **2018**, *272*, 3.

- [44] D. P. Adams, T. M. Mayer, M. J. Vasile, K. Archuleta, *Appl. Surf. Sci.* **2006**, 252, 2432.
- [45] I. Koponen, M. Hautala, O. P. Sievänen, *Phys. Rev. Lett.* **1997**, 78, 2612.
- [46] Z. Ning, D. S. Jolly, G. Li, R. De Meyere, S. D. Pu, Y. Chen, J. Kasemchainan, J. Ihli, C. Gong, B. Liu, D. L. R. Melvin, A. Bonnin, O. Magdysyuk, P. Adamson, G. O. Hartley, C. W. Monroe, T. J. Marrow, P. G. Bruce, *Nat. Mater.* **2021**, 20, 1121.
- [47] B. Kinzer, A. L. Davis, T. Krauskopf, H. Hartmann, W. S. LePage, E. Kazyak, J. Janek, N. P. Dasgupta, J. Sakamoto, *Matter* **2021**, 4, 1947.

### 3.3 Publication 3: “Overcoming Anode Instability in Solid-State Batteries through Control of the Lithium Metal Microstructure”

In publication 3 of this dissertation, the influence of lithium metal microstructure, e.g. grain size and grain boundaries, on the pore formation during stripping was investigated. Therefore, two different lithium metal foils were prepared by utilizing extremely different thermal processing parameters and investigated in combination with LLZO as the SE while different stack pressures are applied.

Therefore, lithium metal was heated to be in a liquid state inside the glovebox at 350 °C. To obtain large grains (~150 µm), this liquid was then slowly cooled to room temperature on the hotplate. On the other hand, small grained foil (~ 20 µm) was fabricated by quenching the liquid lithium with liquid nitrogen within the glovebox, thereby rapidly cooling down the mixture. The grain sizes were obtained by SEM imaging.

Utilizing a combination of galvanostatic electrochemical impedance spectroscopy (GEIS) and post-mortem SEM analysis offers the possibility to investigate the influence of the lithium microstructure on pore formation during stripping. It could be shown that when a pressure of 0.2 MPa is applied, which is below the yield strength for typical lithium, large-grained lithium performs better and offers a higher stripping capacity than small-grained lithium. However, if pressures of 2.0 MPa are applied during dissolution, the small-grained lithium offers a very high capacity of > 10 mAh cm<sup>-2</sup>. The small grain size will lead to higher strain-rate (or lithium replenishing rate) due to dislocation pipe diffusion assisting Nabarro-Herring creep, which generally improves for small grains within a metal.

Differences are not only present when comparing the amount of stripped lithium, but also the morphology of growing pores. Top-view SEM imaging shows that the pores forming when large-grained lithium is employed are larger and less homogeneously distributed than when small-grained lithium is used. In the latter case, pores are smaller and more evenly distributed. This shows that the pore formation can in principle be controlled by adjusting the grain size of employed lithium foil, which is a novel concept not investigated in literature beforehand.

This work offers fundamental insights into how the metal microstructure may influence the electrode performance. However, employing engineered lithium foils is probably not useful, as subsequent cycling will realistically lead to the deposition of fresh lithium with changed microstructure. However, the gathered knowledge could prove to be especially useful to assess the lithium quality grown in RFCs, since different deposition parameters most likely lead to different lithium microstructures. However, it is not clear to date what grain size of deposited lithium would prove to be beneficial for future cell cycling. This work lays the foundation to investigate this question.

T. Fuchs and Dr. D. K. Singh share the first authorship as they designed and conducted all of the experiments equally supervised by Dr. F. H. Richter and Prof. J. Janek. C. Krempaszky, Dr. B. Mogwitz and Dr. S. Burkhardt assisted with important scientific discussions. The original draft was written by T. Fuchs and Dr. D. K. Singh and edited by all co-authors.

## RESEARCH ARTICLE

# Overcoming Anode Instability in Solid-State Batteries through Control of the Lithium Metal Microstructure

Dheeraj Kumar Singh,\* Till Fuchs, Christian Kremaszky, Boris Mogwitz, Simon Burkhardt, Felix H. Richter,\* and Jürgen Janek\*

Enabling the lithium metal anode (LMA) in solid-state batteries (SSBs) is the key to developing high energy density battery technologies. However, maintaining a stable electrode–electrolyte interface presents a critical challenge to high cycling rate and prolonged cycle life. One such issue is the interfacial pore formation in LMA during stripping. To overcome this, either higher stack pressure or binary lithium alloy anodes are used. Herein, it is shown that fine-grained ( $d = 20 \mu\text{m}$ ) polycrystalline LMA can avoid pore formation by exploiting the microstructural dependence of the creep rates. In a symmetric cell set-up, i.e.,  $\text{LiLi}_{6.25}\text{Al}_{0.25}\text{La}_3\text{Zr}_2\text{O}_{12}(\text{LLZO})\|\text{Li}$ , fine-grained LMA achieves  $> 11.0 \text{ mAh cm}^{-2}$  compared to  $\approx 3.6 \text{ mAh cm}^{-2}$  for coarse-grained LMA ( $d = 295 \mu\text{m}$ ) at  $0.1 \text{ mA cm}^{-2}$  and at moderate stress of  $2.0 \text{ MPa}$ . Smaller diffusion lengths ( $\approx 20 \mu\text{m}$ ) and higher diffusivity pathway along dislocations ( $D_d \approx 10^{-7} \text{ cm}^2 \text{ s}^{-1}$ ), generated during cell fabrication, result in enhanced viscoplastic deformation in fine-grained polycrystalline LMA. The electrochemical performances corroborate well with estimated creep rates. Thus, microstructural control of LMA can significantly reduce the required stack pressure during stripping. These results are particularly relevant for “anode-free” SSBs wherein both the microstructure and the mechanical state of the lithium are critical parameters.

## 1. Introduction

The drive for the improvement of electric energy storage systems causes long-term interest in lithium metal ( $3860 \text{ mAh g}^{-1}$ , and  $-3.04 \text{ V vs SHE}$ ) based solid-state batteries (SSBs) with high energy density.<sup>[1,2]</sup> The replacement of conventional flammable organic liquid electrolytes with non-flammable inorganic solid-electrolytes (ISEs,  $\sigma_{\text{ion}} > 1 \text{ mS cm}^{-1}$ ) in SSBs additionally promises enhanced safety and longer cycle life.<sup>[3–5]</sup> However, maintaining a stable electrode–electrolyte interface is one of the key challenges that currently impedes the development of SSBs.<sup>[6,7]</sup> At the anode, apart from the solid–electrolyte interface (SEI), and mixed conducting interface (MCI) formation at the Li/ISE interface,<sup>[8,9]</sup> the interfacial pore formation/accumulation<sup>[6]</sup> in the lithium electrode severely contributes to increasing impedance and decreasing power density of the cell.

Therefore, overcoming pore formation during stripping is one of the fundamental issues that needs to be addressed in the development of fast-(dis)charging SSBs. The so-called critical current for stripping (CCS) in SSBs is still lower than the critical current for plating (CCP).<sup>[10]</sup> The presence of non-equilibrium defects, i.e., grain boundaries, and dislocations in lithium anode results in inhomogeneous Li/ISE interfacial kinetics resulting in spatially varying interfacial contacts.<sup>[11]</sup>

Generally, high stack pressures are applied to avoid pore formation during stripping in research. This results in plastic deformation of lithium in contact with the ISEs, thereby maintaining a good interfacial contact.<sup>[12,13]</sup> The magnitude of the required stress is governed by interfacial roughness, fracture toughness of ISEs, thermomechanical processing history of metal etc.<sup>[14–17]</sup> In practice, the applied stack pressure should be as low as possible for the following reasons. First, engineering and cost constraints in the fabrication of practical battery packs argue against the use of high stack pressures. Second, sulfur-based superionic conductors,<sup>[18–21]</sup> which are industrially relevant candidates, possess a low fracture toughness ( $K_{\text{IC}} \leq 0.23 \text{ MPa m}^{1/2}$ ).<sup>[22]</sup> High pressures would lead to extensive interfacial fracture within these ISEs, and the resulting cracks would serve as favorable pathways for dendrite growth

D. K. Singh, T. Fuchs, B. Mogwitz, S. Burkhardt, F. H. Richter, J. Janek  
Institute of Physical Chemistry  
Justus-Liebig-University Giessen  
Heinrich-Buff-Ring 17, D-35392 Giessen, Germany  
E-mail: dheeraj.k.singh@pc.jlug.de; felix.h.richter@pc.jlug.de;  
Juergen.Janek@phys.Chemie.uni-giessen.de

D. K. Singh, T. Fuchs, B. Mogwitz, F. H. Richter, J. Janek  
Center for Materials Research (ZfM)  
Justus-Liebig-University Giessen  
Heinrich-Buff-Ring 16, D-35392 Giessen, Germany

C. Kremaszky  
Institute of Materials Science and Mechanics of Materials  
Technical University of Munich  
Boltzmannstrasse 15, D-85748 Garching, Germany

 The ORCID identification number(s) for the author(s) of this article can be found under <https://doi.org/10.1002/adfm.202211067>.

© 2022 The Authors. Advanced Functional Materials published by Wiley-VCH GmbH. This is an open access article under the terms of the Creative Commons Attribution-NonCommercial-NoDerivs License, which permits use and distribution in any medium, provided the original work is properly cited, the use is non-commercial and no modifications or adaptations are made.

DOI: 10.1002/adfm.202211067

through the bulk microstructure.<sup>[23–26]</sup> In effect, this lowers the critical current density (CCD), i.e., the maximum current density before shorting.<sup>[27]</sup> Since ceramics in general do not exhibit fatigue,<sup>[28]</sup> these interfacial fractured zones are expected to significantly affect the long-term cyclability. Additionally, the application of high pressure enhances the propensity for dendrite propagation.<sup>[29]</sup>

In another approach, binary lithium alloys (with Si, Sn, Al, Mg, As, Bi, Zn, In, etc.) are used.<sup>[30,31]</sup> Herein, enhanced lithium chemical diffusivity ( $\bar{D}_{Li} \approx 10^{-7} \text{ cm}^2 \text{ s}^{-1}$ ) compared to the much lower self-diffusivity ( $D_{Li} \approx 10^{-11} \text{ cm}^2 \text{ s}^{-1}$ ) in pure lithium is utilized to mitigate pore formation issue by facilitating faster interfacial Li flux.<sup>[6,32]</sup> However, alloy anodes are constrained by both electrochemical as well as mechanical issues that tend to be system specific, and are governed by the width of the homogeneous composition range, mechanical properties of the alloys, density of the secondary component, inter-diffusion kinetics, volume change during alloying–dealloying, etc.<sup>[30,31,33]</sup> One issue specific to alloys is the drift of redox-potential with composition. For example, the In–Li anode has a potential of 0.62 V versus  $\text{Li}^+/\text{Li}$  when > 50 at.% In is present, i.e., in the In–InLi two-phase field.<sup>[34]</sup> This limits both the theoretical and the practical specific capacity of alloys. Furthermore, alloying would lead to mechanical strengthening (usually of several orders)<sup>[35]</sup> of the anode material in general. Also, economic aspects pertaining to the cost of the alloying element need to be considered.

Chemo–mechanical degradation of alloy anodes at higher current rates or repeated alloying–dealloying may become another critical issue,<sup>[31]</sup> e.g., a charge extraction of 1.5 mAh causes the  $\beta \rightarrow \alpha$  phase transition in the Mg–70 wt.% Li system, thereby simultaneously compromising mechanical integrity, and kinetics ( $D_\alpha < D_\beta$ ).<sup>[36]</sup> Also, alloys are prone to weakening of the redox plateau upon repeated cycling.<sup>[31]</sup>

Lastly, the alloyed element must itself be stable to oxidation, e.g., the potential window of Mg in Li–Mg alloy is limited as it is oxidized at 1.35 V versus  $\text{Li}^+/\text{Li}$ .<sup>[37]</sup>

Hence, in view of these arguments, the use of (pure) lithium metal is desirable, ideally at very low stack pressure. Herein, we show that creep of polycrystalline lithium can be effectively utilized to overcome the pore formation associated interfacial instability observed during anodic stripping. Creep is a diffusion controlled, and hence, time-dependent plastic (viscoplastic) deformation of materials occurring below yield stresses, and/or at elevated temperature, i.e., high homologous temperatures,  $T_H = T/T_{fus} > 0.3\text{--}0.4$  ( $T$  and  $T_{fus}$  are the temperature of operation and the melting temperature respectively).<sup>[38]</sup> Creep is a complex process depending particularly on microstructural properties, such as grain size, grain shape, dislocation density, etc., which we aim to control.

In the present work, by implementing fine-grained polycrystalline lithium ( $d = 20 \text{ }\mu\text{m}$ ), we harness the shorter diffusion lengths ( $\approx 20 \text{ }\mu\text{m}$ ) via high diffusivity pathways (dislocation pipe diffusion,  $D_d \approx 10^{-7} \text{ cm}^2 \text{ s}^{-1}$ ) to effect higher creep deformation or creep rates. The results are compared to data obtained with coarse-grained polycrystalline lithium (295  $\mu\text{m}$ ) anodes. In symmetric transference cells, we perform galvanostatic electrochemical impedance spectroscopy (GEIS) measurements and correlate the overpotential evolution

(indicating the contact area) with the creep rates. Lastly, the contributions of different mechanisms viz. diffusional creep (Nabarro–Herring creep and Coble creep) and dislocation creep are discussed, and we assign the predominant operating mechanism under the present experimental conditions. Based on the observed anode performance, we propose microstructure-dependent deformation mechanism map for lithium. We show that an optimized microstructure of lithium metal can significantly reduce the required stack pressure in solid-state batteries.

Here, we chose  $\text{Li}_{6.25}\text{Al}_{0.25}\text{La}_3\text{Zr}_2\text{O}_{12}$  (LLZO) SE to study the creep behavior of the synthesized polycrystalline lithium metal for the following reasons. First, the Li|LLZO interface forms a microscopically smooth interface, thereby eliminating the effect of interfacial load inhomogeneity.<sup>[6,14]</sup> Second, LLZO is practically stable against lithium,<sup>[39–41]</sup> and third, LLZO exhibits a higher fracture toughness (among studied ISEs,  $\approx 1.25 \text{ MPa m}^{1/2}$ )<sup>[42]</sup> that ensures that the applied pressure will primarily lead to lithium creep without compromising its mechanical stability.

## 2. Results

In order to depict the advantage of the microstructure assisted enhanced creep behavior of polycrystalline samples,<sup>[38,43]</sup> symmetric cells, i.e.,  $\text{Li}_d|\text{LLZO}|c/\text{h-Li}$ , implementing strained fine-grained lithium or c-Li ( $d = 20 \text{ }\mu\text{m}$ ), and strained coarse-grained lithium or h-Li ( $d = 295 \text{ }\mu\text{m}$ ) as working electrode were prepared as depicted schematically in **Figure 1** (see Supporting Information for details). Phase purity of the synthesized LLZO samples was demonstrated via powder X-ray diffraction (PXRD) measurements (Figure S1a, Supporting Information). The obtained diffraction pattern is indexed to the calculated Bragg reflections for the cubic garnet structure with the  $Ia\bar{3}d$  space group. Cross-sectional scanning electron microscopy (SEM) images of a fractured LLZO pellet indicate that the grains are predominantly in the range of  $\approx 10 \text{ }\mu\text{m}$ . Furthermore, Figure S1b (Supporting Information) shows that the microstructure predominantly contains intergranular porosity with small contribution of closed porosity in the grain interiors. This is in accordance with the calculated density ( $\approx 93\%$ ) of the synthesized pellets as higher density pellets ( $\approx 97\%$ ) predominantly contain closed porosity. The conductivity of the LLZO pellet under ion-blocking conditions was found to be  $0.53 \text{ mS cm}^{-1}$  using potentiostatic electrochemical impedance spectroscopy (PEIS) (Figure S1c, Supporting Information), which is virtually equal with the ionic conductivity due to the very high transference number of lithium ions in LLZO.<sup>[44]</sup> A representative Nyquist plot at 298 K is shown in Figure S1c (Supporting Information) and is fitted with an equivalent circuit as shown in the inset of the corresponding figure. The equivalent circuit consists of a series connection of two parallel  $R\text{--}Q$  (resistor–constant phase element) elements in series with a  $Q$  element. The high frequency (4 MHz) and the middle frequency (50 kHz) semi-circles are assigned to the bulk and grain boundary transport based on their capacitance values,<sup>[45]</sup> while the low frequency component is attributed to the double-layer at the Au|LLZO interface. Arrhenius plots yield the activation

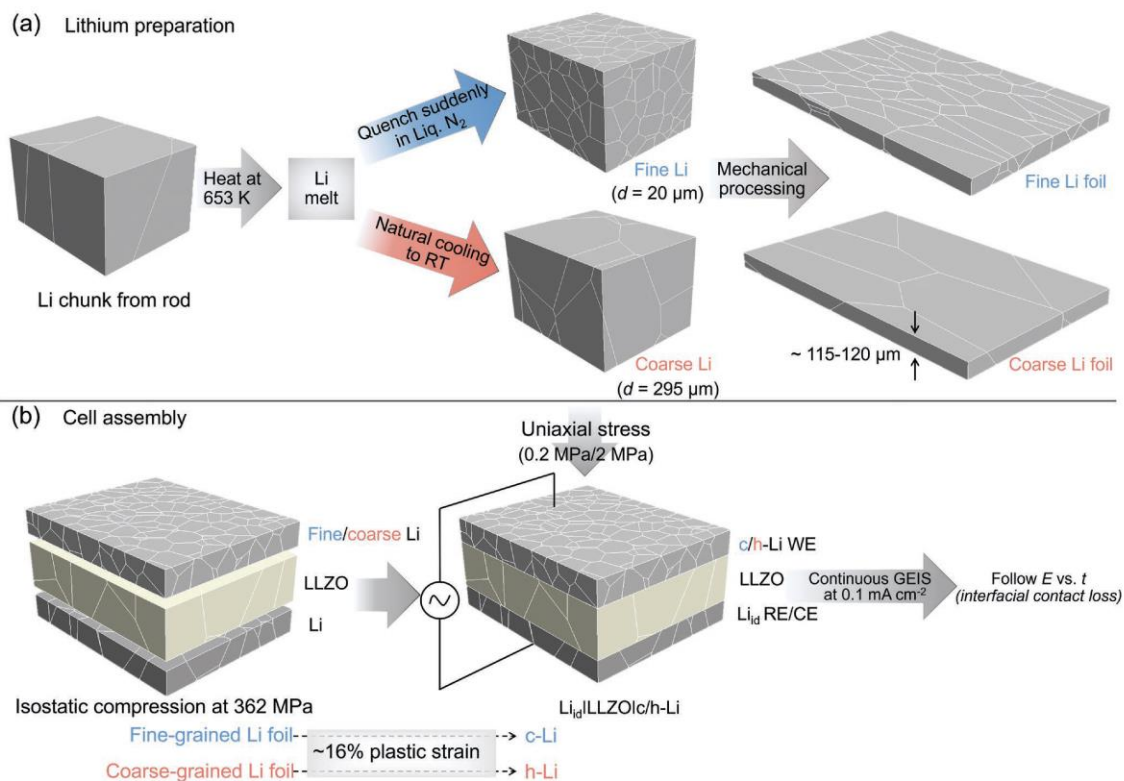


**Figure 1.** a) Preparation of fine-grained and coarse-grained polycrystalline lithium metal samples. Fine-/coarse-grained lithium foils of thickness  $\approx 115\text{--}120\ \mu\text{m}$  were obtained via mechanical processing of the respective lithium chunks. b) Fabrication of lithium symmetric cells for studying the creep deformation behavior of the anodes. During fabrication, the foils were strained to  $\approx 16\%$ , indicating significant strain hardening. Post-strained state of fine- and coarse-grained working electrodes are referred to as c-Li and h-Li, respectively.

energies,  $E_A(\text{bulk}) = 0.32\ \text{eV}$  and  $E_A(\text{GB}) = 0.42\ \text{eV}$ , for the bulk and the grain-boundary transport, respectively, fitting well to reported values.<sup>[6,46,47]</sup>

**Figure 2a,b** shows scanning electron microscopy (SEM) images of fine- and coarse-grained polycrystalline lithium foils (Please refer to Figure 1). The grain boundaries and the triple junctions are clearly visible in Figure 2a,b. The mean linear

intercept method reveals that the in-plane<sup>[48]</sup> grain size of fine-grained foil is  $\approx 20\ \mu\text{m}$  (Figure 2a) whereas for the coarse-grained sample it is  $\approx 295\ \mu\text{m}$  (Figure 2b). Similarly, the grain size of the reference lithium foil was determined to be  $\approx 160\ \mu\text{m}$  (Figure S2, Supporting Information). No differences in the XRD patterns were found for fine- and coarse-grained lithium foils (see Figure S3, Supporting Information). For grain size

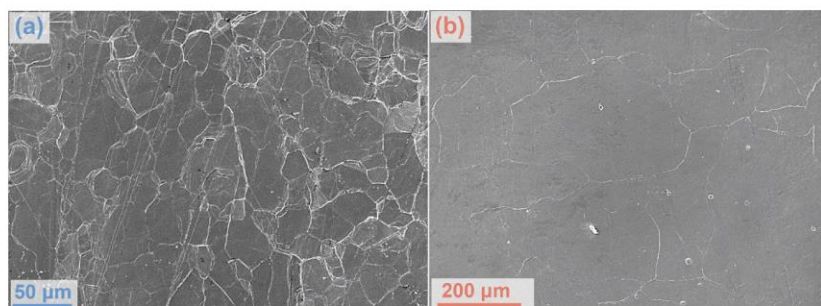


**Figure 2.** Scanning electron micrographs of a) fine-grained and b) coarse-grained lithium foils. Grain boundaries and triple junctions are prominent in the above images.

broadening of reflections to occur, the average grain size must be below 200 nm, which is not the case for the lithium samples used in the present investigation.<sup>[49]</sup>

In order to investigate the creep deformation behavior of the lithium anodes, continuous temporal evolution of galvanostatic electrochemical impedance spectra (GEIS) under unidirectional stripping conditions of the symmetric cells ( $\text{Li}_{\text{id}}\text{LLZO}/\text{c}/\text{h-Li}$ ) was recorded at  $0.1 \text{ mA cm}^{-2}$  with a cut-off voltage of 1.0 V. The advantage of GEIS measurements lies in the fact that they allow to follow and to deconvolute the relative contribution of an electrode process to the overall cell impedance under operating conditions. As lithium and LLZO form a chemically stable interface, following the temporal evolution of potential gives information about the interfacial contact loss or equivalently the strain/deformation rate of the lithium metal anode (Figure 1). The measurements were performed at two different stresses, i.e., 0.2 and 2.0 MPa, as creep is an activated process that is facilitated below yield stresses, as discussed later in detail.

The initial Nyquist plot of  $\text{Li}_{\text{id}}\text{LLZO}/\text{c}/\text{h-Li}$  symmetric cells, as shown in Figure 3, reflects the bulk and the grain boundary

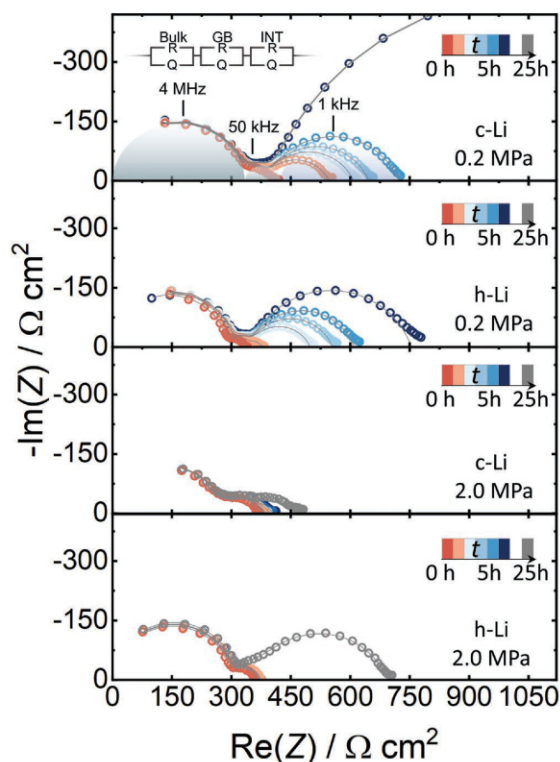


**Figure 3.** Selected Nyquist plots at different times of the temporally evolving continuous galvanostatic electrochemical impedance spectroscopy (GEIS) measurements of  $\text{Li}_{\text{id}}\text{LLZO}/\text{c-Li}$  and  $\text{Li}_{\text{id}}\text{LLZO}/\text{h-Li}$  cells at  $0.1 \text{ mA cm}^{-2}$ . GEIS data for each of the cells were separately acquired at two different vertically applied stack pressures of 0.2 and 2.0 MPa. Note: the current is normalized with respect to the initial contact area of lithium electrode.

(GB) contribution to the total impedance. The absence of any interfacial contribution is in accordance with the previously reported data for  $\text{Li}/\text{LLZO}$ , indicating combined effects of chemical stability of lithium against LLZO, and the applied pressure during cell fabrication on interfacial contacts. The obtained initial impedance is fitted with a series connection of two parallel  $R-Q$  elements for bulk and GB contribution, respectively, as shown in the inset of the Figure 3a. The assignment is based on the magnitude of the calculated values for bulk and GB capacitances, i.e.,  $C_{\text{Bulk}} \approx 10^{-11} \text{ F}$  and  $C_{\text{GB}} \approx 10^{-8} \text{ F}$ .<sup>[45]</sup>

Selected Nyquist plots at different times for  $\text{c}/\text{h-Li}$  at 0.2 and 2.0 MPa resulting from continuous GEIS measurements are shown in Figure 3. Clearly, an additional contribution manifests and grows progressively with time for both types of anodes, i.e.,  $\text{c-Li}$  and  $\text{h-Li}$ . The rates strongly differ and depend on the sample and applied stress. This component is attributed to a constriction resistance as the interfacial contact gradually diminishes. An additional parallel  $R-Q$  combination is added to the above circuit to account for this contribution (inset of Figure 3).

The corresponding temporal potential profiles for the continuous GEIS measurements are shown in Figure 4a. At a stack pressure of 0.2 MPa, the  $\text{c-Li}$  anode exhibits a faster contact loss (after  $\approx 10.0 \text{ h}$ ) compared to the  $\text{h-Li}$  anode (after  $\approx 34.5 \text{ h}$ ). This indicates that the deformation rates at 0.2 MPa are different for  $\text{c-Li}$  and  $\text{h-Li}$ . The time until contact loss in the potential profile is an indicator of the differences in the mechanical strengths of  $\text{c-Li}$  and  $\text{h-Li}$  since stress is constant (0.2 MPa) in both cases (as discussed later in detail). Therefore,  $\text{h-Li}$  is deformed more (lower strength) compared to  $\text{c-Li}$  and exhibits a higher strain rate. At 2.0 MPa, both anode materials show longer discharge until the cut-off potential (depletion) is reached. In this case, however,  $\text{c-Li}$  exhibits a longer stripping time ( $\approx 114 \text{ h}$ ) compared to  $\text{h-Li}$  ( $\approx 37 \text{ h}$ ). Note that the trend in interfacial resistance ( $R_{\text{int}}$ ) is similar to that of the voltage profile indicating the exclusive contribution of interfacial contact-loss to the observed overpotential. This is discussed below in detail.

The temporal evolution of the interfacial contact-loss imposed impedance ( $R_{\text{int}}$ ) obtained by fitting GEIS spectra is shown in Figure 4b. The trend in  $R_{\text{int}}$  is analogous to the voltage profile, indicating the exclusive contribution of interfacial contact-loss to the observed overpotential. The relationship is not one-to-one as the overpotential also includes the resistance contribution from bulk transport in the ISE ( $R_{\text{ohmic}} = 1/\sigma_{\text{ion}} \cdot L/A$ ), and across the interface ( $R_{\text{int}}$ ) as analyzed in Figure 3. The origin of  $R_{\text{int}}$  is attributed to the progressively depleting interfacial contacts upon continuous unidirectional stripping, resulting in an ensemble of constrictions or point contacts.<sup>[50,51]</sup> The impedance of such ensembles can be approximated as  $R_{\text{int}} \approx 1/(2Nd\sigma_{\text{ion}})$  ( $\sigma_{\text{ion}}$  is the ionic conductivity of the ISE,  $N$  is the number of non-interfering point contacts, and  $d$  is the diameter of each contact).<sup>[52]</sup> Clearly, upon progressive cycling,  $N$  decreases as does  $d$ , resulting in the increase of  $R_{\text{int}}$ . The extracted temporal interfacial capacitances ( $C_{\text{int}}$ ) are shown in Figure 4c. The capacitance is the result of progressively depleting contacts and concurrently evolving gaps.<sup>[52,53]</sup> Clearly, the  $\text{c-Li}$  sample exhibits faster decrease in capacitance at 0.2 MPa due to greater degree of pore accumulation (as gaps have lower permittivity) that complements the trend of  $R_{\text{int}}$ .

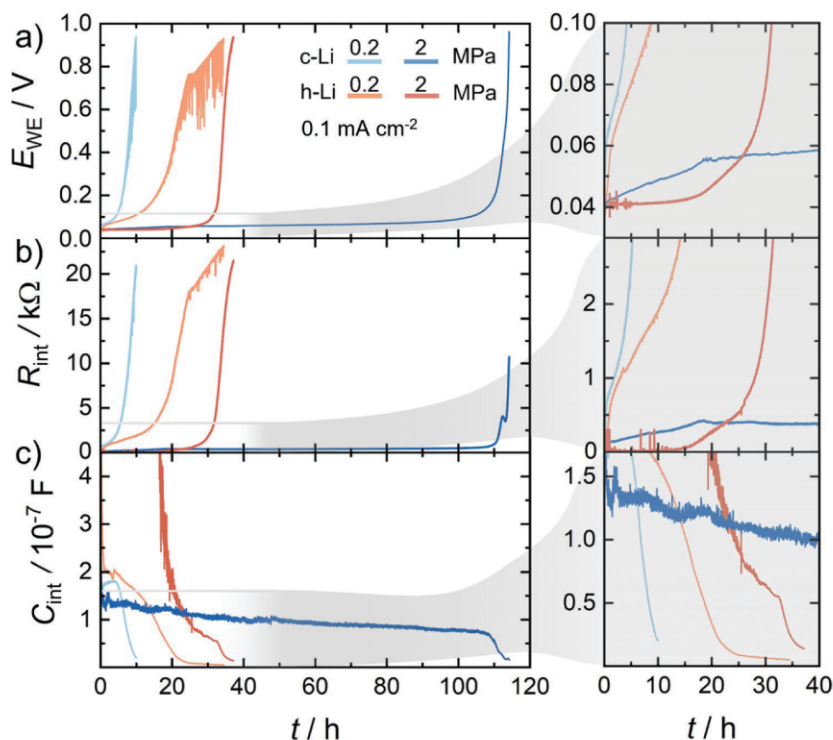


**Figure 4.** a) Potential versus time profiles during GEIS measurements for c-Li and h-Li at 0.2 and 2.0 MPa. b) Corresponding temporal evolution of the interfacial contact-loss imposed impedance ( $R_{int}$ ) and c) the corresponding extracted interfacial capacitances ( $C_{int}$ ) obtained by fitting of GEIS spectra shown in Figure 3. The right side of the graphs depicts magnified data of the first 40 h during stripping.

To correlate the electrochemical measurements with the morphology of the stripped electrodes, SEM images of the stripped working c/h-Li electrodes were acquired. After the cut-off potential of 1.0 V is reached, electrodes stripped at a stack pressure of 0.2 MPa were detached without damage. On the contrary, if 2.0 MPa was applied, it was not possible to peel of the electrodes, even after 1 V is reached. Comparison of SEM images of the stripped anodes at low magnification indicates that the c-Li exhibits relatively uniform stripping (Figure 5a) whereas h-Li has higher roughness with pores in the dimensions of tens of microns (Figure 5c). This fits well with the electrochemical data as a higher amount of charge ( $\approx 3.41 \text{ mAh cm}^{-2}$ ) was extracted from the surface of h-Li at 0.2 MPa (Figure 4) compared to  $\approx 1.00 \text{ mAh cm}^{-2}$  for c-Li. High magnification images (Figure 5b,d) reveal the presence of diminished contact points for both c/h-Li anodes as expected for constrictions (Figures 3 and 4a).

### 3. Discussion

The interfacial contact is governed by either time-independent plastic flow via glide and/or time-dependent plastic flow (climb creep and diffusional creep) depending on the magnitude of the applied stress relative to yield strength, and the microstructure (grain size, grain shape, dislocation density, etc.). The

microstructure evolution is influenced by the thermomechanical processing history of the metal. Since the yield strength of the material depends on the microstructure and is significantly affected by the applied stress during cell fabrication, we first discuss the influence of above factors on the yield strengths of c/h-Li prior to electrochemical measurements. Thereafter, we correlate the effects of the above factors on the deformation rates with the observed electrochemical data using relevant constitutive equations for the creep.

#### 3.1. Effect of the Grain Size on the Yield Strengths of c/h-Li

Strengthening of metals involves impeding/reducing dislocation mobility. Plastic flow is mediated by the dislocation glide whereas grain boundaries act as barriers to the dislocation motion.<sup>[54]</sup> The stochastically oriented neighboring grains with their randomly oriented slip systems require higher stresses for the dislocations to cross the grain boundaries. As a result, dislocations tend to pile up at the grain boundaries. Therefore, the higher the number density of the grain boundaries, the greater is the impediment, resulting in enhanced strength. This type of strengthening is referred to as grain boundary strengthening, and it is described empirically by the Hall–Petch relationship,<sup>[55,56]</sup>

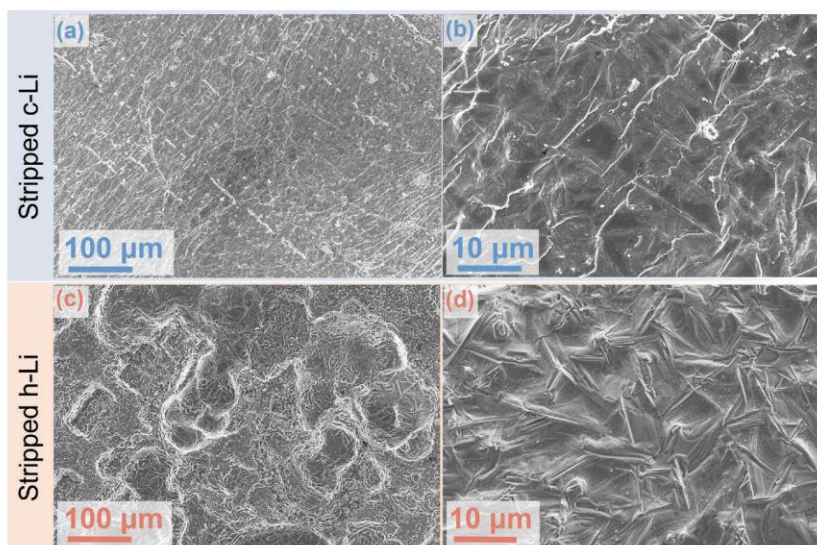


**Figure 5.** a) Low and b) high magnification SEM images of the stripped c-Li working electrode, acquired after the GEIS measurements at 0.2 MPa. (c) and (d) are the corresponding low and high magnification SEM micrographs for the stripped h-Li electrode.

$$\sigma_y = \sigma_i + k_y d^{-1/2} \quad (1)$$

where  $\sigma_y$  is the yield strength of the metal with the mean grain size  $d$ ,  $\sigma_i$  is the inherent lattice friction or Peierls–Nabarro stress, and  $k_y$  is the strengthening coefficient. Therefore, according to Equation (1), c-Li is expected to have higher yield strength compared to h-Li on account of its smaller grain size.

### 3.2. Effect of the Applied Stress during Cell Fabrication on the Yield Strengths of c/h-Li

An applied stress of 362 MPa during cell fabrication exceeds the yield strength of bulk lithium ( $\sigma_y \approx 0.8$  MPa). Therefore, during isostatic compression (Figure 1), significant plastic deformation occurs ( $\approx 16\%$  plastic strain), and the dislocation density increases in lithium metal via dislocation generation either at the grain boundaries or predominantly via the Frank–Read mechanism (a dislocation multiplication process involving shearing of the pinned dislocation and subsequent rearrangement).<sup>[54,57,58]</sup> This further impedes dislocation motion and additional stress is required to cause plastic flow. This results in strengthening of the metal, and is referred to as work hardening or strain hardening.<sup>[28]</sup> A dislocation density on the order of around  $10^{16} \text{ m}^{-2}$  can be expected during this step. The increase in required shear stress ( $\Delta\tau$ ) to overcome the dislocation barrier is proportional to dislocation density,  $\rho$  and is given by:<sup>[59]</sup>

$$\Delta\tau \propto Gb\sqrt{\rho} \quad (2)$$

where  $\alpha$  is a constant,  $G$  is the shear modulus,  $b$  is the length of the Burgers vector, and  $\rho$  is the dislocation density. The influence of the increased dislocation density on creep deformation is discussed later in detail.

### 3.3. Effect of Grain Size on Dislocation Density

Investigations by Conrad et al. on the body centered cubic structure of niobium, a structure-analog of lithium showed that for a given strain, fine-grained polycrystalline samples have higher dislocation densities compared to coarse-grained specimen (as  $\rho$  varies as  $1/d$ ) on account of a smaller free slip length.<sup>[60,61]</sup> Therefore, by analogy, it is expected that c-Li shows an increased strain hardening rate compared to h-Li.

Therefore, the overall strengthening can be summarized by as:

$$\sigma_y = \sigma_i + k_y d^{-1/2} + \alpha Gb\sqrt{\rho} \quad (3)$$

where  $\alpha$  is a constant,  $\sigma_i$  is the inherent lattice friction,<sup>[58]</sup> the second and third terms on the right hand side of the above equation are the contributions from grain boundary strengthening, and strain hardening, respectively.

From the above considerations, it is clear that c-Li has a much higher strength compared to large bulk lithium and h-Li, i.e.,  $\sigma_y$  (c-Li)  $>$   $\sigma_y$  (h-Li)  $>$   $\sigma_y$  (bulk). In fact, recent work indicates that the effective yield strength of similarly processed coarse-grained lithium foil is  $(16 \pm 2)$  MPa.<sup>[12]</sup> Therefore, applied stresses of 0.2 and 2.0 MPa are below the yield strengths of both c-Li and h-Li. Hence, the strengths of the lithium implemented in the electrochemical setup are different from those obtained from bulk mechanical measurements.

## 4. Creep Deformation Mechanism

Various deformation mechanisms operate simultaneously during the creep of a polycrystalline sample and contribute to

its plastic deformation. The set of parameters viz. temperature, applied stress, microstructure, i.e., grain size and grain shape, dislocation density, etc., determines that creep mechanism is predominant or rate-controlling.<sup>[62]</sup>

At low stresses and low temperatures, the net flux of atoms predominantly takes place along the grain boundaries (on account of its lower activation energy for migration), resulting in the change in the grain shape. Under this condition, the diffusion along the grain boundaries contributes toward predominant deformation and is referred to as Coble creep. The constitutive equation for the steady-state, grain boundary assisted diffusional creep is given by as:<sup>[63]</sup>

$$\dot{\epsilon}_c = k_2 \left( \frac{D_{GB} b}{d^3} \right) \left( \frac{E b^3}{kT} \right) \left( \frac{\sigma}{E} \right) \quad (4)$$

At higher temperatures, it represents the net transport of atoms through the lattice that contributes predominantly to creep and is known as the Nabarro–Herring creep. The constitutive equation for the steady-state lattice diffusional creep or Nabarro–Herring creep is given by:<sup>[63]</sup>

$$\dot{\epsilon}_{NH} = k_1 \left( \frac{D_L}{d^2} \right) \left( \frac{E b^3}{kT} \right) \left( \frac{\sigma}{E} \right) \quad (5)$$

At higher stresses, the non-conservative motion of edge dislocations, either via absorption or emission of vacancies (referred to as climb), results in the macroscopic plastic deformation of the material. If vacancy diffusion is assisted via low activation dislocation regions, then it is referred to as pipe diffusion-controlled dislocation climb creep (DCC) or power law creep. The constitutive relationship is given by:<sup>[63]</sup>

$$\dot{\epsilon}_{DCC} = k_3 \left( \frac{D_d}{b^2} \right) \left( \frac{\sigma}{E} \right)^n \quad (6)$$

where  $\dot{\epsilon}_{NH}$ ,  $\dot{\epsilon}_c$ , and  $\dot{\epsilon}_{DCC}$  are the strain rates for Nabarro–Herring, Coble and dislocation climb creep respectively,  $k_i$  is a material constant,  $D_L$  and  $D_{GB}$  are the lattice diffusivity and grain boundary diffusivity, respectively,  $d$  is the grain size,  $E$  is Young's modulus,  $b$  is the length of the Burgers vector,  $k$  is the Boltzmann constant,  $T$  is the absolute temperature,  $n$  is the stress exponent for the power-law creep, and  $\sigma$  is the applied stress (see Table S1, Supporting Information, for details).

Both Coble creep and Nabarro–Herring creep exhibit a strong dependence on the microstructure, i.e., grain size, and depend linearly on the stress (Equations 4,5) whereas dislocation climb creep exhibits a power-law dependence on stress (Equation 6).

When all the creep mechanisms operate simultaneously at a given  $T$ ,  $\sigma$ , and  $d$ , then the total strain rate is determined by the sum of the individual strain rates:<sup>[64]</sup>

$$\dot{\epsilon}_{\text{overall}} = \sum \dot{\epsilon}_i \quad (7)$$

From Equation (7), it is clear that the fastest deformation process governs the overall creep rate.

#### 4.1. Creep Mechanism at 2.0 MPa

To determine the predominant deformation mechanism under the given conditions, we calculated the strain rates for each of the above processes using constitutive Equations (4–6) (see Supporting Information for details). We substituted  $D_d$  for  $D_L$  in Equation (5) to account for strain hardening ( $\approx 16\%$  strain) as discussed above. This leads to an upper bound estimation of Nabarro–Herring creep rate. For c-Li ( $d = 20 \mu\text{m}$ ) at 2.0 MPa, we calculate  $\dot{\epsilon}_{NH}$  ( $4.2 \times 10^{-2} \text{ s}^{-1}$ )  $>$   $\dot{\epsilon}_{DCC}$  ( $0.9 \times 10^{-2} \text{ s}^{-1}$ )  $>$   $\dot{\epsilon}_c$  ( $2.3 \times 10^{-6} \text{ s}^{-1}$ ) whereas we obtain  $\dot{\epsilon}_{DCC}$  ( $0.9 \times 10^{-2} \text{ s}^{-1}$ )  $>$   $\dot{\epsilon}_{NH}$  ( $1.9 \times 10^{-4} \text{ s}^{-1}$ )  $>$   $\dot{\epsilon}_c$  ( $7.1 \times 10^{-10} \text{ s}^{-1}$ ) for h-Li ( $d = 295 \mu\text{m}$ ), see the Supporting Information for details. We like to note that the strain rate for DCC calculated from Equation (4) is expected to be higher compared to the actual operating rate as it does not consider the effect of dislocation density.

The strain rate calculations at 2.0 MPa reveal the following: i) the strain rates are higher in c-Li compared to h-Li, ii) dislocation pipe diffusion assisted Nabarro–Herring creep is the predominant deformation mechanism in c-Li along with the dislocation pipe diffusion assisted DCC, whereas the latter is the primary deformation mechanism in the h-Li, and iii) Coble creep accounts for much smaller strain rates in either microstructure compared to the other two mechanisms and is around four orders smaller in h-Li compared to c-Li.

The calculated higher strain rate in c-Li at 2.0 MPa corroborates well with the electrochemical data (Figure 4a). The combined higher strain rates via Nabarro–Herring creep and DCC ( $\approx 5.7$  times higher compared to h-Li) ensures a stable interface for  $\approx 110$  h, via faster deformation in the bulk of c-Li as opposed to  $\approx 35$  h for h-Li. The smaller diffusion lengths (equal to the grain size  $d \approx 20 \mu\text{m}$ ) in c-Li along fast diffusion pathways (dislocation pipe diffusion,  $D_d = 8.8 \times 10^{-7} \text{ cm}^2 \text{ s}^{-1}$ , see the Supporting Information for detailed calculations) lead to an increased transport of atoms from one grain boundary to the other under a local stress gradient (Figure 6a–c). Therefore, Nabarro–Herring creep causes a higher strain rate in c-Li compared to h-Li wherein the diffusion length is  $\approx 15$  times longer. Also, the contribution of Coble creep to the overall deformation is small on account of much smaller cross-sectional area over which they operate. Although it affects a three order higher strain rate in the c-Li microstructure on account of the much higher density of grain boundaries (Figure 6b,c). The above observation is summarized in the form of the proposed deformation mechanism map that allows to visualize the predominant microscopic deformation mechanism effecting creep in the stress-temperature space, indicating the effect of microstructure on the deformation pathway (Figure 6d).

#### 4.2. Creep Mechanism at 0.2 MPa

As above, to determine the predominant deformation mechanism, the strain rates for different processes were calculated and compared using Equations (4–6). Therefore, at 0.2 MPa and for c-Li ( $d = 20 \mu\text{m}$ ), we obtain the following  $\dot{\epsilon}_{NH}$  ( $4.2 \times 10^{-3} \text{ s}^{-1}$ )  $>$   $\dot{\epsilon}_c$  ( $2.3 \times 10^{-7} \text{ s}^{-1}$ )  $>$   $\dot{\epsilon}_{DCC}$  ( $2.3 \times 10^{-9} \text{ s}^{-1}$ ) whereas we obtain  $\dot{\epsilon}_{NH}$  ( $1.9 \times 10^{-5} \text{ s}^{-1}$ )  $>$   $\dot{\epsilon}_{DCC}$  ( $2.3 \times 10^{-9} \text{ s}^{-1}$ )  $>$   $\dot{\epsilon}_c$  ( $7.1 \times 10^{-11} \text{ s}^{-1}$ ) for h-Li ( $d = 295 \mu\text{m}$ ).

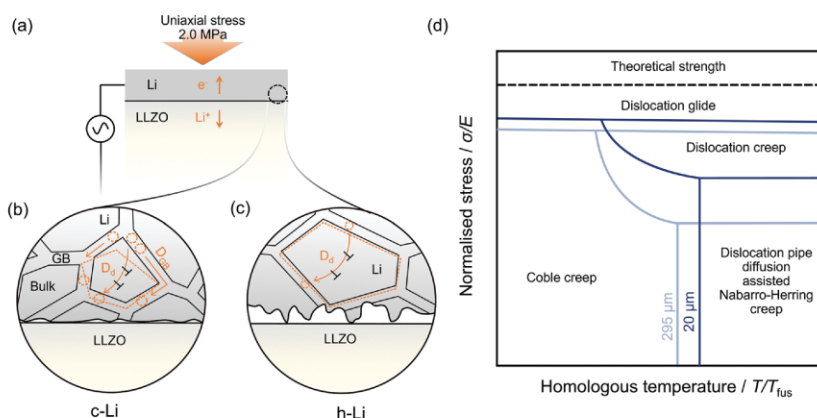


**Figure 6.** a) Anodic side of the symmetric cell, i.e.,  $\text{Li}_d/\text{LLZO}/\text{c}/\text{h-Li}$ . The interfacial region indicated by the dotted black circle is expanded in (b) and (c). Schematic indicating creep deformation in the bulk of the lithium microstructure, in the vicinity of the interface for (b) c-Li and (c) h-Li. b) At 2.0 MPa, Nabarro–Herring creep via dislocation pipe diffusion ( $D_p$ , indicated by the curved solid orange line) being the predominant deformation mechanism. Higher flux of atoms (indicated by the dotted orange circles) is realized on account of shorter diffusion length ( $d = 20 \mu\text{m}$ ) from one grain boundary to the other in the direction of the stress gradient. Dislocation pipe diffusion assisted dislocation climb creep also shown in (b). Coble creep mechanism via grain boundary predominated microstructure of c-Li results in significantly higher atomic transport along the grain boundaries ( $D_{GB}$ , indicated by the solid orange lines in (b)) resulting in higher strain rate in (b) c-Li compared to (c) h-Li. c) Dislocation pipe diffusion assisted dislocation climb creep is the predominant deformation mechanism in h-Li followed by Nabarro–Herring creep via dislocation pipe diffusion (shown by the curved solid orange line). The effect of higher strain rate in c-Li compared to h-Li is shown by the dotted orange lines indicating the shape change of a representative grain during creep in either microstructure viz. b) c-Li and c) h-Li. d) Schematic of the proposed deformation mechanism map for lithium indicating the effect of the grain size.

The strain rate evaluation reveals the following: i) the order of the strain rates in either microstructure at 0.2 MPa is smaller compared to 2.0 MPa, ii) dislocation pipe diffusion assisted Nabarro–Herring creep is the major deformation mechanism in either microstructure, iii) Coble creep, although much smaller, causes greater deformation in c-Li, and iv) the deformation rate in c-Li is two orders of magnitude higher compared to h-Li.

The effect of comparatively lower strain rates at 0.2 MPa can be seen from Figure 4a, wherein both c-Li and h-Li at 2.0 MPa maintain a stable interface over longer times. As expected, at lower stresses, diffusional creep via Nabarro–Herring dominates in both microstructures (Equation (5)). The higher grain boundary density leads to comparably higher strain rate in c-Li via Coble creep compared to h-Li (Equation (4)). However, contrary to the calculated strain rates ( $\dot{\epsilon}_{\text{NH}}$  for c-Li  $>$   $\dot{\epsilon}_{\text{NH}}$  for h-Li), h-Li is observed to deform faster compared to c-Li (Figure 4a). The apparent discrepancy between the calculated strain rates and the observed electrochemical behavior can be understood by considering the different deformation rates in the bulk and at the interface at 0.2 MPa as shown in Figure S4 (Supporting Information).

We divide the deformation in the LMA into two regimes viz.: i) deformation at the interface and ii) deformation in the vicinity of the interface or in the bulk. The logic of this subdivision stems from the fact that the inhomogeneous stripping (Figure 5; Figure S4, Supporting Information) coupled with much smaller creep rates in the bulk leads to progressively decreasing interfacial contact area at 0.2 MPa (Figure 4). Depleting contacts result in progressively increasing contact stresses, i.e., stress amplification on account of low load bearing

area whereas comparably lower and uniform stress exist in the bulk (Figure S4, Supporting Information). Therefore, the deformation at the interface progressively switches from elastic and mixed elastic-plastic to plastic flow via glide with time.

Therefore, at the interface, the contact is mediated by the competition between progressively decreasing contact (in response to the applied current) and continuously increasing contact stresses resulting in overpotential fluctuations as evident from Figure S5 (Supporting Information, magnified view of Figure 4a at 0.2 MPa). The amplitude of the overpotential fluctuations increases with time and its magnitude is an indicator of the progressively increasing contact stresses (far exceeding the strengths of Li). It is to be noted that the amplitude of the fluctuations also depends on the contact geometry and the strength of Li. Figure S5 (Supporting Information) shows that at higher overpotentials, the amplitude of fluctuations is larger in h-Li. This can be reasoned from the SEM images (Figure 5) of the stripped lithium, wherein c-Li shows higher fraction of nominally flat contact regions (and hence higher load bearing area) compared to h-Li, which shows low density of isolated point contacts. This, when combined with low strength of h-Li, results in higher plastic deformation compared to c-Li.

The combined strain rates for the plastic deformation at the interface and viscoplastic deformation (creep) in the bulk of the lithium metal anode is unable to cope up with the imposed current at 0.2 MPa as the overpotential builds up progressively right from the beginning of the electrochemical measurements (Figure 4a).

The deformation at 0.2 MPa in c/h-Li can further be divided into two parts viz.: regime I) The low overpotential regime

( $E < 0.1$  V) wherein the approximation of contact stress ( $\sigma_{\text{contact}} \approx \sigma_{\text{applied}}$ ) holds true, and regime II) the high overpotential regime ( $E > 0.4$  V) wherein contact stress (a function of time, i.e.,  $\sigma_{\text{contact}}(t) \gg \sigma_{\text{applied}}$ ) applies. In this regime, local pressure exceeds the strength of the lithium, i.e.,  $\sigma_{\text{contact}}(t) > \sigma_y$ , resulting in the voltage fluctuations as discussed above whereas in regime I, we have  $\sigma_{\text{contact}} < \sigma_y$ .

Since the overpotential is directly related to the interfacial contact area, comparing the initial  $E$  versus  $t$  slopes gives an idea about the strengths of the material. Figure 4a shows that the overpotential for c-Li at any given time  $t$  in regime I is higher compared to h-Li and, also the initial slope ( $E$  vs  $t$ ) for c-Li is larger indicating relatively faster contact loss (or slower deformation) on account of its enhanced strength via grain boundary strengthening and strain hardening, as discussed in Section 3.1 and 3.2. The higher strain rates in the bulk at 2.0 MPa do not allow for the development of stress amplification, resulting in the absence of voltage fluctuations as observed at 0.2 MPa (Figure 4a).

### 5. Relevance in “Anode-free” Lithium Metal Batteries

Although it appears as if the present investigation highlights the critical role of lithium microstructure only during the first stripping cycle; however, we believe that the present results also provide fundamental insight into the role of the microstructure of cathodically deposited (plated) lithium in “anode-free” SSBs.<sup>[65]</sup> The large volume expansion during plating exerts high stress on the deposited lithium and thus to the interface.<sup>[66–68]</sup> This can lead to a microstructural state (i.e., dislocation density, grain size, etc.) either similar or different to the present study, thus dictating the diffusion and deformation behavior in a complex way. The study of the lithium microstructure in enabling “anode-free” cell configurations becomes highly important, and we assume that it is strongly influenced by the microstructure of the current collector (on account of different lithium surface diffusion barriers and adsorption energies) and on the plating rate.<sup>[67,69]</sup>

### 6. Conclusions

The influence of the lithium metal microstructure on the anodic pore formation during stripping (discharge) has been studied experimentally. Fine-grained (c-Li,  $d = 20$   $\mu\text{m}$ ) and coarse-grained polycrystalline lithium (h-Li,  $d = 295$   $\mu\text{m}$ ) anodes were prepared and stripped in a symmetric cell set-up at two different pressures viz., 0.2 and 2.0 MPa at 0.1 mA cm<sup>-2</sup>. The pressure-dependent electrochemical performance was then corroborated with creep rates calculated via established constitutive equations from creep mechanics. The deformation mechanism in the lithium anode has significantly influenced its thermo-mechanical processing history, i.e., grain boundary strengthening and strain hardening (increase in dislocation density). Our investigations indicate that the mechanical properties of lithium anodes in SSBs are different from that of bulk (single crystalline) lithium. We show that dislocation pipe diffusion assisted Nabarro–Herring creep followed by dislo-

cation climb creep effects a higher strain rate in fine-grained polycrystalline lithium (c-Li) at 2.0 MPa resulting in a stable interface for  $\approx 110$  h compared to  $\approx 5$  h for coarse-grained polycrystalline lithium (h-Li). Dislocation pipe diffusion assisted climb creep is the predominant deformation pathway in h-Li, and the observed electrochemical behavior is supported by the strain rate calculations that are  $\approx 5.7$  times smaller compared to strain rates in c-Li. The relative strengths of c/h-Li and the overpotential govern the deformation behavior at 0.2 MPa. In the low overpotential regime ( $< 0.1$  V), the interfacial contact is governed by the strength of the material whereas at the higher potential ( $> 0.4$  V), the slow creep deformation in the bulk leads to stress inhomogeneity at the interface resulting predominantly in the plastic deformation via glide. Based on the observed electrochemical performance, we propose a microstructure-dependent deformation mechanism map for lithium. We thus show that microstructural control of plated lithium metal may help to significantly reduce the stack pressure in solid-state batteries.

### Supporting Information

Supporting Information is available from the Wiley Online Library or from the author.

### Acknowledgements

D.K.S. and T.F. contributed equally to this work. Financial support from the Federal Ministry of Education and Research (Bundesministerium für Bildung und Forschung, BMBF) within the FESTBATT consortium (projects 03XP0177A and 03XP0430A) is gratefully acknowledged, as well as within the US-German joint program supported by the US Department of Energy (DOE) and German Federal Ministry of Education and Research (BMBF) within the project “LiSI”, grant identifier 03XP0224E.

Open access funding enabled and organized by Projekt DEAL.

### Conflict of Interest

The authors declare no conflict of interest.

### Data Availability Statement

The data that support the findings of this study are available from the corresponding author upon reasonable request.

### Keywords

creep, diffusion, interface, lithium metal anode, microstructure

Received: September 23, 2022

Published online:

[1] P. Albertus, S. Babinec, S. Litzelman, A. Newman, *Nat. Energy* **2018**, *3*, 16.

[2] T. Krauskopf, F. H. Richter, W. G. Zeier, J. Janek, *Chem. Rev.* **2020**, *120*, 7745.

- [3] T. M. Bandhauer, S. Garimella, T. F. Fuller, *J. Electrochem. Soc.* **2011**, *158*, R1.
- [4] X. Liu, D. Ren, H. Hsu, X. Feng, G.-L. Xu, M. Zhuang, H. Gao, L. Lu, X. Han, Z. Chu, J. Li, X. He, K. Amine, M. Ouyang, *Joule* **2018**, *2*, 2047.
- [5] J. Janek, W. G. Zeier, *Nat. Energy* **2016**, *1*, 16141.
- [6] T. Krauskopf, H. Hartmann, W. G. Zeier, J. Janek, *ACS Appl. Mater. Interfaces* **2019**, *11*, 14463.
- [7] S. Wenzel, T. Leichtweiß, D. Krüger, J. Sann, J. Janek, *Solid State Ionics* **2015**, *278*, 98.
- [8] S. Wenzel, S. Randau, T. Leichtweiß, D. A. Weber, J. Sann, W. G. Zeier, J. Janek, *Chem. Mater.* **2016**, *28*, 2400.
- [9] P. Bron, B. Roling, S. Dehnen, *J. Power Sources* **2017**, *352*, 127.
- [10] J. Kasemchainan, S. Zekoll, D. S. Jolly, Z. Ning, G. O. Hartley, J. Marrow, P. G. Bruce, *Nat. Mater.* **2019**, *18*, 1105.
- [11] S. S. Shishvan, N. A. Fleck, V. S. Deshpande, *J. Power Sources* **2021**, *488*, 229437.
- [12] X. Zhang, Q. J. Wang, K. L. Harrison, S. A. Roberts, S. J. Harris, *Cell Rep* **2020**, *1*, 100012.
- [13] M. J. Wang, R. Choudhury, J. Sakamoto, *Joule* **2019**, *3*, 2165.
- [14] B. N. J. Persson, *Surf. Sci. Rep.* **2006**, *61*, 201.
- [15] C. Xu, Z. Ahmad, A. Aryanfar, V. Viswanathan, J. R. Greer, *Proc. Natl. Acad. Sci. USA* **2016**, *114*, 57.
- [16] M. Klinsmann, F. E. Hildebrand, M. Ganser, R. M. McMeeking, *J. Power Sources* **2019**, *442*, 227226.
- [17] B. Verlinden, J. Driver, I. Samajdar, R. D. Doherty, *Thermo-Mechanical Processing of Metallic Materials*, Elsevier Science, Amsterdam **2007**.
- [18] P. R. Rayavarapu, N. Sharma, V. K. Peterson, S. Adams, *J. Solid State Electrochem.* **2012**, *16*, 1807.
- [19] M. A. Kraft, S. P. Culver, M. Calderon, F. Böcher, T. Krauskopf, A. Senyshyn, C. Dietrich, A. Zevalkink, J. Janek, W. G. Zeier, *J. Am. Chem. Soc.* **2017**, *139*, 10909.
- [20] N. Kamaya, K. Homma, Y. Yamakawa, M. Hirayama, R. Kanno, M. Yonemura, T. Kamiyama, Y. Kato, S. Hama, K. Kawamoto, A. Mitsui, *Nat. Mater.* **2011**, *10*, 682.
- [21] Y. Kato, R. Saito, M. Sakano, A. Mitsui, M. Hirayama, R. Kanho, *J. Power Sources* **2014**, *271*, 60.
- [22] F. P. McGrogan, T. Swamy, S. R. Bishop, E. Eggleton, L. Porz, X. Chen, Y.-M. Chiang, K. J. V. Vliet, *Adv. Energy Mater.* **2017**, *7*, 1602011.
- [23] P. Barai, K. Higa, A. T. Ngo, L. A. Curtiss, V. Srinivasan, *J. Electrochem. Soc.* **2019**, *166*, A1752.
- [24] X. Tingdong, Z. Lei, *Philos. Mag. Lett.* **2004**, *84*, 225.
- [25] E. J. Cheng, A. Sharafi, J. Sakamoto, *Electrochim. Acta* **2017**, *223*, 85.
- [26] D. K. Singh, A. Henss, B. Mogwitz, A. Gautam, J. Horn, T. Krauskopf, S. Burkhardt, J. Sann, F. H. Richter, J. Janek, *Cell Reports Phys. Sci.* **2022**, *3*, 101043.
- [27] A. Sharafi, H. M. Meyer, J. Nanda, J. Wolfenstine, J. Sakamoto, *J. Power Sources* **2016**, *302*, 135.
- [28] J. Roesler, H. Harders, M. Baeker, *Mechanical Behaviour of Engineering Materials: Metals, Ceramics, Polymers, and Composites*, Springer, Berlin, Heidelberg **2007**.
- [29] J.-M. Doux, H. Nguyen, D. H. S. Tan, A. Banerjee, X. Wang, E. A. Wu, C. Jo, H. Yang, Y. S. Meng, *Adv. Energy Mater.* **2020**, *10*, 1903253.
- [30] P. Kurzweil, K. Brandt, in (Eds. J. Garche, Brandt Systems, and Applications, K. B. T.-E. P. S. F.) pp. 47–82, Elsevier, Amsterdam **2019**, <https://doi.org/10.1016/B978-0-444-63777-2.00003-7>.
- [31] J. Yang, J. I. Wang, in (Eds. J. B. T.-E. of E. P. S. Garche), pp. 225–236, (Elsevier, Amsterdam **2009**, <https://doi.org/10.1016/B978-0-44452745-5.00190-8>).
- [32] T. Krauskopf, B. Mogwitz, C. Rosenbach, W. G. Zeier, J. Janek, *Adv. Energy Mater.* **2019**, *9*, 1902568.
- [33] A. Anani, R. A. Huggins, *J. Power Sources* **1992**, *38*, 351.
- [34] A. L. Santhosha, L. Medenbach, J. R. Buchheim, P. Adelhelm, *Batter Supercaps* **2019**, *2*, 524.
- [35] R. W. Cahn, P. Haasen, *Physical Metallurgy*, 4th ed., (Eds: R. W. Cahn, P. Haasen), Elsevier Science, Amsterdam **1996**.
- [36] Y. Zhang, K. S. R. Chandran, M. Jagannathan, H. Z. Bilheux, J. C. Bilheux, *J. Electrochem. Soc.* **2016**, *164*, A28.
- [37] Z. Shi, M. Liu, D. Naik, J. L. Gole, *J. Power Sources* **2001**, *92*, 70.
- [38] H. J. Frost, M. F. Ashby, *Deformation-Mechanism Maps: The Plasticity and Creep of Metals and Ceramics*, Elsevier Science Limited, Amsterdam **1982**.
- [39] Y. Zhu, G. J. Connell, S. Tepavcevic, P. Zapol, R. Garcia-Mendez, N. J. Taylor, J. Sakamoto, B. J. Ingram, L. A. Curtiss, J. W. Freeland, D. D. Fong, N. M. Markovic, *Adv. Energy Mater.* **2019**, *9*, 1803440.
- [40] Y. Zh, X. He, Y. Mo, *ACS Appl. Mater. Interfaces* **2015**, *7*, 23685.
- [41] J. G. Connell, T. Fuchs, H. Hartmann, T. Krauskopf, Y. Zhu, J. Sann, R. Garcia-Mendez, J. Sakamoto, S. Tepavcevic, J. Janek, *Chem. Mater.* **2020**, *32*, 10207.
- [42] J. Wolfenstine, H. Jo, Y.-H. Cho, I. N. David, P. Askeland, E. D. Case, H. Kim, H. Choe, J. Sakamoto, *Mater. Lett.* **2013**, *96*, 117.
- [43] P. M. Sargent, M. F. Ashby, *Scr. Metall.* **1984**, *18*, 145.
- [44] H. Buschmann, J. Dölle, S. Berendts, A. Kuhn, P. Bottke, M. Wilkening, P. Heitjans, A. Senyshyn, H. Ehrenberg, A. Lotnyk, V. Doppel, L. Kienle, J. Janek, *Phys. Chem. Chem. Phys.* **2011**, *13*, 19378.
- [45] J. T. S. Irvine, D. C. Sinclair, A. R. West, *Adv. Mater.* **1990**, *2*, 132.
- [46] T. Fuchs, B. Mogwitz, S.-K. Otto, S. Passerini, F. H. Richter, J. Janek, *Batter Supercaps* **2021**, *4*, 1145.
- [47] Y. Zhang, F. Chen, J. Li, L. Zhang, J. Gu, D. Zhang, K. Saito, Q. Guo, P. Luo, S. Dong, *Electrochim. Acta* **2018**, *261*, 137.
- [48] G. F. V. Voort, *Prakt. Metallogr.* **2013**, *50*, 239.
- [49] U. Holzwarth, N. Gibson, *Nat. Nanotechnol.* **2011**, *6*, 534.
- [50] J. Fleig, J. Maier, *Solid State Ionics* **1996**, *85*, 17.
- [51] J. Fleig, J. Maier, *Solid State Ionics* **1996**, *86–88*, 1351.
- [52] J. Fleig, J. Maier, *J. Electroceramics* **1997**, *1*, 73.
- [53] J.-H. Hwang, K. S. Kirkpatrick, T. O. Mason, E. J. Garboczi, *Solid State Ionics* **1997**, *98*, 93.
- [54] J. P. Hirth, J. Lothe, *Theory of Dislocations*, Wiley, New Jersey, USA **1982**.
- [55] E. O. Hall, *Proc. Phys. Soc., London, Sect. B* **1951**, *64*, 747.
- [56] N. J. Petch, *J. Iron Steel Inst.* **1953**, *174*, 25.
- [57] F. C. Frank, W. T. Read, *Phys. Rev.* **1950**, *79*, 722.
- [58] A. H. Cottrell, *Prog. Met. Phys.* **1953**, *4*, 205.
- [59] R. W. Hertzberg, *Deformation and Fracture Mechanics of Engineering Materials*, Wiley, New Jersey, USA **1996**.
- [60] H. Conrad, S. Feuerstein, L. Rice, *Mater. Sci. Eng.* **1967**, *2*, 157.
- [61] J. A. El-Awady, *Nat. Commun.* **2015**, *6*, 5926.
- [62] R. W. Hertzberg, R. P. Vinci, J. L. Hertzberg, *Deformation and Fracture Mechanics of Engineering Materials*, 5th ed., Wiley, New Jersey, USA **2012**.
- [63] O. A. Ruano, J. Wadsworth, O. D. Sherby, *J. Mater. Sci.* **1985**, *20*, 3735.
- [64] W. J. Kim, H. T. Jeong, *J. Mater. Res. Technol.* **2020**, *9*, 13434.
- [65] B. J. Neudecker, N. J. Dudney, J. B. Bates, *J. Electrochem. Soc.* **2000**, *147*, 517.
- [66] M. Motoyama, M. Ejiri, Y. Iriyama, *J. Electrochem. Soc.* **2015**, *162*, A7067.
- [67] V. Pande, V. Viswanathan, *ACS Energy Lett.* **2019**, *4*, 2952.
- [68] A. J. Louli, M. Genovese, R. Weber, S. G. Hames, E. R. Logan, J. R. Dahn, *J. Electrochem. Soc.* **2019**, *166*, A1291.
- [69] I. T. Roe, S. K. Schnell, *J. Mater. Chem. A* **2021**, *9*, 11042.

### 3.4 Publication 4: “Increasing the Pressure-Free Stripping Capacity of the Lithium Metal Anode in Solid-State-Batteries by Carbon Nanotubes”

In publication 4 of this dissertation, composite anodes consisting of 10 – 40 wt% of CNTs dispersed in lithium were investigated regarding the ability to either suppress or compensate pore formation during anodic dissolution, which still imposes severe limitations during cell operation.

The combination of cryogenic FIB-SEM imaging with operando GEIS allowed to follow and interpret the morphological evolution of the Li-CNT|LLZO system during stripping. It could be shown that by incorporating the CNTs into the lithium matrix, a greatly increased stripping capacity of above  $> 20 \text{ mAh cm}^{-2}$  is achieved, which presents a 10 – 15-fold increase when compared to pure lithium. Additionally, impedance spectroscopy showed changes in the contributions from the interface due to constriction, which suggests changes in the morphology of formed pores. Cryogenic FIB-SEM revealed that the pore formation is not only restricted to the interface to the SE, but also occurs in the bulk of the composite anode. This is explained by the CNT functioning as “diffusion-highways” to facilitate the dissolution from within the bulk electrode and therefore increasing the stripping capacity. Since the pore geometry is fundamentally different than for pure lithium metal, the impedance of the cell is also changing, which offers unique fundamental insights into the nature of constriction at metal anodes.

In combination with the working group of Prof. J. Sakamoto, the mechanical properties of the composite were explored further and correlated with changes of the electrochemical properties. A clear increase in yield strength, Young’s modulus and Vickers hardness was observed with increasing CNT content as investigated by stress-strain measurements, acoustic analysis and micro-indentation. Due to the increased strength of the material, it only shows superior stripping capacity to lithium when no pressure is applied to a cell. However, if stack pressure is applied, lithium is proven to be superior due to its better deformability to counteract pore formation when stripping.

Overall, this work shows the valuable possibility to tune the electrode material both in its electrochemical and mechanical properties by dispersing CNTs into lithium metal. Using this method or possible variations thereof, the anode material can be specifically tailored to fit the requirements of certain applications, e.g. when high discharge capacities or a low sensitivity to external pressure is desired.

T. Fuchs designed and conducted all of the experiments with laboratory support from C. G. Haslam, A.C. Moy and C. Lerch under the supervision of Prof. J. Sakamoto, Dr. F. H. Richter and Prof. J. Janek. All authors contributed to the scientific discussion. The original draft was written by T. Fuchs and edited by five co-authors.

## RESEARCH ARTICLE



www.advenerymat.de

# Increasing the Pressure-Free Stripping Capacity of the Lithium Metal Anode in Solid-State-Batteries by Carbon Nanotubes

Till Fuchs, Catherine G. Haslam, Alexandra C. Moy, Christian Lerch, Thorben Krauskopf, Jeff Sakamoto,\* Felix H. Richter,\* and Jürgen Janek\*

Lithium metal is the key anode material for solid-state-batteries as its successful implementation will drastically increase their energy and power densities. However, anode contact loss during stripping leads to dendrites upon plating and subsequent cell failure. Design strategies to mitigate these issues are crucial to enable the use of lithium metal anodes. This paper reports the dissolution kinetics of composite anodes made of lithium metal and carbon nanotubes (CNTs) with a garnet-type solid electrolyte (SE). In addition to an enhancement of the effective diffusion within the anode, its dissolution is fundamentally changed from being 2D to 3D. By maintaining contact with the SE, the CNTs facilitate lithium transport to the interface, which yields more than 20 mAh cm<sup>-2</sup> discharge capacity at 100 μA cm<sup>-2</sup> without the application of external stack pressure (>1 MPa). Conclusions drawn from electrochemical data on the anode microstructure are validated using cryo-focused-ion-beam scanning electron microscopy and correlated with the mechanical properties. Micro-indentation, acoustic analysis, and stress-strain testing show that mechanical properties of the anode, like yield strength and hardness, are adjustable. Overall, it is shown that the mechanical and electrochemical properties of Li-CNT composite electrodes can be tailored to suit the requirements of a practical cell.

## 1. Introduction

Recently, all-solid-state batteries gained increasing attention as candidates to supersede lithium-ion-batteries as energy storage devices, for example, in the power train of electric vehicles.<sup>[1,2]</sup> While they are deemed to be safer and less flammable than lithium-ion batteries,<sup>[3]</sup> their main promise is that solid electrolytes (SEs) may enable the use of lithium metal as the anode material.<sup>[4,5]</sup> With 3861 mAh g<sup>-1</sup>, lithium shows the highest theoretical capacity<sup>[6]</sup> as well as the lowest redox potential with -3.04 V versus the standard hydrogen electrode potential,<sup>[7]</sup> which makes it an attractive goal for the next generation of lithium batteries.

However, pore formation during lithium dissolution (stripping) and later dendrite growth triggered by the resulting heterogeneous interface hinders their application at high current densities so far.<sup>[8-10]</sup> For every lithium

ion stripped from the electrode, a vacancy is “injected” in the metal. If the rate of vacancy injection, governed by the applied current density, is higher than the rate of vacancy annihilation by diffusion into the anode bulk,<sup>[8,11-13]</sup> vacancies accumulate at the interface — as originally shown by Janek and Majoni for the stripping of silver metal.<sup>[14]</sup> An accumulation of vacancies results in pore formation and contact loss, as well as facilitating dendrite formation upon current reversal.<sup>[4,10]</sup> To circumvent these issues, either the annihilation of vacancies from the interface needs to be accelerated or the local current density needs to be lowered. While the first mitigation strategy succeeds by applying stack pressures in the MPa range,<sup>[8,15,16]</sup> it is preferred to increase the vacancy annihilation rate by enhanced diffusion in the metal.

Increasing the lithium diffusion inside the electrode material to avoid pore formation is possible by alloying with other metals.<sup>[4,17]</sup> For example, 10 wt% of magnesium enhances the effective diffusion coefficient by a factor of three up to  $2.3 \times 10^{-11}$  cm<sup>2</sup> s<sup>-1</sup>. However, due to different mechanical properties, pure lithium is superior to Li-Mg when external pressure in the MPa range is applied. As pressure most likely needs to be applied in large cell stacks, knowledge of the mechanical properties of the anode material is highly important. Careful modification of the lithium metal anode's elastic and plastic properties changes the sensitivity of cells

T. Fuchs, C. Lerch, T. Krauskopf, F. H. Richter, J. Janek  
Institute of Physical Chemistry  
Justus-Liebig-University Giessen  
Heinrich-Buff-Ring 17, D-35392 Giessen, Germany  
E-mail: Felix.H.Richter@pc.jlug.de; Juergen.Janek@pc.jlug.de

T. Fuchs, C. Lerch, T. Krauskopf, F. H. Richter, J. Janek  
Center for Materials Research (ZfM)  
Justus-Liebig-University Giessen  
Heinrich-Buff-Ring 16, D-35392 Giessen, Germany

C. G. Haslam, A. C. Moy, J. Sakamoto  
Department of Materials Science and Engineering  
University of Michigan  
Ann Arbor, MI 48109, USA  
E-mail: jeffsaka@umich.edu

C. G. Haslam, J. Sakamoto  
Department of Mechanical Engineering  
University of Michigan  
Ann Arbor, MI 48109, USA

The ORCID identification number(s) for the author(s) of this article can be found under <https://doi.org/10.1002/aenm.202201125>.

© 2022 The Authors. Advanced Energy Materials published by Wiley-VCH GmbH. This is an open access article under the terms of the Creative Commons Attribution-NonCommercial-NoDerivs License, which permits use and distribution in any medium, provided the original work is properly cited, the use is non-commercial and no modifications or adaptations are made.

DOI: 10.1002/aenm.202201125

to applied stack pressures, opening up a variety of different applications with specific pressure requirements.

Instead of increasing the vacancy diffusion rate inside the anode or relying on the plastic flow or creep, it is also possible to lower the local current density by creating a 3D-architecture of the Li|SE-interface,<sup>[18]</sup> of which several approaches have been reported.<sup>[19–22]</sup> One example is the inner coating of a porous SE with carbon nanotubes (CNTs), which then act as a current collector for lithium nucleation.<sup>[19]</sup> Continuous plating and stripping of 5.0 mAh cm<sup>-2</sup> with current densities up to 2.5 mA cm<sup>-2</sup> based on the geometrical area was reported,<sup>[18]</sup> which is around five times that of planar interfaces.<sup>[4,23]</sup> However, the preparation of porous electrode configurations is challenging. Therefore, a planar electrode|SE interface is preferred, especially when considering stacked cell systems.

Additionally, CNTs can enhance the effective diffusion inside the metal electrode. Not only are lithium ions conducted within the walls of CNTs, but also lithium atom diffusion inside CNTs has been demonstrated.<sup>[6]</sup> When lithiated, CNTs are mixed ionic-electronic conductors (MIECs) and form a stable interface with lithium.<sup>[6,24]</sup> However, while well-engineered carbonaceous felts, membranes, or meshes wetted by lithium show a great improvement in anode performance,<sup>[25–27]</sup> the lithium transport mechanism and transport properties in these composites remain elusive.

In this work, we investigate the anodic dissolution and pore formation of composite anodes consisting of lithium metal and CNTs. It was possible to combine two approaches by 1) generating a CNT scaffold to obtain a MIEC 3D interface without the need for specially structured garnet SE and 2) accelerating lithium atom diffusion by mixing lithium metal with CNTs. With this heterogeneous solid-state composite, it was possible to strip more than 20 mAh cm<sup>-2</sup> of lithium without the need for high applied external pressure and also tune the mechanical properties of the material, paving the way for the optimization of lithium electrodes.

## 2. Results and Discussion

### 2.1. Composite Characterization

The herein investigated composites were prepared by dispersing 10–40 wt% of multiwalled CNTs in liquid lithium metal at 350 °C and cooling of the resulting mixture to ambient temperature. During the mixing process, a distinct transition between nonwetting and wetting of the tubes in liquid lithium occurs. After the transition, the mixture appeared homogeneous and shiny to the naked eye (see Figure S1, Supporting Information). The measurement of the geometric density of the solidified mixtures shows a slight increase from around 0.54 g cm<sup>-3</sup> for pure lithium to around 0.58 g cm<sup>-3</sup> for Li–CNT30 (Figure 1a). During handling of the solidified composite, a decrease of ductility and increase in hardness compared with pure lithium metal was evident.

X-ray diffraction (XRD) measurements prove that both the CNTs and lithium metal keep their respective crystal structures, which indicates the chemical stability of the mixture. Both lithium and CNTs show specific and pronounced reflections which match with literature (Figure 1b).<sup>[17,28]</sup> From the reflections at 36.1°, 52.0°, and 64.9°, marked in grey, it is evident that the lithium crystal structure is still intact after preparing the composite electrode material and the lattice parameters have not changed either. This is reasonable, as no alloy is formed between the materials, which would most likely alter the lattice.<sup>[17]</sup>

The pure CNT powder shows broad reflections around 25.6°, 43.4°, and 53.4°, which correspond to the (002), (100), and (004) planes. As the indexing is based on the hexagonal graphite structure, (002) and (004) reflections correspond to an interplane and (100) to an intraplane distance.<sup>[29,30]</sup> Additionally, a slight asymmetry of the reflections to higher 2θ angles is observed for pure CNTs, which usually indicates nonideal stacking in turbostratic graphite layers.<sup>[29,31]</sup>

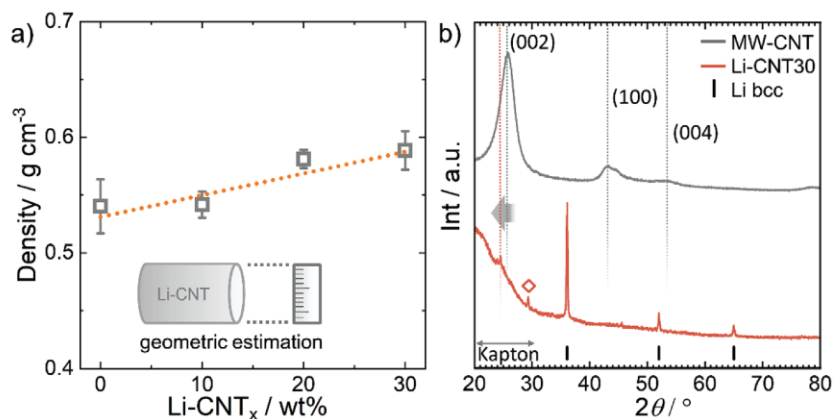


**Figure 1.** a) Density of the composite in dependence of the CNT content. The dashed line acts as a guide to the eye. b) The XRD pattern of the composite electrode Li–CNT30 is compared to that of pure CNTs and the reflection card of bcc lithium metal. The background increasing with small  $2\theta$  angles originates from the use of Kapton foil for air-tight sample preparation and is not indicative of the sample structure. A nonidentified impurity phase (presumably from reaction with atmosphere) also shows a reflection at 30°, marked with a diamond. The indexing of the CNT reflections is explained in Figure S1c,d, Supporting Information, regarding the (00l) and (d00) planes with an example CNT with three layers and a chirality of 20.

The reflection pattern of the composite shows that the CNT reflections both decrease in intensity and shift to higher  $2\theta$  angles. This indicates changes of the CNT structure. When calculating the CNT wall distance via the (002) reflection using the Bragg formula, an increase from 3.57 Å for the pristine state to 3.73 Å in the composite is observed. The increased distance corresponds well to the layer distance in lithiated graphite. We therefore assume that the CNTs are lithiated during the mixing process, and thus, also widened.<sup>[32,33]</sup> Likewise, lithiation of graphite coatings on SEs via liquid lithium was previously shown by Shao et al.<sup>[34]</sup> and is expected to occur at defects, holes, or at the end of the CNTs, which was shown for other graphitic structures.<sup>[35]</sup>

Additionally, the (002) reflection observed for the pristine CNT powder is broader than in the composite, as a shoulder at lower  $2\theta$  angles originates from the distance between different, separated CNTs.<sup>[36]</sup> When CNTs are incorporated into the lithium matrix this effect diminishes. In general, the XRD results show that the CNTs are lithiated in the composite and that the lithium matrix retains its crystal structure. To assess the electrochemical properties of the composites, impedance tests were carried out and shown in the next section.

## 2.2. Electrochemical Analysis of Impedance and Lithium Stripping

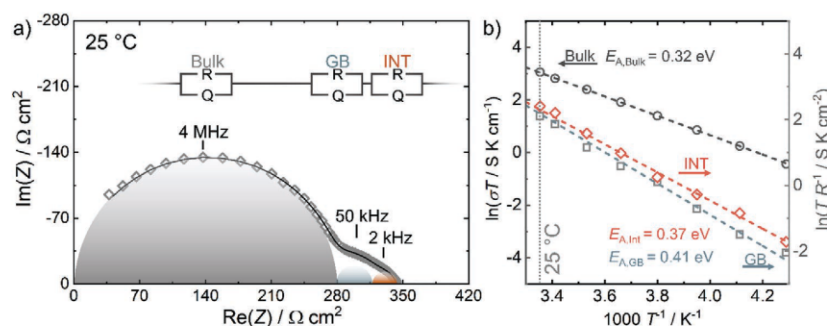
To analyze the dissolution and impedance of Li-CNT composite electrodes,  $\text{Li}_{\text{id}}|\text{LLZO}|\text{Li-CNT}$  cells were prepared, where the ideally reversible electrode ( $\text{Li}_{\text{id}}$ ) shows negligible interfacial impedance, and thus, acts as a combined reference and counter electrode.<sup>[8,37]</sup> Therefore, any observed interfacial impedance and changes thereof solely originate from the Li-CNT|LLZO-interface. Using this method, the maximum current density is limited to around  $200 \mu\text{A cm}^{-2}$ , as the  $\text{Li}_{\text{id}}$  anode is not resistant to dendrites at higher current densities. Foils of lithium for the preparation of the  $\text{Li}_{\text{id}}$  electrode and the Li-CNT composite were both prepared by mechanically flattening a chunk of each material, which was freed before from any passivation layer with a ceramic knife. In contrast to the high pressure utilized for  $\text{Li}_{\text{id}}$  (400 MPa) the herein prepared composite anode was initially pressed onto the pellet using a small hand pressing tool ( $\approx 30$  MPa).

The impedance data of  $\text{Li}_{\text{id}}|\text{LLZO}|\text{Li-CNT40}$  at 25 °C are shown in Figure 2a in the Nyquist representation alongside

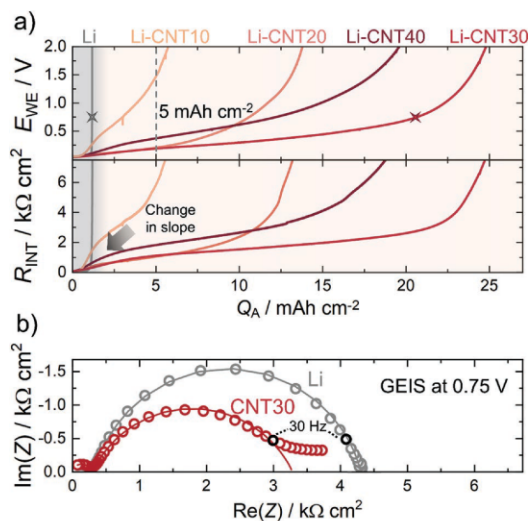
an equivalent circuit used for fitting. Lithium lanthanum zirconium oxide (LLZO) bulk and grain boundary (GB) contributions are identified at high (4 MHz) and middle (50 kHz) frequencies, respectively.<sup>[8,37]</sup> At low frequencies (1 kHz), a small interfacial contribution is observed. Hence, our equivalent circuit consists of a series combination of three parallel  $R$ - $Q$  elements, where  $R$  and  $Q$  represent a resistor and nonideal capacity (constant-phase element). All obtained fit parameters are displayed in Table S1, Supporting Information. The apex frequencies and capacitances of the processes match well to data in the literature.<sup>[38]</sup> With only  $27 \Omega \text{ cm}^2$ , the impedance for the Li-CNT40|LLZO interface is relatively low. This is remarkable as neither elevated temperature nor large pressures were utilized for the attachment of the Li-CNT40 electrode. Furthermore, the active contact area between lithium in the composite and LLZO might even be lower than geometrically estimated due to the lower area fraction of lithium at the interface.

Figure 2b shows an Arrhenius-plot of the three fitted impedance components. Note that the GB and interface processes are difficult to deconvolute as the interfacial resistance is small and the frequency ranges overlap. The linear fits of the graphs show that these are all temperature activated processes. The activation energies for bulk ( $E_{\text{A,Bulk}} = 0.32 \text{ eV}$ ), GB ( $E_{\text{A,GB}} = 0.41 \text{ eV}$ ) and interfacial transport ( $E_{\text{A,Int}} = 0.37 \text{ eV}$ ) fit well to previously reported results.<sup>[8,37,39,40]</sup> It is reasonable that the Li-CNT|LLZO interface has a similar activation barrier as the Li|LLZO interface, as charge transfer occurs at the direct contact areas between lithium and LLZO.

The assessment of lithium dissolution is possible by long-term stripping experiments, which are performed on  $\text{Li}_{\text{id}}|\text{LLZO}|\text{Li-CNT}$  cells as a function of CNT weight fraction and current density. Electrodes were stripped until contact loss to the SE was observed, which is indicated by a steep increase in voltage and interfacial resistance (i.e., lithium depletion).<sup>[8,17,37]</sup> Figure 3a shows the voltage profiles when stripping with  $100 \mu\text{A cm}^{-2}$  for Li and Li-CNT-composites. The displayed interfacial resistances are extracted via galvanostatic electrochemical impedance spectroscopy (GEIS) according to the fit procedure exemplified in Figure 2. The underlying evolution of the corresponding Nyquist and Bode plots is exemplarily shown for  $\text{Li}_{\text{id}}|\text{LLZO}|\text{Li-CNT40}$  in Figures S2 and S3, Supporting Information. As seen therein, bulk and GB resistance contributions remain constant throughout the experiments,



**Figure 2.** a) Nyquist plot of a  $\text{Li}_{\text{id}}|\text{LLZO}|\text{Li-CNT40}$  cell together with the equivalent circuit for fitting. b) Arrhenius plot of impedance data for the bulk, grain boundary (GB), and interface (Int) processes as function of temperature.



**Figure 3.** a) Voltage profiles during stripping of lithium, Li-CNT10, Li-CNT20, Li-CNT30, and Li-CNT40 at a current density of  $100 \mu\text{A cm}^{-2}$  (top). The corresponding evolution of the interfacial resistance is shown underneath. b) Impedance spectra at 0.75 V (marked with stars in [a]) for lithium and Li-CNT30. Fitting was carried out similar to the impedance data shown in Figure 2.

which confirms that the  $\text{Li}_{\text{id}}$  counter electrode is stable and no dendrites are growing through the ceramic. Thus, for the fitting process, both bulk and GB resistance contributions were fixed to a constant value (determined from impedance measurements at the beginning).

While the lithium electrode reaches the 2 V cutoff (i.e., depletion) condition after only  $1.2 \text{ mAh cm}^{-2}$  (12 h of stripping), the composites delay the depletion by a factor of 20 to around  $25 \text{ mAh cm}^{-2}$  for Li-CNT30. This is the highest reported stripping capacity to date for an all-solid-state system. Albeit the current density is still quite low, the estimated target of  $5 \text{ mAh cm}^{-2}$  by Albertus et al. and Randau et al. is hereby exceeded.<sup>[2,41]</sup> Moreover, most of the stripping capacity in this experiment is available only after severe polarization and interfacial degradation already took place, which is not easily reversible. For pure lithium, the ratio of available capacity prior to degradation compared to the overall capacity is higher. Interestingly, the available capacity increases up to 30 wt% of CNTs being dispersed in lithium but decreases for Li-CNT40. Above a certain threshold, CNTs dispersed in lithium may not homogeneously be distributed anymore. Also, less lithium is present in the sample with higher CNT content.

Not only is a severe increase in stripping capacity observed for the Li-CNT composites, the overall voltage profile changes as well. While pure lithium shows a flat and stable plateau followed by a steep increase in voltage when contact is lost, changes of the electrode potential  $E_{\text{WE}}$  for the composites are more gradual. For the composites, there is an inflection point at around  $1 \text{ mAh cm}^{-2}$  where the slope changes. Interestingly, this corresponds well to the point where pure lithium

loses the contact to the SE. Thereafter, the voltage and interface resistance gradually increase until the cutoff voltage is reached.

Both the time,  $t_{\text{Kink}}$ , of the inflection point and the time,  $t_{\text{CL}}$ , when full contact loss is reached can in principle be used to calculate the effective diffusion coefficient via Sand's equation.<sup>[17,42,43]</sup> Therefore, Figure S4, Supporting Information, shows the stripping profiles of a Li-CNT30 electrode with  $50\text{--}200 \mu\text{A cm}^{-2}$ . The characteristic inflection point occurs earlier during stripping with higher current density. Calculating the effective diffusion coefficient with  $t_{\text{Kink}}$  then yields  $D_{\text{eff, Kink}} = (1.3 \pm 0.3) \times 10^{-11} \text{ cm}^2 \text{ s}^{-1}$ . This value can be understood as the effective Li diffusion coefficient of the composite electrode, which is nearly double that of pure lithium with  $D_{\text{eff, Li}} = (0.8 \pm 0.1) \times 10^{-11} \text{ cm}^2 \text{ s}^{-1}$ . Therefore, the presence of the CNTs clearly improves Li diffusion in the anode. However, as the stripping mode changes at the inflection point, from direct stripping at the LLZO surface to stripping in the 3D Li-CNT network, the conditions are no longer fulfilled to properly interpret the time until full contact is lost in the manner of the Sand's equation.

Changes in stripping are also visible in the impedance spectra acquired at 0.75 V during testing, depicted in Figure 3b. The impedance deviates from a semicircle below 30 Hz for Li-CNT30. This indicates changes of the constriction effect at the interface and therefore a difference in pore morphology. Further conclusions can be drawn from the Bode plot depicted in Figure S2, Supporting Information. After an initial emergence of the interface (constriction) resistance during stripping, its apex frequency remains roughly constant at around 2–3 kHz for Li-CNT40. In the case of pure lithium electrodes, this frequency shifts to higher frequencies at the end of the stripping process.<sup>[8]</sup> However, Li-CNT and Li-Mg both do not show the aforementioned frequency shift,<sup>[17]</sup> which is still elusive. The shift to higher frequencies observed for pure lithium electrodes may be explained by Joule heating of the few contact spots left, due to current focusing through these.<sup>[44,45]</sup> However, the contact spots after stripping Li-Mg alloys are more homogeneously distributed,<sup>[17]</sup> which should reduce the effect of Joule heating. Following this explanation, the contact spots after stripping Li-CNT electrodes should also be distributed more homogeneously as for Li-Mg when compared to lithium.

To evaluate the CNT influence on dendrite resilience, experiments on stripping and plating were carried out. Therefore,  $0.2 \text{ mAh cm}^{-2}$  were cycled in a Li-CNT30|LLZO:Ta|Li-CNT30 cell with increasing current densities (starting at  $100 \mu\text{A cm}^{-2}$  and increasing by  $100 \mu\text{A cm}^{-2}$  each step). As seen in Figure S5, Supporting Information, the cell experiences a short-circuit at around  $600 \mu\text{A cm}^{-2}$ , which is in line with previous results on similar cell designs employing pure lithium as the anode material.<sup>[10,39]</sup> Thus, no clear effect on the dendrite resilience is observed using this test protocol.

Overall, the kink in the overpotential-capacity curve during stripping Li-CNT electrodes and their different low-frequency impedance are still elusive based on the electrochemical experiments alone. To analyze the stripping and resulting pore formation in more detail, top-view and cross-sectional images of the electrodes obtained by scanning electron microscopy (SEM) are discussed in the next section.

### 2.3. Differences of Pore Formation in Lithium and Lithium–CNT Composites

To understand the kink during stripping and resulting pore formation when using composite electrodes, their morphology was imaged using electron microscopy. Figure 4 shows a schematic voltage profile for the stripping process with lithium and a composite. Shown alongside are top and cross-sectional focused-ion-beam SEM (FIB-SEM) images taken before and after depletion occurred during stripping. After depletion (contact loss, CL), the electrodes easily detach from the SE, which is not the case in the pristine state. Therefore, the surface visible in the top-view images is the face of the electrode, which previously was in contact with the LLZO.

The appearance of the as-prepared lithium and composite foils in the SEM images shown in Figure 4a,b is very similar. Both foils show a smooth surface with some bright lines, which most likely originate from the mechanical preparation. The cross-sectional images in Figure 4e,f show that both types of electrodes are free of pores. However, magnified images shown in Figure S6a,b, Supporting Information, display slight differences. It seems like curtaining and rippling, which occur during FIB-preparation,<sup>[46–48]</sup> lead to a more severe stair formation for the composite electrode. Rippling is frequently observed for carbon materials.<sup>[49–51]</sup> Furthermore, the top of the stairs shows a brighter contrast for the composite electrode, which hints at an accumulation of CNTs due to rippling and FIB-preparation.

After stripping had been performed until depletion, the surface morphologies of both electrodes deviate from each other. For pure lithium, large pores in the range of 5–15  $\mu\text{m}$  are visible in

the top-view image in Figure 4c, which correspond well to the typical morphology resulting in contact loss as observed in previous experiments.<sup>[8]</sup> On the contrary, the morphology of the stripped composite electrode displayed in Figure 4d rather shows smaller, deeper valleys in the material instead of pores at the surface. This larger pore volume is expected as around 20  $\text{mAh cm}^{-2}$  or 0.8  $\text{mm}^3$  more lithium was stripped with this electrode. Figure S6d, Supporting Information, displays a higher magnification image of a similar Li–CNT30 electrode after stripping, showing that large parts of the surface only consist of a porous, fiber-like network. This is the residual CNT framework exposed after lithium was nearly completely stripped from the composite.

Cross-sectional images were additionally taken for lithium and Li–CNT40, respectively, as depicted in Figure 4g,h. No change in bulk morphology was observed for pure lithium when compared to the pristine sample in Figure 4e and Figure S6a, Supporting Information. This indicates that the stripping process for pure lithium only takes place at the direct interface to LLZO. However, cross-sectional images of the stripped Li–CNT40 depict a large gap and smaller closed pores in the 100–500 nm range fitting to the top-view micrographs. Another micrograph shows these pores at higher magnifications in Figure S6c, Supporting Information. Pores in this range were neither present in stripped lithium electrodes nor in pristine composites as displayed in Figure 4f. This confirms that closed porosity is generated only during the stripping process of Li–CNT electrodes. Overall, the depicted (FIB)-SEM images show clear differences in dissolution, as was indicated by electrochemical analysis. In the following, we propose a stripping mechanism for these composites based on the obtained results.

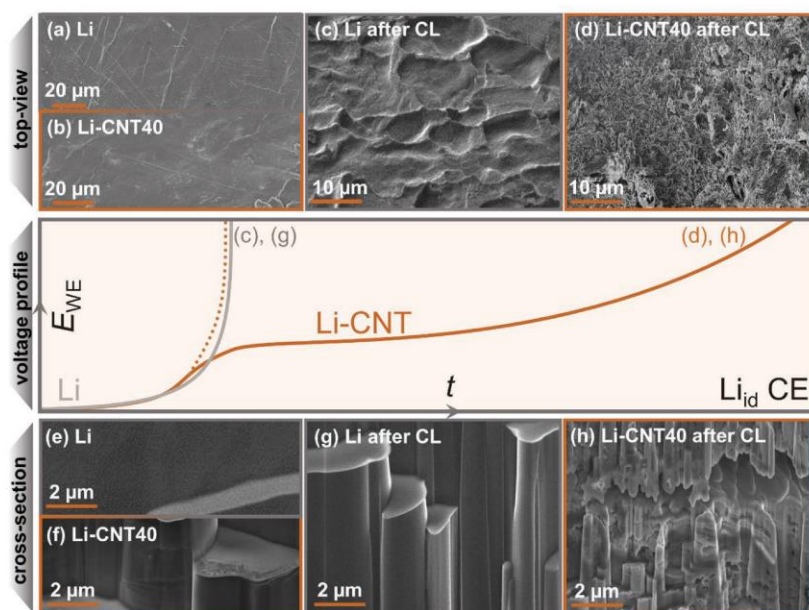


**Figure 4.** Top-view SEM images of the pristine state of a) lithium and b) Li–CNT40. Top-view SEM images of c) lithium and d) Li–CNT40 after stripping, as indicated in the scheme of the voltage profiles in the middle of the figure. Cross-sectional images obtained via cryo-FIB-SEM are depicted for lithium and Li–CNT40 in e,f) pristine state as well as g,h) after stripping, respectively.

It was shown in Figure 3 that stripping is quite similar for lithium and Li–CNT up to the point, where pure lithium shows severe polarization due to formed pores at the interface, that is, due to current constriction at the remaining contact spots. The kink in the voltage profile for Li–CNT electrodes, which indicates that the stripping mechanism changes, occurs at quite the same time. This suggests that lithium from the composite is at first dissolved during stripping at the direct interface to the SE. At the time where the kink appears, this direct interface is depleted. From that point on, the CNTs act as a contact mediator, maintaining contact to the SE and acting as a 3D distributed anode scaffold. Another effect at play could be the increased ionic conductivity of contact spots due to Joule heating,<sup>[44]</sup> which may be one explanation for the improved stripping after the kink.

The difference in pore geometry also influences the low-frequency impedance shown in Figure 2b. As the pore geometry is different, the contribution of surface diffusion of lithium atoms, which typically occurs in that frequency range, is different for lithium and the composites. This results in the more flattened semicircle for Li–CNT30. Note that stripping experiments were additionally carried out with Li-vapor grown carbon fibers (VGCF) composite electrodes. With VGCF, Figure S7, Supporting Information, shows no improvement compared to lithium. We believe that this highlights the favorable role of transport along the graphitic walls of the CNTs.

Due to the continued stripping both through and at the walls of the CNTs, lithium is dissolved also inside the bulk of the electrode and not only at the interface, leading to closed porosity as seen in Figure 4. The proposed stripping mechanism is schematically depicted in Figure 5.

While the observed change to 3D stripping for the composite electrodes leads to a higher anode utilization, mixing lithium with additives inevitably leads to a decrease in the anode's theoretical specific capacity. As these effects counteract each other, there exists an optimum in the composition of the composite electrode, which is around 30 wt% of CNTs according to the stripping profiles provided in Figure 3a. The theoretical specific capacity of Li–CNT30 then amounts to around 2819 mAh g<sup>-1</sup> of which 60% could be stripped with 100 μA cm<sup>-2</sup>. This value well surpasses alternative electrode concepts, such as porous garnet SE infiltrated with lithium metal.<sup>[20]</sup>

#### 2.4. Mechanics of Composite Anodes and Influence on Electrode Kinetics

Incorporating fibers into a ductile matrix can lead to very strong changes in the mechanical properties.<sup>[52,53]</sup> For example, Fu et al. specify that for fibers to have an impact on the strength when randomly distributed in a matrix, a critical fiber length

$$l_c = \frac{\sigma_f \cdot d}{2\tau_m} \quad (1)$$

must be exceeded.<sup>[52,54]</sup> Herein,  $\sigma_f$  and  $d$  denote the fiber tensile strength and diameter, respectively, whereas  $\tau_m$  denotes the shear yield strength of the matrix, if lower than the bonding strength between the phases. With around 5 μm, the herein used CNTs in lithium exceed the calculated  $l_c$  of 128 nm by a factor of 40. This suggests that CNTs have a large impact on the composite anode elastic and plastic properties, as already assumed from the changes in ductility noticed during sample preparation.

In another example, the elastic modulus of matrices is strongly increased by the reinforcing integration of constituents with relatively high elastic modulus, for example, by adding carbon fibers to an epoxy matrix to form carbon-reinforced composites.<sup>[55]</sup> The orientation and volume fraction of the reinforcing (higher elastic modulus) constituent is important in determining whether or not a composite has isotropic or anisotropic mechanical properties. The goal of the present study was to homogeneously disperse CNTs, thus effectively resulting in isotropic properties. However, it is possible that the homogeneity of CNT distribution decreases above a certain volume fraction of CNTs as was suggested by the unexpected deviation in electrochemical performance when increasing from 30–40 wt% CNT.

To investigate the plastic and elastic properties of the composites, compressive and tensile stress–strain testing was carried out on prepared pellets and foils, respectively. These measurements were conducted with a strain rate of 10<sup>-3</sup> mm s<sup>-1</sup> in accordance with Masias et al.<sup>[56,57]</sup> Results are depicted in Figure 6a,b.

The stress–strain curves obtained during compression show a decrease in yield strength of flow stress with increasing

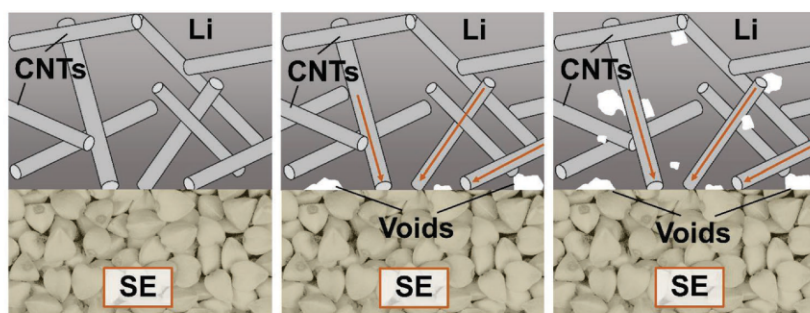


**Figure 5.** Schematic depiction of the lithium stripping process of composite anodes consisting of lithium and CNTs. During stripping, the direct interface between lithium and LLZO is first depleted as in the case of pure lithium electrodes (middle). However, instead of fully losing the contact like pure lithium, the composites allow also stripping along the remaining CNTs, which act as a contact mediator (right). Note that the pores and CNTs are not scaled 1:1 with respect to their true size.

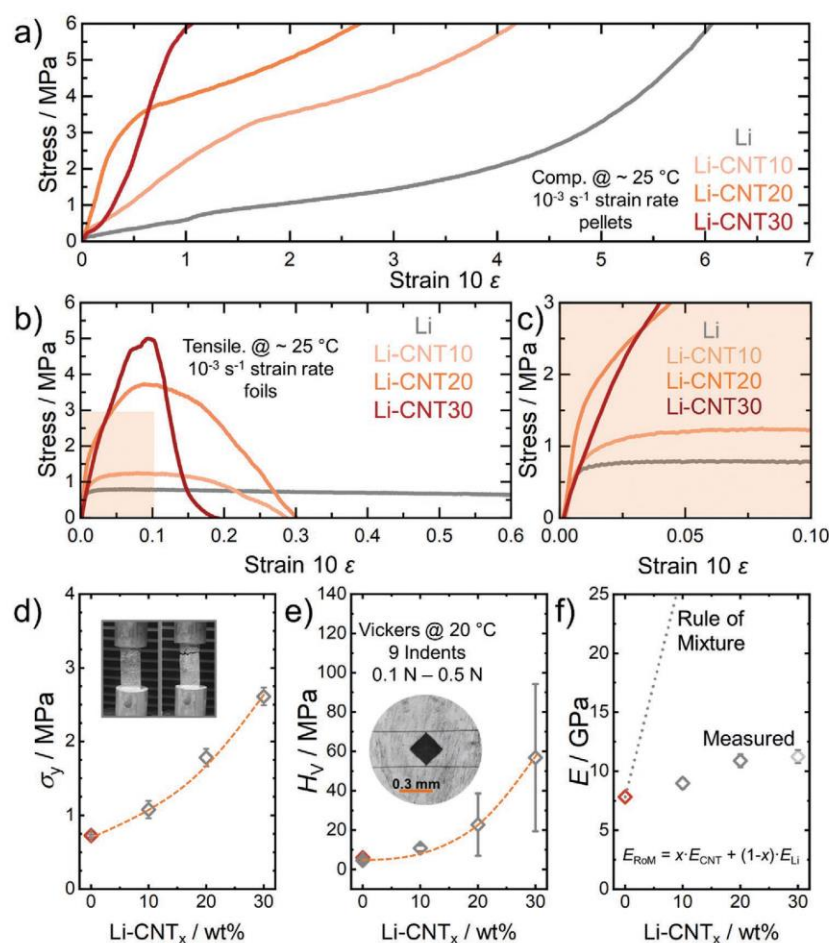


**Figure 6.** a) Compressive stress–strain results for composite pellets. b) Tensile stress–strain tests for composite foils (150  $\mu\text{m}$ ) with the orange inset enlarged in (c). Results are also shown for d) the yield strength  $\sigma_y$ , e) the Vickers hardness  $H_V$ , and f) the elastic modulus  $E$ . The inset in (d) shows an example of the mechanical tensile tests and the inset in (e) shows an indentation mark typically observed after testing of  $H_V$ . Literature values are presented as orange data points.

CNT content. In general, the stress required to increase strain increases with increasing strain. However, the data in Figure 6a are engineering strain and do not consider the increase in sample area. It appears that the characteristic yield inflection point in Figure 6a is found at higher stresses for higher amounts of CNTs. However, the initial shift in strain of the measurement for Li-CNT30, compared to the Li-CNT10 and Li-CNT20, seems to be out of the expected trend. This likely is the result of inhomogeneity within the composites at higher CNT fractions. In addition, after the initial shift in strain, the Li-CNT30 composite has approximately the same stress–strain slope as the Li-CNT20, thus indicating that point of diminishing return for the stiffness is achieved between 20 wt% and 30 wt% CNT. We refrain from including mechanical testing data on Li-CNT40, as large specimens of Li-CNT40 needed for stress–strain measurements, are too heterogeneous to afford

conclusive results for mechanical testing, even though it was possible to obtain reproducible electrochemical performance with such a large fraction of CNTs.

During tensile testing, a trend is observed with increasing CNT content that is similar to that of compression testing. The most obvious differences between the composites and pure lithium are strength maxima, which get increasingly more pronounced with higher CNT contents (up to 5 MPa for Li-CNT30). Likely, these are caused by an effect similar to molecular chain alignment in polymers during tensile testing or fiber alignment in carbon-fiber reinforced composites,<sup>[58]</sup> which arises due to originally randomly oriented CNTs in the metal matrix lining up with deformation. Such an alignment usually strengthens fiber-in-matrix composites.<sup>[52,59]</sup> However, according to Masias et al., elastic properties cannot be extracted from stress–strain measurements of lithium metal,

as plastic deformation overlaps with the elastic regime, which results in a large underestimation of the elastic modulus.<sup>[56]</sup> Creep likely affects the results as well, which is indicated by the high homologous temperature of 0.66 of lithium at room temperature.

Additionally, Figure 6c depicts the low strain-regime during tensile testing, which shows that the first inflection point in these graphs occurs at a later stage for higher CNT contents. These inflection points are interpreted as the yield strength or flow stress.<sup>[56,59]</sup> The estimated yield strength  $\sigma_y$  is summarized in Figure 6d and increases with higher CNT content. Note that the yield strength for pure lithium fits to literature values,<sup>[56]</sup> which are included as orange data points. Also shown are the Vickers hardness,  $H_V$ , in Figure 6e and estimated elastic moduli,  $E$ , in Figure 6f. The latter was obtained from acoustic measurements; please see Figure S8, Supporting Information, for more information.

Like the general stiffness of the material, both the yield strength  $\sigma_y$  and Vickers hardness  $H_V$  increase with CNT content. Note that the Vickers hardness measurement error obtained from the standard deviation is significantly higher for Li-CNT20 and Li-CNT30. This signals inhomogeneity within the samples with higher CNT content as already assumed above. In samples with 30 wt% CNT,  $\sigma_y$  and  $H_V$  increased to 2.61 and 56.8 MPa, respectively, which fits to the previously made observation that the material is mechanically strengthened by the incorporation of CNTs.

The elastic modulus  $E$  displayed in Figure 6f obtained from acoustic measurements shows a similar trend to  $H_V$  and  $\sigma_y$ . Interestingly,  $E$  does not follow the values that would be obtained from a simple rule of mixture. This underlines the assumption that the CNTs are not perfectly and homogeneously dispersed within the lithium matrix and accumulate locally, as already seen in the hardness tests. The increase in  $E$  deviates from linearity for the step between 20 and 30 wt%, yielding a lower value than expected, which strengthens this assumption. Still, an increase of  $E$  up to 11.2 GPa is observed for Li-CNT30. Note that usually single-phase or homogeneous materials are characterized using indentation and acoustic analysis of the elastic properties. However, the large area of the indent ( $200 \mu\text{m} \times 200 \mu\text{m}$ ) and the acoustic wavelength of around 6 m in lithium at 1 kHz averages the observed properties,<sup>[60]</sup> as the tubes are only 5  $\mu\text{m}$  in length.

Our results show that the mechanical properties of lithium metal can be well tailored by the addition of small quantities of CNTs. In this way, anodes can be engineered to be less sensitive to external stack pressures. To showcase this concept, a lithium and a Li-CNT30 anode were stripped for 4 h without any applied pressure. Afterward, a stack pressure of 3.0 MPa was applied and then gradually decreased until 0.5 MPa as depicted in Figure 7a. This method yields the critical stack pressure needed for an electrode material to counteract the strain induced by stripping with a certain current density.<sup>[15]</sup>

At the end of the pressure-free stripping step after 4 h, the lithium electrode shows a higher polarization. When 3.0 MPa are applied thereafter, a large decrease in polarization occurs for lithium while polarization of Li-CNT30 remains nearly constant. This is explained by the pressure-induced closing of the pores at the Li|LLZO interface, which have not yet formed at the

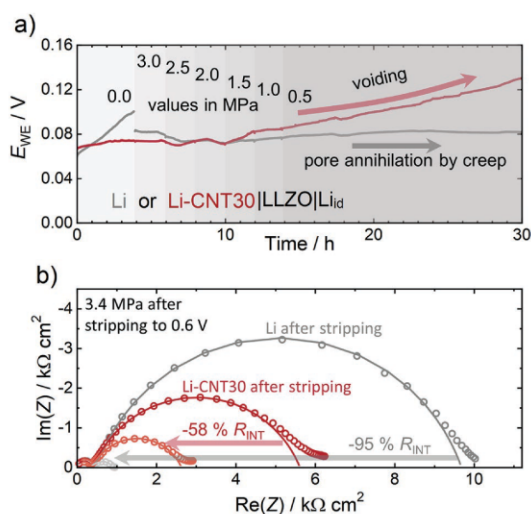


**Figure 7.** a) Voltage profiles of a lithium and a Li-CNT30 electrode during stripping with  $100 \mu\text{A cm}^{-2}$  in combination with a gradual decrease in applied stack pressure. b) Impedance spectra of both Li|LLZO|Li and Li|LLZO|Li-CNT30 directly after pressure-free stripping to 0.6 V and applying 3.4 MPa.

Li-CNT30|LLZO interface. This highlights Li-CNT30 being less dependent on and sensitive to applied stack pressures.

However, while 0.5 MPa pressure applied in the last stage during stripping seems to be enough to counteract strain-induced at  $100 \mu\text{A cm}^{-2}$  for pure lithium, an increase in voltage for the composite begins. This means that pores form, which are not annihilated by creep due to the higher resistance to plastic deformation of the composite.

The higher pressure-sensitivity of pure lithium can also be seen in the Nyquist plots depicted in Figure 7b. Here, the impedance spectra of both lithium and Li-CNT directly after stripping until 0.6 V and after applying 3.4 MPa are plotted. The decrease in  $R_{\text{INT}}$  is far larger for lithium (91%) than for Li-CNT30 (58%). The reason is that pure lithium is more easily deformed, allowing it to regain good contact to the SE. However, the pore geometry is different when considering Li-CNT composites as shown via cross-sectional imaging above. This may require higher pressures to collapse pores independent of the ductility of the material.

### 3. Conclusions

We showcase the tunability of electrochemical and mechanical properties of the lithium metal anode by manufacturing a composite material with CNTs. It is found that the areal discharge (stripping) capacity can be enhanced by a factor of  $>20$  to around  $25 \text{ mAh cm}^{-2}$  at  $100 \mu\text{A cm}^{-2}$  and low pressures ( $<1 \text{ MPa}$ ) by extending the lithium dissolution from the direct electrode|LLZO (2D) interface to the 3D Li-CNT network, albeit at higher electrode potentials  $E_{\text{WE}} > 0.5 \text{ V}$ . This amounts to about 60% of the theoretical specific capacity of  $2819 \text{ mAh g}^{-1}$  calculated for Li-CNT30. Cross-sectional

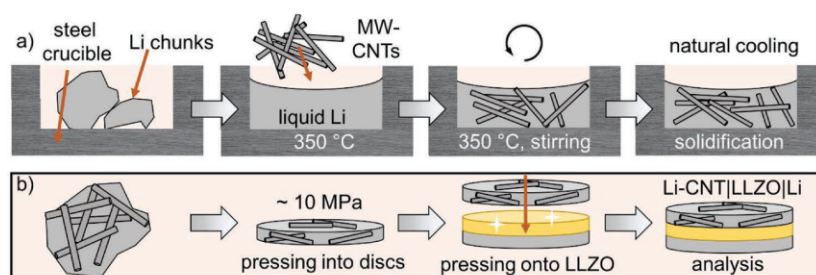


**Figure 8.** Scheme of a) the preparation route to obtain Li-CNT composites and b) electrode preparation and attachment to a polished LLZO pellet for electrochemical analysis.

micrographs obtained with cryo-FIB-SEM prove stripping within the bulk of the anode, guided by CNTs in the composite. The CNT framework clearly helps to maintain electrical contact with LLZO during stripping. Additionally, a twofold increase of the effective diffusion coefficient in the anode material to around  $D_{\text{eff}} = (1.3 \pm 0.3) \times 10^{-11} \text{ cm}^2 \text{ s}^{-1}$  for Li-CNT30 was estimated from stripping and depletion experiments. Stress-strain measurements show a decrease in the ductility of the composite based on its CNT content, which is confirmed by micro-indentation and acoustic analysis. For example, the Vickers hardness and the elastic modulus increase to nearly 60 MPa and 12 GPa, which represents an eightfold and 60% increase relative to pure lithium, respectively.

This tunability of the electrochemo-mechanical properties of the LMA presents an attractive route of tailoring the anode material to suit the requirements of practical applications. For example, Li-CNT electrodes would be suitable for high-energy applications without the possibility of applying stack pressures. As a large fraction of the available discharge capacity is only available with an overvoltage  $>0.5 \text{ V}$ , pure lithium is more suitable for high-power applications, especially when stack pressure can be applied due to its more ductile nature.

#### 4. Experimental Section

**Preparation of Solid Electrolytes and Composite Electrodes:** The nominal composition of the herein prepared LLZO:Al, based on the used precursors, was  $\text{Li}_{6.25}\text{Al}_{0.25}\text{La}_3\text{Zr}_2\text{O}_{12}$  (LLZO). First,  $\text{Li}_2\text{CO}_3$  ( $>99.0 \%$ , Sigma-Aldrich),  $\text{ZrO}_2$  (99.9%, Sigma-Aldrich),  $\text{La}(\text{OH})_3$  (99.9 %, Sigma-Aldrich), and  $\text{Al}_2\text{O}_3$  (99.8 %, abcr) were homogenized with two ball-milling steps (10 min with 20 min pause at 350 rpm, 24 cycles). Subsequent calcination of 25 mm diameter pellets was carried out in MgO-crucibles under oxygen flow (150 sccm) by heating the material up to 1000 °C, which was held for 4 h. The following steps were exclusively performed under an argon environment (MBraun,  $<0.1 \text{ ppm H}_2\text{O}$ ,  $<0.1 \text{ ppm O}_2$ ). First, to obtain small particles for sintering, the material was ball-milled with the same parameters as above for 40 cycles. Pellets were then sintered (isostatically pressed beforehand, 380 MPa) under oxygen flow in MgO-crucibles with mother powder (calcined LLZO powder). For this, samples were first heated in 9 h to 900 °C, which was held for 5 h. Thereafter, the temperature was increased in 2 h to 1100 °C and again held for 5 h. Last, in 1 h, the temperature was increased again to 1230 °C and held for 4 h, followed by a natural cooling. For CCD tests, LLZO:Ta ( $\text{Li}_{6.5}\text{La}_3\text{Ta}_{0.5}\text{Zr}_{1.5}\text{O}_{12}$ ) was used, which was prepared as previously reported by Taylor et al.<sup>[61]</sup>

Composite electrodes were prepared by homogeneously dispersing CNTs (Sigma Aldrich,  $>95\%$ ,  $6\text{--}9 \text{ nm} \times 5 \mu\text{m}$ ) into liquid lithium at 350 °C on a hotplate inside a glovebox. After solidification of the

mixture, small chunks of the material were cut off with a ceramic knife and pressed into disc electrodes with 6 mm in diameter and around 120  $\mu\text{m}$  thickness. Prepared electrodes were described, for example, with “Li-CNT30,” meaning that 30 wt% of CNTs was nominally mixed into liquid lithium. This procedure is schematically depicted in Figure 8.

**Material Characterization:** Structural characterization of LLZO was performed using a PANalytical Empyrean powder diffractometer in Bragg-Brentano  $\theta\text{--}\theta$  geometry with  $\text{Cu K}\alpha$  radiation ( $\lambda_1 = 1.5405980 \text{ \AA}$ ;  $\lambda_2 = 1.5444260 \text{ \AA}$ ;  $I(\lambda_2)/I(\lambda_1) = 0.5$ ). Measurements were carried out in the  $2\theta$  range between 20° and 80° with a step size of 0.026°. Air-sensitive samples were protected with thin Kapton foil during the measurement.

**Cell Assembly and Electrochemical Characterization:** Cells were assembled by polishing the garnet pellets with grit P1000 SiC-paper and subsequent electrode attachment. Both pure lithium and composite electrodes were freshly pressed into thin foils. As a counter electrode, a resistance-free, ideally reversible electrode  $\text{Li}_{\text{ref}}$  was prepared following previous reports utilizing high isostatic pressure (380 MPa for 30 min).<sup>[8,37]</sup> Composite electrodes were attached to the SE by a small hand-pressing tool under an applied torque of 10 N m. Cells used for testing the CCD were prepared by polishing the Ta:LLZO following the procedures of Sharafi et al.<sup>[39]</sup> and then heat treating and applying lithium electrodes following the procedures of Wang et al.<sup>[15]</sup>

Electrochemical characterization was carried out using a VMP300 potentiostat by BioLogic in combination with the software EC-Lab (V. 11). Temperature dependent measurements were carried out in a climate chamber WKL 64 by WEISS. For electrochemical measurements, cells were contacted with nickel current collector tabs and sealed in pouch cells. The current collector tabs were fixed using small clamps to secure contact to the electrodes. Please note, however, that by the use of this setup, the clamps exerted a small pressure ( $<1 \text{ MPa}$ ) to maintain the current collectors in place, which was much lower than reported before and was therefore addressed here as pressure-free.

If not stated otherwise, potentiostatic electrochemical impedance spectroscopy (PEIS) measurements were carried out in the frequency range between 7 MHz and 100 mHz. GEIS measurements were carried out in a different frequency range, 7 MHz–1 Hz, as acquisition of one spectrum needed to be faster in this measurement mode to not disturb the DC current. Usually, 10% of the DC current was used as amplitude to measure the impedance response of the cell. Impedance data interpretation as well as fitting thereof was carried out with RelaxIS 3 software by RhD Instruments.

**FIB-SEM Measurements:** FIB-SEM imaging was carried out using a XEIA3 GMU SEM/Plasma-FIB (Tescan) in combination with a Leica VCT500 transfer module and liquid nitrogen cooling stage. SEM imaging was also carried out using a Zeiss Merlin HRSEM.

**Mechanical Property Characterization:** Mechanical property testing was carried out in an argon-filled glovebox using an Instron 5944 Universal Testing System. The compression tests were carried out according to Masias et al. with a strain rate of  $10^{-3} \text{ s}^{-1}$ .<sup>[56]</sup> To mitigate friction between the sample and the testing device, mineral oil was used as coupling agent. Tensile tests were also carried out using the strain rate of  $10^{-3} \text{ s}^{-1}$ .

Samples were fixed onto the testing device using acrylate-based adhesive. Note that for all graphs the engineering strain was used, which was calculated based on the initial cross-sectional area of the sample.

Both testing of the Vickers hardness and acoustic measurements were performed in a dry room on lithium foil ( $T_d < -50^\circ\text{C}$ ). The micro-indentation tests were carried out with a Vickers hardness tester (HM122V/K Series 810 Micro, Mitutoyo Corporation) using 0.01–0.05 kgf to indent 200  $\mu\text{m}$  thick anode foils, which were previously rolled using a calendaring machine (Creative and Innovative System Corporation). Pulse echo acoustic measurements were carried out using Olympus 5073R Pulser/Receiver (P/R) paired with a Picoscope 2207A PC-based oscilloscope. Longitudinal wave speeds were measured using an Olympus M110-RM contact transducer with mineral oil as a coupling agent to the sample.

### Supporting Information

Supporting Information is available from the Wiley Online Library or from the author.

### Acknowledgements

The authors want to thank Dr. Boris Mogwitz for help with FIB-SEM measurements. This work was conducted as part of the US–German joint collaboration on “Interfaces and Interphases in Rechargeable Li-metal-based Batteries” supported by the US Department of Energy (DOE) and German Federal Ministry of Education and Research (BMBF). This work has been partly funded by the German Federal Ministry of Education and Research (BMBF) under the project “LiSI,” grant identifier 03XP0224E. Financial support from the DOE under the project “CatSE,” grant number DE-AC05-000R22275, is acknowledged.

Open access funding enabled and organized by Projekt DEAL.

### Conflict of Interest

The authors declare no conflict of interest.

### Data Availability Statement

The data that support the findings of this study are available from the corresponding author upon reasonable request.

### Keywords

carbon nanotubes, composite lithium-anodes, diffusion, mechanical properties, three-dimensional lithium dissolution

Received: April 1, 2022

Revised: April 25, 2022

Published online:

- [1] J. Janek, W. G. Zeier, *Nat. Energy* **2016**, *1*, 16141.
- [2] S. Randau, D. A. Weber, O. Kötz, R. Koerver, P. Braun, A. Weber, E. Ivers-Tiffée, T. Adermann, J. Kulisch, W. G. Zeier, F. H. Richter, J. Janek, *Nat. Energy* **2020**, *5*, 259.
- [3] Y. Lee, S. Fujiki, C. Jung, N. Suzuki, N. Yashiro, R. Omoda, D. Ko, T. Shiratsuchi, T. Sugimoto, S. Ryu, J. H. Ku, T. Watanabe, Y. Park, Y. Aihara, D. Im, I. T. Han, *Nat. Energy* **2020**, *5*, 299.
- [4] T. Krauskopf, F. H. Richter, W. G. Zeier, J. Janek, *Chem. Rev.* **2020**, *120*, 7745.

- [5] Y. Zhu, X. He, Y. Mo, *ACS Appl. Mater. Interfaces* **2015**, *7*, 23685.
- [6] Y. Chen, Z. Wang, X. Li, X. Yao, C. Wang, Y. Li, W. Xue, D. Yu, S. Y. Kim, F. Yang, A. Kushima, G. Zhang, H. Huang, N. Wu, Y. W. Mai, J. B. Goodenough, J. Li, *Nature* **2020**, *578*, 251.
- [7] C. Niu, H. Lee, S. Chen, Q. Li, J. Du, W. Xu, J. G. Zhang, M. S. Whittingham, J. Xiao, J. Liu, *Nat. Energy* **2019**, *4*, 551.
- [8] T. Krauskopf, H. Hartmann, W. G. Zeier, J. Janek, *ACS Appl. Mater. Interfaces* **2019**, *11*, 14463.
- [9] T. Krauskopf, B. Mogwitz, H. Hartmann, D. K. Singh, W. G. Zeier, J. Janek, *Adv. Energy Mater.* **2020**, *10*, 2000945.
- [10] E. Kazyak, S. William, C. Haslam, J. Sakamoto, N. P. Dasgupta, E. Kazyak, R. Garcia-mendez, W. S. Lepage, A. Sharafi, A. L. Davis, A. J. Sanchez, K. Chen, C. Haslam, J. Sakamoto, N. P. Dasgupta, *Matter* **2020**, *2*, 1025.
- [11] I. Seymour, A. Aguadero, *J. Mater. Chem. A* **2021**, *9*, 19901.
- [12] S. S. Shishvan, N. A. Fleck, V. S. Deshpande, *J. Power Sources* **2021**, *488*, 229437.
- [13] U. Roy, N. A. Fleck, V. S. Deshpande, *Extreme Mech. Lett.* **2021**, *46*, 101307.
- [14] J. Janek, S. Majoni, *Ber. Bunsen-Ges. Phys. Chem.* **1995**, *99*, 14.
- [15] M. J. Wang, R. Choudhury, J. Sakamoto, *Joule* **2019**, *3*, 2165.
- [16] X. Zhang, Q. J. Wang, K. L. Harrison, S. A. Roberts, S. J. Harris, *Cell Rep. Phys. Sci.* **2019**, *1*, 100012.
- [17] T. Krauskopf, B. Mogwitz, C. Rosenbach, W. G. Zeier, J. Janek, *Adv. Energy Mater.* **2019**, *9*, 1902568.
- [18] G. T. Hitz, D. W. McOwen, L. Zhang, Z. Ma, Z. Fu, Y. Wen, Y. Gong, J. Dai, T. R. Hamann, L. Hu, E. D. Wachsman, *Mater. Today* **2019**, *22*, 50.
- [19] S. Xu, D. W. McOwen, C. Wang, L. Zhang, W. Luo, C. Chen, Y. Li, Y. Gong, J. Dai, Y. Kuang, C. Yang, T. R. Hamann, E. D. Wachsman, L. Hu, *Nano Lett.* **2018**, *18*, 3926.
- [20] C. Wang, Y. Gong, B. Liu, K. Fu, Y. Yao, E. Hitz, Y. Li, J. Dai, S. Xu, W. Luo, E. D. Wachsman, L. Hu, *Nano Lett.* **2017**, *17*, 565.
- [21] K. K. Fu, Y. Gong, B. Liu, Y. Zhu, S. Xu, Y. Yao, W. Luo, C. Wang, S. D. Lacey, J. Dai, Y. Chen, Y. Mo, E. Wachsman, L. Hu, *Sci. Adv.* **2017**, *3*, e1601659.
- [22] H. Xie, C. Yang, Y. Ren, S. Xu, T. R. Hamann, D. W. Mcowen, E. D. Wachsman, L. Hu, *Nano Lett.* **2021**, *21*, 6163.
- [23] A. Sharafi, E. Kazyak, A. L. Davis, S. Yu, T. Thompson, D. J. Siegel, N. P. Dasgupta, J. Sakamoto, *Chem. Mater.* **2017**, *29*, 7961.
- [24] N. Nitta, G. Yushin, *Part. Part. Syst. Charact.* **2014**, *31*, 317.
- [25] D. Lin, Y. Liu, Z. Liang, H. W. Lee, J. Sun, H. Wang, K. Yan, J. Xie, Y. Cui, *Nat. Nanotechnol.* **2016**, *11*, 626.
- [26] J. Zhao, G. Zhou, K. Yan, J. Xie, Y. Li, L. Liao, Y. Jin, K. Liu, P. C. Hsu, J. Wang, H. M. Cheng, Y. Cui, *Nat. Nanotechnol.* **2017**, *12*, 993.
- [27] H. Chen, Y. Yang, D. T. Boyle, Y. K. Jeong, R. Xu, L. S. de Vasconcelos, Z. Huang, H. Wang, H. Wang, W. Huang, H. Li, J. Wang, H. Gu, R. Matsumoto, K. Motohashi, Y. Nakayama, K. Zhao, Y. Cui, *Nat. Energy* **2021**, *6*, 790.
- [28] A. S. Cavanagh, C. A. Wilson, A. W. Weimer, S. M. George, *Nanotechnology* **2009**, *20*, 255602.
- [29] Y. Maniwa, R. Fujiwara, H. Kira, H. Tou, E. Nishibori, M. Takata, M. Sakata, A. Fujiwara, X. Zhao, S. Iijima, S. Iijima, Y. Ando, *Phys. Rev. B: Condens. Matter Mater. Phys.* **2001**, *64*, 731051.
- [30] A. N. Popova, *Coke Chem.* **2017**, *60*, 361.
- [31] B. E. Warren, *Phys. Rev.* **1941**, *59*, 693.
- [32] S. Schweidler, L. De Biasi, A. Schiele, P. Hartmann, T. Brezesinski, J. Janek, *J. Phys. Chem. C* **2018**, *122*, 8829.
- [33] V. Petkov, A. Timmons, J. Camardese, Y. Ren, *J. Phys.: Condens. Matter* **2011**, *23*, 435003.
- [34] Y. Shao, H. Wang, Z. Gong, D. Wang, B. Zheng, J. Zhu, Y. Lu, Y. S. Hu, X. Guo, H. Li, X. Huang, Y. Yang, C. W. Nan, L. Chen, *ACS Energy Lett.* **2018**, *3*, 1212.
- [35] J. Duan, Y. Zheng, W. Luo, W. Wu, T. Wang, Y. Xie, S. Li, J. Li, Y. Huang, *Natl. Sci. Rev.* **2020**, *7*, 1208.

- [36] D. N. Futaba, T. Yamada, K. Kobashi, M. Yumura, K. Hata, *J. Am. Chem. Soc.* **2011**, *133*, 5716.
- [37] T. Fuchs, B. Mogwitz, S. Otto, S. Passerini, F. H. Richter, J. Janek, *Batteries Supercaps* **2021**, *4*, 1145.
- [38] J. T. S. Irvine, D. C. Sinclair, A. R. West, *Adv. Mater.* **1990**, *2*, 132.
- [39] A. Sharafi, C. G. Haslam, R. D. Kerns, J. Wolfenstine, J. Sakamoto, *J. Mater. Chem. A* **2017**, *5*, 21491.
- [40] Y. Matsuki, K. Noi, M. Deguchi, A. Sakuda, A. Hayashi, M. Tatsumisago, *J. Electrochem. Soc.* **2019**, *166*, A5470.
- [41] P. Albertus, S. Babinec, S. Litzelman, A. Newman, *Nat. Energy* **2018**, *3*, 16.
- [42] H. J. S. Sand, *London, Edinburgh Dublin Philos. Mag. J. Sci.* **1901**, *1*, 45.
- [43] L. Stolz, G. Homann, M. Winter, J. Kasnatscheew, *Mater. Today* **2021**, *44*, 9.
- [44] R. D. Rogler, H. Löbl, J. Schmidt, *Eur. Trans. Electr. Power* **1997**, *7*, 331.
- [45] K. D. Kim, D. D. L. Chung, *J. Electron. Mater.* **2002**, *31*, 933.
- [46] T. H. Loeber, B. Laegel, S. Wolff, S. Schuff, F. Balle, T. Beck, D. Eifler, J. H. Fitschen, G. Steidl, *J. Vac. Sci. Technol., B: Nanotechnol. Microelectron.: Mater., Process., Meas., Phenom.* **2017**, *35*, 06GK01.
- [47] F. Santoro, E. Neumann, G. Panaitov, A. Offenhäusser, *Microelectron. Eng.* **2014**, *124*, 17.
- [48] S. Liu, L. Sun, J. Gao, K. Li, *J. Microsc.* **2018**, *272*, 3.
- [49] D. P. Adams, T. M. Mayer, M. J. Vasile, K. Archuleta, *Appl. Surf. Sci.* **2006**, *252*, 2432.
- [50] G. Ran, J. Zhang, Q. Wei, S. Xi, X. Zu, L. Wang, *Appl. Phys. Lett.* **2009**, *94*, 2007.
- [51] I. Koponen, M. Hautala, O. P. Sievänen, *Phys. Rev. Lett.* **1997**, *78*, 2612.
- [52] W. D. Callister, *Materials Science and Engineering: An Introduction*, 8th ed., Wiley, Hoboken, NJ, USA **2009**.
- [53] P. Barai, G. J. Weng, *Int. J. Plast.* **2011**, *27*, 539.
- [54] S.-Y. Fu, B. Lauke, *Compos. Sci. Technol.* **1996**, *56*, 1179.
- [55] I. J. Beyerlein, S. L. Phoenix, *Compos. Sci. Technol.* **1996**, *56*, 75.
- [56] A. Masias, N. Felten, R. Garcia-Mendez, J. Wolfenstine, J. Sakamoto, *J. Mater. Sci.* **2018**, *54*, 2585.
- [57] A. Masias, N. Felten, J. Sakamoto, *J. Mater. Res.* **2021**, *36*, 729.
- [58] W. S. LePage, Y. Chen, E. Kazyak, K.-H. Chen, A. J. Sanchez, A. Poli, E. M. Arruda, M. D. Thouless, N. P. Dasgupta, *J. Electrochem. Soc.* **2019**, *166*, A89.
- [59] P. K. Mallick, *Fiber-Reinforced Composites*, Taylor & Francis Group, LLC, Boca Raton, FL, USA **2007**.
- [60] E. G. Herbert, S. A. Hackney, V. Thole, N. J. Dudney, P. S. Phani, *J. Mater. Res.* **2018**, *33*, 1347.
- [61] N. J. Taylor, S. Stangeland-Molo, C. G. Haslam, A. Sharafi, T. Thompson, M. Wang, R. Garcia-Mendez, J. Sakamoto, *J. Power Sources* **2018**, *396*, 314.

### 3.5 Publication 5: “Working Principle of an Ionic Liquid Interlayer During Pressureless Lithium Stripping on $\text{Li}_{6.25}\text{Al}_{0.25}\text{La}_3\text{Zr}_2\text{O}_{12}$ (LLZO) Garnet-Type Solid Electrolyte”

In publication 5 of this dissertation, an IL interlayer between the LMA and SE was investigated regarding its ability to either suppress or compensate the pore formation during anodic dissolution, which imposes severe limitations during cell operation.

Therefore, a very small amount of 5 – 10  $\mu\text{L}$  of IL was distributed on the SE surface. Subsequently, lithium was attached without the use of an additional separator material. In combination with an ideal reference and counter electrode,<sup>32</sup> the stripping performance and impedance of  $\text{Li}|\text{IL}|\text{SE}$  working electrodes was analyzed.

The combination of cryogenic FIB-SEM imaging with operando GEIS then allows to follow and interpret the morphological evolution of the  $\text{Li}|\text{IL}|\text{SE}$  system during stripping. It could be shown that only a few  $\mu\text{L}$  of IL are sufficient to increase the anodic stripping capacity from only 1.2  $\text{mAh cm}^{-2}$  for lithium to  $> 15 \text{ mAh cm}^{-2}$  without severe overpotentials. Morphological investigations reveal that the pore formation within the lithium metal is not mitigated by the IL but rather compensated due to its ability to freely flow. This mechanism also explains the observation that less viscous ILs are better at filling pores and acting as a contact mediator at the interface to the LMA.

While it is academically valid to strictly limit oneself to all-solid-state batteries, this work discusses an interesting opportunity to utilize small additions of liquids as a facile fix for issues solely originating from the solid nature of the electrolyte. Additionally, as only microliters of low-vapor pressure IL are used, the initial advantages of SSBs over LIBs are not diminished in any way. ILs are not flammable and using only  $\mu\text{L}$ s still prevents leakages or outgassing.

T. Fuchs designed and conducted all of the experiments supervised by Dr. F. H. Richter and Prof. J. Janek. Prof. S. Passerini initiated this work by introducing this system in a previous work of his group.<sup>126</sup> Measurements performed at the XPS and FIB-SEM and related scientific discussions were supported by Dr. B. Mogwitz and Dr. S.-K. Otto. All authors contributed to the scientific discussion. The original draft was written by T. Fuchs and edited by all co-authors.

# Working Principle of an Ionic Liquid Interlayer During Pressureless Lithium Stripping on $\text{Li}_{6.25}\text{Al}_{0.25}\text{La}_3\text{Zr}_2\text{O}_{12}$ (LLZO) Garnet-Type Solid Electrolyte

Till Fuchs,<sup>[a, b]</sup> Boris Mogwitz,<sup>[a, b]</sup> Svenja-Katharina Otto,<sup>[a]</sup> Stefano Passerini,<sup>[c, d]</sup>  
Felix H. Richter,<sup>\*[a, b]</sup> and Jürgen Janek<sup>\*[a, b]</sup>

Solid-state-batteries employing lithium metal anodes promise high theoretical energy and power densities. However, morphological instability occurring at the lithium/solid–electrolyte interface when stripping and plating lithium during cell cycling needs to be mitigated. Vacancy diffusion in lithium metal is not sufficiently fast to prevent pore formation at the interface above a certain current density during stripping. Applied pressure of several MPa can prevent pore formation, but this is not conducive to practical application. This work investigates the concept of ionic liquids as “self-adjusting” interlayers to compensate morphological changes of the lithium anode while avoiding the use of external pressure. A clear improvement of

the lithium dissolution process is observed as it is possible to continuously strip more than 70  $\mu\text{m}$  lithium (i. e., 15  $\text{mAh cm}^{-2}$  charge) without the need for external pressure during assembly and electrochemical testing of the system. The impedance of the investigated electrodes is analyzed in detail, and contributions of the different interfaces are evaluated. The conclusions are corroborated with morphology studies using cryo-FIB-SEM and chemical analysis using XPS. This improves the understanding of the impedance response and lithium stripping in electrodes employing liquid interlayers, acting as a stepping-stone for future optimization.

## 1. Introduction

Using lithium metal as anode material may significantly increase the gravimetric and volumetric energy densities of battery cells due to its high specific capacity ( $3861 \text{ mAh g}^{-1}$ ,  $2062 \text{ mAh cm}^{-3}$ ) as well as low redox potential ( $-3.04 \text{ V}$  vs. SHE).<sup>[1,2]</sup> However, chemical degradation as well as morphological issues such as dendrite and pore formation are hindering the application of lithium metal anodes (LMAs) in conventional systems.<sup>[3–7]</sup> Hybrid battery systems (HBSs) may enable the use of LMAs by attenuating the mentioned issues.<sup>[8–10]</sup> While liquid electrolytes (LEs) can compensate chemo-mechanical problems

of electrode materials common when using inorganic solid electrolytes (ISEs) without the application of pressure,<sup>[11–13]</sup> ISEs promise better chemical stability, safety and the capability of suppressing dendrite formation.<sup>[14–16]</sup> While HBSs are promising, there is an additional interface present in the battery when combining different electrolytes, which may lead to the formation of highly resistive interphases.<sup>[8,17]</sup>

Both Randau et al. and Albertus et al. conclude that a high areal capacity of  $>5 \text{ mAh cm}^{-2}$  is necessary for a cell to be viable for future applications.<sup>[18,19]</sup> Currently, this goal is not met by ISEs. Only about  $1.2 \text{ mAh cm}^{-2}$  were achieved when using a LMA in combination with an ISE for the electro-dissolution (stripping) process at room temperature when using planar oxide ISEs.<sup>[20]</sup> Employing 3D-anodes in combination with oxide ISEs enables cycling with  $3.26 \text{ mAh cm}^{-2}$ .<sup>[21]</sup> Polymer-based SEs enable the reversible stripping and plating of more than  $2 \text{ mAh cm}^{-2}$  with PEO-based cells at  $70^\circ\text{C}$ – $80^\circ\text{C}$ .<sup>[22]</sup> Note that all cited examples rely on high pressures in the MPa range either when preparing the anode or during cycling of the cell. Hence, no lithium metal anode based on ISEs as yet fulfils the requirements for competitive cell setups.

One limiting factor in most systems is a high internal cell resistance, which ideally should be as low as possible to enable practical power densities. Krauskopf et al. were already able to show via microelectrode studies that the charge transfer between a garnet ISE (LLZO) and the LMA is inherently fast and not rate-limiting.<sup>[23]</sup> Interfacial resistances measured in macroscopic cells can rather be interpreted as constriction resistances, as full contact between the LMA and ISE is prevented by pores and surface contaminations.<sup>[20,23,24]</sup> It was furthermore observed that insufficient vacancy diffusion in lithium itself

[a] T. Fuchs, Dr. B. Mogwitz, S.-K. Otto, Dr. F. H. Richter, Prof. J. Janek  
Institute of Physical Chemistry  
Justus-Liebig-University Giessen  
Heinrich-Buff-Ring 17, 35392 Giessen, Germany  
E-mail: felix.h.richter@phys.chemie.uni-giessen.de  
juergen.janek@phys.chemie.uni-giessen.de

[b] T. Fuchs, Dr. B. Mogwitz, Dr. F. H. Richter, Prof. J. Janek  
Center for Materials Research (ZfM)  
Justus-Liebig-University Giessen  
Heinrich-Buff-Ring 16, 35392 Giessen, Germany

[c] Prof. S. Passerini  
Helmholtz Institute Ulm  
Helmholtzstraße 11, 89081 Ulm, Germany

[d] Prof. S. Passerini  
Karlsruhe Institute of Technology (KIT)  
P.O. Box 3640, 76021 Karlsruhe, Germany

Supporting information for this article is available on the WWW under <https://doi.org/10.1002/batt.202100015>

© 2021 The Authors. Batteries & Supercaps published by Wiley-VCH GmbH. This is an open access article under the terms of the Creative Commons Attribution Non-Commercial NoDerivs License, which permits use and distribution in any medium, provided the original work is properly cited, the use is non-commercial and no modifications or adaptations are made.

limits its performance under anodic currents. Pore formation at the Li|ISE interface leads to increasing resistance due to a loss of contact, thus limiting the available areal capacity.<sup>[20]</sup> While high stack pressures (35 MPa and above) suppress pore formation by plastic deformation of the LMA, future work should investigate concepts of mitigating this issue without the necessity of high external pressure, as this is deemed unviable for large-scale applications.

Essentially, two mechanisms increase the internal cell resistance: detrimental side reactions between lithium and most common solid as well as liquid electrolytes,<sup>[25–27]</sup> and current constriction by pore formation when stripping at the LMA.<sup>[20,28]</sup> While lithium deposition<sup>[29–31]</sup> and in parts also dissolution<sup>[32]</sup> are well investigated in classic liquid electrolytes, it is not clear if established concepts can be transferred to HBS. One way to prevent loss of contact during pressureless stripping may be by employing a thin layer of LE between the solid components of a cell as a “self-adjusting” contact mediator, kept at the interface by cohesive and adhesive forces. Not only the morphological instability of the LMA, but also state-of-charge dependent volume changes of electrode materials in general, could be attenuated or compensated without pressure application.

In recent studies by Pervez et al. an ionic liquid electrolyte (ILE, Py<sub>14</sub>FSI with LiTFSI) was already employed alongside garnet electrolytes in symmetric and full cells.<sup>[33,34]</sup> It was shown that the interfacial resistance between the separator and both electrodes could be reduced by a factor of 10. The reduced interfacial resistance enabled stable cycling with 0.3 mA cm<sup>-2</sup> in symmetrical Li|ILE|ISE|ILE|Li cells. In a similar study, cycling of a cell combining an ISE (LLZO-based) and a soft gel electrolyte (GE, PVDF–HFP membrane in combination with LiPF<sub>6</sub> dissolved in a 1:1 mixture of ethylene carbonate and diethyl carbonate) was performed by Liu et al.<sup>[35]</sup> The GE was used as a means to increase wetting between the solid materials, which reduced the interfacial resistance to 214 Ω cm<sup>2</sup> (Li|GE) and to 248 Ω cm<sup>2</sup> (GE|cathode) by orders of magnitude. Employing soft/liquid interlayers between garnet SE and LMAs, the authors explain their success by an improved ionic contact between separator and anode, filling gaps with soft material. However, only short plating and stripping cycles were utilized, and neither was the stripping behavior investigated in detail during cycling nor was the morphology of the LMA observed over an extended period of time. Short stripping and plating experiments are essential to get a quick overview of the viability and longevity of cell setups, but understanding possible failure mechanisms requires long-term experiments.

Naturally, the electrolytes, solid as well as liquid, used in a hybrid battery setup must be chosen with care. Chemical compatibility, sufficient Li<sup>+</sup>-conductivity (>0.5 mS cm<sup>-1</sup>) and good wetting are of utmost importance for cell performance. For our study, we chose the ionic liquid electrolyte Py<sub>14</sub>TFSI, because the extremely low vapor pressure of ILEs<sup>[36,37]</sup> enables post-mortem cell-analysis by UHV-methods. The viscosity of these ILEs can also be tuned by changing the conducting salt concentration.<sup>[33,38]</sup> As a model ISE, Li<sub>6.25</sub>Al<sub>0.25</sub>La<sub>3</sub>Zr<sub>2</sub>O<sub>12</sub> (LLZO) was used as it is chemically compatible with LMAs and can be

prepared with very low porosities. Therefore, detrimental side reactions can be excluded when ISE comes in contact with lithium, which would not be possible with other common ISE, such as thiophosphates or polymers.<sup>[39–41]</sup>

This work investigated a hybrid cell concept employing ionic liquid electrolyte Py<sub>14</sub>TFSI with LiTFSI as an interlayer between inorganic solid electrolyte LLZO and a lithium metal anode. Use of the ionic liquid interlayer enables a pressureless and self-adjusting compensation of pore formation when stripping lithium as shown by electrochemical impedance spectroscopy, cell cycling and morphological studies via electron microscopy of cross-sections prepared by focused ion beam sputtering. Pore formation is compensated to a limited extent, which enables a pressureless and large continuous stripping capacity.

## Experimental Section

### Preparation of Used Electrolytes

The exact composition of the herein prepared LLZO, based on the used precursors, was Li<sub>6.25</sub>Al<sub>0.25</sub>La<sub>3</sub>Zr<sub>2</sub>O<sub>12</sub>. A solid-state synthesis utilizing high temperature sintering in oxygen atmosphere was used.<sup>[20]</sup> Therefore, the precursors were homogenized first with two ball-milling steps (10 min with 20 min pause at 350 rpm, 24 cycles). Subsequent calcination was carried out in MgO-crucibles under dry oxygen atmosphere. The material was pressed beforehand to secure good contact. The pellets were then heated up in 10 hours to 1000 °C, which was held for 4 hours under an oxygen flow of 150 sccm. Every following step was exclusively performed under an argon environment (MBraun glovebox, <0.1 ppm H<sub>2</sub>O, <1 ppm O<sub>2</sub>). First, the material was ball-milled again with the same parameters as above for 40 cycles to obtain small particles for sintering. The sintering was carried out with pellets (isostatically pressed beforehand, 380 MPa) under dry oxygen in MgO-crucibles with mother powder (calcined LLZO powder). Pellets were first heated in 9 hours to 900 °C, which was held for 5 hours. Afterward, the temperature was raised in 2 hours to 1100 °C and again held for 5 hours. Lastly, in 1 hour, the temperature was increased again to 1230 °C and held for 4 hours, followed by a slow cooling. The pellets were then freed of the mother powder in the glovebox, measuring a thickness of around 2 mm and a diameter of 8.2 mm.

Ionic liquid electrolytes (ILE) were prepared by adding 0.25, 0.75, 1.25 or 1.75 mol L<sup>-1</sup> LiTFSI (Lithium bis(trifluoromethanesulfonyl) imide, lolitec, 99%) conducting salt under constant stirring with a magnetic stir bar to Py<sub>14</sub>TFSI (1-Butyl-1-methylpyrrolidinium bis(trifluoromethanesulfonyl)-imide, lolitec, 99%, <150 ppm H<sub>2</sub>O). LiTFSI was dried beforehand under vacuum at 120 °C for 12 hours. All procedures were carried out in an argon environment (MBraun glovebox, <0.1 ppm H<sub>2</sub>O, <0.1 ppm O<sub>2</sub>).

### Materials Characterization

X-ray diffraction of the herein prepared LLZO was performed using a PANalytical Empyrean powder diffractometer in Bragg-Brentano 0-0 geometry with copper K<sub>α</sub> radiation ( $\lambda_1 = 1.5405980 \text{ \AA}$ ;  $\lambda_2 = 1.5444260 \text{ \AA}$ ;  $I(\lambda_2)/I(\lambda_1) = 0.5$ ). To exclude reactions with ambient atmosphere, samples were sealed air-tight with capton foil. Measurements were carried out in the 2 $\theta$  range between 20° and 100° with a step size of 0.026°. Used Py<sub>14</sub>TFSI was characterized regarding its water content using the Karl-Fischer-titration method

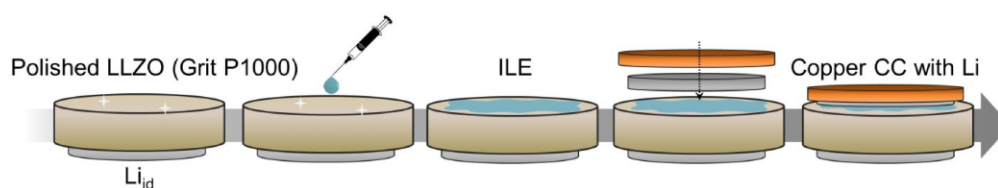


**Figure 1.** Schematic of the cell assembly process. Starting point is a garnet pellet with one ideally reversible lithium electrode at the bottom and a polished surface at the other side. Ideally reversible lithium electrodes ( $\text{Li}_d$ ) were prepared with 380 MPa isostatic pressure.<sup>[20]</sup>

in a glovebox. Their viscosity was obtained by utilizing the Rheometer R/S plus by Brookfield. The distance between sample holder and cone was set to 0.0497 mm, as a C-50 cone was used. Furthermore, confocal microscopy was carried out on LMAs by preparing them airtight inside a glovebox in a home-made setup. Imaging was carried out by a PLu neox 3D optical profiler (Sensorfar).

#### Cell Assembly and Electrochemical Characterization

First, lithium foil was prepared freshly by flattening a small chunk of lithium which was freed of surface layers in a press to obtain a thickness of approximately 100  $\mu\text{m}$ . Symmetric cells with two (ideally) reversible lithium electrodes ( $\text{Li}_d$ ) were prepared by isostatically pressing lithium foil on LLZO with 380 MPa, as reported by Krauskopf et al.<sup>[20]</sup> After confirming negligible interfacial resistance between lithium and LLZO, one lithium electrode was scraped off to be replaced by the  $\text{Li}|\text{ILE}$  system. Therefore, the garnet pellet was polished with SiC sanding paper (P500 followed by P1000). Afterward, one droplet of ionic liquid was placed into the middle of the prepared pellet. The droplet was generated by submerging a small tip into the ILE and pulling it out, creating the droplet by its surface tension. Less than 1  $\mu\text{L}$  of ILE were used per 0.3  $\text{cm}^2$  interface area, which is estimated by evaluating FIB-SEM images (see Results and Discussion). Subsequently, a freshly prepared lithium foil ( $d=6$  mm) was placed on top of the ILE and covered with a sheet of copper ( $d=8$  mm) as the current collector (CC). The described cell building procedure is schematically depicted in Figure 1.

Electrochemical characterization was carried out using either a VMP300 or SP300 potentiostat by BioLogic in combination with the software EC-Lab (version 11). Temperature dependent measurements were carried out in a climate chamber WKL 64 by WEISS. For electrochemical measurements, pellets were contacted with nickel current collectors and sealed in pouch cells or alternatively measured directly in the glovebox using a home-made setup, as described in a previous publication.<sup>[20]</sup> As both used setups do not apply pressure, their respective influence should be negligible.

Potentiostatic electrochemical impedance spectroscopy (PEIS) measurements were carried out in the frequency range between 7 MHz and 100 mHz, if not stated differently. Galvanostatic EIS (GEIS) measurements were carried out in a different frequency range, 7 MHz to 1 Hz, as spectra acquisition needs to be faster in this measurement mode to not disturb the DC experiment. Typically, the current amplitude for measuring the impedance was set to 10% of the DC current applied to the cell. This yields a sufficient quality in impedance data while also not disturbing the DC experiment too much. Impedance data interpretation as well as fitting thereof was carried out by RelaxIS 3 by RhD Instruments. As the resistances of the different processes fitted herein differ substantially, a proportional weighing method was used to fit the spectra.

#### FIB-SEM and EDX Measurements

FIB-SEM imaging was carried out using a XEIA3 GMU SEM/Plasma-FIB (Tescan) in combination with a Leica VCT500 transfer module and liquid nitrogen cooling stage. Corresponding EDX measurements were carried out by an EDAX Octane Elite Super SDD Detector. Samples for FIB-SEM were prepared with a slightly thinner lithium electrode to enable cutting through the whole cell setup into the LLZO. This is necessary to not distort the interfacial arrangement between ILE, lithium and LLZO, as disassembling the cell would destroy morphological properties. Figure 2 displays the described procedure.

#### Surface Analytics Using X-Ray Photoelectron Spectroscopy (XPS)

As the ILE does not evaporate, any visible ILE residue on the pellet surface was gently wiped off using dust-free paper. Washing with a solvent was avoided as to not influence the interphase composition. XPS measurements were carried out using a PHI5000 Versa Probe II instrument (Physical Electronics GmbH, Germany) equipped with a Specs PHOIBOS 150 hemispherical energy analyzer and a monochromated  $\text{Al K}_{\alpha}$  X-ray source. Charge neutralization was carried out for electronically insulating LLZO samples using a low-energy flood gun. The power of the X-ray source was 100 W and the analysis area was 1  $\text{mm}^2$ . Survey spectra were measured using a pass energy of 93.9 eV at a resolution of 0.5 eV/step and a total integration time of 50 ms/point. Core-level spectra were measured using a pass energy of 29.35 eV at a resolution of 0.2 eV/step and a total integration time of 50 ms/point. Spectra were calibrated in relation to the signal of adventitious carbon at 284.8 eV. Depth profiling was carried out using  $\text{Ar}^+$  ions with energies of 0.5 kV or 1 kV. Data evaluation was

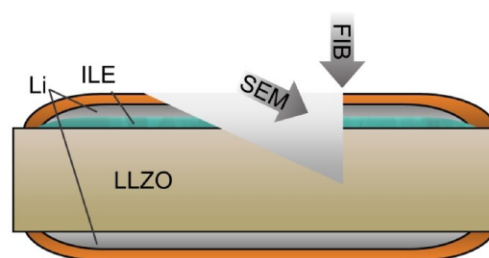


**Figure 2.** Schematic of the geometry how cryo-FIB-SEM measurements were carried out. The thicknesses of the layers were approximately 20  $\mu\text{m}$ , 80  $\mu\text{m}$ , and 20  $\mu\text{m}$  for the copper current collector, LMA and ILE interlayer, respectively. The FIB-crater is not drawn to scale, as it only has a lateral dimension of around 200  $\mu\text{m} \times 150$   $\mu\text{m}$ .

done using the software Casa XPS (version 2-3-22PR1.0, Casa Software Ltd).

the obtained activation energy  $E_{A,GB} = 0.40$  eV for grain boundary transport also fits reasonably to literature data.

## 2. Results and Discussion

### 2.1. Materials Characterization

The phase purity of the used ISE is especially important in this study, as detrimental side reactions have to be excluded. Therefore, the used LLZO was investigated regarding its crystal structure, density as well as electrical properties and morphology before being employed in this work. From XRD (Figure S1a), it is clear that the prepared LLZO crystallized in the well-conducting cubic polymorph without significant presence of the tetragonal side phase. The cross-section of the prepared pellets is shown in Figure S1b by SEM. The pellet density is geometrically estimated to be  $95 \pm 1\%$ , which characterizes a well consolidated phase, as also visible in the cross-section SEM image. A high pellet density is necessary to prevent ILE penetration into the LLZO pellet.

Additionally, Figure S2 displays a Nyquist plot of a symmetrical cell employing two ideal lithium electrodes ( $Li_{id}$ ) on LLZO and an obtained Arrhenius plot. The Nyquist plot displays two processes, corresponding to bulk and grain boundary transport in the material. The absence of a third process confirms that our preparation yields a negligible interface resistance for  $Li_{id}|LLZO$ . As seen in Figure S2b, both bulk and grain boundary processes follow an Arrhenius-type temperature dependence. The herein prepared LLZO shows an ionic conductivity of  $0.56$  mS cm $^{-1}$  at  $25$  °C as well as an activation energy  $E_{A,bulk} = 0.34$  eV, which is in accordance with previous published data for aluminum doped garnet ISE.<sup>[20,42–44]</sup> Likewise,

### 2.2. Impedance Analysis of the System and its Time Dependency

To investigate the effect of ILE on interfacial properties, three different types of cells were built and investigated. All cells employ ideal lithium electrodes ( $Li_{id}$ , prepared with 380 MPa pressure) as counter-electrode, as its contribution to the overall impedance is negligible.<sup>[20]</sup> Therefore, changes in resistance can fully be attributed to changes of the working electrode.

First, a cell with a non-ideal lithium working-electrode ( $Li_{nid}$ ) was prepared by attaching lithium with a small uniaxial pressure forming a non-ideal  $Li_{nid}|LLZO$  interface. The corresponding fit of the Nyquist plot is displayed as a dashed line in Figure 3 as reference. A full spectrum of that cell is shown in Figure S3. Additionally, the Nyquist-plot of a symmetrical cell with two ideal lithium electrodes prepared under high pressures,  $Li_{id}|LLZO|Li_{id}$ , and that of a cell employing the ILE as an interlayer between LLZO and Li are shown for means of a direct comparison. For the preparation of such a  $Li|ILE|LLZO$  electrode configuration, no external pressure (beyond atmospheric pressure) is applied (see Figure 1). Used equivalent circuits are depicted in the respective figures. Generally, semicircles were fit using an equivalent circuit composed of a series of parallel circuits of a resistance ( $R$ ) and non-ideal capacitance ( $P$ ).

As the herein built cells all include LLZO as separator, both high frequency processes (HF, 7 MHz–50 kHz) are identical in each case. In accordance with previous publications, these processes represent bulk and grain boundary transport within

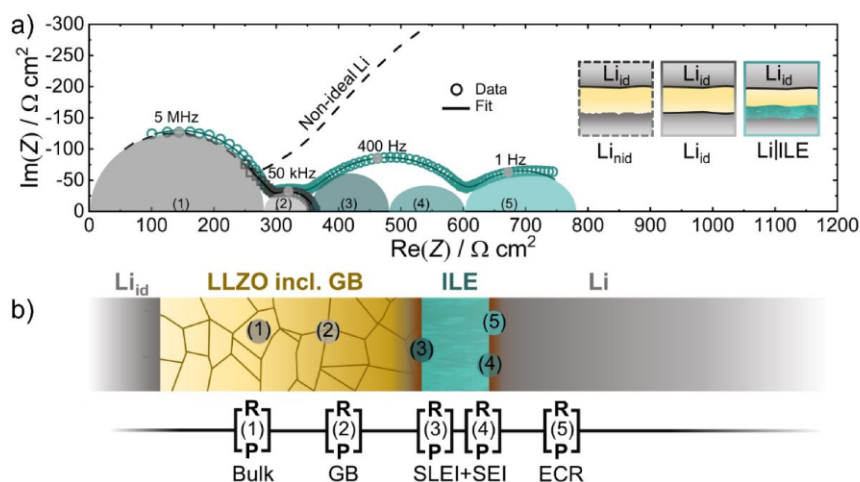


**Figure 3.** a) Comparison of Nyquist plots of impedances of  $Li_{nid}|LLZO|Li_{id}$  (dashed),  $Li_{id}|LLZO|Li_{id}$  (grey) and  $Li|ILE|LLZO|Li_{id}$  (green) cells with their respective fits and characteristic peak frequencies. Two additional semicircles appear when the ILE interlayer is added to the cell, which probably represent the interphases between the ILE and the two solids as well as an electrochemical reaction (ECR) at the lithium electrode. Furthermore, b) shows a schematic of the herein investigated  $Li|ILE|LLZO|Li_{id}$  cell alongside the used equivalent circuit used for fitting and the corresponding origins in the cell.

LLZO.<sup>[20,28,45]</sup> Usually, one would expect to see an additional ohmic drop across the ILE at high frequencies, but its contribution is negligible when the ILE is only present as a very thin interlayer, as in the Li|ILE|LLZO|Li<sub>id</sub> cells. All impedance contributions for the analyzed setups are listed with their characteristic frequencies and capacitances in Table S1.

In contrast to the HF processes, the mid frequency processes (MF, 400 Hz) differ significantly between the cell setups. For the Li<sub>mid</sub>|LLZO electrode, a large semicircle is visible, which can be linked to the high interfacial resistance  $R_{int}$  between LLZO and lithium. Said  $R_{int}$  becomes negligibly small for ideal lithium electrodes prepared under high pressures (Li<sub>id</sub>|LLZO) as seen in dark grey. When employing a Li|ILE electrode pressureless, another process is observed. The additional semicircle in the MF range is severely depressed, which indicates that two transport processes overlap in this frequency range: the transport through interphases with the ILE (ILE|LLZO and Li|ILE).<sup>[45–47]</sup> As their interphase compositions and with that, the time constants, are suspected to be similar, they cannot be resolved separately. Hence, only the sum of both is considered in the following as  $R_{SSEI}$ .

A further semicircle, located in the low frequency range (LF, 1 Hz), is observed for the Li|ILE electrode. We interpret this process as electrochemical reaction (ECR) at the LMA, as lithium is plated and stripped at frequencies around 1 Hz.<sup>[45,48]</sup> Even though the diffusion in the ILE may also explain a contribution in this frequency range,<sup>[35]</sup> we rule this out by investigating Li|ILE|Li cells with thicker ILE layers (Figure S4).

To further resolve the contributions in the MF range and aging of the Li|ILE electrode, Table 1 summarizes the MF resistance contributions of the prepared cells. For one, the table compares the MF response of Li<sub>id</sub>|LLZO|Li<sub>id</sub>, Li<sub>mid</sub>|LLZO|Li<sub>id</sub> and Li|ILE|LLZO|Li<sub>id</sub> cells as built. For another, the resistance values of the MF semicircle of a Li|ILE|LLZO|Li<sub>id</sub> cell are compared as built and after aging for 100 hours. Finally, after aging, parts of the cell were gradually replaced with fresh components, followed by an EIS analysis at each step. First, aged lithium was replaced by a freshly prepared foil. Then, the LLZO surface was polished and both ILE and lithium were renewed, again followed by impedance measurements. All corresponding Nyquist plots are appended in Figure S5.

It is important to note that the interfacial resistance of Li|LLZO electrodes is highly dependent on the applied pressure while attaching lithium during preparation.<sup>[20,24]</sup> When attaching lithium to a polished interface by hand, an interfacial resistance of  $> 1 \text{ k}\Omega \text{ cm}^2$  is obtained. It was shown that this high value is in fact not intrinsic to the material combination, but can rather

be explained by current constriction, which originates from surface inhomogeneities.<sup>[23,24]</sup> These can either be impurity phases, like Li<sub>2</sub>CO<sub>3</sub>, or morphological roughness due to polishing with SiC-paper. By pressing freshly prepared lithium isostatically with 380 MPa onto polished LLZO, the interfacial resistance in Li<sub>id</sub>|LLZO becomes negligibly small ( $< 1 \Omega \text{ cm}^2$ ) by obtaining optimal contact due to the ductility of lithium metal. However, utilizing high pressures is not optimal for cell preparation, especially when considering the scaling of production. Therefore, if the ILE is employed to enable better contact between LLZO and lithium, an interfacial resistance of only  $232 \Omega \text{ cm}^2$  yields without pressure application.

Aging of the Li|ILE|LLZO|Li<sub>id</sub> cell for 100 hours led to a five-fold increase in the MF resistance contribution, which can be linked to a growing ILE|LLZO or Li|ILE interphase, or actually both. In order to evaluate the individual contributions, we first replaced the aged LMA with a freshly prepared one. This increases the MF resistance marginally, possibly as the ILE has not fully wet the new lithium surface yet, and shows that the Li|ILE interphase is not the major contributor to MF resistance. Subsequently polishing the LLZO surface and employing fresh ILE and lithium again yields a low resistance comparable to that of the as-built cell. Hence, it can be concluded that the Li|ILE interphase is fairly stable and passivating if no current is applied, whereas the ILE|LLZO interphase grows with time and is the major contributor to the MF resistance.

Therefore, we analyzed the composition of the ILE|LLZO interphase by XPS depth profiling on fresh LLZO and on pellets which were used in cells in combination with the ILE. Our results (Figure S6) confirm the analysis reported in a previous study by Pervez et al.<sup>[33]</sup> and highlight the formation of LiF at the interface between LLZO and ILE.

The impedance of Li|ILE|LLZO|Li<sub>id</sub> shows quite similar features to that of cells employing GE by Liu et al.<sup>[35]</sup> The overall impedance of the interphases between ILE/GE with Li and LLZO is in the same range ( $200 \Omega \text{ cm}^2$ – $300 \Omega \text{ cm}^2$ ). Like found here for the LLZO|ILE|Li electrode, the Li|GE|LLZO electrode shows overlapping contributions from the Li|GE interphase as well as the GE|LLZO interphases in a similar frequency range. However, in this case the process at around 1 Hz represents a diffusion resistance of the GE, which is found in a much lower frequency range in our case (1 mHz). In our study, we attribute this LF frequency process therefore to an ECR resistance at the LMA. The difference may be explained by different diffusion properties of ILE and GE and cell geometry, specifically the thickness of the soft interlayer.

**Table 1.** Summary of mid-frequency resistances ( $R_{MF}$ , 400 Hz) and their different origins for herein prepared cell setups.

Cell setup	$R_{MF}$ [ $\Omega \text{ cm}^2$ ]	Contribution MF
Li <sub>mid</sub>  LLZO Li <sub>id</sub> as built	1201	Li <sub>mid</sub>  LLZO interface
Li <sub>id</sub>  LLZO Li <sub>id</sub> as built	$< 1$	Li <sub>id</sub>  LLZO interface
Li ILE LLZO Li <sub>id</sub> as built	232	Interphases, process (3) and (4)
Li ILE LLZO Li <sub>id</sub> aged 100 hours	1112	Interphases, process (3) and (4)
Li ILE LLZO Li <sub>id</sub> fresh lithium on aged cell	1469	Interphases, process (3) and (4)
Li ILE LLZO Li <sub>id</sub> polished LLZO and fresh ILE and lithium	222	Interphases, process (3) and (4)

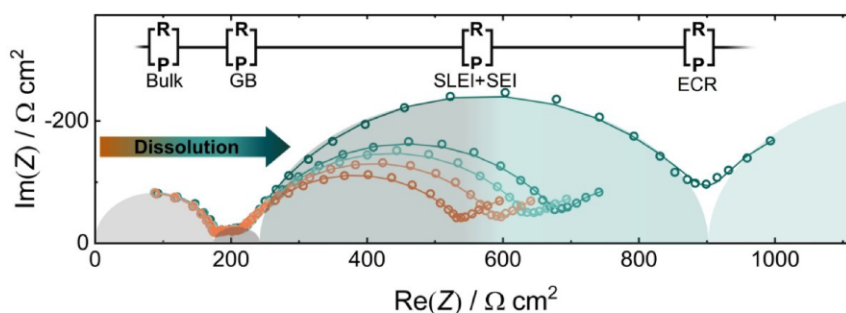


**Figure 4.** Nyquist plots of impedances measured approximately every 12 hours when stripping with  $100 \mu\text{A cm}^{-2}$  (the equivalent circuit used for fitting is shown above the data). Note that the SEI at the Lithium electrode and the SLEI between ILE and LLZO cannot be separately resolved due to similar characteristic frequencies.

### 2.3. Influence on Lithium Stripping

In the following, we investigate the  $\text{Li}|\text{ILE}|\text{LLZO}$  electrode during current load. At the solid|solid interface, an anodic current leads to severe morphological issues at the LMA in combination with an ISE.<sup>[20,24]</sup> Due to a rather slow vacancy diffusion in lithium metal, vacancies accumulate at the interface above a certain current threshold, leading to pore formation and subsequent contact loss. Stripping and plating experiments at the LMA can be analyzed well by galvanostatic EIS (GEIS), where a DC current is superimposed to ongoing EIS measurements.

In order to investigate the influence of the employed ILE on the pore formation during prolonged stripping at the LMA, GEIS measurements were carried out at  $100 \mu\text{A cm}^{-2}$  until a severe change in the potential was registered for the Li working electrode in the  $\text{Li}|\text{ILE}|\text{LLZO}|\text{Li}_d$ . Exemplarily, Figure 4 shows the evolution of the obtained Nyquist plot over time. For clarity, only a few representative spectra were selected and shown in this figure. It is evident that – while the bulk and grain boundary contributions stay constant – major changes can be observed in the mid and low frequency region, linked above to the SEIs and ECR.

To better assess the observed resistance evolution, Figure 5 displays the voltage profile as well as the resistance contributions over time, which were obtained by fitting the spectra in Figure 4. The general behavior of  $\text{Li}_d|\text{LLZO}|\text{Li}_d$  (grey)<sup>[20]</sup> and the herein built  $\text{Li}|\text{ILE}|\text{LLZO}|\text{Li}_d$  (green) is quite similar. For a major part of the stripping processes, the voltage is quite stable and only increases slightly for both setups. The overall higher cell resistance when employing the hybrid electrode setup also leads to a higher voltage plateau. Subsequently, a sudden steep voltage increase causes cell failure. However, this is delayed by a factor of 10–15 when employing ILE as an interlayer, leading to an areal capacity of around  $16 \text{ mAh cm}^{-2}$ , which is about 3 times higher than the required goal  $5 \text{ mAh cm}^{-2}$ .<sup>[18,19]</sup> As no pressure was applied to the cell during stripping, this is a significant result. An equally large stripping capacity can otherwise only be achieved by applying high pressures during the stripping process.<sup>[20]</sup>

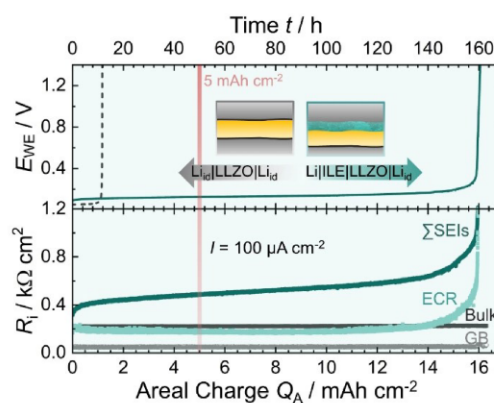


**Figure 5.** The top part of the figure displays the voltage profiles of two different cells over time during pressureless stripping at a current density of  $100 \mu\text{A cm}^{-2}$ . While having a lower voltage plateau, the  $\text{Li}_d|\text{LLZO}|\text{Li}_d$  (grey)<sup>[20]</sup> cell setup experiences earlier voltage increase, which is delayed by approximately  $15 \text{ mAh cm}^{-2}$  when using an ILE interlayer (green). The bottom part of the Figure displays the corresponding resistance evolution obtained by fitting the GEIS data, indicating that the ECR as well as the SEI resistances are responsible for the voltage increase.

The steep voltage increase for  $\text{Li}_d|\text{LLZO}|\text{Li}_d$  cells is explained by a rising interfacial resistance due to contact loss at the working electrode.<sup>[20]</sup> While bulk and grain boundary processes are constant over the whole stripping process, the observed SEI and ECR resistance contributions also increase at the end and are responsible for the voltage increase. Consequently, it can be concluded that interfacial issues are still responsible for cell failure, even when employing ILE as an interlayer. While significantly delaying contact loss by employing an ILE interlayer, it will still occur after a large amount of lithium has been stripped. This indicates that contact loss still occurs at the already discussed SLEI between LLZO and ILE or even between ILE and Li when more lithium is stripped than can be compensated by excess ILE present at the interface.

To further investigate the influence of ILE properties on stripping, different cells employing more viscous ILEs were

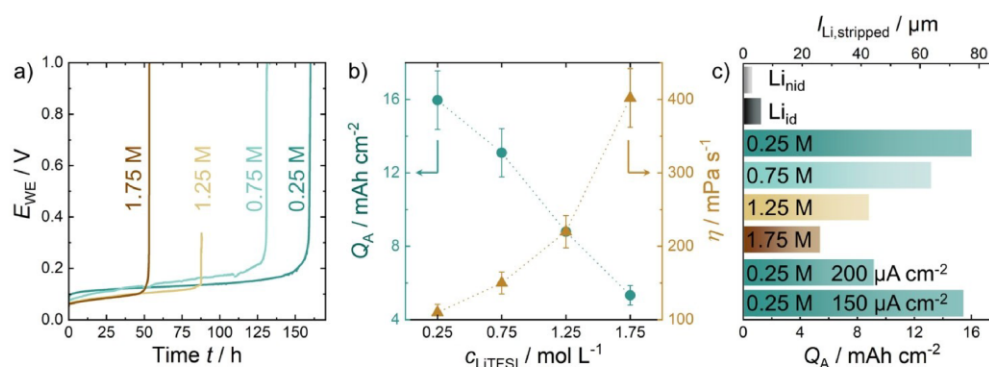


**Figure 6.** a) Voltage profiles of cells employing 1.75 M, 1.25 M, 0.75 M and 0.25 M LiTFSI. b) Calculated areal capacity  $Q_A$  and measured viscosity of the ILEs versus their LiTFSI concentration. Error bars are estimated according to reproduced experiments and experimental uncertainties. c) Comparison of areal capacities between different cell setups. Measurements were conducted with  $100 \mu\text{A cm}^{-2}$  unless stated otherwise.

prepared and characterized. As the viscosity can be fine-tuned via the salt concentration  $c_{\text{LiTFSI}}$ ,<sup>[38]</sup> cells with 0.25–1.75 ( $\Delta = 0.5$ )  $\text{mol L}^{-1}$  of LiTFSI in Py<sub>14</sub>TFSI were subjected to long-term stripping within this work. Nyquist plots of as-built cells are shown in Figure S7. No clear differences can be observed in the cell impedance before stripping.

Figure 6a shows the voltage profiles when stripping lithium in the abovementioned cells. Cell failure occurs earlier when more LiTFSI is dissolved in the ILE. Moreover, Figure 6b shows the calculated available areal charge capacity  $Q_A$  as well as the viscosity  $\eta$  as function of the salt concentration  $c_{\text{LiTFSI}}$ . A linear decrease in  $Q_A$  is observed with increasing  $c_{\text{LiTFSI}}$ . As  $\eta$  increases with  $c_{\text{LiTFSI}}$ , this indicates that a lower viscosity improves the stripping performance – almost linearly (Figure S8). The obtained viscosity for the 0.25 M ILE is in good agreement with literature data on similar systems, being around  $90 \text{ mPa s}$ .<sup>[49,50]</sup>

An overview over the prepared cells employing ILE and bare Li|LLZO|Li<sub>id</sub> electrodes is displayed in Figure 6c, showcasing the improved stripping behavior for all ILEs, even under higher current density. Note that by increasing  $c_{\text{LiTFSI}}$  not only the viscosity is increased, but also the ionic conductivity  $\sigma$  is decreased, see Table S2. As the ILE only contributes only to a minor extent to the overall cell resistance, we assume that the differences in stripping behavior are due to changes in  $\eta$  instead of  $\sigma$ . Clearly, the ILEs with lower viscosity and therefore also lower surface tension<sup>[51,52]</sup> can follow morphology changes of the interface easier, and therefore, act more efficiently as “contact buffer”.

#### 2.4. Reversibility of Li|ILE-Electrode Configurations

As already shown above, the employed ILE interlayer greatly improves the available areal specific capacity under anodic operating conditions, compensating pore formation at the interface without the application of pressure. Naturally, also the behavior under cathodic conditions was investigated here.

Figure 7 shows a voltage profile and resistance evolution for stripping and plating with  $100 \mu\text{A cm}^{-2}$  in an asymmetrical Li|ILE|LLZO|Li<sub>id</sub> setup. Within the herein cycled areal capacity of lithium (approximately  $25 \mu\text{Ah cm}^{-2}$  or 125 nm per step, if stripped homogeneously), the Li<sub>id</sub> counter electrode is morphologically stable and does not contribute to the observed changes in resistance.<sup>[20]</sup> We deliberately chose not to employ two Li|ILE electrodes, as changes while stripping on one side may overlap with changes while plating on the other.

As the cell setup is not strictly symmetrical, the observed voltage profile is also not completely symmetrical despite using two lithium electrodes, which originates from the fact that Li<sub>id</sub> was prepared under high pressures and unlike the other electrode does not employ ILE between the ISE and lithium. However, it is striking that the first stripping step has a stable, rather unchanged voltage compared to subsequent stripping steps, showing a step-like voltage profile. We believe that

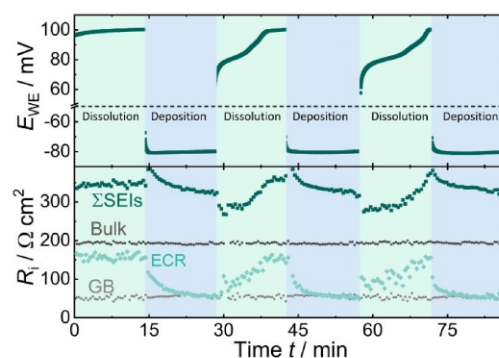


**Figure 7.** The top of the graph shows the voltage profile during pressureless stripping (green) and plating (blue) at the ILE side of the prepared Li|ILE|LLZO|Li<sub>id</sub> cell setup. The bottom part of the graph shows the evolution of the different resistance contributions present in the impedance spectrum obtained via GEIS measurements.

lithium stripping is quite homogenous in the beginning, as morphological inhomogeneities have not formed yet. After reversing the current, plating occurs at the Li|ILE electrode, which probably leads to inhomogeneous lithium deposition.<sup>[53–55]</sup>

Understanding this observation is possible by analyzing changes in the different resistance contributions. As expected, bulk and grain boundary resistances are constant during the measurements, as the separator does not change. However, the voltage profile is closely mirrored by the changes in  $R_{\text{SEI}}$  and  $R_{\text{ECR}}$ . At first, both contributions are constant during homogeneous stripping. Subsequent morphological changes during plating lead to an increasing surface area of the LMA and therefore to an apparent decrease of the ECR resistance contribution. This is similar to what was observed for Li<sub>mid</sub>|LLZO regarding the interfacial resistance at around 1 kHz.<sup>[20]</sup> Additionally, similar but attenuated effects are visible for the sum of the interphase resistances in the middle frequency range. Again, by increasing the actual surface area of the LMA during plating, the apparent SEI resistance between ILE and lithium decreases. This also confirms that the SLEI resistance between ILE and LLZO does not depend on changes in the LMA morphology. Despite the SEI resistance only having a small contribution to the sum of both SEI and SLEI, it still impacts the observed total value.

Previous studies employing ILE or GE as interlayers showed a stable cycling performance in symmetrical cells up to around  $0.3 \text{ mA cm}^{-2}$ .<sup>[34,35]</sup> In these examples, small amounts of lithium were transferred in many cycles, which is especially important to assess long-term stability and potential for possible applications of a cell setup. However, the experiments shown here rather focus on the microscopic evolution and changes in cell resistance contributions to better understand the physico-chemical behavior of the setup. Still, in the cited studies, a more symmetric voltage profile was obtained for cells with two hybrid electrode configurations when compared to the herein prepared Li|ILE|LLZO|Li<sub>mid</sub> cell with only one Li|ILE electrode. This is surprising, but may be explained by different morphology and surface composition of used LMAs as well as the difference in the counter electrode.

### 2.5. Evaluation of Morphological Changes During Stripping

As the ILE's viscosity is suspected to play a crucial role in the origin of the voltage increase and speculated contact loss, cryo-FIB-SEM imaging was performed to analyze changes in lithium and ILE morphology. Therefore, the cells to be investigated with FIB-SEM, were frozen with liquid N<sub>2</sub> before imaging, to fix the otherwise liquid ILE in place. Then, FIB-cutting was performed through the Cu CC, LMA and ILE into the LLZO (see Figure 2). Subsequently, SEM images of the cross-section were recorded.

Figure 8b–d displays SEM images of the cross section for a cell which was characterized as-built. Similar images for Li|ILE electrodes, which experienced an anodic current of  $100 \mu\text{A cm}^{-2}$  without failure, are displayed in Figure 8e–f. Addi-

tionally, an electrode which passed the steep voltage increase was characterized and the cross section is displayed in Figure 8g–h. To unequivocally link the imaged layers to the materials used herein, Figure 8i also depicts the results of an EDX-line-scan that was performed on the cross section of the as-built cell, indicated by the dotted line in Figure 8b. Note that due to the inherent morphological changes during the experiments, different cells had to be used to assess the different stages in the stripping process. Hence, layer thicknesses of lithium and ILE are not necessarily identical in the different cells and FIB cuts. However, we assume that the general morphology evolution is comparable nonetheless. Additional images are presented in Figure S9.

First, the as-built cell has a relatively smooth layered structure of Li, ILE and LLZO. From top to bottom, the layers get progressively brighter as visible in the BSE image in Figure 8b, which is plausible as the involved average atomic mass of elements increases in the order of  $\text{Li} < \text{ILE} < \text{LLZO}$ . The very dark appearance of the top layer identifies it as lithium metal. The next layer corresponds to frozen ILE, followed by LLZO ISE. This is confirmed by measuring an EDX line-scan, as depicted in Figure 8i. For the sake of simplicity, only O, F and C K-line signals are selected. Three separate regions are visible in the element distribution. In the first layer, oxygen levels are clearly elevated which fits to the LLZO layer. The next layer has an enrichment of C and F, which are both present in the ILE. The third layer only gives a low O signal, which probably originates from a passivation on the lithium surface. The lithium itself is not visible with the herein used EDX detector.

Another interesting observation for the first cell is that the contact between the different layers is quite good, indicating satisfactory wetting of the ILE on LLZO and lithium. Only between LLZO and ILE there is a very thin gap ( $\sim 200 \text{ nm}$ ), which is probably simply caused by different thermal expansion factors and the large temperature change when cooling with liquid N<sub>2</sub>. Otherwise, some vertical lines are visible. This “curtaining” is known in literature and frequently happens when performing FIB cuts and is therefore not to be attributed to the samples morphology.<sup>[56–58]</sup>

Moving to the second cell, which experienced anodic current without severe voltage change, a clear change in morphology is visible. The Li|ILE interface now shows roughness in the  $\mu\text{m}$  scale, which fits well to the amount of lithium that was stripped until this point. This observation also indicates that pore formation due to uneven lithium dissolution is not attenuated by the ILE interlayer, but rather compensated. This compensation is very well displayed in Figure 8e, as the ILE is not a homogeneous layer anymore, but fills pores in the lithium metal. A partial contact loss is already visible in Figure 8f, as the available ILE cannot fill the whole pore volume. However, we note that lithium metal is closer to the separator than it was before. This is probably the case due to the mobility of the ILE and the used cell setup, somewhat shifting the lithium. Interestingly, another cut in this sample was prepared and analyzed, which did not show severe morphology changes but a rather thick lithium layer, see Figure S9. This hints at large inhomogeneities in the stripping process.

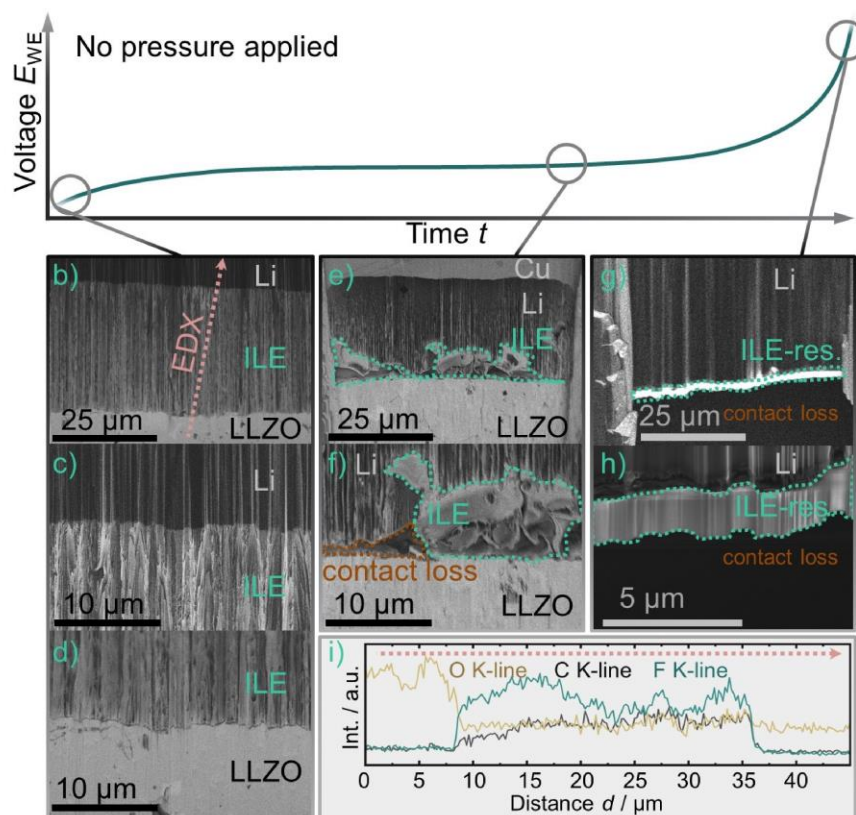


**Figure 8.** a) Schematic of a typical voltage profile during stripping of lithium in a Li|ILE|LLZO|Li<sub>0</sub> cell. Cross-sectional images were obtained via cryo-FIB-SEM to assess the morphology of the interfaces at different stages while stripping. In b–d), SEM images of the ILE|LLZO and Li|ILE interfaces in an as-built Li|ILE|LLZO|Li<sub>0</sub> cell are displayed. The SEM images in e) and f) show the morphology of the ILE|LLZO and Li|ILE interfaces after stripping was performed and before cell failure has set in. Finally, g) and h) display cross-sectional images of a cell after the steep increase in voltage. To unequivocally link the different layers in the SEM images with the cell components, an EDX-line scan was carried out on the as-built cell and is displayed in i). Note that all FIB and SEM measurements were carried out at around 140 K–150 K, cooled with liquid nitrogen, so the ILE is solid and lithium metal does not melt when cut with the FIB.

The third column displays the full contact loss after the distinct voltage increase under anodic current. Only some ILE residue (res.) is left bound to the lithium metal, but LLZO is not visible anymore, as the FIB-crater unfortunately was not deep enough to also display the separator. Note that these SEM images were selected to showcase the morphology evolution under anodic current although measurements at different spots partially show other morphologies, see Figure S9. This leads to the conclusion, that pore formation/lithium dissolution is quite uneven and has even macroscopic differences under prolonged stripping as already indicated by the previous sample. Macroscopic pores were also visible to the naked eye when disassembling the cells after measurement. This conclusion is further strengthened by the fact that approximately  $16 \text{ mAh cm}^{-2}$  could be stripped, which corresponds to about  $75 \mu\text{m}$  of lithium if it were stripped homogeneously. The resulting strong spatial inhomogeneity is also seen in images obtained via confocal microscopy, as displayed in Figure 9.

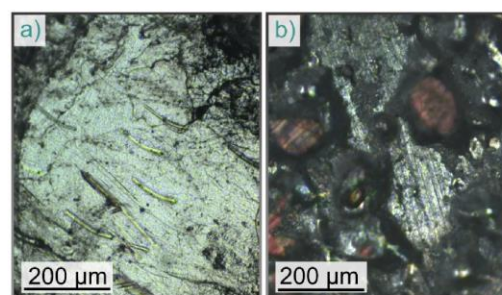


**Figure 9.** Comparison of confocal microscopy (top view) images of a) freshly prepared lithium foil and b) lithium foil which was stripped until the voltage spike occurred.

Pores spanning several micrometers as well as holes down to the copper current collector are found for the treated LMA. The

freshly prepared foil only shows long marks, probably because of pressing the foil in preparation, but no large pores as visible for the treated LMA.

To summarize the morphology evolution during stripping, Figure 10 displays the suggested mechanism and subsequent contact loss when using ILE as an interlayer. Besides that the ILE partially compensates pore formation, the general mechanism of contact loss is surprisingly similar to that already reported for the solid|solid Li|LLZO interface.<sup>[20]</sup> This is supported by the decrease in interfacial capacity of the RQ-elements in the MF and LF range while stripping as seen in Figure S10, which is quite similar to the bare Li<sub>id</sub>|LLZO interface.

It is an interesting question why the voltage profile shows such a long and stable plateau before increasing steeply instead of a continuous voltage increase. The reason is yet not completely clear but involves effects on both the nm and μm scale. The effect on the nm-scale is the surface diffusion of lithium, which is constantly supplying new lithium to be stripped at the interface as already discussed in the work of Krauskopf et al.<sup>[20]</sup> On the μm scale, the ILE is compensating freshly forming inhomogeneities first, which then fails when the excess ILE reservoir has been used up to compensate the continuously growing inhomogeneity. Our findings are supported by experiments where a new cell was assembled in combination with an already stripped lithium anode as in Figure 5. In this case, large stripping capacities are observed again, as new ILE is compensating the pores upon building the cell. From this experiment, it can also be concluded, that lithium does not need to be perfectly flat when preparing cells with liquid interlayers to work.

An additional reason for the sudden and drastic increase in cell resistance may be the change of wetting of the ILE on an increasingly rough lithium surface. With increasing viscosity, the surface tension also increases,<sup>[51,52]</sup> which facilitates the transition from the Wenzel state (wetting on rough surfaces) to the Cassie-Baxter state (dewetting on rough surfaces) at a lower stripping capacity.<sup>[59]</sup> This sudden dewetting may also be responsible for the observed contact loss.

### 3. Conclusions

We analyze a hybrid electrode employing lithium metal as the anode, ionic liquid electrolyte (Py<sub>14</sub>TFSI with LiTFSI) as an interlayer as well as LLZO as a solid electrolyte separator. This electrode configuration is characterized in a Li|ILE|LLZO|Li<sub>id</sub> cell setup mainly with (galvanostatic) electrochemical impedance spectroscopy, FIB-SEM and XPS, regarding the stripping and plating behavior, morphology of the layers and their reactivity, respectively. Generally, the cell resistance is lowered by employing the ILE respective to the conventional (non-ideal solid|solid) LMA preparation. It was additionally found that this cell setup enhances the areal charge capacity for lithium stripping (> 15 mAh cm<sup>-2</sup>) by a factor of 10 to 15 in comparison to an ideal Li<sub>id</sub>|LLZO interface (1.2 mAh cm<sup>-2</sup>) without the need of external pressure while preparing or cycling the cell. Cryo-FIB-SEM imaging reveals that pore formation while stripping at the lithium electrode is not entirely prevented with the herein used setup, but contact loss is rather delayed as the mobile ILE fills growing pores to some extent. Furthermore, this work analyzes the concept of self-adjusting liquid interlayers and possible failure mechanisms, which could be prevented in future studies by employing optimized materials, e.g., ILEs with lower viscosities or cell setups with excess ILE.

### Acknowledgements

The authors thank Dr. Simon Burkhardt for measurements with the optical microscope. This work was conducted as part of the US-German joint collaboration on "Interfaces and Interphases in Rechargeable Li-metal based Batteries" supported by the US Department of Energy (DOE) and German Federal Ministry of Education and Research (BMBF). This work has been partly funded by the German Federal Ministry of Education and Research (BMBF) under the project "LISI", grant identifier 03XP0224E. F.H.R. is grateful for funding under the project "FLiPS", grant identifier 03XP0261. J.J. and S.P. acknowledge fruitful discussions within the BMBF cluster of competence FESTBATT (projects 03XP0176D and 03XP0175B). S.P. acknowledges the basic funding from the Helmholtz Association. Open access funding enabled and organized by Projekt DEAL.

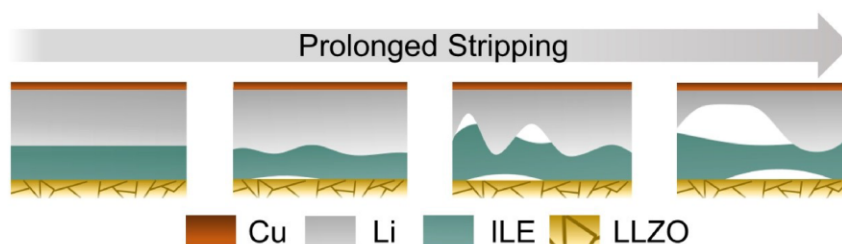


**Figure 10.** Schematic of morphology changes occurring during prolonged stripping of the investigated Li|ILE electrode setup. Pores are forming when lithium is stripped and are compensated by the ILE to some extent. When excess ILE has been used up, this compensation is not upheld upon further stripping of lithium. Note that to increase clarity, the formed SEI and SLEI are deliberately omitted in this image.

### Conflict of Interest

The authors declare no conflict of interest.

**Keywords:** hybrid battery · lithium metal anode · solid electrolyte · ionic liquid · pore formation

- [1] C. Niu, H. Lee, S. Chen, Q. Li, J. Du, W. Xu, J. G. Zhang, M. S. Whittingham, J. Xiao, J. Liu, *Nat. Energy* **2019**, *4*, 551–559.
- [2] H. Wang, D. Yu, C. Kuang, L. Cheng, W. Li, X. Feng, Z. Zhang, X. Zhang, Y. Zhang, *Chem* **2019**, *5*, 313–338.
- [3] Y. Takeda, O. Yamamoto, N. Imanishi, *Electrochemistry* **2016**, *84*, 210–218.
- [4] K. Xu, *Chem. Rev.* **2004**, *104*, 4303–4417.
- [5] J. M. Tarascon, M. Armand, *Nature* **2001**, *414*, 359–367.
- [6] K. Nishikawa, T. Mori, T. Nishida, Y. Fukunaka, M. Rosso, T. Homma, *J. Electrochem. Soc.* **2010**, *157*, A1212.
- [7] H. E. Park, C. H. Hong, W. Y. Yoon, *J. Power Sources* **2008**, *178*, 765–768.
- [8] M. Weiss, F. J. Simon, M. R. Busche, T. Nakamura, D. Schröder, F. H. Richter, J. Janek, *Electrochem. Energy Rev.* **2020**, *3*, 221–238.
- [9] M. R. Busche, T. Drossel, T. Leichtweiss, D. A. Weber, M. Falk, M. Schneider, M. L. Reich, H. Sommer, P. Adelhelm, J. Janek, *Nat. Chem.* **2016**, *8*, 426–434.
- [10] M. Keller, A. Varzi, S. Passerini, *J. Power Sources* **2018**, *392*, 206–225.
- [11] R. Ruess, S. Schweidler, H. Hemmelmann, G. Conforto, A. Bielefeld, D. A. Weber, J. Sann, M. T. Elm, J. Janek, *J. Electrochem. Soc.* **2020**, *167*, 100532.
- [12] R. Koerver, W. Zhang, L. De Biasi, S. Schweidler, A. O. Kondrakov, S. Kolling, T. Brezesinski, P. Hartmann, W. G. Zeier, J. Janek, *Energy Environ. Sci.* **2018**, *11*, 2142–2158.
- [13] R. Koerver, I. Aygün, T. Leichtweiß, C. Dietrich, W. Zhang, J. O. Binder, P. Hartmann, W. G. Zeier, J. Janek, *Chem. Mater.* **2017**, *29*, 5574–5582.
- [14] J. Janek, W. G. Zeier, *Nat. Energy* **2016**, *1*, 1–4.
- [15] Y. Kato, S. Hori, T. Saito, K. Suzuki, M. Hirayama, A. Mitsui, M. Yonemura, H. Iba, R. Kanno, *Nat. Energy* **2016**, *1*, 1–7.
- [16] C. Monroe, J. Newman, *J. Electrochem. Soc.* **2004**, *151*, 880–886.
- [17] C. Z. Zhao, B. C. Zhao, C. Yan, X. Q. Zhang, J. Q. Huang, Y. Mo, X. Xu, H. Li, Q. Zhang, *Energy Storage Mater.* **2020**, *24*, 75–84.
- [18] S. Randau, D. A. Weber, O. Kötz, R. Koerver, P. Braun, A. Weber, E. Ivers-Tiffée, T. Adermann, J. Kulisch, W. G. Zeier, F. H. Richter, J. Janek, *Nat. Energy* **2020**, *5*, 259–270.
- [19] P. Albertus, S. Babinec, S. Litzelman, A. Newman, *Nat. Energy* **2018**, *3*, 16–21.
- [20] T. Krauskopf, H. Hartmann, W. G. Zeier, J. Janek, *ACS Appl. Mater. Interfaces* **2019**, *11*, 14463–14477.
- [21] E. D. Wachsman, L. Hu, Y. Mo, Washington, DC, **2016**.
- [22] P. Hovington, M. Lagacé, A. Guerfi, P. Bouchard, A. Mauger, C. M. Julien, M. Armand, K. Zaghib, *Nano Lett.* **2015**, *15*, 2671–2678.
- [23] T. Krauskopf, B. Mogwitz, H. Hartmann, D. K. Singh, W. G. Zeier, J. Janek, *Adv. Energy Mater.* **2020**, *2000945*.
- [24] T. Krauskopf, F. H. Richter, W. G. Zeier, J. Janek, *Chem. Rev.* **2020**, *120*, 7745–7794.
- [25] D. Aurbach, A. Zaban, *J. Electroanal. Chem.* **1993**, *348*, 155–179.
- [26] D. Aurbach, A. Zaban, *J. Electroanal. Chem.* **1994**, *365*, 41–45.
- [27] Y. Zhu, X. He, Y. Mo, *J. Mater. Chem. A* **2016**, *4*, 3253–3266.
- [28] T. Krauskopf, R. Dippel, H. Hartmann, K. Peppeler, B. Mogwitz, F. H. Richter, W. G. Zeier, J. Janek, *Joule* **2019**, *3*, 2030–2049.
- [29] K. N. Wood, M. Noked, N. P. Dasgupta, *ACS Energy Lett.* **2017**, *2*, 664–672.
- [30] F. Sun, L. Zielke, H. Markötter, A. Hilger, D. Zhou, R. Moroni, R. Zengerle, S. Thiele, J. Banhart, I. Manke, *ACS Nano* **2016**, *10*, 7990–7997.
- [31] K. N. Wood, E. Kazyak, A. F. Chadwick, K. H. Chen, J. G. Zhang, K. Thornton, N. P. Dasgupta, *ACS Cent. Sci.* **2016**, *2*, 790–801.
- [32] D. Aurbach, E. Zinigrad, Y. Cohen, H. Teller, *Solid State Ionics* **2002**, *148*, 405–416.
- [33] S. A. Pervez, B. P. Vinayan, M. A. Cambaz, G. Melinte, T. Diemant, T. Braun, G. Karkera, R. J. Behm, M. Fichtner, *J. Mater. Chem. A* **2020**, *8*, 16451–16462.
- [34] S. A. Pervez, G. Kim, B. P. Vinayan, M. A. Cambaz, M. Kuenzel, M. Hekmatfar, M. Fichtner, S. Passerini, *Small* **2020**, *16*.
- [35] B. Liu, Y. Gong, K. Fu, X. Han, Y. Yao, G. Pastel, C. Yang, H. Xie, E. D. Wachsman, L. Hu, *ACS Appl. Mater. Interfaces* **2017**, *9*, 18809–18815.
- [36] P. Wasserscheid, T. Welton, Eds., *Ionic Liquids in Synthesis*, Wiley-VCH, Weinheim, **2002**.
- [37] Y. U. Paulechka, D. H. Zaitsau, G. J. Kabo, A. A. Strechan, *Thermochim. Acta* **2005**, *439*, 158–160.
- [38] A. Eftekhari, Y. Liu, P. Chen, *J. Power Sources* **2016**, *334*, 221–239.
- [39] F. J. Simon, M. Hanauer, A. Henss, F. H. Richter, J. Janek, *ACS Appl. Mater. Interfaces* **2019**, *11*, 42186–42196.
- [40] S. Wenzel, S. J. Sedlmaier, C. Dietrich, W. G. Zeier, J. Janek, *Solid State Ionics* **2018**, *318*, 102–112.
- [41] S. Wenzel, D. A. Weber, T. Leichtweiss, M. R. Busche, J. Sann, J. Janek, *Solid State Ionics* **2016**, *286*, 24–33.
- [42] A. Sharafi, C. G. Haslam, R. D. Kerns, J. Wolfenstine, J. Sakamoto, *J. Mater. Chem. A* **2017**, *5*, 21491–21504.
- [43] L. Cheng, W. Chen, M. Kunz, K. Persson, N. Tamura, G. Chen, M. Doeff, *ACS Appl. Mater. Interfaces* **2015**, *7*, 2073–2081.
- [44] Y. Matsuki, K. Noi, M. Deguchi, A. Sakuda, A. Hayashi, M. Tatsumisago, *J. Electrochem. Soc.* **2019**, *166*, A5470–A5473.
- [45] J. T. S. Irvine, D. C. Sinclair, A. R. West, *Adv. Mater.* **1990**, *2*, 132–138.
- [46] J. Zheng, M. Gu, H. Chen, P. Meduri, M. H. Engelhard, J. G. Zhang, J. Liu, J. Xiao, *J. Mater. Chem. A* **2013**, *1*, 8464–8470.
- [47] J. Y. Song, H. H. Lee, Y. Y. Wang, C. C. Wan, *J. Power Sources* **2002**, *111*, 255–267.
- [48] M. J. Wang, R. Choudhury, J. Sakamoto, *Joule* **2019**, *3*, 2165–2178.
- [49] G. A. Elia, U. Ulissi, S. Jeong, S. Passerini, J. Hassoun, *Energy Environ. Sci.* **2016**, *9*, 3210–3220.
- [50] M. L. P. Le, F. Alloin, P. Strobel, J. C. Leprêtre, L. Cointeaux, C. P. del Valle, *Ionics (Kiel)* **2012**, *18*, 817–827.
- [51] H. Schonhorn, *J. Chem. Eng. Data* **1967**, *12*, 524–525.
- [52] M. Zheng, J. Tian, A. Mulero, *Fluid Phase Equilib.* **2013**, *360*, 298–304.
- [53] C. Monroe, J. Newman, *J. Electrochem. Soc.* **2003**, *150*, A1377.
- [54] P. Bai, J. Li, F. R. Brushett, M. Z. Bazant, *Energy Environ. Sci.* **2016**, *9*, 3221–3229.
- [55] W. Xu, J. Wang, F. Ding, X. Chen, E. Nasymbulin, Y. Zhang, J. G. Zhang, *Energy Environ. Sci.* **2014**, *7*, 513–537.
- [56] S. Liu, L. Sun, J. Gao, K. Li, *J. Microsc.* **2018**, *272*, 3–11.
- [57] F. Santoro, E. Neumann, G. Panaitov, A. Offenhäusser, *Microelectron. Eng.* **2014**, *124*, 17–21.
- [58] T. H. Loeber, B. Laegel, S. Wolff, S. Schuff, F. Balle, T. Beck, D. Eifler, J. H. Fitschen, G. Steidl, *J. Vac. Sci. Technol., B: Nanotechnol. Microelectron.: Mater., Process., Meas., Phenom.* **2017**, *35*, 06GK01.
- [59] H. Yildirim Erbil, C. Elif Cansoy, *Langmuir* **2009**, *25*, 14135–14145.

Manuscript received: January 15, 2021  
 Revised manuscript received: March 14, 2021  
 Accepted manuscript online: March 15, 2021  
 Version of record online: March 26, 2021



## 4 Conclusions

Despite lots of progress and research performed on the Li|SE interface, several challenges remain to be overcome before commercialization of SSBs with an LMA. This work presents novel insights regarding both the chemical compatibility of oxide SEs with lithium metal as well as morphological issues when lithium is electrochemically dissolved or deposited at interfaces. Lastly, different methods on compensating morphological challenges, like employing liquid wetting agents or using composites, are conceptually presented and investigated regarding their viability to match specific requirements. Additionally, pitfalls in current research on metal electrodes are analyzed within this dissertation, which currently are ignored by many researchers. Based on these findings, guidelines on how to properly test the limits of Li|SE interfaces are given to streamline future research and gain comparable data.

As literature results still are conflicting on whether and to what extent an SEI forms between lithium and LLZO:Al, said interface was investigated in dependence on the lithium deposition method. One key finding previously overlooked in literature is that the energy input during lithium deposition influences the outcome and extent of interphase formation. While high-energy input methods such as sputter deposition result in a partial reduction of  $Zr^{4+}$  within LLZO:Al, low-energy input methods such as electron-beam vapor deposition do not induce a reaction between lithium and LLZO:Al.

Since most SEs react with lithium metal, which additionally forms a resistive passivation layer, so-called RFCs gain importance in battery research. If the lithium reservoir is omitted upon assembly but rather deposited within a first formation step, the handling of reactive lithium foils can be circumvented. Furthermore, the time where lithium is in contact with the SE is minimized as well. Therefore, a novel operando method was introduced within this dissertation that allows the characterization of the plating morphology within RFCs as a function of different external parameters, such as applied current density or CC thickness. The gathered knowledge will help to overcome the major challenge that still hinders the feasibility of RFCs, being very heterogeneous and difficult to control deposition morphologies.

Rather, heterogeneous morphologies including whiskers, dendrites and islands seem to occur simultaneously. To elucidate different influential parameters, our novel SEM operando technique allowed the cross-sectional and top-view observation of lithium growth at Cu|SE interfaces. A strong dependency of the morphology on the applied current density, CC thickness and SE density could be found. In our case, thicker CCs and denser electrolytes in combination with high current densities lead to a high areal coverage of lithium, paving the way for future optimization and analysis of RFCs.

However, the biggest hurdles yet to be overcome before successful LMA implementation are contact-related issues, i.e. pore formation during stripping. Independent of whether classical SSBs or RFCs are used, the insufficient vacancy diffusion and low vacancy detachment rate from the interface are physically limiting the applicable discharge current. While this cannot be fundamentally changed for the Li|SE interface, several mitigation strategies were conceived and analyzed within this dissertation, including tailoring of lithium grain size, liquid interlayers and blending lithium with CNTs.

The grain size of lithium foil was tailored using different thermal processing histories for the first time. Thereby, a pronounced influence of the grain size on anodic dissolution of lithium could be shown, with small grains leading to a higher capacity at moderate pressures (2 MPa) as grain boundaries and dislocations facilitate the replenishment of lithium vacancies at the interface via

dislocation pipe diffusion and Nabarro-Herring creep. Yet, linking the lithium microstructure to dissolution performance is only directly relevant within the first discharge of an LMA. In the case of full cells and RFCs, however, lithium is first deposited onto either a lithium reservoir or a metal CC yielding an unknown grain size and dislocation density. Linking the LMA microstructure to the discharge performance therefore serves as data to be able to assess the microstructure of deposited lithium in RFCs and full cells.

Another strategy to overcome morphological changes during lithium dissolution is the use of composite electrodes. Within this dissertation, composites consisting of lithium and CNTs were investigated regarding their electro- and chemo-mechanical properties. It could be shown that dispersed CNTs act as lithium pathways, which lead to lithium dissolution from the bulk of the anode material instead of only from the interface. This is then confirmed by visualizing pores within the bulk with cryogenic FIB-SEM. Hence, very high capacities  $> 20 \text{ mAh cm}^{-2}$  without the application of external stack pressures can be achieved, albeit not at high current densities.

Additionally, dispersing fibers in lithium also offers the possibility of tuning the mechanical properties to the desired requirements. For example, 30 wt% of CNTs dispersed in lithium increases its yield strength and Vickers Hardness to 2.7 GPa and 60 MPa, respectively. If no pressure is applied during stripping, Li-CNT composites offer higher stripping capacities compared to pure lithium. However, if a moderate pressure of around 1 MPa is applied, pure lithium metal will deform and creep, effectively suppressing pore formation. As the composites have a higher yield strength, they are not as sensitive to external pressure with regards to the available stripping capacity.

Furthermore, employing an IL as a wetting agent at the Li|LLZO interface was analyzed to be a valuable improvement to the electrode's stripping capacity. It could be shown that the pore formation within the metal is not suppressed, but rather compensated. Despite only around 5 – 10  $\mu\text{L}$  of IL present at the interface, growing pores are filled to a large extent by IL flowing into the voids. This results in stripping capacities of  $> 15 \text{ mAh cm}^{-2}$ , exceeding targets set in literature.<sup>10,57</sup> However, while this concept is a viable improvement of the discharge capacity, it still lacks proof that it leads to improved cycling overall. It still is academically important, as it shows exemplarily that sacrificing the concept of an all-ceramic SSB for a hybrid approach can lead to drastic improvements in certain properties while simultaneously not undermining the benefits of SSBs. After all, a few microliters of a non-flammable, low vapor pressure IL do not diminish the safety gained by employing a solid, ceramic separator.

Overall, this dissertation offers novel techniques to both investigate and overcome morphological issues present during dissolution of LMAs and deposition of lithium in RFCs. Addressing these challenges is of utmost importance to realize a stable and reliable operation of SSBs employing a lithium electrode.

## 5 Outlook

As one part of this dissertation, it could be shown that RFCs present an elegant way to avoid the handling of pure lithium metal during SSB fabrication. A powerful tool was introduced to study the optimal interface conditions, CC properties and lithium deposition parameters, which will be used in the future to guide the search for suitable conditions allowing the homogeneous deposition of lithium films at a CC|SE interface. As of now, there seems to be no physicochemical reason why a proper realization of an RFC could not work, which is very promising regarding future cell optimization.

However, despite significant insights gained regarding microstructural and morphological effects and strategies to overcome them at the Li|SE interface, one key question remains with regards to large-scale realization of LMAs.

*Can the Pore Formation during Stripping of Metal Electrodes be Overcome while Keeping their Expected Advantages?*

Both for RFCs and traditional SSBs, lithium stripping during cell discharge presents an enormous challenge to realize cycling of significant charges ( $> 5 \text{ mAh cm}^{-2}$ ) at a realistic current density ( $> 5 \text{ mA cm}^{-2}$ ) due to pore formation.<sup>7,57</sup> The two promising concepts presented within this dissertation, being liquid pore filling agents in the case of hybrid electrodes<sup>39</sup> or composite electrodes employing carbon scaffolds<sup>40</sup> show great improvements, thereby lowering the necessary pressure and increasing the available discharge capacity to  $> 20 \text{ mAh cm}^{-2}$ . However, high discharge rates still remain a challenge on a physicochemical level due to the insufficient vacancy diffusion within lithium metal resupplying lithium to the interface.

Furthermore, investigation is needed on how the presented results on pore formation and mitigation transfer to promising sodium metal electrodes.<sup>127</sup> Sodium-based SSBs could potentially offer nearly the same energy and power density as traditional lithium-based systems without the need for critical elements such as lithium itself or cobalt.<sup>128</sup> Early works on the interface kinetics indicate that a knowledge transfer between lithium and sodium metal electrodes is indeed possible, as the charge transfer between sodium and  $\text{Na}_{3.4}\text{Zr}_2\text{Si}_{2.4}\text{P}_{0.6}\text{O}_{12}$  seems to also be negligible when very clean interfaces are prepared, as in the case for Li|LLZO.<sup>129</sup> Interestingly, pore formation during stripping seems to be equally challenging for Na|SE interfaces.

High stack pressures in the range of several tens of MPa can mitigate pore formation by resupplying alkali metal atoms to the interface via creep and plastic deformation.<sup>37</sup> However, the use of pressure frames able to apply high pressures on a system level leads to an overall system energy density that is lower or at best on par with traditional LIBs. While some companies claim to be able to discharge SSBs with an LMA at low pressures and high rates,<sup>24</sup> it is not yet commonly understood how this should be achieved. The role of pressure and especially its magnitude therefore still remains elusive in enabling the use of alkali metal electrodes within SSBs and will be of great interest in future studies.

Another solution to pore formation is the utilization of three-dimensional, porous SE bi- or trilayers, as the local current density is very low despite areal current densities in the range of  $10 \text{ mA cm}^{-2}$ . Within these structures, porous SE layers are filled with electrode material and are separated by a dense SE layer in the middle, not thicker than  $20 - 30 \text{ }\mu\text{m}$ . This concept is promising, especially as pressure requirements and volume changes are mitigated. However, this method also lowers the specific capacity and thus the biggest benefit alkali metals provide as anode materials. It may still be worth the effort though, as it is an elegant way to enable practical current densities in the range

of several  $\text{mA cm}^{-2}$ .<sup>109</sup> Calculations additionally reveal that an LLZO bilayer with a planar LMA attached to the dense side and NCM811 infiltrated into the porous layer (75 vol. %) could lead to  $500 \text{ Wh kg}^{-1}$  being feasible.<sup>130</sup> However, it is questionable if this can actually be realized, as high interfacial resistances between NCM811 and garnet SEs as well as the low conductivity of the SE would severely limit the available cathode capacity when current densities of several  $\text{mA cm}^{-2}$  are applied.<sup>71,130</sup>

As of now, it can be concluded that the slow vacancy diffusion and detachment at planar metal|SE interfaces during stripping poses a fundamental physicochemical challenge for the realization of practical current densities of several  $\text{mA cm}^{-2}$  when metal anodes are used. Mitigation strategies, such as applying high stack pressures, using liquid pore filling agents or three-dimensional interfaces exist and work to a certain extent. However, these concepts so far diminish the initially promised advantages of realizing an alkali metal as the anode material.

Future research is needed to understand if hybrid concepts are able to mitigate or avoid pore formation during cell discharge while keeping the advantages associated with using alkali metal electrodes. This fundamentally challenges the academic view of next-generation batteries having to be all-solid. If hybrid concepts show the best cell performance, they should be considered for use despite still employing liquid parts.

## 6 References

- (1) Shukla, P. R.; Skea, J.; Calvo Buendia, E.; Masson-Delmotte, V.; Pörtner, H.-O.; Roberts, D. C.; Zhai, P.; Slade, R.; Connors, S.; van Diemen, R.; Ferrat, M.; Haughey, E.; Luz, S.; Neogi, S.; Pathak, M.; Petzold, J.; Portugal Pereira, J.; Vyas, P.; Huntley, E.; Kissick, K.; Belkacemi, M.; Malley, J. *IPCC, 2019: Climate Change and Land: An IPCC Special Report on Climate Change, Desertification, Land Degradation, Sustainable Land Management, Food Security, and Greenhouse Gas Fluxes in Terrestrial Ecosystems*; 2019.
- (2) United Nations Framework Convention on Climate Change. Paris Agreement. Article 2(A). **2015**.
- (3) Wietschel, M.; Kühnbach, M.; Rüdiger, D. Die Aktuelle Treibhausgas-Emissionsbilanz von Elektrofahrzeugen in Deutschland. In *Working Paper Sustainability and Innovation*; 2019.
- (4) Schmidt, O.; Hawkes, A.; Gambhir, A.; Staffell, I. The Future Cost of Electrical Energy Storage Based on Experience Rates. *Nat. Energy* **2017**, *2*, 17110. <https://doi.org/10.1038/nenergy.2017.110>.
- (5) Larcher, D.; Tarascon, J. M. Towards Greener and More Sustainable Batteries for Electrical Energy Storage. *Nat. Chem.* **2014**, *7*, 19–29. <https://doi.org/10.1038/nchem.2085>.
- (6) Nitta, N.; Wu, F.; Lee, J. T.; Yushin, G. Li-Ion Battery Materials: Present and Future. *Mater. Today* **2015**, *18*, 252–264. <https://doi.org/10.1016/j.mattod.2014.10.040>.
- (7) Krauskopf, T.; Richter, F. H.; Zeier, W. G.; Janek, J. Physicochemical Concepts of the Lithium Metal Anode in Solid-State Batteries. *Chem. Rev.* **2020**, *120*, 7745–7794. <https://doi.org/10.1021/acs.chemrev.0c00431>.
- (8) Janek, J.; Zeier, W. G. A Solid Future for Battery Development. *Nat. Energy* **2016**, *1*, 16141. <https://doi.org/10.1038/nenergy.2016.141>.
- (9) Lee, Y.; Fujiki, S.; Jung, C.; Suzuki, N.; Yashiro, N.; Omoda, R.; Ko, D.; Shiratsuchi, T.; Sugimoto, T.; Ryu, S.; Ku, J. H.; Watanabe, T.; Park, Y.; Aihara, Y.; Im, D.; Han, I. T. High-Energy Long-Cycling All-Solid-State Lithium Metal Batteries Enabled by Silver-Carbon Composite Anodes. *Nat. Energy* **2020**, *5*, 299–308. <https://doi.org/10.1038/s41560-020-0575-z>.
- (10) Albertus, P.; Babinec, S.; Litzelman, S.; Newman, A. Status and Challenges in Enabling the Lithium Metal Electrode for High-Energy and Low-Cost Rechargeable Batteries. *Nat. Energy* **2018**, *3*, 16–21. <https://doi.org/10.1038/s41560-017-0047-2>.
- (11) Krauskopf, T.; Richter, F. H.; Zeier, W. G.; Janek, J. Physicochemical Concepts of the Lithium Metal Anode in Solid-State Batteries. *Chem. Rev.* **2020**, *120*, 7745–7794. <https://doi.org/10.1021/acs.chemrev.0c00431>.
- (12) Otto, S.; Riegger, L. M.; Fuchs, T.; Kayser, S.; Schweitzer, P.; Burkhardt, S.; Henss, A.; Janek, J. In Situ Investigation of Lithium Metal – Solid Electrolyte Anode Interfaces with ToF-SIMS. *Adv. Mater. Interfaces* **2022**, *2102387*. <https://doi.org/10.1002/admi.202102387>.

- (13) Wenzel, S.; Leichtweiss, T.; Krüger, D.; Sann, J.; Janek, J. Interphase Formation on Lithium Solid Electrolytes — An in Situ Approach to Study Interfacial Reactions by Photoelectron Spectroscopy. *Solid State Ionics* **2015**, *278*, 98–105. <https://doi.org/10.1016/j.ssi.2015.06.001>.
- (14) Zhu, Y.; He, X.; Mo, Y. Origin of Outstanding Stability in the Lithium Solid Electrolyte Materials: Insights from Thermodynamic Analyses Based on First-Principles Calculations. *ACS Appl. Mater. Interfaces* **2015**, *7*, 23685–23693. <https://doi.org/10.1021/acsami.5b07517>.
- (15) Ma, C.; Cheng, Y.; Yin, K.; Luo, J.; Sharafi, A.; Sakamoto, J.; Li, J.; More, K. L.; Dudney, N. J.; Chi, M. Interfacial Stability of Li Metal-Solid Electrolyte Elucidated via in Situ Electron Microscopy. *Nano Lett.* **2016**, *16*, 7030–7036. <https://doi.org/10.1021/acs.nanolett.6b03223>.
- (16) Connell, J. G.; Fuchs, T.; Hartmann, H.; Krauskopf, T.; Zhu, Y.; Sann, J.; Garcia-mendez, R.; Sakamoto, J.; Tepavcevic, S.; Janek, J. Kinetic versus Thermodynamic Stability of LLZO in Contact with Lithium Metal. *Chem. Mater.* **2020**, *32*, 10207–10215. <https://doi.org/10.1021/acs.chemmater.0c03869>.
- (17) Otto, S. K.; Fuchs, T.; Moryson, Y.; Lerch, C.; Mogwitz, B.; Sann, J.; Janek, J.; Henss, A. Storage of Lithium Metal: The Role of the Native Passivation Layer for the Anode Interface Resistance in Solid State Batteries. *ACS Appl. Energy Mater.* **2021**, *4*, 12798–12807. <https://doi.org/10.1021/acsaem.1c02481>.
- (18) Otto, S. K.; Moryson, Y.; Krauskopf, T.; Peppler, K.; Sann, J.; Janek, J.; Henss, A. In-Depth Characterization of Lithium-Metal Surfaces with XPS and ToF-SIMS: Toward Better Understanding of the Passivation Layer. *Chem. Mater.* **2021**, *33*, 859–867. <https://doi.org/10.1021/acs.chemmater.0c03518>.
- (19) Wang, M. J.; Carmona, E.; Gupta, A.; Albertus, P.; Sakamoto, J. Enabling “Lithium-Free” Manufacturing of Pure Lithium Metal Solid-State Batteries through in Situ Plating. *Nat. Commun.* **2020**, *11*, 5201. <https://doi.org/10.1038/s41467-020-19004-4>.
- (20) Neudecker, B. J.; Dudney, N. J.; Bates, J. B. “Lithium-Free” Thin-Film Battery with In Situ Plated Li Anode. *J. Electrochem. Soc.* **2000**, *147*, 517–523. <https://doi.org/10.1149/1.1393226>.
- (21) Krauskopf, T.; Dippel, R.; Hartmann, H.; Peppler, K.; Mogwitz, B.; Richter, F. H.; Zeier, W. G.; Janek, J. Lithium-Metal Growth Kinetics on LLZO Garnet-Type Solid Electrolytes. *Joule* **2019**, *3*, 2030–2049. <https://doi.org/10.1016/j.joule.2019.06.013>.
- (22) Strauss, F.; de Biasi, L.; Kim, A.-Y.; Hertle, J.; Schweidler, S.; Janek, J.; Hartmann, P.; Brezesinski, T. Rational Design of Quasi-Zero-Strain NCM Cathode Materials for Minimizing Volume Change Effects in All-Solid-State Batteries. *ACS Mater. Lett.* **2020**, *2*, 84–88. <https://doi.org/10.1021/acsmaterialslett.9b00441>.
- (23) Goodenough, J. B.; Park, K. S. The Li-Ion Rechargeable Battery: A Perspective. *J. Am. Chem. Soc.* **2013**, *135*, 1167–1176. <https://doi.org/10.1021/ja3091438>.
- (24) Holme, T. A Discussion of QuantumScape’s Battery Technology Performance Results, <https://www.quantumscape.com/resources/blog/a-discussion-of-quantumscares-battery-technology-performance-results/>, accessed at 16th of

- December 2022.
- (25) Nie, K.; Hong, Y.; Qiu, J.; Li, Q.; Yu, X.; Li, H.; Chen, L. Interfaces between Cathode and Electrolyte in Solid State Lithium Batteries: Challenges and Perspectives. *Front. Chem.* **2018**, *6*, 616. <https://doi.org/10.3389/fchem.2018.00616>.
- (26) Koerver, R.; Aygün, I.; Leichtweiß, T.; Dietrich, C.; Zhang, W.; Binder, J. O.; Hartmann, P.; Zeier, W. G.; Janek, J. Capacity Fade in Solid-State Batteries: Interphase Formation and Chemomechanical Processes in Nickel-Rich Layered Oxide Cathodes and Lithium Thiophosphate Solid Electrolytes. *Chem. Mater.* **2017**, *29*, 5574–5582. <https://doi.org/10.1021/acs.chemmater.7b00931>.
- (27) Ruess, R.; Schweidler, S.; Hemmelmann, H.; Conforto, G.; Bielefeld, A.; Weber, D. A.; Sann, J.; Elm, M. T.; Janek, J. Influence of NCM Particle Cracking on Kinetics of Lithium-Ion Batteries with Liquid or Solid Electrolyte. *J. Electrochem. Soc.* **2020**, *167*, 100532. <https://doi.org/10.1149/1945-7111/ab9a2c>.
- (28) Ye, L.; Li, X. A Dynamic Stability Design Strategy for Lithium Metal Solid State Batteries. *Nature* **2021**, *593*, 218–222. <https://doi.org/10.1038/s41586-021-03486-3>.
- (29) Zahiri, B.; Patra, A.; Kiggins, C.; Yong, A. X. Bin; Ertekin, E.; Cook, J. B.; Braun, P. V. Revealing the Role of the Cathode–Electrolyte Interface on Solid-State Batteries. *Nat. Mater.* **2021**, *20*, 1392–1400. <https://doi.org/10.1038/s41563-021-01016-0>.
- (30) Kwak, H.; Han, D.; Lyoo, J.; Park, J.; Jung, S. H.; Han, Y.; Kwon, G.; Kim, H.; Hong, S. T.; Nam, K. W.; Jung, Y. S. New Cost-Effective Halide Solid Electrolytes for All-Solid-State Batteries: Mechanochemically Prepared Fe<sup>3+</sup>-Substituted Li<sub>2</sub>ZrCl<sub>6</sub>. *Adv. Energy Mater.* **2021**, *11*, 2003190. <https://doi.org/10.1002/aenm.202003190>.
- (31) Koerver, R.; Zhang, W.; De Biasi, L.; Schweidler, S.; Kondrakov, A. O.; Kolling, S.; Brezesinski, T.; Hartmann, P.; Zeier, W. G.; Janek, J. Chemo-Mechanical Expansion of Lithium Electrode Materials-on the Route to Mechanically Optimized All-Solid-State Batteries. *Energy Environ. Sci.* **2018**, *11*, 2142–2158. <https://doi.org/10.1039/c8ee00907d>.
- (32) Krauskopf, T.; Hartmann, H.; Zeier, W. G.; Janek, J. Toward a Fundamental Understanding of the Lithium Metal Anode in Solid-State Batteries - An Electrochemo-Mechanical Study on the Garnet-Type Solid Electrolyte Li<sub>6.25</sub>Al<sub>0.25</sub>La<sub>3</sub>Zr<sub>2</sub>O<sub>12</sub>. *ACS Appl. Mater. Interfaces* **2019**, *11*, 14463–14477. <https://doi.org/10.1021/acsami.9b02537>.
- (33) Krauskopf, T.; Mogwitz, B.; Rosenbach, C.; Zeier, W. G.; Janek, J. Diffusion Limitation of Lithium Metal and Li–Mg Alloy Anodes on LLZO Type Solid Electrolytes as a Function of Temperature and Pressure. *Adv. Energy Mater.* **2019**, *9*, 1902568. <https://doi.org/10.1002/aenm.201902568>.
- (34) Raj, V.; Venturi, V.; Kankanallu, V. R.; Kuiri, B.; Viswanathan, V.; Aetukuri, N. P. B. Direct Correlation between Void Formation and Lithium Dendrite Growth in Solid-State Electrolytes with Interlayers. *Nat. Mater.* **2022**, *21*, 1050–1056. <https://doi.org/10.1038/s41563-022-01264-8>.

- (35) Spencer Jolly, D.; Ning, Z.; Darnbrough, J. E.; Kasemchainan, J.; Hartley, G. O.; Adamson, P.; Armstrong, D. E. J.; Marrow, J.; Bruce, P. G. Sodium/Na B" Alumina Interface: Effect of Pressure on Voids. *ACS Appl. Mater. Interfaces* **2020**, *12*, 678–685. <https://doi.org/10.1021/acsami.9b17786>.
- (36) Kasemchainan, J.; Zekoll, S.; Spencer Jolly, D.; Ning, Z.; Hartley, G. O.; Marrow, J.; Bruce, P. G. Critical Stripping Current Leads to Dendrite Formation on Plating in Lithium Anode Solid Electrolyte Cells. *Nat. Mater.* **2019**, *18*, 1105–1111. <https://doi.org/10.1038/s41563-019-0438-9>.
- (37) Wang, M. J.; Choudhury, R.; Sakamoto, J. Characterizing the Li-Solid-Electrolyte Interface Dynamics as a Function of Stack Pressure and Current Density. *Joule* **2019**, *3*, 2165–2178. <https://doi.org/10.1016/j.joule.2019.06.017>.
- (38) Wang, C.; Gong, Y.; Liu, B.; Fu, K.; Yao, Y.; Hitz, E.; Li, Y.; Dai, J.; Xu, S.; Luo, W.; Wachsman, E. D.; Hu, L. Conformal, Nanoscale ZnO Surface Modification of Garnet-Based Solid-State Electrolyte for Lithium Metal Anodes. *Nano Lett.* **2017**, *17*, 565–571. <https://doi.org/10.1021/acs.nanolett.6b04695>.
- (39) Fuchs, T.; Mogwitz, B.; Otto, S.; Passerini, S.; Richter, F. H.; Janek, J. Working Principle of an Ionic Liquid Interlayer During Pressureless Lithium Stripping on  $\text{Li}_{6.25}\text{Al}_{0.25}\text{La}_3\text{Zr}_2\text{O}_{12}$  (LLZO) Garnet-Type Solid Electrolyte. *Batter. Supercaps* **2021**, *4*, 1145–1155. <https://doi.org/10.1002/batt.202100015>.
- (40) Fuchs, T.; Haslam, C. G.; Moy, A. C.; Lerch, C.; Krauskopf, T.; Sakamoto, J.; Richter, F. H.; Janek, J. Increasing the Pressure-Free Stripping Capacity of the Lithium Metal Anode in Solid-State-Batteries by Carbon Nanotubes. *Adv. Energy Mater.* **2022**, *12*, 2201125. <https://doi.org/10.1002/aenm.202201125>.
- (41) Zhu, Y.; He, X.; Mo, Y. First Principles Study on Electrochemical and Chemical Stability of Solid Electrolyte-Electrode Interfaces in All-Solid-State Li-Ion Batteries. *J. Mater. Chem. A* **2016**, *4*, 3253–3266. <https://doi.org/10.1039/c5ta08574h>.
- (42) Liu, X.; Garcia-Mendez, R.; Lupini, A. R.; Cheng, Y.; Hood, Z. D.; Han, F.; Sharafi, A.; Idrobo, J. C.; Dudney, N. J.; Wang, C.; Ma, C.; Sakamoto, J.; Chi, M. Local Electronic Structure Variation Resulting in Li ‘Filament’ Formation within Solid Electrolytes. *Nat. Mater.* **2021**, *20*, 1485–1490. <https://doi.org/10.1038/s41563-021-01019-x>.
- (43) Wenzel, S.; Leichtweiss, T.; Weber, D. A.; Sann, J.; Zeier, W. G.; Janek, J. Interfacial Reactivity Benchmarking of the Sodium Ion Conductors  $\text{Na}_3\text{PS}_4$  and Sodium  $\beta$ -Alumina for Protected Sodium Metal Anodes and Sodium All-Solid-State Batteries. *ACS Appl. Mater. Interfaces* **2016**, *8*, 28216–28224. <https://doi.org/10.1021/acsami.6b10119>.
- (44) Tong, Z.; Wang, S. B.; Liao, Y. K.; Hu, S. F.; Liu, R. S. Interface between Solid-State Electrolytes and Li-Metal Anodes: Issues, Materials, and Processing Routes. *ACS Appl. Mater. Interfaces* **2020**, *12*, 47181–47196. <https://doi.org/10.1021/acsami.0c13591>.
- (45) Hartmann, P.; Leichtweiss, T.; Busche, M. R.; Schneider, M.; Reich, M.; Sann, J.; Adelhelm, P.; Janek, J. Degradation of NASICON-Type Materials in Contact with Lithium Metal: Formation of Mixed Conducting Interphases (MCI) on Solid

- Electrolytes. *J. Phys. Chem. C* **2013**, *117*, 21064–21074. <https://doi.org/10.1021/jp4051275>.
- (46) Krauskopf, T.; Mogwitz, B.; Hartmann, H.; Singh, D. K.; Zeier, W. G.; Janek, J. The Fast Charge Transfer Kinetics of the Lithium Metal Anode on the Garnet-Type Solid Electrolyte  $\text{Li}_{6.25}\text{Al}_{0.25}\text{La}_3\text{Zr}_2\text{O}_{12}$ . *Adv. Energy Mater.* **2020**, *10*, 2000945. <https://doi.org/10.1002/aenm.202000945>.
- (47) Zhu, Y.; Connell, J. G.; Tepavcevic, S.; Zapol, P.; Garcia-Mendez, R.; Taylor, N. J.; Sakamoto, J.; Ingram, B. J.; Curtiss, L. A.; Freeland, J. W.; Fong, D. D.; Markovic, N. M. Dopant-Dependent Stability of Garnet Solid Electrolyte Interfaces with Lithium Metal. *Adv. Energy Mater.* **2019**, *9*, 1803440. <https://doi.org/10.1002/aenm.201803440>.
- (48) Tsai, C.; Thuy Tran, N. T.; Schierholz, R.; Liu, Z.; Windmüller, A.; Lin, C. A.; Xu, Q.; Lu, X.; Yu, S.; Tempel, H.; Kungl, H.; Lin, S. K.; Eichel, R. A. Instability of Ga-Substituted  $\text{Li}_7\text{La}_3\text{Zr}_2\text{O}_{12}$  toward Metallic Li. *J. Mater. Chem. A* **2022**, 10998–11009. <https://doi.org/10.1039/d1ta10215j>.
- (49) Buschmann, H.; Berendts, S.; Mogwitz, B.; Janek, J. Lithium Metal Electrode Kinetics and Ionic Conductivity of the Solid Lithium Ion Conductors “ $\text{Li}_7\text{La}_3\text{Zr}_2\text{O}_{12}$ ” and  $\text{Li}_{7-x}\text{La}_3\text{Zr}_{2-x}\text{Ta}_x\text{O}_{12}$  with Garnet-Type Structure. *J. Power Sources* **2012**, *206*, 236–244. <https://doi.org/10.1016/j.jpowsour.2012.01.094>.
- (50) Sharafi, A.; Kazyak, E.; Davis, A. L.; Yu, S.; Thompson, T.; Siegel, D. J.; Dasgupta, N. P.; Sakamoto, J. Surface Chemistry Mechanism of Ultra-Low Interfacial Resistance in the Solid-State Electrolyte  $\text{Li}_7\text{La}_3\text{Zr}_2\text{O}_{12}$ . *Chem. Mater.* **2017**, *29*, 7961–7968. <https://doi.org/10.1021/acs.chemmater.7b03002>.
- (51) Kim, S.; Kim, J. S.; Miara, L.; Wang, Y.; Jung, S. K.; Park, S. Y.; Song, Z.; Kim, H.; Badding, M.; Chang, J. M.; Roev, V.; Yoon, G.; Kim, R.; Kim, J. H.; Yoon, K.; Im, D.; Kang, K. High-Energy and Durable Lithium Metal Batteries Using Garnet-Type Solid Electrolytes with Tailored Lithium-Metal Compatibility. *Nat. Commun.* **2022**, *13*, 1883. <https://doi.org/10.1038/s41467-022-29531-x>.
- (52) Williams, J. S. Ion Implantation of Semiconductors. *Mater. Sci. Eng.* **1988**, *A253*, 38–52. <https://doi.org/10.1179/imr.1988.33.1.38>.
- (53) Okumura, H.; Suihkonen, S.; Lemettinen, J.; Uedono, A.; Zhang, Y.; Piedra, D.; Palacios, T. AlN Metal–Semiconductor Field-Effect Transistors Using Si-Ion Implantation. *Jpn. J. Appl. Phys.* **2018**, *57*, 04FR11. <https://doi.org/10.7567/JJAP.57.04FR11>.
- (54) Chu, P. K.; Qin, S.; Chan, C.; Cheung, N. W.; Larson, L. A. Plasma Immersion Ion Implantation—a Fledgling Technique for Semiconductor Processing. *Mater. Sci. Eng. R Reports* **1996**, *17*, 207–280. [https://doi.org/10.1016/S0927-796X\(96\)00194-5](https://doi.org/10.1016/S0927-796X(96)00194-5).
- (55) Haarmann, L.; Rohrer, J.; Albe, K. On the Origin of Zero Interface Resistance in the  $\text{Li}_{6.25}\text{Al}_{0.25}\text{La}_3\text{Zr}_2\text{O}_{12}|\text{Li}^0$  System: An Atomistic Investigation. *ACS Appl. Mater. Interfaces* **2021**, *13*, 52629–52635. <https://doi.org/10.1021/acsami.1c15400>.
- (56) Kim, S.; Yoon, G.; Jung, S. K.; Park, S.; Kim, J. S.; Yoon, K.; Lee, S.; Kang, K. High-Power Hybrid Solid-State Lithium-Metal Batteries Enabled by Preferred Directional Lithium Growth Mechanism. *ACS Energy Lett.* **2023**, *8*, 9–20.

- <https://doi.org/10.1021/acseenergylett.2c02150>.
- (57) Randau, S.; Weber, D. A.; Kötz, O.; Koerver, R.; Braun, P.; Weber, A.; Ivers-Tiffée, E.; Adermann, T.; Kulisch, J.; Zeier, W. G.; Richter, F. H.; Janek, J. Benchmarking the Performance of All-Solid-State Lithium Batteries. *Nat. Energy* **2020**, *5*, 259–270. <https://doi.org/10.1038/s41560-020-0565-1>.
- (58) Liu, F.; Xu, R.; Wu, Y.; Boyle, D. T.; Yang, A.; Xu, J.; Zhu, Y.; Ye, Y.; Yu, Z.; Zhang, Z.; Xiao, X.; Huang, W.; Wang, H.; Chen, H.; Cui, Y. Dynamic Spatial Progression of Isolated Lithium during Battery Operations. *Nature* **2021**, *600*, 659–663. <https://doi.org/10.1038/s41586-021-04168-w>.
- (59) Pei, A.; Zheng, G.; Shi, F.; Li, Y.; Cui, Y. Nanoscale Nucleation and Growth of Electrodeposited Lithium Metal. *Nano Lett.* **2017**, *17*, 1132–1139. <https://doi.org/10.1021/acs.nanolett.6b04755>.
- (60) Motoyama, M.; Hirota, M.; Yamamoto, T.; Iriyama, Y. Temperature Effects on Li Nucleation at Cu/LiPON Interfaces. *ACS Appl. Mater. Interfaces* **2020**, *12*, 38045–38053. <https://doi.org/10.1021/acsami.0c02354>.
- (61) Motoyama, M.; Ejiri, M.; Iriyama, Y. In-Situ Electron Microscope Observations of Electrochemical Li Deposition/Dissolution with a LiPON Electrolyte. *Electrochemistry* **2014**, *82*, 364–368. <https://doi.org/10.5796/electrochemistry.82.364>.
- (62) Motoyama, M.; Ejiri, M.; Yamamoto, T.; Iriyama, Y. In Situ Scanning Electron Microscope Observations of Li Plating/Stripping Reactions with Pt Current Collectors on LiPON Electrolyte. *J. Electrochem. Soc.* **2018**, *165*, A1338–A1347. <https://doi.org/10.1149/2.0411807jes>.
- (63) Kazyak, E.; Wang, M. J.; Lee, K.; Yadavalli, S.; Sanchez, A. J.; Thouless, M. D.; Sakamoto, J.; Dasgupta, N. P. Understanding the Electro-Chemo-Mechanics of Li Plating in Anode-Free Solid-State Batteries with Operando 3D Microscopy. *Matter* **2022**, *5*, 3912–3934. <https://doi.org/10.1016/j.matt.2022.07.020>.
- (64) Lv, S.; Verhallen, T.; Vasileiadis, A.; Ooms, F.; Xu, Y.; Li, Z.; Li, Z.; Wagemaker, M. Operando Monitoring the Lithium Spatial Distribution of Lithium Metal Anodes. *Nat. Commun.* **2018**, *9*, 2152. <https://doi.org/10.1038/s41467-018-04394-3>.
- (65) Klemm, W.; Volavsek, B. Zur Kenntnis Des Systems Lithium-Kupfer. *Zeitschrift für Anorg. und Allg. Chemie* **1958**, *296*, 184–187. <https://doi.org/10.1002/zaac.19582960118>.
- (66) Rupp, R.; Caerts, B.; Vantomme, A.; Fransaer, J.; Vlad, A. Lithium Diffusion in Copper. *J. Phys. Chem. Lett.* **2019**, *10*, 5206–5210. <https://doi.org/10.1021/acs.jpcllett.9b02014>.
- (67) Okamoto, H. Cu-Li (Copper-Lithium). *J. Phase Equilibria Diffus.* **2011**, *32*, 172. <https://doi.org/10.1007/s11669-010-9840-3>.
- (68) Pelton, A. D. The Ag–Li (Silver-Lithium) System. *Bull. Alloy Phase Diagrams* **1986**, *7*, 223–228. <https://doi.org/10.1007/bf02868993>.

- (69) Solchenbach, S.; Pritzl, D.; Kong, E. J. Y.; Landesfeind, J.; Gasteiger, H. A. A Gold Micro-Reference Electrode for Impedance and Potential Measurements in Lithium Ion Batteries. *J. Electrochem. Soc.* **2016**, *163*, A2265–A2272. <https://doi.org/10.1149/2.0581610jes>.
- (70) Bielefeld, A.; Weber, D. A.; Janek, J. Microstructural Modeling of Composite Cathodes for All-Solid-State Batteries. *J. Phys. Chem. C* **2019**, *123*, 1626–1634. <https://doi.org/10.1021/acs.jpcc.8b11043>.
- (71) Bielefeld, A.; Weber, D. A.; Janek, J. Modeling Effective Ionic Conductivity and Binder Influence in Composite Cathodes for All-Solid-State Batteries. *ACS Appl. Mater. Interfaces* **2020**, *12*, 12821–12833. <https://doi.org/10.1021/acsami.9b22788>.
- (72) Minnmann, P.; Quillmann, L.; Burkhardt, S.; Richter, F. H.; Janek, J. Quantifying the Impact of Charge Transport Bottlenecks in Composite Cathodes of All-Solid-State Batteries. *J. Electrochem. Soc.* **2021**, *168*, 040537. <https://doi.org/10.1149/1945-7111/abf8d7>.
- (73) Motoyama, M.; Ejiri, M.; Iriyama, Y. Modeling the Nucleation and Growth of Li at Metal Current Collector/LiPON Interfaces. *J. Electrochem. Soc.* **2015**, *162*, A7067–A7071. <https://doi.org/10.1149/2.0051513jes>.
- (74) Sharafi, A.; Haslam, C. G.; Kerns, R. D.; Wolfenstine, J.; Sakamoto, J. Controlling and Correlating the Effect of Grain Size with the Mechanical and Electrochemical Properties of  $\text{Li}_7\text{La}_3\text{Zr}_2\text{O}_{12}$  Solid-State Electrolyte. *J. Mater. Chem. A* **2017**, *5*, 21491–21504. <https://doi.org/10.1039/c7ta06790a>.
- (75) Flatscher, F.; Philipp, M.; Ganschow, S.; Wilkening, H. M. R.; Rettenwander, D. The Natural Critical Current Density Limit for  $\text{Li}_7\text{La}_3\text{Zr}_2\text{O}_{12}$  Garnets. *J. Mater. Chem. A* **2020**, *8*, 15782–15788. <https://doi.org/10.1039/c9ta14177d>.
- (76) Sharafi, A.; Meyer, H. M.; Nanda, J.; Wolfenstine, J.; Sakamoto, J. Characterizing the Li- $\text{Li}_7\text{La}_3\text{Zr}_2\text{O}_{12}$  Interface Stability and Kinetics as a Function of Temperature and Current Density. *J. Power Sources* **2016**, *302*, 135–139. <https://doi.org/10.1016/j.jpowsour.2015.10.053>.
- (77) Porz, L.; Swamy, T.; Sheldon, B. W.; Rettenwander, D.; Frömling, T.; Thaman, H. L.; Berendts, S.; Uecker, R.; Carter, W. C.; Chiang, Y. M. Mechanism of Lithium Metal Penetration through Inorganic Solid Electrolytes. *Adv. Energy Mater.* **2017**, *7*, 1701003. <https://doi.org/10.1002/aenm.201701003>.
- (78) Taylor, N. J.; Stangeland-Molo, S.; Haslam, C. G.; Sharafi, A.; Thompson, T.; Wang, M.; Garcia-Mendez, R.; Sakamoto, J. Demonstration of High Current Densities and Extended Cycling in the Garnet  $\text{Li}_7\text{La}_3\text{Zr}_2\text{O}_{12}$  Solid Electrolyte. *J. Power Sources* **2018**, *396*, 314–318. <https://doi.org/10.1016/j.jpowsour.2018.06.055>.
- (79) Kim, S.; Jung, C.; Kim, H.; Thomas-Alyea, K. E.; Yoon, G.; Kim, B.; Badding, M. E.; Song, Z.; Chang, J. M.; Kim, J.; Im, D.; Kang, K. The Role of Interlayer Chemistry in Li-Metal Growth through a Garnet-Type Solid Electrolyte. *Adv. Energy Mater.* **2020**, *1903993*, 1–11. <https://doi.org/10.1002/aenm.201903993>.
- (80) Fuchs, T.; Becker, J.; Haslam, C. G.; Lerch, C.; Sakamoto, J.; Richter, F. H.; Janek, J. Current-Dependent Lithium Metal Growth Modes in “Anode-Free” Solid-

- State Batteries at the Cu|LLZO Interface. *Adv. Energy Mater.* **2022**, 2203174. <https://doi.org/10.1002/aenm.202203174>.
- (81) Schmalzried, H.; Janek, J. Chemical Kinetics of Phase Boundaries in Solids. *Ber. Bunsenges. Phys. Chem.* **1998**, *102*, 127–143. <https://doi.org/10.1038/242587a0>.
- (82) Jow, T. R.; Liang, C. C. Interface Between Solid Electrode and Solid Electrolyte—A Study of the Li/LiI (Al<sub>2</sub>O<sub>3</sub>) Solid-Electrolyte System. *J. Electrochem. Soc.* **1983**, *130*, 737–740. <https://doi.org/10.1149/1.2119795>.
- (83) Janek, J.; Majoni, S. Investigation of Charge Transport Across the Ag|AgI-Interface: (I) Occurrence of Periodic Phenomena During Anodic Dissolution of Silver. *Ber. Bunsenges. Phys. Chem.* **1995**, *99*, 14–20. <https://doi.org/10.1002/bbpc.19950990104>.
- (84) Shishvan, S. S.; Fleck, N. A.; Deshpande, V. S. The Initiation of Void Growth during Stripping of Li Electrodes in Solid Electrolyte Cells. *J. Power Sources* **2021**, *488*, 229437. <https://doi.org/10.1016/j.jpowsour.2020.229437>.
- (85) Agier, J. A. B.; Shishvan, S. S.; Fleck, N. A.; Deshpande, V. S. Void Growth within Li Electrodes in Solid Electrolyte Cells. *Acta Mater.* **2022**, *240*, 118303. <https://doi.org/10.1016/j.actamat.2022.118303>.
- (86) Haarmann, L.; Fuchs, T.; Rohrer, J.; Janek, J.; Albe, K. On the Cause of Pore Formation and the Limitation of Pore Annihilation at Lithium Metal|solid Electrolyte Interfaces. *in preparation* **2022**.
- (87) Seymour, I.; Aguadero, A. Suppressing Void Formation in All-Solid-State Batteries: The Role of Interfacial Adhesion on Alkali Metal Vacancy Transport. *J. Mater. Chem. A* **2021**, *9*, 19901–19913. <https://doi.org/10.1039/D1TA03254B>.
- (88) Lu, Y.; Zhao, C.; Hu, J.; Sun, S.; Yuan, H.; Fu, Z.; Chen, X.; Huang, J.-Q.; Ouyang, M.; Zhang, Q. The Void Formation Behaviors in Working Solid-State Li Metal Batteries. *Sci. Adv.* **2022**, *8*, eadd0510. <https://doi.org/10.1126/sciadv.add0510>.
- (89) Barai, P.; Fuchs, T.; Trevisanello, E.; Richter, F. H.; Janek, J.; Srinivasan, V. Phase Field Based Modeling of the Void Formation Mechanism at the Lithium-Metal|Solid-Electrolyte Interface. *in preparation* **2022**.
- (90) Fleig, J.; Maier, J. The Influence of Current Constriction on the Impedance of Polarizable Electrodes: Application to Fuel Cell Electrodes. *J. Electrochem. Soc.* **1997**, *144*, L302–L305. <https://doi.org/10.1149/1.1838076>.
- (91) Fleig, J.; Pham, P.; Sztulzaft, P.; Maier, J. Inhomogeneous Current Distributions at Grain Boundaries and Electrodes and Their Impact on the Impedance. *Solid State Ionics* **1998**, *113–115*, 739–747. [https://doi.org/10.1016/s0167-2738\(98\)00400-7](https://doi.org/10.1016/s0167-2738(98)00400-7).
- (92) Fleig, J.; Maier, J. The Impedance of Ceramics with Highly Resistive Grain Boundaries: Validity and Limits of the Brick Layer Model. *J. Eur. Ceram. Soc.* **1999**, *19*, 693–696. [https://doi.org/10.1016/s0955-2219\(98\)00298-2](https://doi.org/10.1016/s0955-2219(98)00298-2).
- (93) Fleig, J.; Maier, J. Point Contacts in Solid State Ionics: Finite Element Calculations and Local Conductivity Measurements. *Solid State Ionics* **1996**, *86–88*, 1351–1356. [https://doi.org/10.1016/0167-2738\(96\)00316-5](https://doi.org/10.1016/0167-2738(96)00316-5).

- (94) Irvine, J. T. S.; Sinclair, D. C.; West, A. R. Electroceramics: Characterization by Impedance Spectroscopy. *Adv. Mater.* **1990**, *2*, 132–138. <https://doi.org/10.1002/adma.19900020304>.
- (95) Eckhardt, J. K.; Klar, P. J.; Janek, J.; Heiliger, C. Interplay of Dynamic Constriction and Interface Morphology between Reversible Metal Anode and Solid Electrolyte in Solid State Batteries. *ACS Appl. Mater. Interfaces* **2022**, *14*, 35545–35554. <https://doi.org/10.1021/acsami.2c07077>.
- (96) Eckhardt, J. K.; Fuchs, T.; Burkhardt, S.; Klar, P. J.; Janek, J.; Heiliger, C. 3D Impedance Modeling of Metal Anodes in Solid-State Batteries – Incompatibility of Pore Formation and Constriction Effect in Physical-Based 1D Circuit Models. *ACS Appl. Mater. Interfaces* **2022**, *14*, 42757–42769. <https://doi.org/https://doi.org/10.1021/acsami.2c12991>.
- (97) Eckhardt, J. K.; Fuchs, T.; Klar, P. J.; Janek, J.; Heiliger, C. Recipe for Analyzing the Impedance Response of the Metal Anode Interface of All-Solid-State Batteries. *in preparation* **2022**.
- (98) Wang, M.; Wolfenstine, J. B.; Sakamoto, J. Temperature Dependent Flux Balance of the Li/Li<sub>7</sub>La<sub>3</sub>Zr<sub>2</sub>O<sub>12</sub> Interface. *Electrochim. Acta* **2019**, *296*, 842–847. <https://doi.org/10.1016/j.electacta.2018.11.034>.
- (99) Tsai, C. L.; Roddatis, V.; Chandran, C. V.; Ma, Q.; Uhlenbruck, S.; Bram, M.; Heitjans, P.; Guillon, O. Li<sub>7</sub>La<sub>3</sub>Zr<sub>2</sub>O<sub>12</sub> Interface Modification for Li Dendrite Prevention. *ACS Appl. Mater. Interfaces* **2016**, *8*, 10617–10626. <https://doi.org/10.1021/acsami.6b00831>.
- (100) Kinzer, B.; Davis, A. L.; Krauskopf, T.; Hartmann, H.; LePage, W. S.; Kazyak, E.; Janek, J.; Dasgupta, N. P.; Sakamoto, J. Operando Analysis of the Molten Li|LLZO Interface: Understanding How the Physical Properties of Li Affect the Critical Current Density. *Matter* **2021**, *4*, 1947–1691. <https://doi.org/10.1016/j.matt.2021.04.016>.
- (101) Andersson, A. M.; Edström, K. Chemical Composition and Morphology of the Elevated Temperature SEI on Graphite. *J. Electrochem. Soc.* **2001**, *148*, A1100–A1109. <https://doi.org/10.1149/1.1397771>.
- (102) LePage, W. S.; Chen, Y.; Kazyak, E.; Chen, K.-H.; Sanchez, A. J.; Poli, A.; Arruda, E. M.; Thouless, M. D.; Dasgupta, N. P. Lithium Mechanics: Roles of Strain Rate and Temperature and Implications for Lithium Metal Batteries. *J. Electrochem. Soc.* **2019**, *166*, A89–A97. <https://doi.org/10.1149/2.0221902jes>.
- (103) Masias, A.; Felten, N.; Garcia-Mendez, R.; Wolfenstine, J.; Sakamoto, J. Elastic, Plastic, and Creep Mechanical Properties of Lithium Metal. *J. Mater. Sci.* **2018**, *54*, 2585–2600. <https://doi.org/10.1007/s10853-018-2971-3>.
- (104) Haslam, C. G.; Wolfenstine, J.; Sakamoto, J. The Effect of Aspect Ratio on the Mechanical Behavior of Li Metal in Solid-State Cells. *J. Power Sources* **2022**, *520*, 230831. <https://doi.org/https://doi.org/10.1016/j.jpowsour.2021.230831>.
- (105) Janek, J. *Zum Ladungsdurchtritt an Phasengrenzen in Festkörpern. Habilitation*; Universität Hannover: Hannover, 1997.
- (106) Campbell, C.; Lee, Y. M.; Cho, K. Y.; Lee, Y. G.; Lee, B.; Phatak, C.; Hong, S.

- Effect of Nanopatterning on Mechanical Properties of Lithium Anode. *Sci. Rep.* **2018**, *8*, 2514. <https://doi.org/10.1038/s41598-018-20773-8>.
- (107) Singh, D. K.; Fuchs, T.; Krempaszky, C.; Mogwitz, B.; Burkhardt, S.; Richter, F. H.; Janek, J. Overcoming Anode Instability in Solid-State Batteries through Control of the Lithium Metal Microstructure. *Adv. Funct. Mater.* **2022**, 2211067. <https://doi.org/10.1002/adfm.202211067>.
- (108) Liu, B.; Zhang, L.; Xu, S.; McOwen, D. W.; Gong, Y.; Yang, C.; Pastel, G. R.; Xie, H.; Fu, K.; Dai, J.; Chen, C.; Wachsman, E. D.; Hu, L. 3D Lithium Metal Anodes Hosted in Asymmetric Garnet Frameworks toward High Energy Density Batteries. *Energy Storage Mater.* **2018**, *14*, 376–382. <https://doi.org/10.1016/j.ensm.2018.04.015>.
- (109) Hitz, G. T.; McOwen, D. W.; Zhang, L.; Ma, Z.; Fu, Z.; Wen, Y.; Gong, Y.; Dai, J.; Hamann, T. R.; Hu, L.; Wachsman, E. D. High-Rate Lithium Cycling in a Scalable Trilayer Li-Garnet-Electrolyte Architecture. *Mater. Today* **2019**, *22*, 50–57. <https://doi.org/10.1016/j.mattod.2018.04.004>.
- (110) Liu, B.; Gong, Y.; Fu, K.; Han, X.; Yao, Y.; Pastel, G.; Yang, C.; Xie, H.; Wachsman, E. D.; Hu, L. Garnet Solid Electrolyte Protected Li-Metal Batteries. *ACS Appl. Mater. Interfaces* **2017**, *9*, 18809–18815. <https://doi.org/10.1021/acsami.7b03887>.
- (111) Fu, K.; Gong, Y.; Hitz, G. T.; McOwen, D. W.; Li, Y.; Xu, S.; Wen, Y.; Zhang, L.; Wang, C.; Pastel, G.; Dai, J.; Liu, B.; Xie, H.; Yao, Y.; Wachsman, E. D.; Hu, L. Three-Dimensional Bilayer Garnet Solid Electrolyte Based High Energy Density Lithium Metal-Sulfur Batteries. *Energy Environ. Sci.* **2017**, *10*, 1568–1575. <https://doi.org/10.1039/c7ee01004d>.
- (112) Huo, H.; Chen, Y.; Li, R.; Zhao, N.; Luo, J.; Pereira Da Silva, J. G.; Mücke, R.; Kaghazchi, P.; Guo, X.; Sun, X. Design of a Mixed Conductive Garnet/Li Interface for Dendrite-Free Solid Lithium Metal Batteries. *Energy Environ. Sci.* **2020**, *13*, 127–134. <https://doi.org/10.1039/c9ee01903k>.
- (113) Huo, H.; Chen, Y.; Zhao, N.; Lin, X.; Luo, J.; Yang, X.; Liu, Y.; Guo, X.; Sun, X. In-Situ Formed Li<sub>2</sub>CO<sub>3</sub>-Free Garnet/Li Interface by Rapid Acid Treatment for Dendrite-Free Solid-State Batteries. *Nano Energy* **2019**, *61*, 119–125. <https://doi.org/10.1016/j.nanoen.2019.04.058>.
- (114) Flatscher, F.; Philipp, M.; Ganschow, S.; Wilkening, H. M. R.; Rettenwander, D. The Natural Critical Current Density Limit for Li<sub>7</sub>La<sub>3</sub>Zr<sub>2</sub>O<sub>12</sub> Garnets. *J. Mater. Chem. A* **2020**, 15782–15788. <https://doi.org/10.1039/c9ta14177d>.
- (115) Zheng, H.; Wu, S.; Tian, R.; Xu, Z.; Zhu, H.; Duan, H.; Liu, H. Intrinsic Lithiophilicity of Li-Garnet Electrolytes Enabling High-Rate Lithium Cycling. *Adv. Funct. Mater.* **2020**, *30*. <https://doi.org/10.1002/adfm.201906189>.
- (116) Cui, J.; Yao, S.; Guerfi, A.; Kim, C.; Goodenough, J. B.; Khani, H. Melt-Quenching of Artificial Metallic Interlayer Enables a Resistance-Free Garnet/Lithium Interface for All-Solid-State Lithium-Metal Batteries. *Energy Storage Mater.* **2022**, *53*, 899–908. <https://doi.org/10.1016/j.ensm.2022.10.002>.
- (117) Herbert, E. G.; Tenhaeff, W. E.; Dudley, N. J.; Pharr, G. M. Mechanical Characterization of LiPON Films Using Nanoindentation. *Thin Solid Films* **2011**,

- 520, 413–418. <https://doi.org/10.1016/j.tsf.2011.07.068>.
- (118) Buschmann, H.; Dölle, J.; Berendts, S.; Kuhn, A.; Bottke, P.; Wilkening, M.; Heitjans, P.; Senyshyn, A.; Ehrenberg, H.; Lotnyk, A.; Duppel, V.; Kienle, L.; Janek, J. Structure and Dynamics of the Fast Lithium Ion Conductor “Li<sub>7</sub>La<sub>3</sub>Zr<sub>2</sub>O<sub>12</sub>”. *Phys. Chem. Chem. Phys.* **2011**, *13*, 19378–19392. <https://doi.org/10.1039/c1cp22108f>.
- (119) Cheng, L.; Chen, W.; Kunz, M.; Persson, K.; Tamura, N.; Chen, G.; Doeff, M. Effect of Surface Microstructure on Electrochemical Performance of Garnet Solid Electrolytes. *ACS Appl. Mater. Interfaces* **2015**, *7*, 2073–2081. <https://doi.org/10.1021/am508111r>.
- (120) Wang, M. J.; Kazyak, E.; Dasgupta, N. P.; Sakamoto, J. Transitioning Solid-State Batteries from Lab to Market: Linking Electro-Chemo-Mechanics with Practical Considerations. *Joule* **2021**, *5*, 1371–1390. <https://doi.org/10.1016/j.joule.2021.04.001>.
- (121) Ning, Z.; Jolly, D. S.; Li, G.; De Meyere, R.; Pu, S. D.; Chen, Y.; Kasemchainan, J.; Ihli, J.; Gong, C.; Liu, B.; Melvin, D. L. R.; Bonnin, A.; Magdysyuk, O.; Adamson, P.; Hartley, G. O.; Monroe, C. W.; Marrow, T. J.; Bruce, P. G. Visualizing Plating-Induced Cracking in Lithium-Anode Solid-Electrolyte Cells. *Nat. Mater.* **2021**, *20*, 1121–1129. <https://doi.org/10.1038/s41563-021-00967-8>.
- (122) Sharafi, A.; Yu, S.; Naguib, M.; Lee, M.; Ma, C.; Meyer, H. M.; Nanda, J.; Chi, M.; Siegel, D. J.; Sakamoto, J. Impact of Air Exposure and Surface Chemistry on Li-Li<sub>7</sub>La<sub>3</sub>Zr<sub>2</sub>O<sub>12</sub> interfacial Resistance. *J. Mater. Chem. A* **2017**, *5*, 13475–13487. <https://doi.org/10.1039/c7ta03162a>.
- (123) Zhao, B.; Ma, W.; Li, B.; Hu, X.; Lu, S.; Liu, X.; Jiang, Y.; Zhang, J. A Fast and Low-Cost Interface Modification Method to Achieve High-Performance Garnet-Based Solid-State Lithium Metal Batteries. *Nano Energy* **2022**, *91*, 106643. <https://doi.org/10.1016/j.nanoen.2021.106643>.
- (124) Cho, J. H.; Kim, K.; Chakravarthy, S.; Xiao, X.; Rupp, J. L. M.; Sheldon, B. W. An Investigation of Chemo-Mechanical Phenomena and Li Metal Penetration in All-Solid-State Lithium Metal Batteries Using In Situ Optical Curvature Measurements. *Adv. Energy Mater.* **2022**, *12*, 2200369. <https://doi.org/10.1002/aenm.202200369>.
- (125) Singh, D. K.; Henss, A.; Mogwitz, B.; Gautam, A.; Horn, J.; Krauskopf, T.; Burkhardt, S.; Sann, J.; Richter, F. H.; Janek, J. Li<sub>6</sub>PS<sub>5</sub>Cl Microstructure and Influence on Dendrite Growth in Solid-State Batteries with Lithium Metal Anode. *Cell Reports Phys. Sci.* **2022**, *3*, 101043. <https://doi.org/10.1016/j.xcrp.2022.101043>.
- (126) Pervez, S. A.; Kim, G.; Vinayan, B. P.; Cambaz, M. A.; Kuenzel, M.; Hekmatfar, M.; Fichtner, M.; Passerini, S. Overcoming the Interfacial Limitations Imposed by the Solid–Solid Interface in Solid-State Batteries Using Ionic Liquid-Based Interlayers. *Small* **2020**, *16*, 2000279. <https://doi.org/10.1002/smll.202000279>.
- (127) Ohno, S.; Zeier, W. G. Sodium Is the New Lithium. *Nat. Energy* **2022**, *7*, 686–687. <https://doi.org/10.1038/s41560-022-01084-9>.
- (128) European Commission. Critical Raw Materials Resilience: Charting a Path towards

- Greater Security and Sustainability; Brussels, 2020.  
<https://doi.org/10.4324/9781003001317-3>.
- (129) Ortmann, T.; Burkhardt, S.; Eckhardt, J. K.; Fuchs, T.; Ding, Z.; Sann, J.; Rohnke, M.; Ma, Q.; Tietz, F.; Fattakhova-Rohlfing, D.; Kübel, C.; Guillon, O.; Heiliger, C.; Janek, J. Kinetics and Pore Formation of the Sodium Metal Anode on NASICON-Type  $\text{Na}_{3.4}\text{Zr}_2\text{Si}_{2.4}\text{P}_{0.6}\text{O}_{12}$  for Sodium Solid-State Batteries. *Accepted at Adv. Energy Mater.* **2022**.
- (130) Ren, Y.; Danner, T.; Moy, A.; Finsterbusch, M.; Hamann, T.; Dippell, J.; Fuchs, T.; Müller, M.; Hoft, R.; Weber, A.; Curtiss, L. A.; Zapol, P.; Klenk, M.; Ngo, A. T.; Barai, P.; Wood, B. C.; Shi, R.; Wan, L. F.; Heo, T. W.; Engels, M.; Nanda, J.; Richter, F. H.; Latz, A.; Srinivasan, V.; Janek, J.; Sakamoto, J.; Wachsman, E. D.; Fattakhova-Rohlfing, D. Oxide-Based Solid-State Batteries: A Perspective on Composite Cathode Architecture. *Adv. Energy Mater.* **2022**, 2201939.  
<https://doi.org/10.1002/aenm.202201939>.

## 7 Appendix

### 7.1 Supporting Information

- 7.1.1 Publication 1: “Kinetic versus Thermodynamic Stability of LLZO in Contact with Lithium Metal”

## Supporting Information

### Kinetic versus Thermodynamic Stability of LLZO in Contact with Lithium Metal

Justin G. Connell<sup>†,‡,∇</sup>, Till Fuchs<sup>§,||,∇</sup>, Hannah Hartmann<sup>§,||</sup>, Thorben Krauskopf<sup>§</sup>, Yisi Zhu<sup>†</sup>,  
Joachim Sann<sup>§,||</sup>, Regina Garcia-Mendez<sup>⊥</sup>, Jeff Sakamoto<sup>⊥,‡</sup>, Sanja Tepavcevic<sup>\*,†</sup> and Jürgen  
Janek<sup>\*\*,§,||</sup>

<sup>†</sup>Materials Science Division, Argonne National Laboratory,  
Lemont, Illinois 60439, United States

<sup>‡</sup>Joint Center for Energy Storage Research, Argonne National Laboratory,  
Lemont, Illinois 60439, United States

<sup>§</sup>Institute of Physical Chemistry, Justus-Liebig-University Giessen,  
Heinrich-Buff-Ring 17, D-35392 Giessen, Germany

<sup>||</sup>Center for Materials Research (ZfM), Justus-Liebig-University Giessen,  
Heinrich-Buff-Ring 16, D-35392 Giessen, Germany

<sup>⊥</sup>Department of Materials Science and Engineering, University of Michigan,  
Ann Arbor, Michigan 48109, United States

<sup>#</sup>Department of Mechanical Engineering, University of Michigan,  
Ann Arbor, Michigan 48109, United States

<sup>∇</sup>J.G.C. and T.F. contributed equally to this work.

\*E-Mail: sanja@anl.gov

\*\*E-Mail: juergen.janek@pc.jlug.de

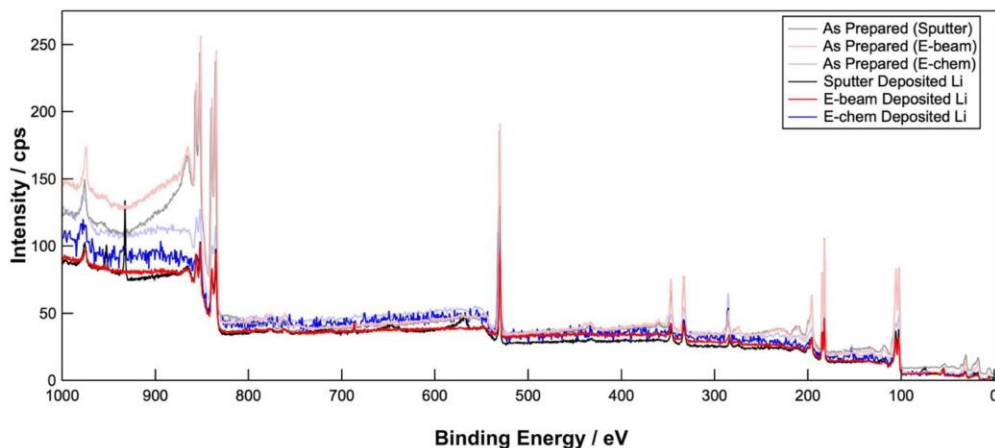


**Figure S1.** Comparison of XPS signal attenuation by Li deposition via sputtering and e-beam evaporation. Spectra for the electrochemically-deposited samples are scaled by a factor of 0.006 for comparison due to the different pass energies used to collect these spectra.

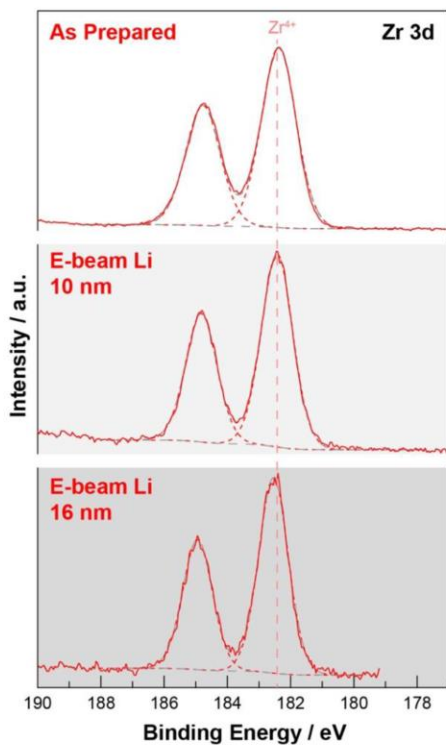


**Figure S2.** Comparison of the Zr 3d XPS signal depending on the thickness of Li deposited via e-beam. The 10 nm deposition was performed on hot-pressed LLZO and the 16 nm deposition was performed on sintered pellets. Both samples exhibited identical surface chemistry prior to Li deposition.

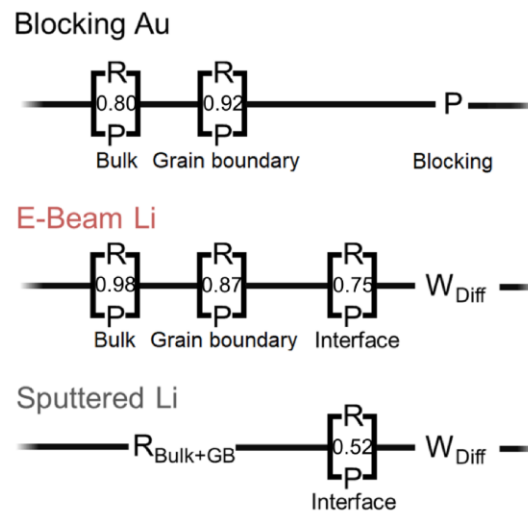


**Figure S3.** Equivalent circuits used for the different cell setups and EIS measurements including alpha-values for each R-P element.

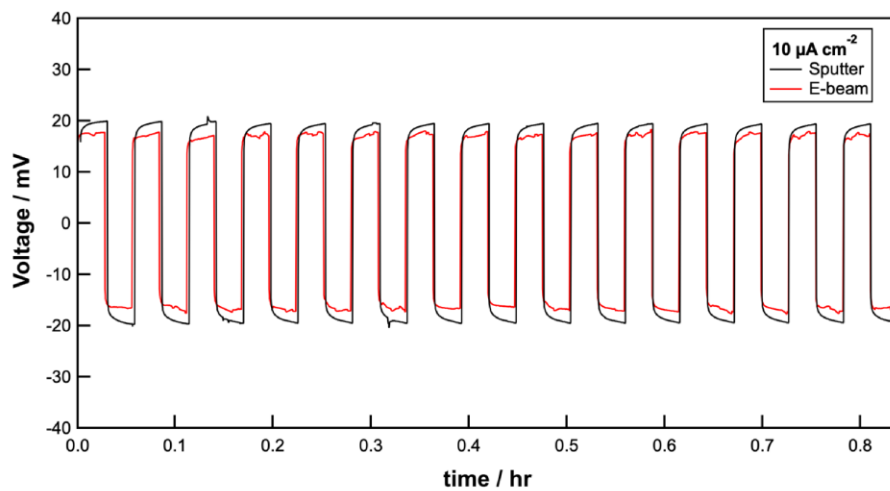


**Figure S4.** Cycling of symmetric Li|LLZO|Li cells with Li deposited via sputtering or e-beam deposition.

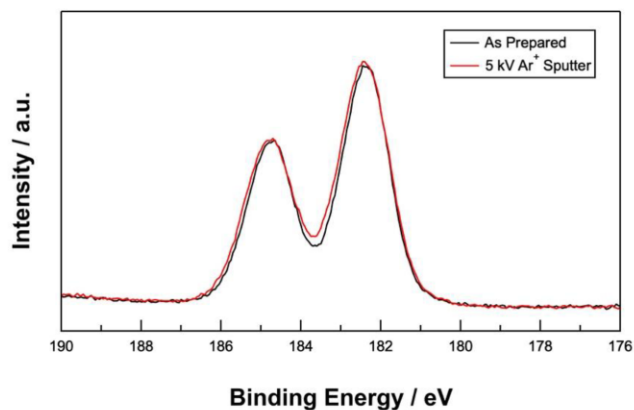


**Figure S5.** Zr 3d core-level XPS spectrum showing no reduction of Zr takes place after 5 kV Ar<sup>+</sup> bombardment in the absence of Li metal.

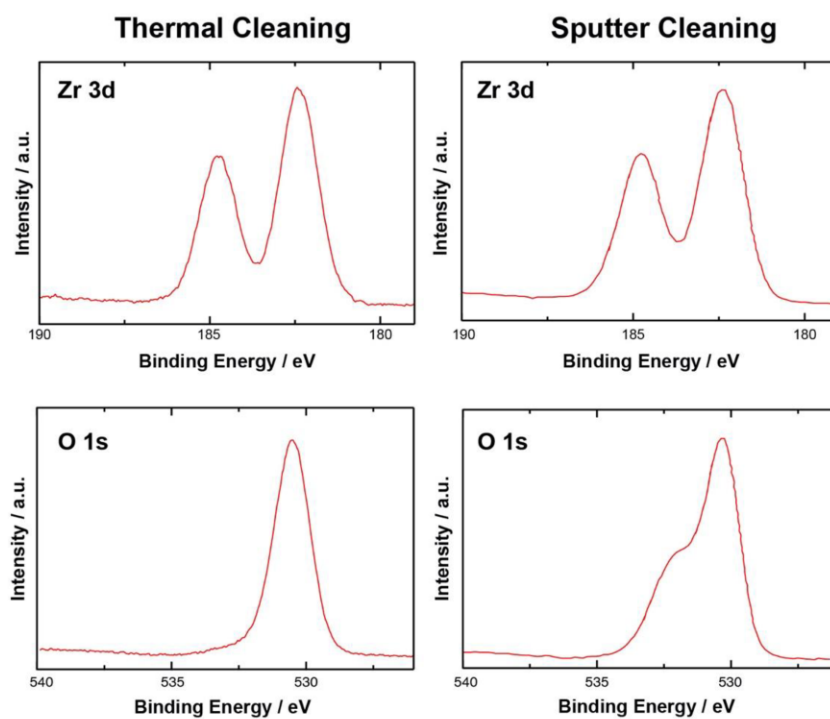


**Figure S6.** O 1s and Zr 3d core-level XPS spectra after thermal annealing (left) and sputter cleaning (right).

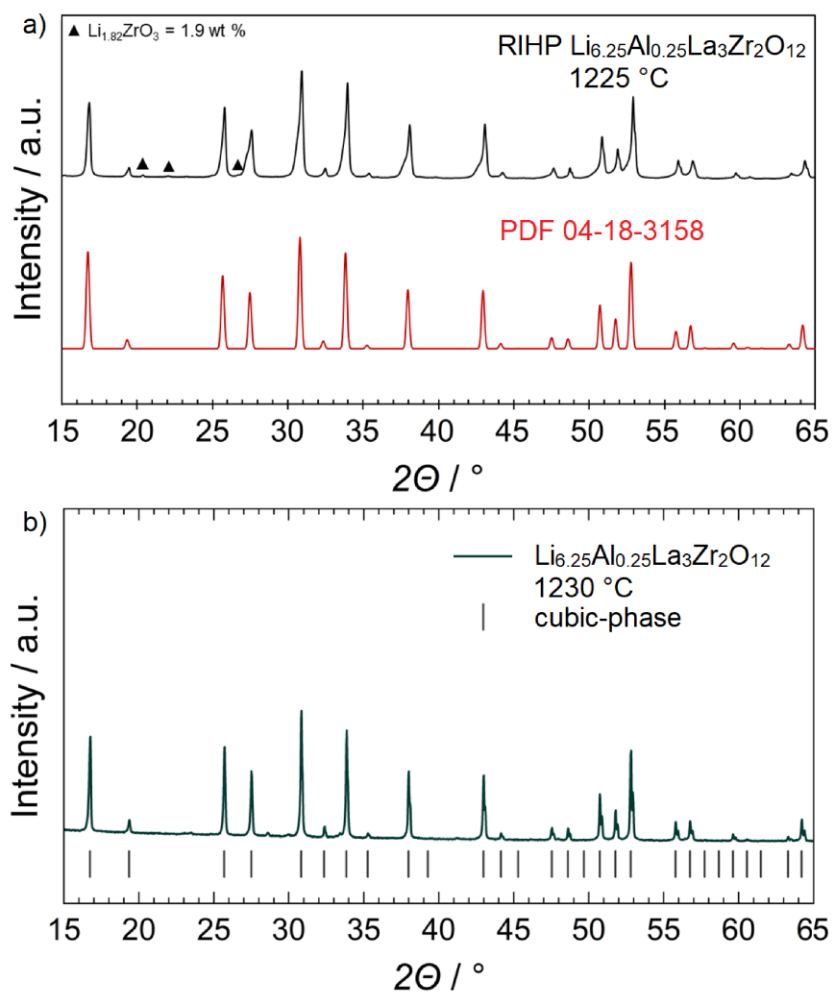


**Figure S7.** a) X-Ray diffraction pattern of an Al-LLZO sample densified via Rapid Induction Hot-Pressing (RIHP) at 1225 °C. Rietveld refinement showed presence of pyrochlore (1.9 wt. %), marked on the pattern. b) X-Ray diffraction pattern of Al-LLZO sintered at 1230 °C.

- 7.1.2 Publication 2: “Current-Dependent Lithium Metal Growth Modes in ‘Anode-Free’ Solid-State-Batteries at the Cu|LLZO Interface”



## Supporting Information

for *Adv. Energy Mater.*, DOI: 10.1002/aenm.202203174

Current-Dependent Lithium Metal Growth Modes in  
“Anode-Free” Solid-State Batteries at the Cu|LLZO  
Interface

*Till Fuchs, Juri Becker, Catherine G. Haslam, Christian  
Lerch, Jeff Sakamoto, Felix H. Richter,\* and Jürgen  
Janek\**

## Current-Dependent Lithium Metal Growth Modes in ‘Anode-Free’ Solid-State-Batteries at the Cu|LLZO Interface

Till Fuchs<sup>1,2,Δ</sup>, Juri Becker<sup>1,2,Δ</sup>, Catherine G. Haslam<sup>3,4</sup>, Christian Lerch,<sup>1,2</sup>  
Jeff Sakamoto<sup>3,4</sup>, Felix H. Richter<sup>1,2\*</sup> and Jürgen Janek<sup>1,2\*</sup>

<sup>1</sup>Institute of Physical Chemistry, Justus-Liebig-University Giessen, Heinrich-Buff-Ring 17,  
D-35392 Giessen, Germany.

<sup>2</sup>Center for Materials Research (ZfM), Justus-Liebig-University Giessen, Heinrich-Buff-Ring 16,  
D-35392 Giessen, Germany.

<sup>3</sup>Department of Materials Science and Engineering, University of Michigan,  
Ann Arbor, MI 48109, USA

<sup>4</sup>Department of Mechanical Engineering, University of Michigan,  
Ann Arbor, MI 48109, USA

Δ denotes equal contributions

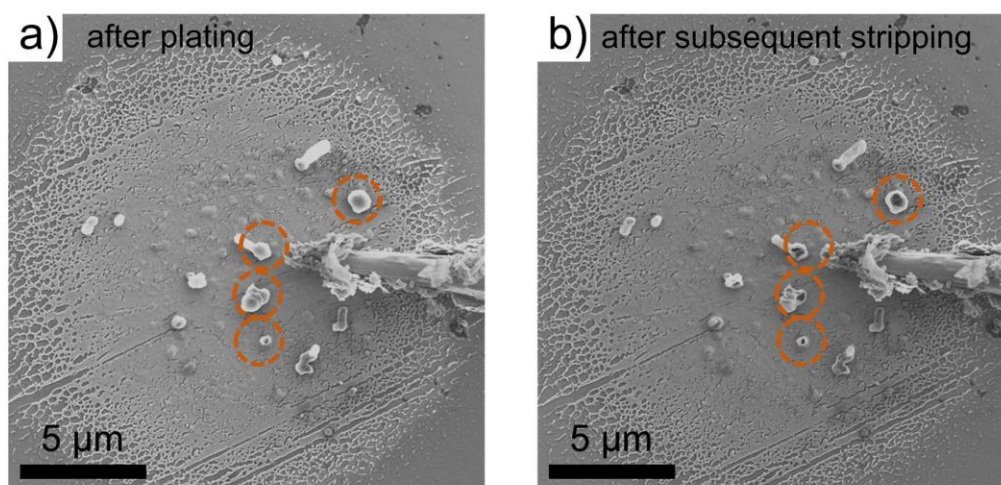


Figure S1. The lithium morphology after plating with  $50 \mu\text{A cm}^{-2}$  is shown on the left in a). During stripping, a fast contact loss and increase in overvoltage is reached due to the low areal coverage of lithium. This is visible in the particles collapsing upon stripping, herein marked with orange circles. This resulted in a low coulombic efficiency of 13%.

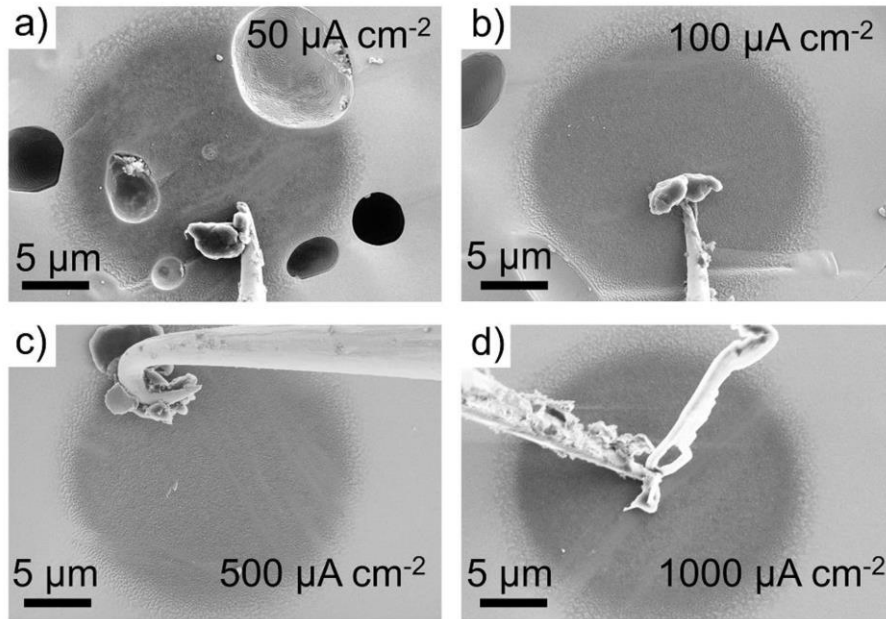


Figure S2. a) SEM micrographs depicting the lithium morphology after plating with  $50 \mu\text{A cm}^{-2}$  at  $\text{Cu}|\text{LLZO}_{\text{sc}}$  interfaces. The single-crystalline LLZO surface was achieved by controlling the LLZO grain size to be larger than the copper current collector patch. Morphologies after plating with  $100 \mu\text{A cm}^{-2}$ ,  $500 \mu\text{A cm}^{-2}$  and  $1000 \mu\text{A cm}^{-2}$  are depicted in b), c) and d), respectively.

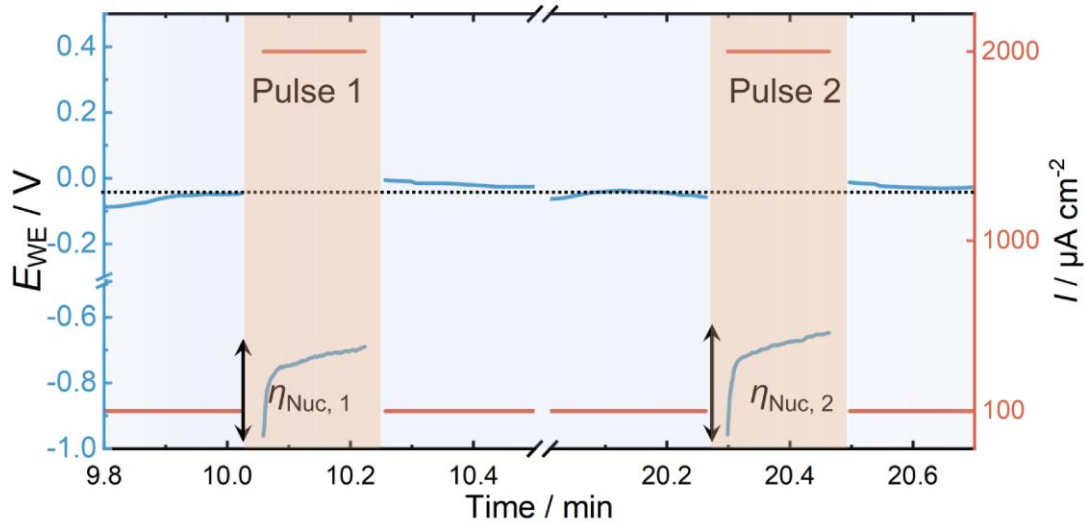


Figure S3. Magnified plot of the current pulses during the plating experiment. The overvoltage shows that lithium nucleates at new spots despite growth happening already at other areas within the sample.

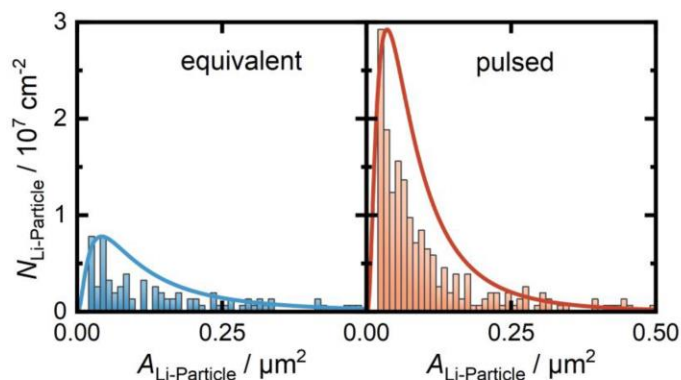


Figure S4. Histogram of the particle size distribution after plating continuously with  $100 \mu\text{A cm}^{-2}$  (left) and after using a pulsed “advanced charging” (right). A clear increase in the number of smaller particles is evident.

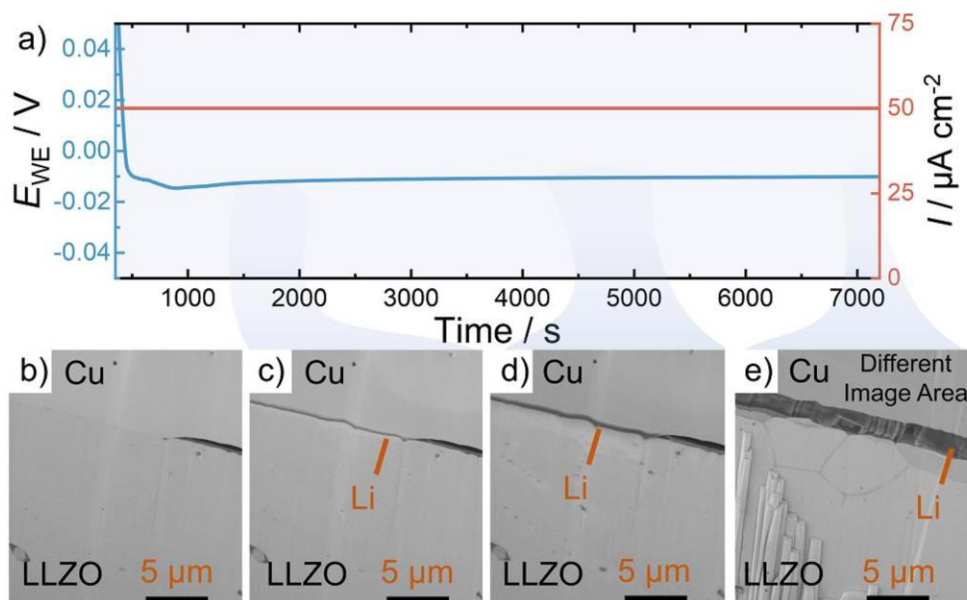


Figure S5. a) Voltage profile of lithium deposition observed at a  $\text{Cu}_{\text{foil}}|\text{LLZO}$  cross-section with  $50 \mu\text{A cm}^{-2}$  applied. Respective SEM images during the process are depicted in b) – e). Note that e) shows a different image area than the other SEM images. Grain boundaries are visible after prolonged observation times due to electron beam induced lithium plating. Similar to the growth process with  $100 \mu\text{A cm}^{-2}$ , a mix between whisker (mode (1)) and layer growth (mode (2)) is observed without any indication of lithium filament/dendrite growth. Additionally, the thickness of grown lithium is not perfectly homogeneous over the whole cross-section.

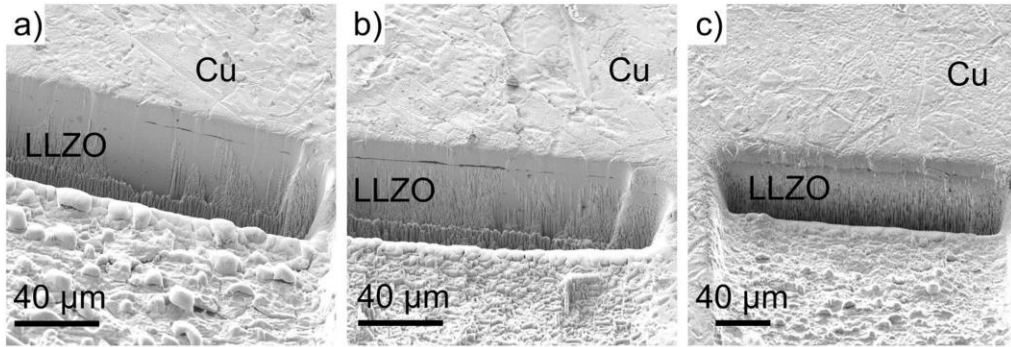


Figure S6. Low-magnification images of the cross-sections used for plating with  $50 \mu\text{A cm}^{-2}$  (a),  $100 \mu\text{A cm}^{-2}$  (b) and  $500 \mu\text{A cm}^{-2}$  (c). Note that due to the tilted sample geometry, the error bar is not scaled perfectly.

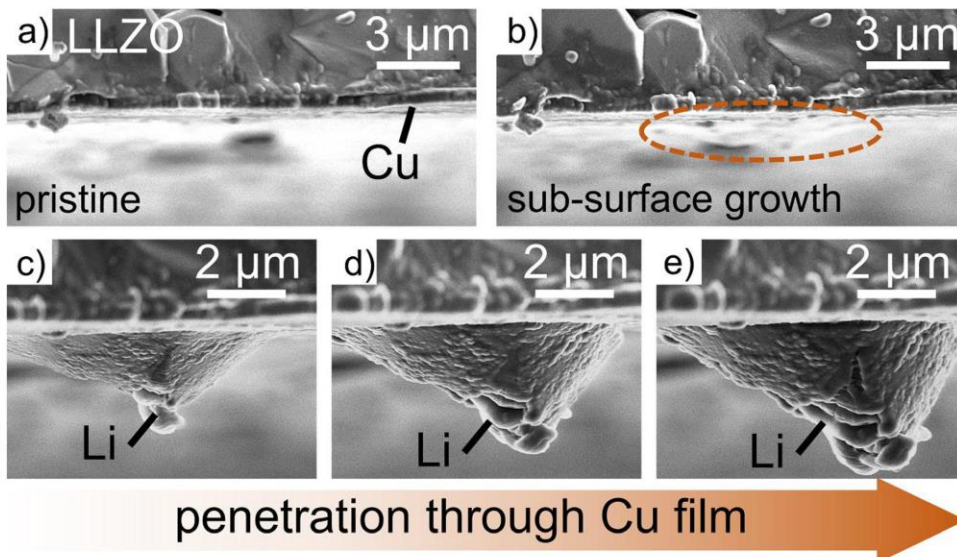


Figure S7. a) Cross-sectional overview over the herein investigated  $\text{LLZO}|\text{Cu}_{\text{film},400\text{nm}}$  electrode system. A film thickness of 400 nm was chosen to obtain a better cross-sectional visibility for the SEM experiment. We believe that the gained qualitative insight can be transferred to thinner films. At the beginning of the plating, sub-surface growth is visible in b), which then breaks through the copper layer as magnified at different stages in c), d) and e).

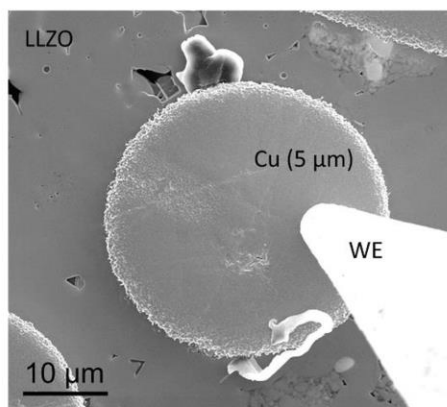


Figure S8: SEM micrograph of lithium being plated at thick  $\text{Cu}_{5\mu\text{m}}$  films deposited on LLZO. Only at the edges of the prepared Cu patch, lithium is visibly growing, which only occurs due to the small size of the electrode. While this setup is unsuitable for characterizing the lithium growth as a function of the current density, it shows that the thicker Cu film is mechanically more stable and suppresses the penetration of growing lithium whiskers and particles through the current collector when compared to thin films used as shown in Figure 2.

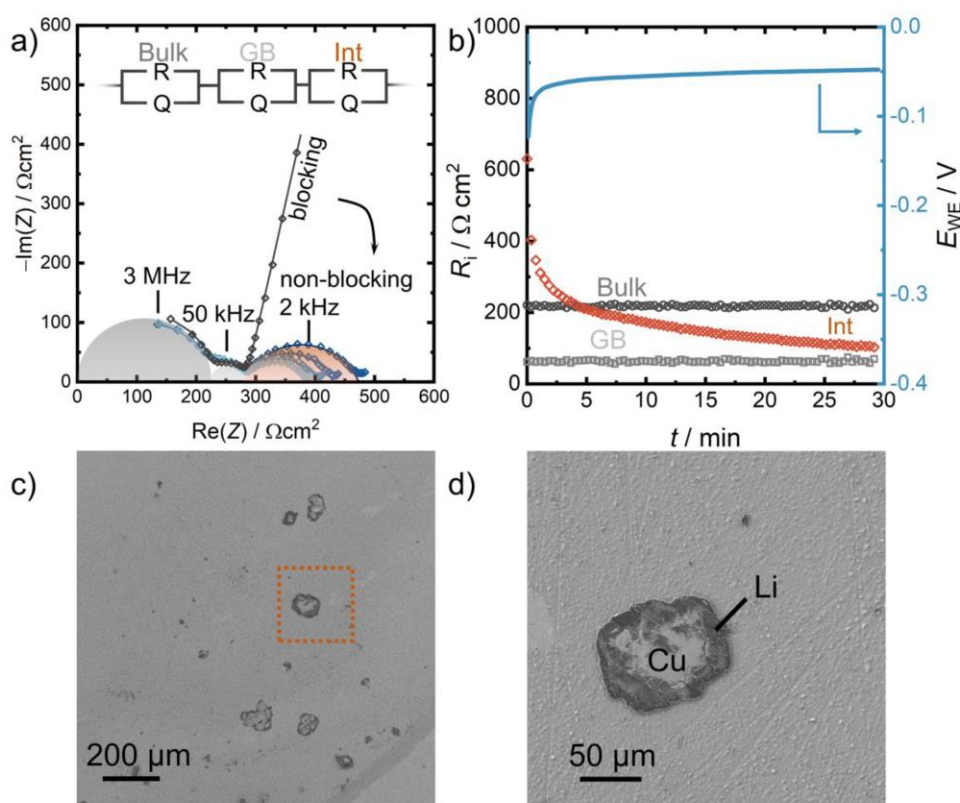


Figure S9. a) Impedance evolution when plating lithium at a  $\text{Cu}_{\text{film}}|\text{LLZO}$  interface with  $100 \mu\text{A cm}^{-2}$  and 2 MPa of pressure applied. A clear transition between blocking and non-blocking impedance is observed once lithium has been deposited. Also, the good resolution and well separated

contributions of bulk and GB transport even before lithium plating indicate a conformal contact between  $\text{Cu}_{\text{film}}$  and LLZO. The extracted values of the three impedance contributions from a fit with the equivalent circuit in a) are depicted as a function of time in b) together with the voltage profile. SEM micrographs after plating are additionally shown in low (c) and high (d) magnification. Two different morphologies of grown lithium are visible. Below the thin Cu film, there is a large number of lithium particles in the size of around  $1 \mu\text{m}$  present. The second observed lithium growth mode is that of a deformed whisker, which is in the size range of several tens of  $\mu\text{m}$ . Due to the small copper patch on top of the whisker, we conclude that once lithium penetrated the current collector film, it was plastically deformed and deposited above the rest of the CC. This is detrimental to the cell's performance, as no new contact area between lithium and LLZO is generated thereby.

- 7.1.3 Publication 3: “Overcoming Anode Instability in Solid-State Batteries through Control of the Lithium Metal Microstructure”



## Supporting Information

for *Adv. Funct. Mater.*, DOI: 10.1002/adfm.202211067

Overcoming Anode Instability in Solid-State Batteries  
through Control of the Lithium Metal Microstructure

*Dheeraj Kumar Singh,\* Till Fuchs, Christian  
Krempaszky, Boris Mogwitz, Simon Burkhardt, Felix H.  
Richter,\* and Jürgen Janek\**

## Supporting Information

### Overcoming Anode Instability in Solid-State Batteries through Control of the Lithium Metal Microstructure

Dheeraj Kumar Singh,<sup>1,2†,\*</sup> Till Fuchs,<sup>1,2†</sup> Christian Krempaszky,<sup>3</sup> Boris Mogwitz,<sup>1,2</sup> Simon Burkhardt,<sup>1</sup> Felix H. Richter,<sup>1,2,\*</sup> and Jürgen Janek<sup>1,2,\*</sup>

<sup>1</sup>Institute of Physical Chemistry, Justus-Liebig-University Giessen, Heinrich-Buff-Ring 17, D-35392 Giessen, Germany.

<sup>2</sup>Center for Materials Research (ZfM), Justus-Liebig-University Giessen, Heinrich-Buff-Ring 16, D-35392 Giessen, Germany.

<sup>3</sup>Institute of Materials Science and Mechanics of Materials, Technical University of Munich, Boltzmannstraße 15, D-85748 Garching, Germany.

†Equal Contributions

\* Corresponding authors: [dheeraj.k.singh@pc.jlug.de](mailto:dheeraj.k.singh@pc.jlug.de); [felix.h.richter@pc.jlug.de](mailto:felix.h.richter@pc.jlug.de); [juergen.janek@pc.jlug.de](mailto:juergen.janek@pc.jlug.de)

**Preparation of solid electrolyte.** The inorganic solid electrolyte (ISE)  $\text{Li}_{6.25}\text{Al}_{0.25}\text{La}_3\text{Zr}_2\text{O}_{12}$  (LLZO) was prepared using a high-temperature solid-state synthesis. Briefly, stoichiometric amounts of  $\text{La}(\text{OH})_3$  (99.9 %, Sigma-Aldrich),  $\text{Li}_2\text{CO}_3$  (>99.0 %, chemPur, with an excess of 3wt.%),  $\text{ZrO}_2$  (99.9 %, Sigma-Aldrich) and  $\text{Al}_2\text{O}_3$  (99.8 %, abcr) were homogenized via ball-milling (Fritsch Pulverisette 7 premium line). The milling was performed at 350 rpm for 24 cycles with each cycle consisting a cooling step of 20 min for every 10 min milling. The resulting mixture was then transferred to the glovebox, maintained under argon environment (MBraun,  $p(\text{O}_2)/p < 0.1$  ppm, and  $p(\text{H}_2\text{O})/p < 0.1$  ppm), and was grounded again using agate pestle and mortar. Thereafter, the ball-milling step was repeated once again with the same set of parameters. Then, in 6.0 g batches, the obtained mixture was pressed into pellets with a diameter of 25 mm. The resulting pellets were then calcined in an open MgO-crucibles in a tube furnace (Nabertherm R40/500/13-P320) under 150 sccm dry oxygen flow at 1000 °C (ramped at 100 °C per hour) for 4 h. The calcined pellets were then transferred to the glovebox and were grounded again to the LLZO powder. The obtained material was ball-milled again for 40 cycles with the same set of parameters as above. Around 600 mg of the resulting powder was then uniaxially compressed into 10 mm pellets in a stainless-steel die, and was then subjected to isostatic compression at 380 MPa for 1 h. The isostatically pressed pellets were then sintered at 900 °C for 5 h under 150 sccm  $\text{O}_2$  flow in an MgO-crucible with LLZO mother powder on the top to avoid unwanted lithium loss. Thereafter, the temperature of the furnace was raised to 1100 °C and was held constant for 5 h followed by further

ramping to 1230 °C in an hour of the preceding step, and was maintained at this temperature for 4 h. The samples were then subjected to natural cooling. All heating steps were roughly carried out with 100 °C per hour. The density of the obtained pellets was determined to be ~93%.

**Preparation of different grain sized polycrystalline lithium.** Lithium metal samples with two different grain sizes were prepared by varying the thermal treatment process of a molten lithium rod (Rockwood lithium GmbH). Briefly, identical quantities of lithium rod were heated in two separate but identical closed steel crucibles at 653 K over a hot plate in an argon environment (MBraun,  $p(\text{O}_2)/p < 0.1$  ppm, and  $p(\text{H}_2\text{O})/p < 0.1$  ppm). On melting, one of the crucibles was quickly quenched in a liquid nitrogen bath (73 K) whereas the other crucible was cooled slowly to room temperature (298 K) by just turning off the hot plate. This resulted in two quite different mean grain sizes of lithium viz., fine- and coarse-grained lithium. When the lithium had solidified in both crucibles, the samples were scooped out using steel spatula. Any surface passivation layer was removed using a ceramic knife. Lithium foil electrodes with a thickness of ~115 to 120  $\mu\text{m}$  were then prepared by mechanical processing of the chunks of respective lithium samples using a hand pressing stainless-steel tool. Thereafter, lithium symmetric cells implementing fine-/coarse-grained polycrystalline lithium as working electrode, were fabricated. Mechanically processed and thermally untreated lithium foil (Rockwood lithium GmbH) was used as quasi-reversible counter and reference electrode, see following section for details.

**Fabrication of lithium symmetric cell ( $\text{Li}_{\text{id}}|\text{LLZO}|c/h\text{-Li}$ ).** The reference/counter electrode ( $\text{Li}_{\text{id}}$ ) was made from the mechanically processed chunks from the lithium rod (Rockwood Lithium GmbH). Briefly, small pieces of the rod were cut and any surface passivation layers were removed with the help of a ceramic knife. The Li was then mechanically pressed using a homemade, hand pressing stainless-steel tool. This step resulted in a thickness of ~115-120  $\mu\text{m}$  of the obtained lithium foils. Similarly, either fine- and coarse-grained lithium electrode foils were processed in an analogous manner and were used as working electrodes. The respective lithium foils with a diameter of 6 mm were then appended on either side of the LLZO pellet using finger applied stress with additional layers of thin Cu foils (8 mm diameter) on its top. Thereafter, the assembled cells were then vacuum sealed under argon atmosphere (MBraun,  $p(\text{O}_2)/p < 0.1$  ppm, and  $p(\text{H}_2\text{O})/p < 0.1$  ppm) using three protective layers of rubber reinforcements of Sonodomen (CPR GmbH). The sealed assembly was then isostatically compressed at 362 MPa for 30 min to obtain symmetric cells. During this step, the working electrodes undergoes straining to about 15-18 %, indicating significant strain hardening. We refer to this post-strained state of fine-and coarse-grained polycrystalline lithium electrode to as c-Li and h-Li respectively. In the resulting symmetric cell, i.e.,  $\text{Cu}|\text{Li}_{\text{id}}|\text{LLZO}|c/h\text{-Li}|\text{Cu}$ ,  $\text{Li}_{\text{id}}$  has negligible interfacial resistance and is morphologically stable during the experimental conditions (see below for details) and hence does not contribute towards observed cell impedance.

**Electrochemical measurements.** The ionic conductivity of LLZO pellets were determined under ion-blocking conditions by using an Au symmetric cell of the type  $\text{Au}|\text{LLZO}|\text{Au}$ . Around 200 nm thick

electrodes of gold with a diameter of 6 mm were vapour-deposited on both sides of a LLZO pellet under vacuum using a homemade setup. Thereafter pouch cells were fabricated using Ni current collectors by sealing under the above conditions. Potentiostatic electrochemical impedance spectroscopy (PEIS) data were then acquired with an amplitude of 10 mV with a frequency range of 7 MHz-100 mHz using VMP300 (Bio-Logic). The activation energies for the bulk and grain boundary transport processes were determined using temperature-dependent measurements between 233 K to 333 K with an equilibration time of 1 h (Weiss Klimatechnik climate chamber).

Continuous galvanostatic electrochemical impedance spectroscopy (GEIS) measurements were performed at  $0.1 \text{ mA cm}^{-2}$  with an amplitude of  $0.01 \text{ mA cm}^{-2}$  on VMP300 in the frequency range of 7 MHz to 1 Hz with a cut-off potential of 1.0 V. The lower frequency limit was set to 1 Hz in order to avoid strong distortion of the data due to higher time-period of the acquisition at frequencies  $< 1 \text{ Hz}$ , causing substantial interfacial changes thus leading to the violation of the steady state condition. The pressure-dependent measurements were performed using a homemade setup equipped with a force sensor (KMT55-20kN, Inelta Sensorsysteme GmbH & Co. KG). Additionally, the setup was equipped with a spring to compensate for any pressure relaxation during the measurements. All the measurements were performed in the climate chamber at 298 K in order to avoid any influence of thermal fluctuations on the measurements.

**Instrumentation and material characterization.** X-ray diffraction (XRD) patterns of the samples were acquired using PANalytical Empyrean powder diffractometer in Bragg-Brentano  $\theta$ - $\theta$  geometry with  $\text{Cu K}_\alpha$  radiation to ascertain the phase purity of the samples. The measurement range and the corresponding step-size were varied depending on the nature of the samples viz. c/h-Li or LLZO. LLZO powder and as well as mechanically processed thin foils of c/h-Li of thickness  $\sim 100 \mu\text{m}$  were loaded onto (911) oriented silicon zero background holder equipped with Kapton<sup>®</sup> protective film for the XRD measurements. Supra 55 VP-4132 Carl Zeiss scanning electron microscopy (SEM) Merlin was used to obtain electron micrographs of the samples. An acceleration voltage of 3.00 kV and a current of 100 pA was used to acquire the images. The SEM chamber pressure was  $\sim 7 \cdot 10^{-6}$  mbar. A Leica transfer module system (EM VCT 500) was used to transfer samples from the glovebox to the SEM chamber under air-tight conditions.

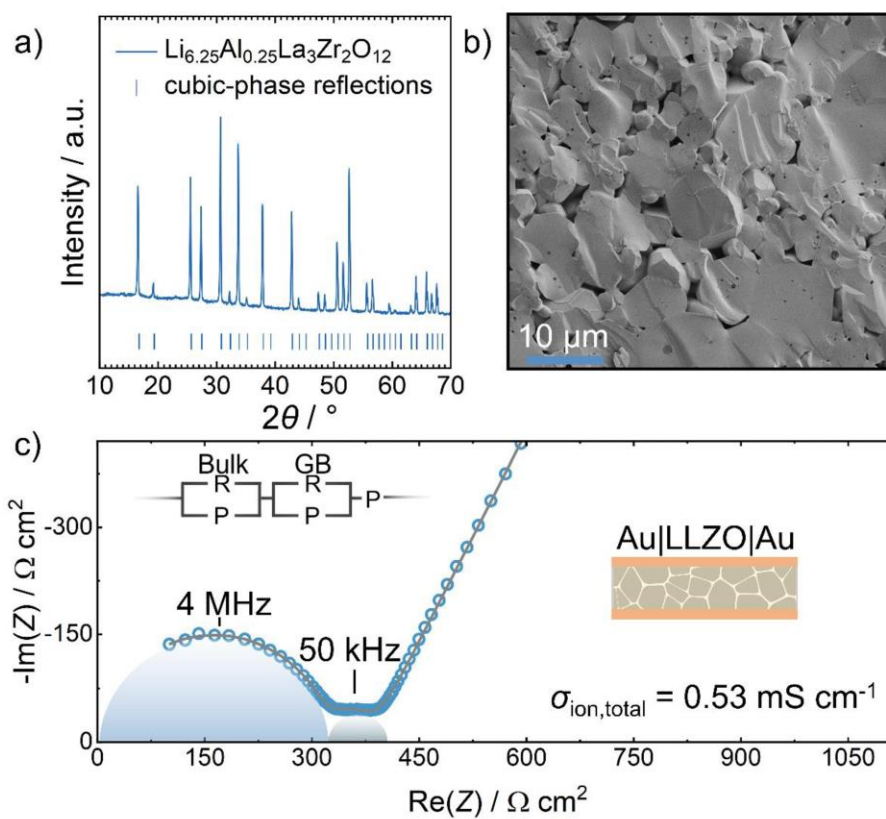


Figure S1. (a) Depicts a diffractogram of the herein used cubic LLZO together with the respective reference data. A cross-sectional SEM image of the LLZO is shown in (b). The impedance and utilized fit model of a Au|LLZO|Au cell are shown in (c).

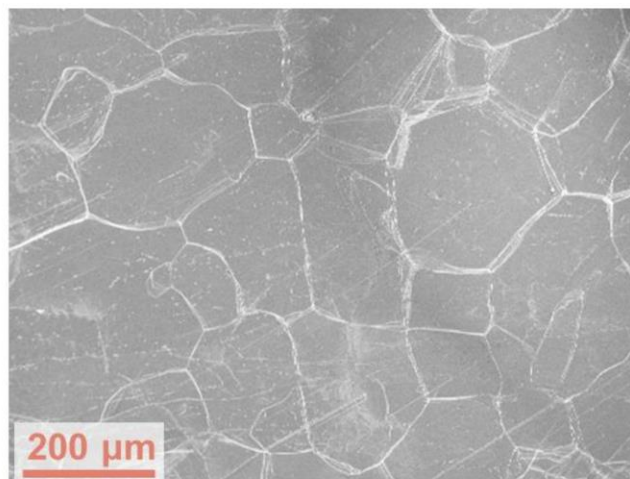


Figure S2. SEM image of reference lithium foil.

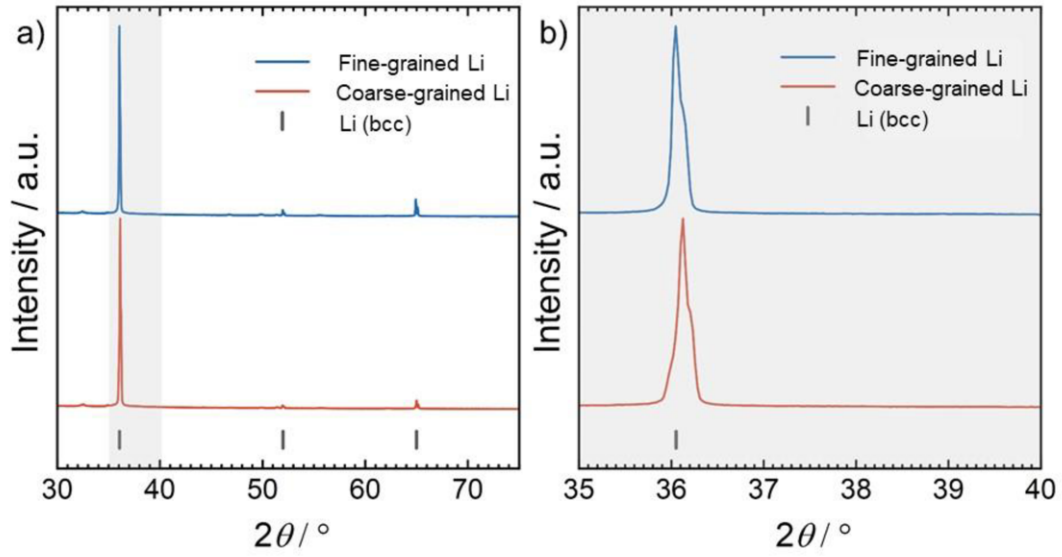


Figure S3. (a) Diffraction pattern of fine-grained Li and coarse-grained Li foils. An inset of the brightest reflection is shown in (b).

### Constitutive equations

The constitutive equation for the steady-state lattice diffusional creep or the Nabarro-Herring creep is given by:<sup>1</sup>

$$\dot{\epsilon}_{\text{NH}} = k_1 \left( \frac{D_L}{d^2} \right) \left( \frac{Eb^3}{kT} \right) \left( \frac{\sigma}{E} \right) \quad (\text{S1})$$

And, the corresponding relationship for the grain boundary assisted diffusional flow or Coble creep is given by:<sup>1</sup>

$$\dot{\epsilon}_{\text{C}} = k_2 \left( \frac{D_{\text{GB}}b}{d^3} \right) \left( \frac{Eb^3}{kT} \right) \left( \frac{\sigma}{E} \right) \quad (\text{S2})$$

For the pipe diffusion controlled, dislocation climb creep (DCC) or the power law creep, the constitutive relationship is expressed as:<sup>1</sup>

$$\dot{\epsilon}_{\text{DCC}} = k_3 \left( \frac{D_d}{b^2} \right) \left( \frac{\sigma}{E} \right)^n \quad (\text{S3})$$

Where,  $\dot{\epsilon}_{\text{NH}}$ ,  $\dot{\epsilon}_{\text{C}}$ , and  $\dot{\epsilon}_{\text{DCC}}$  are the strain rates for Nabarro-Herring, Coble and dislocation climb creep respectively,  $k_1$  are material constants and its values are determined from the theoretical models ( $k_1 = 14$ ,  $k_2 = 50$ , and  $k_3 = 5 \cdot 10^{12}$ ),<sup>1</sup>  $D_{\text{L}}$  and  $D_{\text{GB}}$  are the lattice diffusivity and grain boundary diffusivity respectively,  $d$  is the grain size,  $E$  is Young's modulus,  $b$  is the length of the Burgers vector,  $k$  is the Boltzmann constant,  $T$  is the absolute temperature,  $n$  is the stress exponent for the power-law creep, and  $\sigma$  is the applied stress.

**Table S1. Data for lithium metal<sup>1,2</sup>**

$b$  is the length of the Burgers vector,  $D_{\text{L}0}$  and  $D_{\text{GB}0}$  are the pre-exponential factors for the lattice diffusivity and grain boundary diffusivity respectively,  $Q_{\text{L}}$  and  $Q_{\text{GB}}$  are the activation energies for lattice diffusivity and grain boundary diffusivity respectively,  $\delta$  is the grain boundary thickness and is approximated to be  $2b$ ,  $E$  is Young's elastic modulus, and  $T_{\text{fus}}$  is the melting temperature.

	$b$ (m)	$3.04 \cdot 10^{-10}$	
<b>Calculations for self-diffusivity at 298 K</b>	$D_{\text{L}0}$ ( $\text{m}^2 \text{s}^{-1}$ )	$3.9 \cdot 10^{-5}$	<b>K</b>
The self-diffusivity is given by: <sup>3</sup>	$Q_{\text{L}}$ ( $\text{kJ mol}^{-1}$ )	56.1	
$D = D_0 e^{-\left(\frac{Q}{RT}\right)}$ (S4)	$\delta D_{\text{GB}0}$ ( $\text{m}^3 \text{s}^{-1}$ )	$4.3 \cdot 10^{-14}$	
Substituting values for the appropriate in Eq. S4 gives the following:	$Q_{\text{GB}}$ ( $\text{kJ mol}^{-1}$ )	33.7	constants from Table S1
$D_{\text{L}} = 5.7 \cdot 10^{-11} \text{ cm}^2 \text{ s}^{-1}$	$E$ (GPa)	7.82	
$D_{\text{GB}} = D_{\text{d}} = 8.8 \cdot 10^{-7} \text{ cm}^2 \text{ s}^{-1}$	$n$	6.6	
Clearly, the self-diffusivity along the dislocation pipe diffusion ( $D_{\text{d}}$ ) is ~4 bulk or lattice diffusivity ( $D_{\text{L}}$ ).	$T_{\text{fus}}$ (K)	452	grain boundary ( $D_{\text{GB}}$ ) or orders higher compared to

**Calculations of the strain rates for  $\sigma = 2.0$  MPa, and  $T = 298$  K:**

For  $d = 20 \mu\text{m}$ ,

$$\dot{\epsilon}_{\text{NH}} = 4.2 \cdot 10^{-2} \text{ s}^{-1}$$

$$\dot{\epsilon}_{\text{C}} = 2.3 \cdot 10^{-6} \text{ s}^{-1}$$

$$\dot{\epsilon}_{\text{DCC}} = 0.9 \cdot 10^{-2} \text{ s}^{-1}$$

Similarly, for  $d = 295 \text{ }\mu\text{m}$ , we have:

$$\dot{\epsilon}_{\text{NH}} = 1.9 \cdot 10^{-4} \text{ s}^{-1}$$

$$\dot{\epsilon}_{\text{C}} = 7.1 \cdot 10^{-10} \text{ s}^{-1}$$

$$\dot{\epsilon}_{\text{DCC}} = 0.9 \cdot 10^{-2} \text{ s}^{-1}$$

**Calculations of the strain rates for  $\sigma = 0.2 \text{ MPa}$ , and  $T = 298 \text{ K}$ :**

For  $d = 20 \text{ }\mu\text{m}$ ,

$$\dot{\epsilon}_{\text{NH}} = 4.2 \cdot 10^{-3} \text{ s}^{-1}$$

$$\dot{\epsilon}_{\text{C}} = 2.3 \cdot 10^{-7} \text{ s}^{-1}$$

$$\dot{\epsilon}_{\text{DCC}} = 2.3 \cdot 10^{-9} \text{ s}^{-1}$$

Similarly, for  $d = 295 \text{ }\mu\text{m}$ , we have:

$$\dot{\epsilon}_{\text{NH}} = 1.9 \cdot 10^{-5} \text{ s}^{-1}$$

$$\dot{\epsilon}_{\text{C}} = 7.1 \cdot 10^{-11} \text{ s}^{-1}$$

$$\dot{\epsilon}_{\text{DCC}} = 2.3 \cdot 10^{-9} \text{ s}^{-1}$$

**Note:** In calculating steady-state strain rate for Nabarro-Herring creep,  $D_{\text{d}}$  was substituted for  $D_{\text{L}}$  in Eq. S1 to account for strain hardening.

When all the creep mechanisms operate simultaneously at a given  $T$ ,  $\sigma$ , and  $d$ , then the total strain rate is determined by the sum of the individual strain rates:

$$\dot{\epsilon}_{\text{overall}} = \Sigma \dot{\epsilon}_i \quad (\text{S5})$$

From Eq. S2 it is clear that the fastest deformation process governs the overall creep rate.

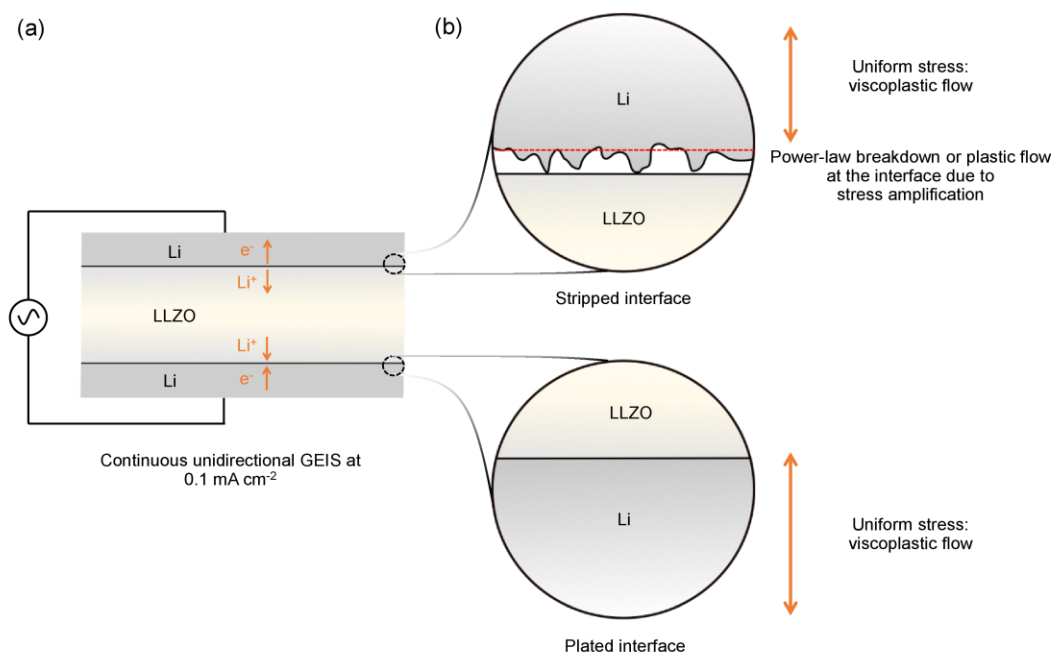


Figure S4. (a) Schematic of a symmetric  $\text{Li}_{id}/\text{LLZO}_{c/h}/\text{Li}$  cell subjected to continuous unidirectional GEIS stripping at  $0.1 \text{ mA cm}^{-2}$ . The stripped and the plated interface, indicated by the dotted black circles in (a) are magnified in (b). A uniform stress exists across the thickness of the lithium at the plated side whereas the stress distribution in the lithium anode can be divided into two parts (as indicated by the discontinuous red line). At the stripped interface, depleting contact would result in higher contact stresses (stress amplification on account low load bearing area). As a consequence, the deformation will be according to power-law breakdown<sup>4</sup> initially with progressive shift towards plastic flow via glide with depleting contact. In the bulk (the region above the dotted line) uniform stress would result in time-dependent plastic flow (viscoplasticity).

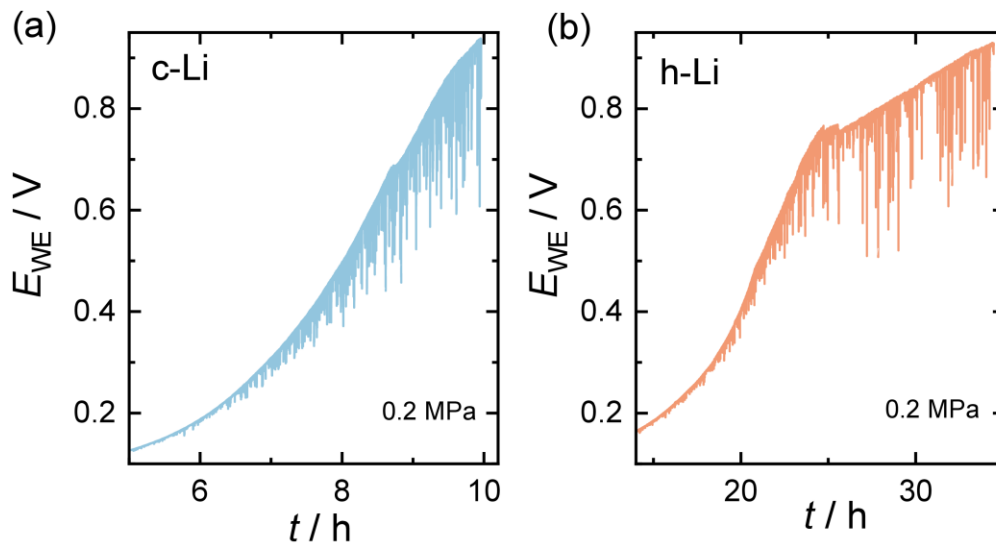


Figure S5. Overpotential evolution for (a) c-Li, and (b) h-Li during continuous unidirectional GEIS measurements performed at  $0.1 \text{ mA cm}^{-2}$  and  $0.2 \text{ MPa}$ . At the interface, the contact is dictated by the competition between progressively decreasing contact area and the continuously increasing contact stress resulting in the overpotential fluctuations. The amplitude of the overpotential fluctuations increases with time and its magnitude is an indicator of the contact area. It can be seen that combined strain rates for the plastic deformation at the interface and viscoplastic deformation (creep) in the bulk of the lithium metal anode are unable to cope up with the imposed current at  $0.2 \text{ MPa}$ . The amplitude of the fluctuations depends on the contact geometry and the strength of the lithium metal anode.

## References

1. Ruano, O. A., Wadsworth, J. & Sherby, O. D. Deformation mechanisms in an austenitic stainless steel (25Cr-20Ni) at elevated temperature. (1985) doi:10.1007/BF01113782.
2. Sargent, P. M. & Ashby, M. F. Deformation mechanism maps for alkali metals. *Scr. Metall.* **18**, 145–150 (1984).
3. Mehrer, H. *Diffusion in Solids: Fundamentals, Methods, Materials, Diffusion-Controlled Processes*. (Springer Berlin Heidelberg, 2007).
4. Roesler, J., Harders, H. & Baeker, M. *Mechanical Behaviour of Engineering Materials: Metals, Ceramics, Polymers, and Composites*. (Springer Berlin Heidelberg, 2007).

- 7.1.4 Publication 4: “Increasing the Pressure-Free Stripping Capacity of the Lithium Metal Anode in Solid-State-Batteries by Carbon Nanotubes”



## Supporting Information

for *Adv. Energy Mater.*, DOI: 10.1002/aenm.202201125

Increasing the Pressure-Free Stripping Capacity of the Lithium Metal Anode in Solid-State-Batteries by Carbon Nanotubes

*Till Fuchs, Catherine G. Haslam, Alexandra C. Moy, Christian Lerch, Thorben Krauskopf, Jeff Sakamoto,\* Felix H. Richter,\* and Jürgen Janek\**

## **Increasing the Pressure-Free Stripping Capacity of the Lithium Metal Anode in Solid-State-Batteries by Carbon Nanotubes**

Till Fuchs<sup>1,2</sup>, Catherine G. Haslam<sup>3,4</sup>, Alexandra C. Moy<sup>3</sup>, Christian Lerch<sup>1,2</sup>,  
Thorben Krauskopf<sup>1,2</sup>, Jeff Sakamoto<sup>3,4\*</sup>, Felix H. Richter<sup>1,2\*</sup> and Jürgen Janek<sup>1,2\*</sup>

<sup>1</sup>Institute of Physical Chemistry, Justus-Liebig-University Giessen, Heinrich-Buff-Ring 17,  
D-35392 Giessen, Germany.

<sup>2</sup>Center for Materials Research (ZfM), Justus-Liebig-University Giessen, Heinrich-Buff-Ring 16,  
D-35392 Giessen, Germany.

<sup>3</sup>Department of Materials Science and Engineering, University of Michigan,  
Ann Arbor, MI 48109, USA

<sup>4</sup>Department of Mechanical Engineering, University of Michigan,  
Ann Arbor, MI 48109, USA

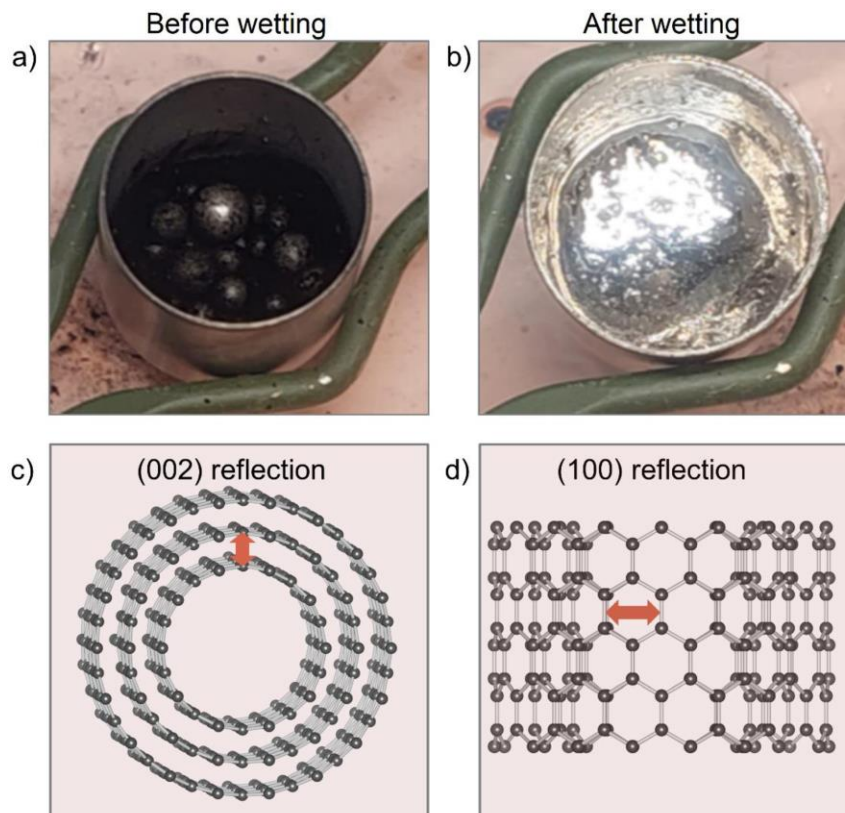


Figure S1. a) Digital photograph of the mixture during dispersing the CNT within liquid lithium at 350 °C. At a certain point during preparation, the CNTs are wetted by liquid lithium, which is shown in b). Differences in wetting are to be expected when other kinds of CNTs are used in dependence of their structure and geometric parameters. c) and d) Schematic explanation of the (002) and (100) reflections of CNT visible in the XRD in Figure 1.

Table S1. Overview of impedance fitting parameters of  $\text{Li}_{\text{id}}|\text{LLZO}|\text{Li-CNT40}$ . The fitted experimental spectrum is shown in Figure 2. The constant phase element  $Q$  exhibits the impedance  $Z_Q = (i\omega C)^{-\alpha}$  with  $\omega$ ,  $C$  and  $\alpha$  being the excitation frequency, capacitance and ideality factor thereof, respectively.

Parameter	Value	Error / $\pm$	Typical <sup>[1,5]</sup>
$R_{\text{Bulk}} / \Omega \text{ cm}^2$	280.0	0.6	-
$Q_{\text{Bulk}} / \text{F cm}^2$	$1.65 \cdot 10^{-11}$	$0.01 \cdot 10^{-11}$	$10^{-11} - 10^{-10}$
$\alpha_{\text{Bulk}}$	0.97	0.00	0.9 - 1.0
$R_{\text{GB}} / \Omega \text{ cm}^2$	36.4	4.3	-
$Q_{\text{GB}} / \text{F cm}^2$	$3.7 \cdot 10^{-9}$	$1.3 \cdot 10^{-9}$	$10^{-9} - 10^{-8}$
$\alpha_{\text{GB}}$	0.98	0.03	0.8 - 1.0
$R_{\text{Int}} / \Omega \text{ cm}^2$	26.9	4.2	-
$Q_{\text{Int}} / \text{F cm}^2$	$3.9 \cdot 10^{-8}$	$8 \cdot 10^{-9}$	$10^{-8} - 10^{-6}$
$\alpha_{\text{Int}}$	0.82	0.04	0.7 - 1.0

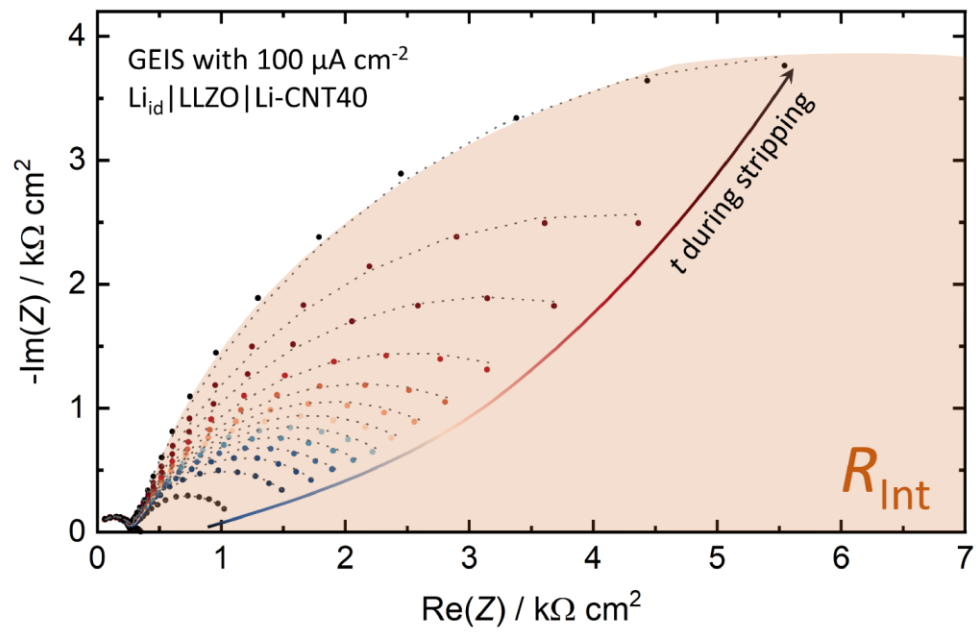


Figure S2. Evolution of the impedance during stripping of  $\text{Li}_{\text{id}}|\text{LLZO}|\text{Li-CNT40}$  with  $100 \mu\text{A cm}^{-2}$  displayed in selected Nyquist-Plots. Bulk and grain boundary resistance remain constant, indicating that no dendrite growth is taking place.

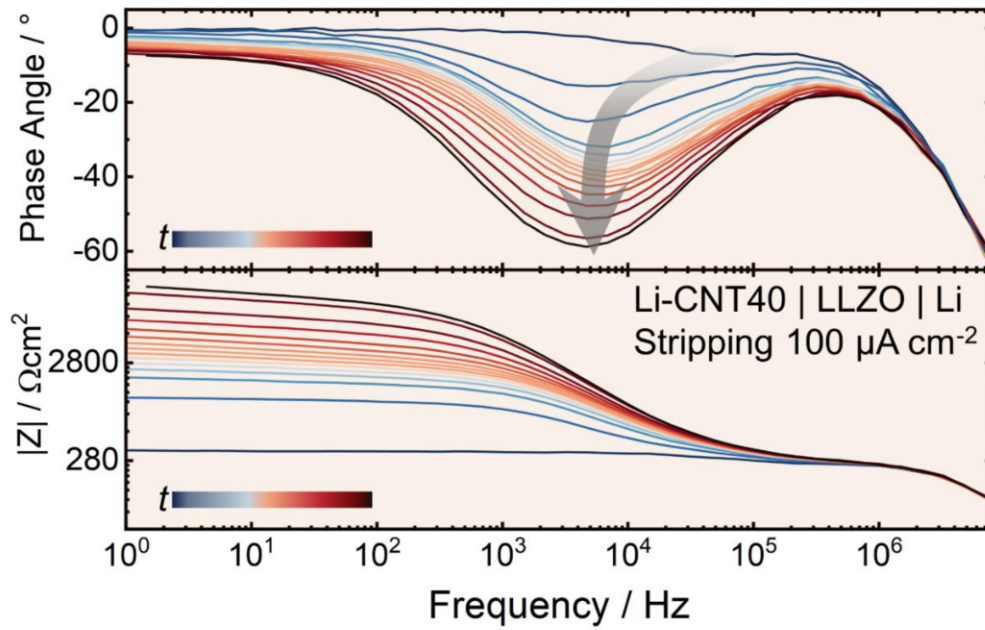


Figure S3. The top figure depicts the phase angle and the bottom one the value of the impedance  $|Z|$  versus frequency in a Bode plot. While the time constant of the constriction resistance shifts to higher frequencies for pure lithium electrodes, it remains roughly constant for composite electrodes.<sup>[1,2]</sup> This is explained by a more homogenous contact spot distribution for Li-CNT, as also seen with Li-Mg alloys, too. In these cases, the current is more homogeneously distributed, leading to less Joule heating at the contact spots. The bottom graph shows that the overall resistance increase mainly occurs in the low frequency regions below  $10^3 - 10^4$  Hz, consistent with the evolution of the Nyquist plots shown in Figure S2.

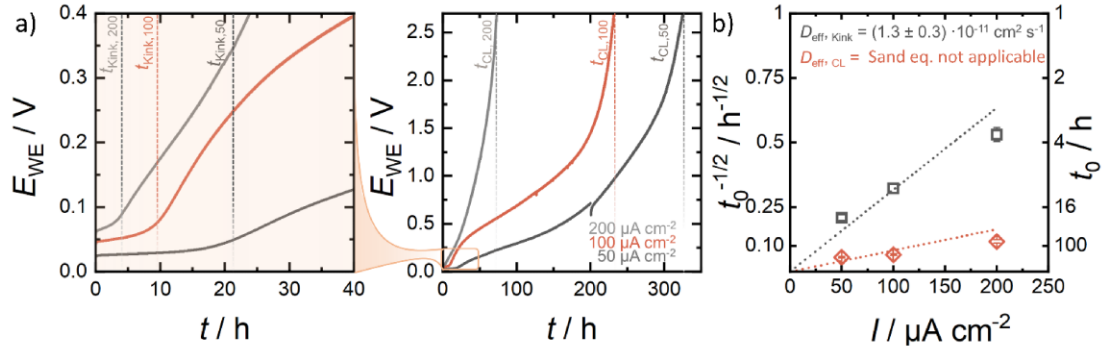


Figure S4. a) Voltage profiles during stripping of Li-CNT30 at different magnifications. The stripping current densities  $i$  were chosen as  $50 \mu\text{A cm}^{-2}$ ,  $100 \mu\text{A cm}^{-2}$  and  $200 \mu\text{A cm}^{-2}$ . Dashed lines indicate the times until a distinct change of slope occurs ( $t_{\text{kink}, i}$ ) and until full contact loss is observed ( $t_{\text{CL}, i}$ ). To obtain the respective diffusion coefficients via the Sand equation, b) displays a plot of  $t_{\text{kink}}^{-1/2}$  and  $t_{\text{CL}}^{-1/2}$  versus the applied current density. Note that the little discontinuity in a) at 200 h for  $50 \mu\text{A cm}^{-2}$  originates from a short pause in data acquisition.

Via the Sand equation

$$\frac{1}{\sqrt{t_i}} = \frac{2}{c_0 F \cdot \sqrt{\pi} \cdot D_{\text{eff},j}} \cdot i \quad (1)$$

it is possible to calculate an effective diffusion coefficient  $D_{\text{eff}}$  by plotting  $t_i^{-1/2}$  versus the applied current density  $i$ .<sup>[3,4]</sup> Herein,  $c_0$  and  $t_j$  denote the initial concentration of lithium inside the material and the time until contact loss occurs during dissolution. However, the values obtained for the contact loss of the composite electrode are flawed, as the electrode thickness  $d$  is only slightly larger than the hypothetical thickness of stripped lithium, which leads to the requirement

$$d \gg \sqrt{i_i \cdot D_{\text{eff}}^{-1}} \quad (2)$$

not being fulfilled. This leads to an underestimation of  $t_{\text{CL},50}$  for low current densities, as seen in the orange data point in Figure S4b. Additionally, it is shown that – while the Sand equation describes 1-dimensional diffusion – competing 3D diffusion processes like surface adatom diffusion or diffusion through and along CNTs in this case, play an important role as well. Nevertheless, general and qualitative conclusions about  $D_{\text{eff}}$  can still be drawn from the time until the kink occurs.

Figure S4a displays the voltage profile during stripping of Li-CNT30 with varying applied current densities. It is reasonable, that with higher current densities, the electrode is depleted faster and a lower capacity is obtained, as also reported for Li-Mg alloys.<sup>[2]</sup> However, the inflection point within

the profile (“kink”) also occurs earlier with higher applied current densities. Interestingly, the kink occurs roughly at the same time, when non-composite  $\text{Li}_{\text{id}}|\text{LLZO}$  interfaces show full contact loss.<sup>[2]</sup> Using  $t_{\text{kink}}$  to calculate an effective diffusion coefficient via Sand’s equation,  $D_{\text{eff}} = (1.3 \pm 0.3) \cdot 10^{-11} \text{ cm}^2 \text{ s}^{-1}$  results. The estimated value for  $D_{\text{eff}}$  should not be mistaken as self-diffusion coefficient of lithium, which does not include the diffusion and creep along defects, such as dislocations, grain boundaries and surfaces. For a detailed overview of diffusion coefficients for lithium obtained by different methods, the reader is referred to a work by Krauskopf et al.<sup>[2]</sup>

The effective diffusion coefficient calculated from the time until contact is lost cannot be calculated in the manner of the Sand’s equation, as the interface is no longer planar beyond the inflection point. Additionally, the condition given in Eq. (2) for Sand’s equation to be valid is not fulfilled anymore due to the high amount of lithium being stripped from the electrode.

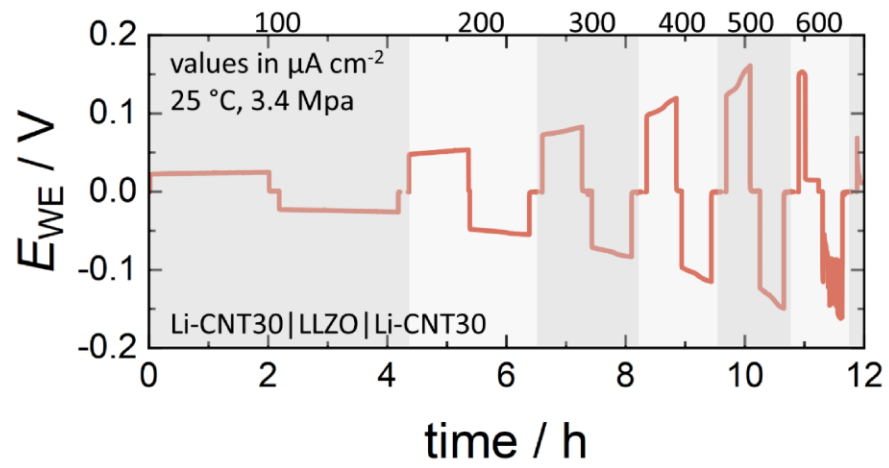


Figure S5. A voltage profile of Li-CNT30|LLZO|Li-CNT30 with increasing current density to obtain a critical current density of about  $600 \mu A cm^{-2}$  when (dis)charging  $0.2 mAh cm^{-2}$  is shown.

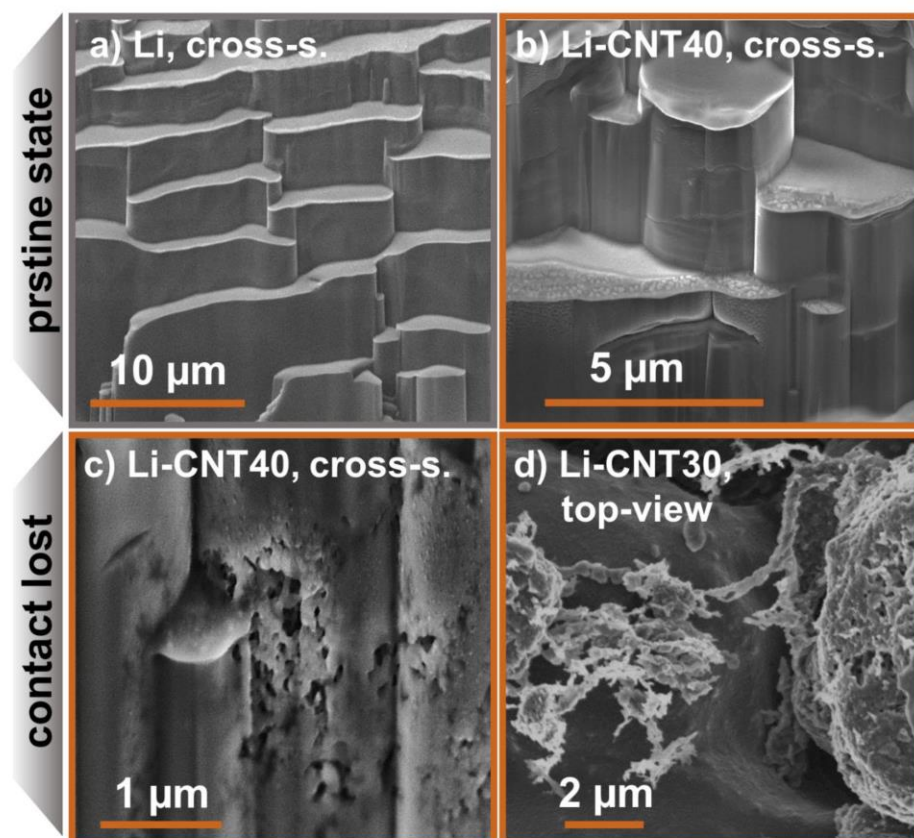


Figure S6. SEM images of a) pristine lithium and b) pristine Li-CNT40 in cross-sectional view. Cross-sectional and top-view SEM images of Li-CNT40 in higher magnifications after stripping are shown in c) and d).

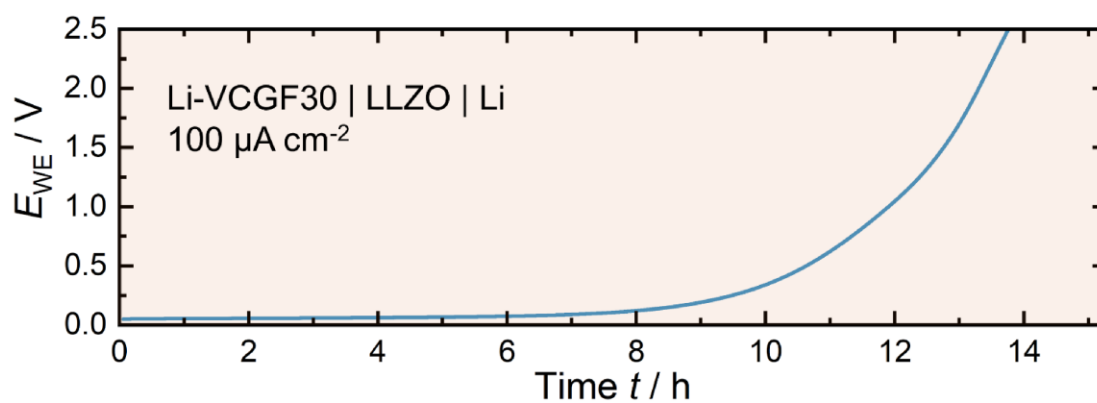


Figure S7. Voltage profile when stripping a Li-VCGF30 composite electrode. The performance is unchanged when compared to pure lithium. This may either be explained by the poor wetting of lithium on VCGF and thus, inhomogeneous distribution thereof, or rather that the VCGF is not capable in the same way of increasing the effective diffusion coefficient and guiding contact like CNTs.

Table S2. Summary of shear ( $v_s$ ) and longitudinal ( $v_l$ ) soundwave velocity in the analyzed specimens. Note that due to increasing inhomogeneity of Li-CNT30, shear wave velocity  $v_s$  was not assessable from acoustic measurements and was thus estimated to be  $2.6 \text{ km s}^{-1}$ . Wave speeds were averaged from several measurements on different parts of the analyzed specimens.

Material	$\rho / \text{g cm}^{-3}$	$v_s / \text{km s}^{-1}$	$v_l / \text{km s}^{-1}$	$E / \text{GPa}$
Li (Ref <sup>[6]</sup> )	0.533	$2.30 \pm 0.02$	$5.28 \pm 0.26$	7.82
Li-CNT10	0.540	$2.4 \pm 0.1$	$5.7 \pm 0.4$	8.97
Li-CNT20	0.581	$2.6 \pm 0.1$	$5.7 \pm 0.1$	10.89
Li-CNT30	0.588	2.6	$6.7 \pm 0.1$	11.23

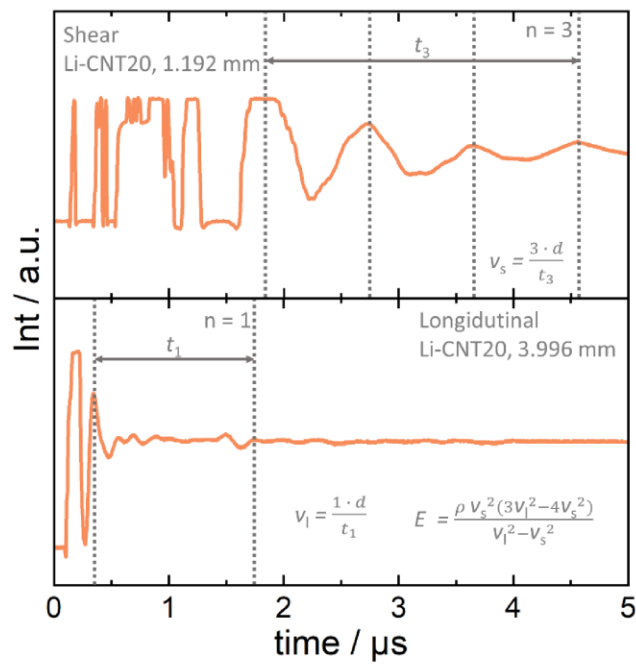


Figure S8. Example of the data acquisition for speed of sound measurements conducted within this work in the case of Li-CNT20 for shear wave speeds (top) and longitudinal wave speeds (bottom).

## Literature

- [1] T. Krauskopf, H. Hartmann, W. G. Zeier, J. Janek, *ACS Appl. Mater. Interfaces* **2019**, *11*, 14463–14477.
- [2] T. Krauskopf, B. Mogwitz, C. Rosenbach, W. G. Zeier, J. Janek, *Adv. Energy Mater.* **2019**, *9*, 1902568.
- [3] L. Stolz, G. Homann, M. Winter, J. Kasnatscheew, *Mater. Today* **2021**, *44*, 9–17.
- [4] H. J. S. Sand, *London, Edinburgh, Dublin Philos. Mag. J. Sci.* **1901**, *1*, 45–79.
- [5] J. T. S. Irvine, D. C. Sinclair, A. R. West, *Adv. Mater.* **1990**, *2*, 132–138.
- [6] A. Masias, N. Felten, R. Garcia-Mendez, J. Wolfenstine, J. Sakamoto, *J. Mater. Sci.* **2018**, *54*, 2585–2600.

- 7.1.5 Publication 5: “Working Principle of an Ionic Liquid Interlayer During Pressureless Lithium Stripping on  $\text{Li}_{6.25}\text{Al}_{0.25}\text{La}_3\text{Zr}_2\text{O}_{12}$  (LLZO) Garnet-Type Solid Electrolyte”

# Batteries & Supercaps

## Supporting Information

### **Working Principle of an Ionic Liquid Interlayer During Pressureless Lithium Stripping on $\text{Li}_{6.25}\text{Al}_{0.25}\text{La}_3\text{Zr}_2\text{O}_{12}$ (LLZO) Garnet-Type Solid Electrolyte**

Till Fuchs, Boris Mogwitz, Svenja-Katharina Otto, Stefano Passerini, Felix H. Richter,\* and Jürgen Janek\*

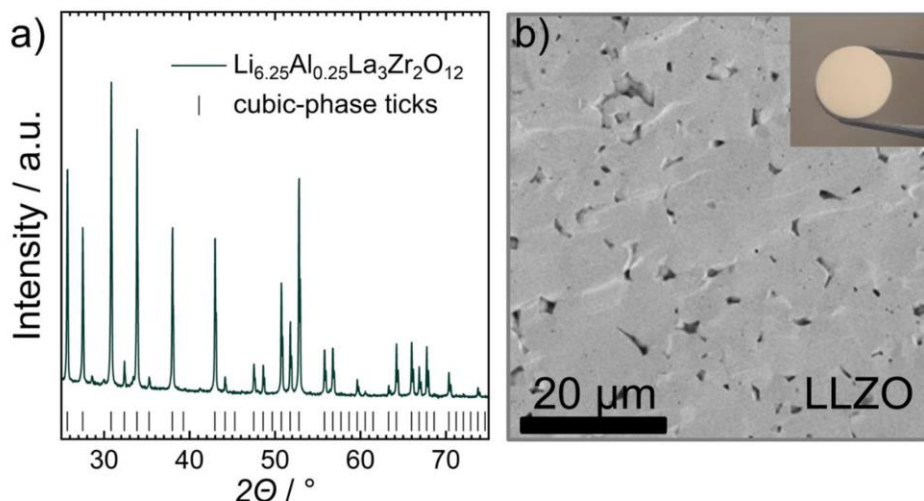


Figure S1. a) Powder diffraction pattern of the as-prepared LLZO alongside the phase ticks for the cubic polymorph. The impurity fractions are negligible. b) displays a typical cross section SEM image of a freshly broken LLZO pellet to access its microstructure without any polishing. It can be seen that the herein prepared pellets are fairly dense ( $95 \pm 1\%$  as obtained geometrically). The inset shows a digital photograph of a polished, homogeneous pellet.

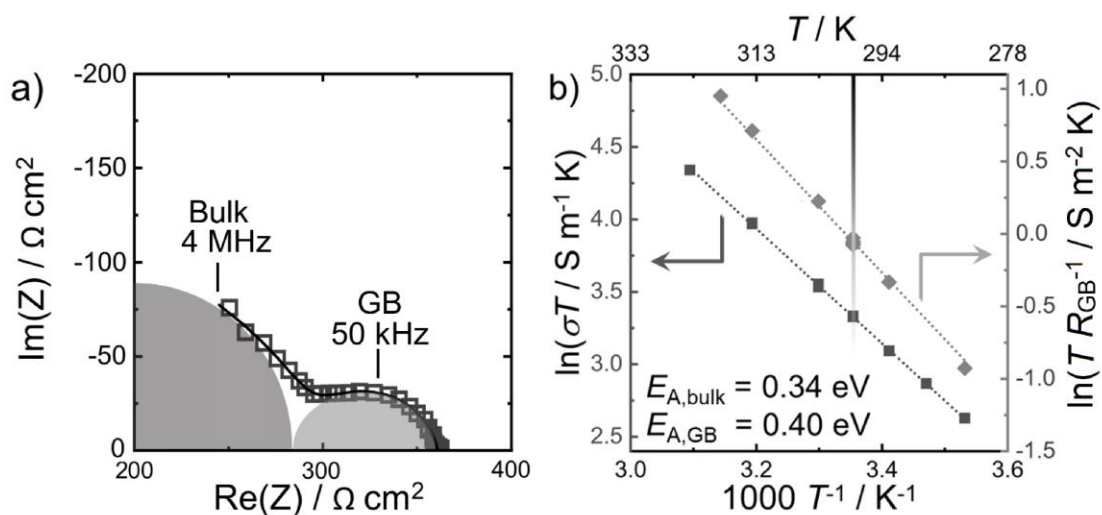


Figure S2. a) Nyquist-plot of  $\text{Li}_{\text{id}}|\text{LLZO}|\text{Li}_{\text{id}}$ . Contributions from bulk and grain boundary transport are well separated. The absence of a third contribution confirms negligible interfacial resistance between lithium and LLZO as already reported for this preparation route by Krauskopf et al.<sup>[1]</sup> b) Arrhenius plot and calculated activation energies for bulk and grain boundary contributions in LLZO.

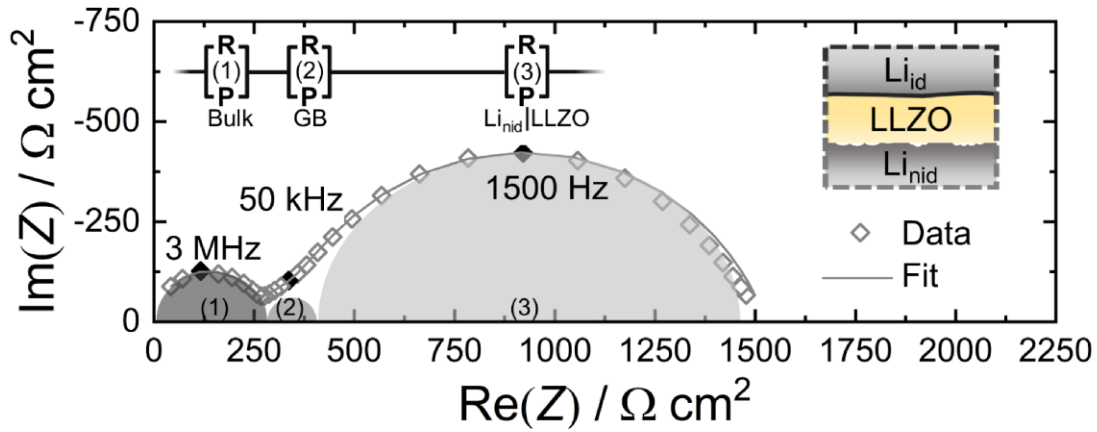


Figure S3. Impedance spectrum of a  $\text{Li}_{\text{nid}}|\text{LLZO}|\text{Li}_{\text{id}}$  cell displayed alongside the used equivalent circuit for fitting. Three different contributions are visible. In the high-frequency region, the bulk  $\text{Li}^+$ -transport in the material is contributing, followed by the grain boundary contribution. For mid to low frequencies the non-ideal  $\text{Li}_{\text{nid}}|\text{LLZO}$  interface is located at around 1500 Hz.

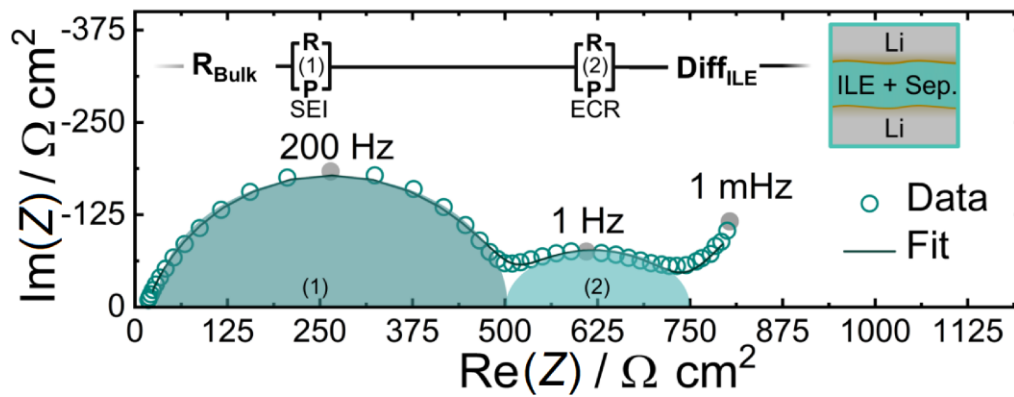


Figure S4. Impedance spectrum of a symmetric  $\text{Li}|\text{ILE}|\text{Li}$  cell displayed alongside the equivalent circuit used for fitting. Four different contributions are visible. The bulk resistance of the ionic liquid is located at very high frequencies, followed by the first semicircle, linked to the transport through the SEI. At low frequencies the semicircle corresponding to the electrochemical reactions (ECR) at the lithium electrode. At very low frequencies (1 mHz), a new process is indicated, herein linked to  $\text{Li}^+$  diffusion in the ILE, thus confirming that the previous semicircle can be unequivocally linked to the ECR.

To unequivocally rule out ILE diffusion in the observed LF impedance, symmetrical  $\text{Li}|\text{ILE}|\text{Li}$  cells without garnet separator were built and analyzed. Figure S4 displays the impedance response in the frequency range of 7 MHz to 1 mHz from a  $\text{Li}|\text{ILE}|\text{Li}$  cell with a corresponding equivalent circuit. An ohmic resistance followed by two semicircles is observed. Moreover, at very low frequencies

(1 mHz) another additional emerging process is indicated. We interpret the ohmic resistance at high frequencies to be caused by the bulk resistance of the used ILE (which yields an ionic conductivity of  $9.9 \text{ mS cm}^{-1}$ ). As the ILE thickness is approximately 1.5 mm in the Li|ILE|Li cell, the ohmic drop is not negligible as it is when only present as a thin interlayer in the above Li|ILE|LLZO|Li<sub>id</sub> cells.

Table S1. Summary of visible impedance contributions for as-built cell setups.

Cell setup	$f_{\text{Peak}} / \text{Hz}$	$R_i / \Omega \text{ cm}^2$	$C_{\text{RP}} / \text{F}$	Contribution
Li <sub>id</sub>  LLZO Li <sub>id</sub>	~7 M	298	$10^{-11}$	bulk
	~50 k	62	$10^{-8}$	grain boundary
Li ILE LLZO Li <sub>id</sub>	~7 M	285	$10^{-11}$	bulk
	~50 k	59	$10^{-8}$	grain boundary
	~400	232	$10^{-7}$	SLEI ILE LLZO SEI Li ILE
	~1	179	$10^{-4}$	ECR
Li <sub>nid</sub>  LLZO Li <sub>id</sub>	~7 M	308	$10^{-11}$	bulk
	~50 k	70	$10^{-9}$	grain boundary
	~2000	1201	$10^{-8}$	Li <sub>nid</sub>  LLZO
Li ILE Li	> 7 M	18	not resolved	bulk ILE
	~200	226	$10^{-7}$ - $10^{-6}$	SEI Li ILE
	~1	165	$10^{-4}$	ECR
	~1 m	not resolved	$>10^{-4}$	diffusion ILE

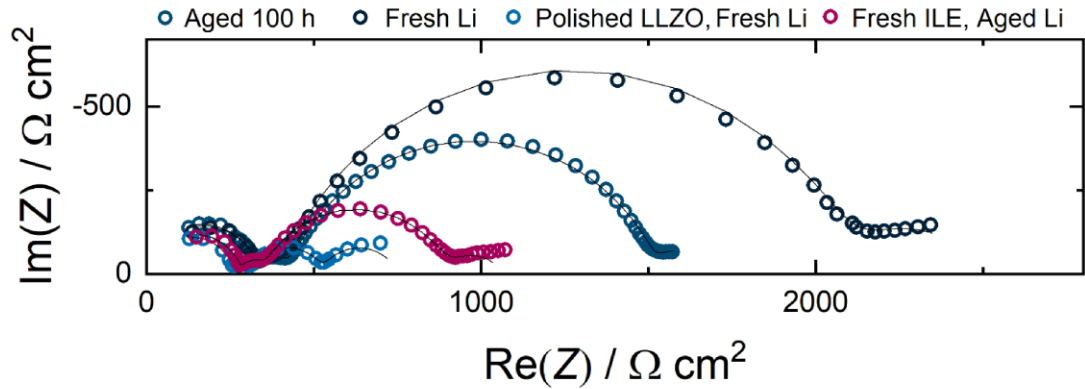


Figure S5. Nyquist plots of an aged Li|ILE|LLZO|Li cell, showing the effect of successively exchanging cell components to gain information about the aging of specific interphases.

Figure S5 not only shows the corresponding Nyquist plots to the cells analyzed in Table 1, but also one additional cell, where only the ILE was exchanged after aging. A reduction in  $R_{\text{MF}}$  is observed despite nothing else being changed. Two different effects may account for this decrease. One being that the ILE may degrade during electrode aging and change the interphase chemistry. Another being that, by exchanging the ILE, existing interphases are partially teared off or punctured, also

decreasing the resistance. It is, however, not possible to quantitatively determine these effects without detailed 4-electrode measurements, which were not performed in this work.

Table S2. Overview of the ionic conductivity  $\sigma$  of prepared ILEs.

$c_{\text{LiTFSI}} / \text{mol L}^{-1}$	$\sigma / \text{mS cm}^{-1}$
0.25	9.3
0.75	5.5
1.25	1.9
1.75	1.7

### Formation of LiF on LLZO

As electrochemical data suggest formation of a resistive SLEI between LLZO and ILE, this interphase was further analyzed with XPS. Note that since ILE residues on top of the SE pellet do not evaporate and can also not be washed away without potentially altering the SLEI, reliable depth profiling is not possible for these samples. However, a qualitative comparison between garnet from disassembled cells and fresh material can be made. Figure S5 displays the C 1s, F 1s and Zr 3d detail spectra for a pellet which was freshly polished compared to a cycled one after different sputter steps. For the cleaned LLZO pellet experimentally unavoidable surface impurities of aliphatic carbon (C-C) as well as residual -O-C=O, -C-O-C and -CO<sub>3</sub> species were observed. All corresponding signal intensities decrease with sputtering into the sample. For a pellet which was in contact with the ILE and electrochemically characterized, -CF<sub>3</sub> species, which are part of the used ILE, are additionally observed. Also, a higher intensity of -O-C=O and -C-O-C species was detected, which are probably decomposition products, as already seen by Pervez et al.<sup>1</sup> When sputtering deeper into the cycled sample, all carbon signals decrease in intensity, what indicates an interphase and/or ILE residue on the surface.

Looking at the F 1s region in Figure S5b, only weak signals are present for the polished pellet. They are most likely originated from surface contamination. However, when the pellet was in contact with ILE, two intense signals are observed, corresponding to -CF<sub>3</sub> and metal fluorides (LiF).<sup>1</sup> As the -CF<sub>3</sub> is most intense on the surface and the LiF signal is getting more intense with sputtering, LiF was probably formed at the interphase between LLZO and ILE. The increase of the Zr 3d signal in Figure S5c during sputtering indicates the uncover of the LLZO. The signal is less intense and also appears after longer sputtering times for the cycled cell than for the polished one, which may also indicate the formation of an additional interphase.

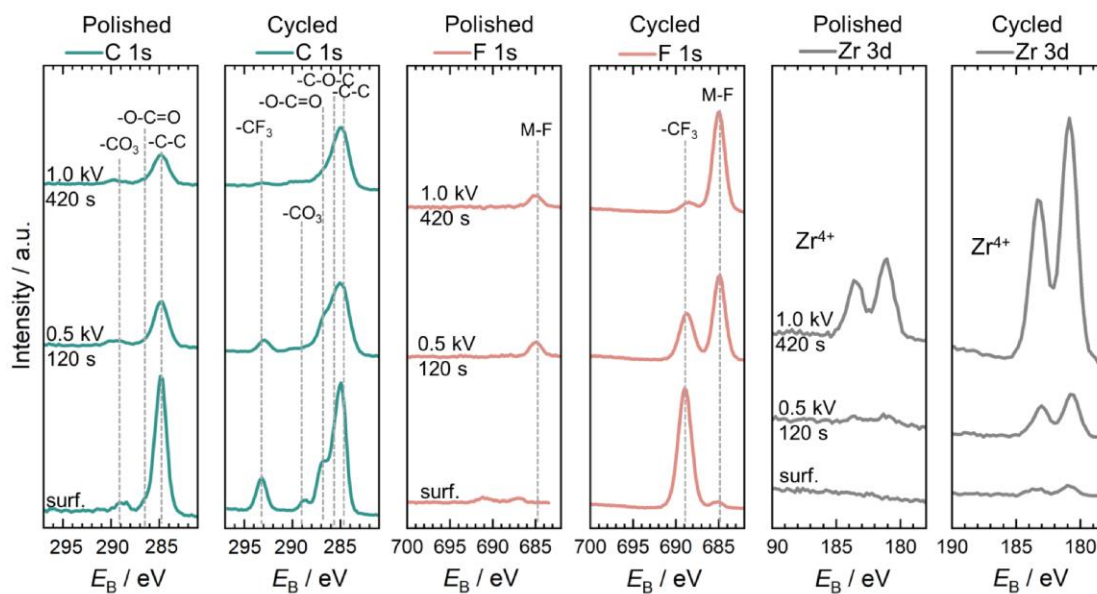


Figure S6. a) C 1s b) F 1s and c) Zr 3d XPS detail spectra without sputtering and after sputtering for 2 minutes with 0.5 kV and for 6 - 7 minutes with 1 kV  $\text{Ar}^+$ . The position of the different species is indicated according to Pervez et al.<sup>[2]</sup>

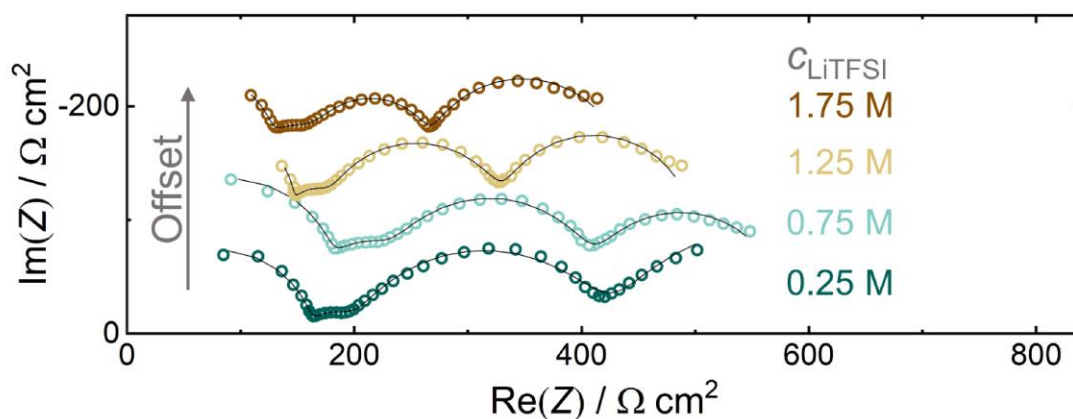


Figure S7. Nyquist plots of cells before stripping which employ ILEs with different salt concentrations and thus, viscosities. No obvious difference is observed; only slight variations occur which are explained by small variations in the electrode area and different LLZO pellets used.

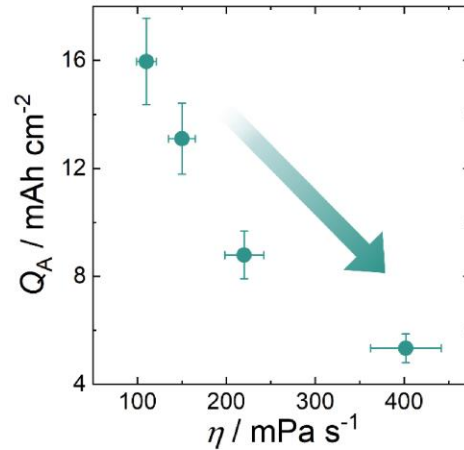


Figure S8. Plot showing the almost linear decrease in areal charge capacity  $Q_A$  with the ILE interlayer viscosity  $\eta$ .

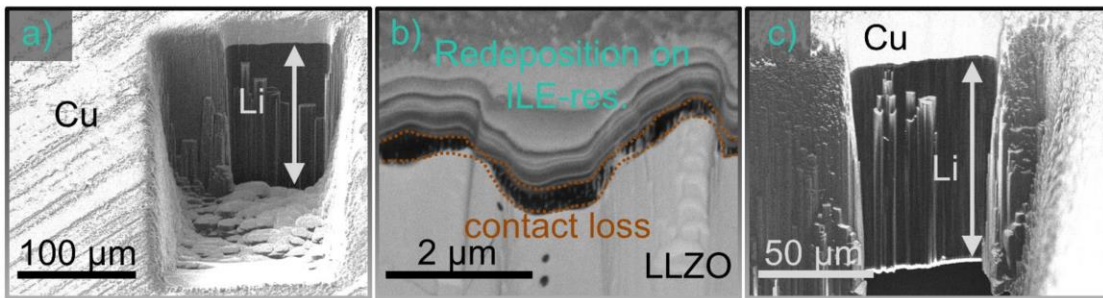


Figure S9. Additional FIB-SEM images to support statements in the main text. a) Crater in a cell, which experienced anodic current without contact loss. Despite deep cutting, only lithium is visible in the cross-section (100  $\mu\text{m}$ ), which hints at large inhomogeneities in the lithium thickness. b) Cut through a cell, which experienced anodic current until contact was completely lost. As only the LMA was visible in the image displayed in Figure 8, this image displays a cell, which was disassembled before FIB-SEM measurements. A small gap can still be observed between redeposition from FIB-cutting and the ILE residue to the LLZO ISE. c) Full image of a cut through the LMA where contact was completely lost to the LLZO electrolyte.

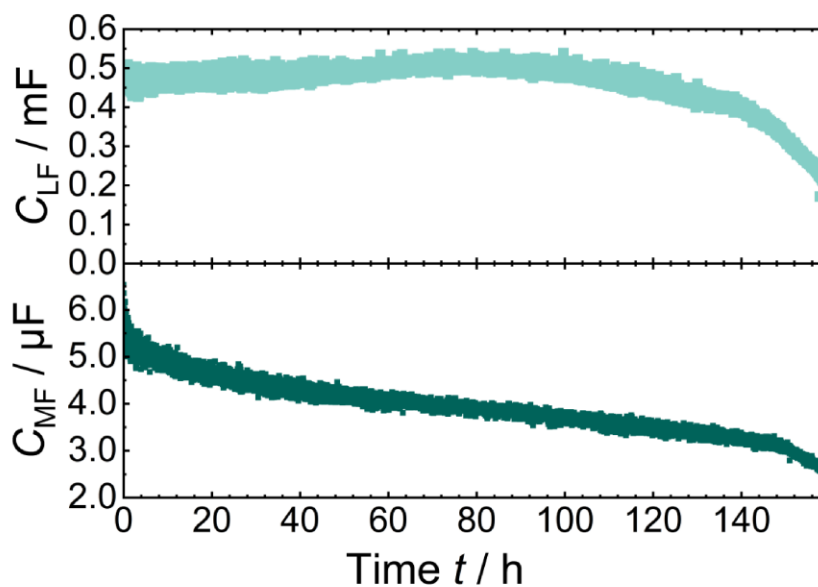


Figure S10. Evolution of obtained capacities when fitting the semicircles in mid-frequency (MF) range and low-frequency (LF) range. Mid-frequency corresponds to the interphases between ILE and Li and ILE and LLZO. The low-frequency process is attributed to ECR at the LMA.

## Literature

- [1] T. Krauskopf, H. Hartmann, W. G. Zeier, J. Janek, *ACS Appl. Mater. Interfaces* **2019**, *11*, 14463–14477.
- [2] S. A. Pervez, B. P. Vinayan, M. A. Cambaz, G. Melinte, T. Diemant, T. Braun, G. Karkera, R. J. Behm, M. Fichtner, *J. Mater. Chem. A* **2020**, 16451–16462.

## 7.2 Scientific Contributions

### 7.2.1 List of publications published online as checked on the 19<sup>th</sup> of December 2022

<sup>^</sup>Indicates shared first authorship

- 2022 Ren, Y.; Danner, T.; Moy, A.; Finsterbusch, M.; Hamann, T.; Dippell, J.; **Fuchs, T.**; Müller, M.; Hoft, R.; Weber, A.; Curtiss, L. A.; Zapol, P.; Klenk, M.; Ngo, A. T.; Barai, P.; Wood, B. C.; Shi, R.; Wan, L. F.; Heo, T. W.; Engels, M.; Nanda, J.; Richter, F. H.; Latz, A.; Srinivasan, V.; Janek, J.; Sakamoto, J.; Wachsmann, E. D.; Fattakhova-Rohlfing, D. Oxide-Based Solid-State Batteries: A Perspective on Composite Cathode Architecture. *Adv. Energy Mater.* **2022**.
- Fuchs, T.**<sup>^</sup>; Becker, J.<sup>^</sup>; Haslam, C. G.; Lerch, C.; Sakamoto, J.; Richter, F. H.; Janek, J. Current-Dependent Lithium Metal Growth Modes in “Anode-Free” Solid-State Batteries at the Cu|LLZO Interface. *Adv. Energy Mater.* **2022**.
- Eckhardt, J. K.; **Fuchs, T.**; Burkhardt, S.; Klar, P. J.; Janek, J.; Heiliger, C. 3D Impedance Modeling of Metal Anodes in Solid-State Batteries – Incompatibility of Pore Formation and Constriction Effect in Physical-Based 1D Circuit Models. *ACS Appl. Mater. Interfaces* **2022**.
- Singh, D. K.<sup>^</sup>; **Fuchs, T.**<sup>^</sup>; Krempaszky, C.; Mogwitz, B.; Burkhardt, S.; Richter, F. H.; Janek, J. Overcoming Anode Instability in Solid-State Batteries through Control of the Lithium Metal Microstructure. *Adv. Funct. Mater.* **2022**.
- Fuchs, T.**; Haslam, C. G.; Moy, A. C.; Lerch, C.; Krauskopf, T.; Sakamoto, J.; Richter, F. H.; Janek, J. Increasing the Pressure-Free Stripping Capacity of the Lithium Metal Anode in Solid-State-Batteries by Carbon Nanotubes. *Adv. Energy Mater.* **2022**.
- Otto, S.; Riegger, L. M.; **Fuchs, T.**; Kayser, S.; Schweitzer, P.; Burkhardt, S.; Henss, A.; Janek, J. In Situ Investigation of Lithium Metal – Solid Electrolyte Anode Interfaces with ToF-SIMS. *Adv. Mater. Interfaces* **2022**.
- 2021 Otto, S. K.; **Fuchs, T.**; Moryson, Y.; Lerch, C.; Mogwitz, B.; Sann, J.; Janek, J.; Henss, A. Storage of Lithium Metal: The Role of the Native Passivation Layer for the Anode Interface Resistance in Solid State Batteries. *ACS Appl. Energy Mater.* **2021**.
- Fuchs, T.**; Mogwitz, B.; Otto, S.; Passerini, S.; Richter, F. H.; Janek, J. Working Principle of an Ionic Liquid Interlayer During Garnet-Type Solid Electrolyte. *Batter. Supercaps* **2021**.
- 2020 Connell, J. G.<sup>^</sup>; **Fuchs, T.**<sup>^</sup>; Hartmann, H.; Krauskopf, T.; Zhu, Y.; Sann, J.; Garcia-mendez, R.; Sakamoto, J.; Tepavcevic, S.; Janek, J. Kinetic versus Thermodynamic Stability of LLZO in Contact with Lithium Metal. *Chem. Mater.* **2020**.

- Fuchs, T.**; Culver, S. P.; Till, P.; Zeier, W. G. Defect-Mediated Conductivity Enhancements in  $\text{Na}_{3-x}\text{Pn}_{1-x}\text{W}_x\text{S}_4$  (Pn = P, Sb) Using Aliovalent Substitutions. **2020**.
- 2019 Walther, F.; Koerver, R.; **Fuchs, T.**; Ohno, S.; Sann, J.; Rohnke, M.; Zeier, W. G.; Janek, J. Visualization of the Interfacial Decomposition of Composite Cathodes in Argyrodite-Based All-Solid-State Batteries Using Time-of-Flight Secondary-Ion Mass Spectrometry. *Chem. Mater.* **2019**.
- Ohno, S.; Helm, B.; **Fuchs, T.**; Dewald, G.; Kraft, M.; Culver, S.; Senyshyn, A.; Zeier, W. Further Evidence for Energy Landscape Flattening in the Superionic Argyrodites  $\text{Li}_{6+x}\text{P}_{1-x}\text{M}_x\text{S}_5\text{I}$  (M = Si, Ge, Sn). *Chem. Mater.* **2019**.
- 2018 Kraft, M. A.; Ohno, S.; Zinkevich, T.; Koerver, R.; Culver, S. P.; **Fuchs, T.**; Senyshyn, A.; Indris, S.; Morgan, B. J.; Zeier, W. G. Inducing High Ionic Conductivity in the Lithium Superionic Argyrodites  $\text{Li}_{6+x}\text{P}_{1-x}\text{Ge}_x\text{S}_5\text{I}$  for All-Solid-State Batteries. *J. Am. Chem. Soc.* **2018**.

## 7.2.2 List of Conference Contributions

- 2022      Poster Presentation: **Bunsen Meeting on Solid-State Batteries V**, Frankfurt, Deutschland (11/2022): *Current-Dependent Lithium Metal Growth Modes in ‘Anode-Free’ Solid-State Batteries at the Cu/LLZO-Interface*
- Oral Presentation: **MRS Spring 2022, Honolulu, HI, USA. Session “Solid-State Batteries—From Electro-Chemo Mechanics to Devices”** (05/2022): *Carbon Nanotubes as Li<sup>0</sup>-Highways in Lithium Metal Anodes*
- Online Oral Presentation: **Online Symposium “Lithium Metal Anodes and their Application in Batteries”** (02/2022): *Carbon Nanotubes as Li<sup>0</sup>-Highways in Lithium Metal Anodes*
- 2020      Online Oral Presentation: **Online ECS PRiME 2020, Session “Advances, Challenges, and Development of Solid State Battery Electrochemistry and Materials”** (10/2020): *Lithium Dissolution Using Garnet-Type Solid Electrolyte with a Thin Ionic Liquid Interlayer*

## 8 Acknowledgements

At first, I want to express my gratitude to Prof. Jürgen Janek, who as my supervisor gave me the opportunity to work, learn and grow in his working group. Additionally, I would like to thank him for his constant support and curiosity regarding my research and numerous discussions and opportunities which helped me to develop myself professionally and personally.

I especially thank Dr. Felix H. Richter for further supervising and supporting me. I enjoyed our discussions and his persistent improvements to my writing, even when I continued to repeat the same errors again and again.

Furthermore, I would like to thank Prof. Bernd Smarsly for being the 2<sup>nd</sup> reviewer of this dissertation and Prof. Peter Klar for being part of the examination committee of my doctoral defense.

Special thanks also go to Prof. Jeff Sakamoto, who supported my stay at the University of Michigan and supervised my research in his group and kindly also is part of the examination committee. Thanks to his students and my friends Alex Moy, Catherine Haslam and Max Palmer for making my stay in Ann Arbor so very memorable.

I would like to thank my cooperation partners both at JLU and within the US-Germany project I had the pleasure to work with for countless fruitful discussions and joint research. Special thanks also go to Dr. Bjoern Luerßen, Dr. Marcus Rohnke, Dr. Klaus Pepler, Dr. Anja Henß and Dr. Boris Mogwitz within the working group for always being helpful and supportive when I had questions.

I further thank all of my colleagues and friends in the Janek group for generating such a fun and enjoyable working atmosphere and for countless discussions – sometimes on research and sometimes not so much – in the kitchen, during lunch or elsewhere. Also, without the help and support of many former colleagues, much of the work would not have been possible. Therefore, I want to thank Dr. Thorben Krauskopf and Dr. Svenja-Katharina Otto for their continuous help and always being open to so many of my questions. Special thanks also go to my colleagues and friends Simon Kunz, Till Ortmann and Juri Becker. On the one hand I am grateful for their support, but even more I thank them for always being up for talking nonsense and enduring me in our *Zentrale*.

Additionally, I want to thank my friends I made from studying materials science (our little *mawi-gang*) for always looking out for each other and pulling through both our Bachelor and Master program and creating a lot of fun memories.

Last but not least, I want to express my gratitude to my family and especially to my fiancée Kathi, who continuously supported me during my time at the university. I am grateful for having such an open-minded and unconditionally loving family and partner. Ich liebe euch, danke!